University of Glasgow

Thomson, Lisa (2022) *Controlling the formulation structures and properties of Low Molecular Weight Gelators.* PhD thesis.

http://theses.gla.ac.uk/83140/

Controlling the Formulation Structures and Properties of Low Molecular Weight Gelators

Lisa Thomson

Submitted in fulfilment of the requirements for the Degree of Doctor of Philosophy

School of Chemistry
College of Science and Engineering
University of Glasgow
September 2022

Declaration

This Thesis has been written and compiled by the author, Lisa Thomson, who carried out the research at the University of Glasgow between 2018 and 2022 under the supervision of Professor Dave Adams. I declare that this Thesis is the result of my own work, and any contributions from others is explicitly referenced. This work has not been submitted for any other degree at the University of Glasgow or any other institution.

Lisa Thomson

Abstract

Low Molecular Weight Gelators (LMWGs) are a versatile class of material which, when an appropriate stimulus is applied, can form organogels or hydrogels by self-assembly. In general, to form LMWG hydrogels, the LMWG is first suspended in water at high pH to form a precursor solution. This precursor solution can then be used to form hydrogels by various trigger methods including, but not limited to, a pH change, addition of metal ions or by temperature change. Structures are formed by the gelator molecules in both the solution and gel phases. In this Thesis, we report on the ability to control these structures in order to develop materials with a range of interesting properties.

We describe a preparation method for the creation of the LMWG precursor solutions. To do this, we examine the effects of stirring, pH and addition of salt during the solution preparation stage. We show that all three factors investigated have some effect on the solutions which contain "living" worm-like micellar structures. The preparation method is suitable for various concentrations of solution and gives reproducibly similar looking solutions as well as reproducible rheology and images under cross-polarised light.

We then use this preparation method to examine the LMWG solution structures of a single gelator in more detail. To do this, we utilise rheology, polarised optical microscopy and small-angle X-ray scattering. We show that different structures are present in the solutions when the concentration of gelator and the counterions present in the solutions are altered. This in turn alters the overall properties of the solutions. When applying different stimuli to these solutions (temperature and magnetic field) the different structures respond in different ways. We show examples of how we can utilise these different solution properties with specific applications in mind.

Finally, we control the LMWG structures in the gel phase to produce gradient stiffness hydrogels. We do this by incorporating a photoacid generator to the gelator precursor solution and irradiate with ultraviolet light. To examine the overall bulk properties of these gels we use traditional oscillatory rheology and to prove the existence of different stiffnesses within a single sample, we use cavitation rheology. Cavitation rheology is able to detect the subtle differences in stiffness within the gels which traditional bulk rheology cannot. The gradients in stiffness are temporary due to the reversible nature of these

materials. The gradient gels have potential for use in tissue engineering where the different gel stiffnesses mimic the different stiffnesses of tissue in the body.

Overall, we show LMWG systems exhibit diverse structures in both the solution and gel phases. This transfers to the overall properties of both phases. This work provides a greater understanding of the relationship between gelator structures and bulk properties of the materials; and challenges the conception that new gelator molecules must be discovered in order to achieve new or specific properties.

Acknowledgements

Firstly, I would like to thank my supervisor Dave Adams for all his support and time over the last five years. I will never forget you running past me in the lab as a terrified undergrad student and casually asking if I wanted a PhD before running off again. I have loved my time in the lab and I am so grateful for all the opportunities.

There would be a lot less work in this Thesis (and sometimes I wish there was) without all the help from others I have received. With that in mind, thank you to all the technical staff at the University of Glasgow, especially David and Alec for the access to the NMR facilities. To the other collaborators who have contributed towards my projects in this Thesis: Henry Ng, Joe Homer, Eirini Theodosiou, Paul Topham, Louise Serpell, Rob Poole, Emily Draper and Ralf Schweins, thank you for your work. The biggest thank you goes to Annela Seddon. You spent so much time working with my disgusting samples and had to do so much to understand them. I really appreciate the effort and have really enjoyed working with you.

Most of the reason I have loved completing my PhD in the Adams group is the people. To all the Adams family, past (Kate, Bart, Emily, Ana Mari, Demetra, Pedro, Alazne, Zaloa, José, Thaisa, and all the undergraduate project students) and present (Santanu, Dan, Libby, Courtenay, Valentina, Chloe, Max, Qingwen, Simona, Rui, Maria Laura, Ian and Paolo), I cannot thank you all enough for the long lunch breaks hiding in the basement or dodging the falling ceiling in the upstairs office. I thank you all for your encouragement, for listening to my moaning, and for the great memories I am taking with me. Ana Mari – thank you for being the kindest and most supportive person I have ever met. I will never forget our time at Diamond sealing capillaries at 4 am whilst singing and dancing. I am proud to be your first student. Kate – you are an inspiration. I learned so much from you and I am very grateful for that. Libby – thank you for being part of the Group 2 COVID crew. You are such great fun to be around and I know you are going to be so successful in whatever you do next. Dan – our time in the lab (when you were actually in the lab and not on holiday) I have really enjoyed – especially when playing with spider webs qualified as working. I couldn't have got through the PhD without you (and Beth!). I am really sad you're leaving Glasgow but I wish you both all the best back home.

I would also like to say thanks to the rest of the friends I have made in the Raphael lab from the Drapers (Sam, Becky, Jakki, Rebecca, Amina and Nick) and the Symes (Mike, Calum, Thanasis and Paddy). One Drink Egan – I can't believe I still haven't got rid of you yet! Thank you for coming back for your PhD. Although it's maybe not the experience you thought it might be, I am selfishly very grateful you came back, for all your support, the laughs we've had, and that you didn't let Becky film Drag Queen Bingo. Becky – you were always better at writing nice messages! I have really enjoyed getting to know you during our four years together. Drawing angry and sad faces on weighing boats, almost setting the JBB on fire with sweet potato chips and our trip to Cardiff are just some of the many highlights. I wish you and Niall all the best in your next adventure.

To all my family (Mum, Dad, Adam, Gran Clark, Papa Clark, Gran Jess and Papa Thomson), thank you so much for your interest in my work and for supporting me during my PhD. I am very grateful for it and love you all. Also, a huge thank you goes to my friends: Nicola, Iona, Louise, Kenna, Reb, Olivia, Emma N, Katie, Emma C, Eloise and Kirsty. Thank you for always checking in and getting me through. You all mean so much to me.

To Ali, if it wasn't for you I would have fulfilled my dream of giving up and working in a bakery by now. As great as I still think that would be, I am glad you didn't let me give up. Your support has been amazing. I am excited for whatever is next for us. You're my favourite.

Finally, thank you to the University of Glasgow for funding my PhD and for being part of my life for the last eight years. It's been a long eight years, but I wouldn't change any of it.

List of Publications from This Degree

1) **L. Thomson**, D. Osborne, R. Ginesi, E.R. Draper, D.J. Adams, Photothermal Perylene Bisimide Hydrogels, manuscript in preparation.

2) J. Simpson, **L. Thomson**, B. Dietrich, D.J. Adams, N.G. Berry, Predicting the Properties of Supramolecular Gels, manuscript in preparation.

3) **L. Thomson**, D. McDowall, L.J. Marshall, O. Marshall, H. Ng, W.J.A. Homer, E. Theodosiou, P.D. Topham, L.C. Serpell, R.J. Poole, A. Seddon, D.J. Adams, Transferring molecular level changes to bulk properties via tunable self-assembly and hierarchical ordering, submitted.

4) R. Huang, D. McDowall, H. Ng, **L. Thomson**, Y.K. Al-Hilaly, J. Doutch, S. Burholt, L.C. Serpell, R.J. Poole and D.J. Adams, *Chem. Comm.*, 2022, DOI: 10.1039/D2CC03646K.

5) **L. Thomson** and D.J. Adams, Responsive Materials from the Self-assembly of Low Molecular Weight Gelators, in *Chemoresponsive Materials: Smart Materials for Chemical and Biological Stimulation, Second Edition*, RSC, 2022, pp. 96-128.

6) M. Cariello, B. Dietrich, **L. Thomson**, V. Gauci, A. Boyer, S. Sproules, G. Cooke, A. Seddon, D.J. Adams, A Flavin-based Gelator for Visible Photooxidation, *Chem. Eur. J.*, 2022, **28**, e202201725.

7) D. Giuri, L.J. Marshall, B. Dietrich, D. McDowall, **L. Thomson**, J.Y. Newton, C. Wilson, R. Schweins and D.J. Adams, Exploiting and controlling gel-to-crystal transitions in multicomponent supramolecular gels, *Chemical Science*, 2021, **12**, 9720-9725.

8) D. McDowall, B.J. Greeves, R. Clowes, K. McAulay, A.M. Fuentes-Caparrós, **L. Thomson**, N. Khunti, N. Cowieson, M.C. Nolan, M. Wallace, A.I. Cooper, E.R. Draper, A.J. Cowan and D.J. Adams, Controlling Activity by Self-assembly – Tuning Perylene Bisimide Photocatalysts for the Hydrogen Evolution Reaction, *Adv. Energy Mater.*, 2020, **10**, 2002469.

9) K. McAulay, H. Wang, A.M. Fuentes-Caparrós, **L. Thomson**, N. Khunti, N. Cowieson, H. Cui, A. Seddon and D.J. Adams, Isotopic Control over Self-Assembly in Supramolecular Gels, *Langmuir*, 2020, **36**, 8626-8631.

10) **L. Thomson**, R. Schweins, E.R. Draper and D.J. Adams, Creating Transient Gradients in Supramolecular Hydrogels, *Macromol. Rapid Commun.*, 2020, **41**, 2000093.

11) K. McAulay, **L. Thomson**, L. Porcar, R. Schweins, N. Mahmoudi, D.J. Adams and E.R. Draper, Using Rheo-Small-Angle Neutron Scattering to Understand How Functionalised Dipeptides Form Gels, *Organic Materials*, 2020, **2**, 108-115.

12) K. McAulay, P.A. Ucha, H. Wang, A.M. Fuentes-Caparrós, **L. Thomson**, O. Maklad, N. Khunti, N. Cowieson, M. Wallace, H. Cui, R.J. Poole, A. Seddon and D.J. Adams, Controlling the Properties of the Micellar and Gel Phase by Varying the Counterion in Functionalised Dipeptide Systems, *Chem. Comm.*, 2020, **56**, 4094-4097.

Contents

Abbreviations

°C – Degrees Celsius

µg – Micrograms

µm – Micrometers

µL – Microlitres

δ – Chemical shift

λ – Wavelength

λ_E – Extensional relaxation time

θ – Scattering angle

1D – 1 dimensional

^1H – Hydrogen

^{13}C – Carbon

2D – 2 dimensional

^2H – Deuterium

2Nap – 2-Naphthoxyacetic acid

2NapFF – (2S)-2-[(2S)-2-[2-(naphthalen-2-yloxy)acetamido]-3-phenylpropanamido]-3-phenylpropanoic acid

2NapFF-Na – (2S)-2-[(2S)-2-[2-(naphthalen-2-yloxy)acetamido]-3-phenylpropanamido]-3-phenylpropanoic acid, formed with sodium hydroxide

2NapFF-TBA – (2S)-2-[(2S)-2-[2-(naphthalen-2-yloxy)acetamido]-3-phenylpropanamido]-3-phenylpropanoic acid, formed with tetrabutylammonium hydroxide

3D – 3 dimensional

Å – Angstrom

A – Ampere

Boc-F – tert-butyloxycarbonyl-protected phenylalanine

C-terminus – Carboxyl-terminus

Ca^{2+} – Calcium ions in the +2 oxidation state

$CaCl_2$ – Calcium chloride

$CaCO_3$ – Calcium carbonate

$CHCl_3$ – Chloroform

cm – centimetre

CMC – Critical micelle concentration

CMCs – Critical micelle concentrations

CP – Cone-plate

CRAB – Cavitation Rheometer Analyser Box

Cryo-TEM – Cryogenic-transmission electron microscopy

D_2O – Deuterated water

DMSO – Dimethyl sulfoxide

DMSO-d_6 – Deuterated dimethyl sulfoxide

DPIN – diphenyliodonium nitrate

et al. – and others

Fmoc – Fluorenylmethoxycarbonyl protecting group

F-OEt – phenylalanine ethyl ester hydrochloride

g – gram

G – Gauge

G′ – Storage Modulus

G″ – Loss Modulus

GdL – Glucono-δ-lactone

H_2 - Hydrogen

H_2O – Water

HCl – Hydrochloric acid

Hz – Hertz

IBCF – Iso-butyl chloroformate

in vacuo – In a vacuum

IR – Infrared

J – Coupling constant

K – Lysine amino acid

LCST – Lower critical solution temperature

LiOH – Lithium hydroxide

LMWG – Low Molecular Weight Gelator

LMWGs – Low Molecular Weight Gelators

M – mole

MBTT – 2-(4-methoxystyryl)-4,6-bis(trichloromethyl)-1,3,5-triazine

mg – Milligrams

MHz – Megahertz

min – Minute

mL – Millilitre

mm – Millimetre

mM – Millimole

ms – Millisecond

mW – Milliwatt

$\vec{n}$ – Liquid crystal director

N-capped – Amine-capped terminus

N-terminus – Amine-terminus

^{23}Na – Sodium

NaCl – Sodium chloride

NaOH – Sodium hydroxide

nm – Nanometers

NMM – N-methylmorpholine

NMR – Nuclear magnetic resonance

NDIs – Naphthalene diimides

O_2 – Oxygen

Pa – Pascal

PA – Peptide amphiphile

PAs – Peptide amphiphiles

PAG – Photoacid generator

PAGs – Photoacid generators

Pb^{2+} – Lead ions in the +2 oxidation state

PBIs – Perylene bisimides

P_C – Critical pressure

PDMS – Polydimethylsiloxane

PDIs – Perylene diimides

Ph – Phenyl ring

POM – Polarised optical microscopy

PP – Parallel-plate

ppm – Parts per million

Q – Scattering vector

Q* – Structure factor peak

rpm – Revolutions per minute

s – seconds

SANS – Small-angle neutron scattering

SAXS – Small-angle X-ray scattering

SmA – Smectic A

SmC – Smectic C

tanδ – Damping factor

TBAOH – Tetrabutylammonium hydroxide

T_{gel} – Gelation temperature

THF – Tetrahydrofuran

™ – Trademark

UV – Ultraviolet

UV-vis – Ultraviolet-visible

V – Valine amino acid

w/w – Weight per weight

Chapter 1. Introduction

This Chapter is adapted from the following publication:

"Responsive Materials from the Self-assembly of Low Molecular Weight Gelators"

L. Thomson and D.J. Adams, in *Chemoresponsive Materials: Smart Materials for Chemical and Biological Stimulation, Second Edition*, RSC, 2022, pp. 96-128.

LT was responsible for researching, creating figures and writing the publication. DJA supervised the project. LT wrote the initial draft of the manuscript, to which both authors contributed to for the final publication.

1.1. Hydrogels

Hydrogels are a class of soft matter which have increased in popularity in recent years.[1] They are used in many applications including in sensing,[2] electronics,[3] and the food and pharmaceutical industries.[4, 5] Hydrogels exhibit solid-like rheological behaviour, despite being predominantly composed of water. Hydrogel networks can be formed from both natural and synthetic materials.[6-8] Networks can be cross-linked either chemically or physically. In general, polymeric hydrogels are formed via chemical bonds between polymer monomers to form polymeric chains, and chemical bonds or physical cross-links which are formed between chains (Figure 1.1a).[9] Chemically cross-linked hydrogels generate a robust and irreversibly formed gel by the formation of covalent bonds throughout the system. Physically cross-linked hydrogels are held together via weak, non-covalent interactions between the monomers which make up chains and between these chains; this produces reversible hydrogels.[10] Hydrogen bonding, the hydrophobic effect and π-π stacking are examples of such non-covalent interactions.[11, 12] One group of physically cross-linked hydrogels are formed using low molecular weight gelators (LMWGs). These LMWGs will be discussed in this Thesis. LMWGs are molecules with a molar mass of 3000 or less (typically much less than this),[13] and form via self-assembly and surface tension; an entangled network traps water, resulting in hydrogels (Figure 1.1b).[14-16] The two formation mechanisms are not exclusive to the systems described above. For example, our group has recently shown that LMWGs can gel by forming self-assembled chains which can then be covalently cross-linked. Therefore, Figure 1.1 shows a scheme for the general gelation mechanisms for both polymeric and LMWG gelation.
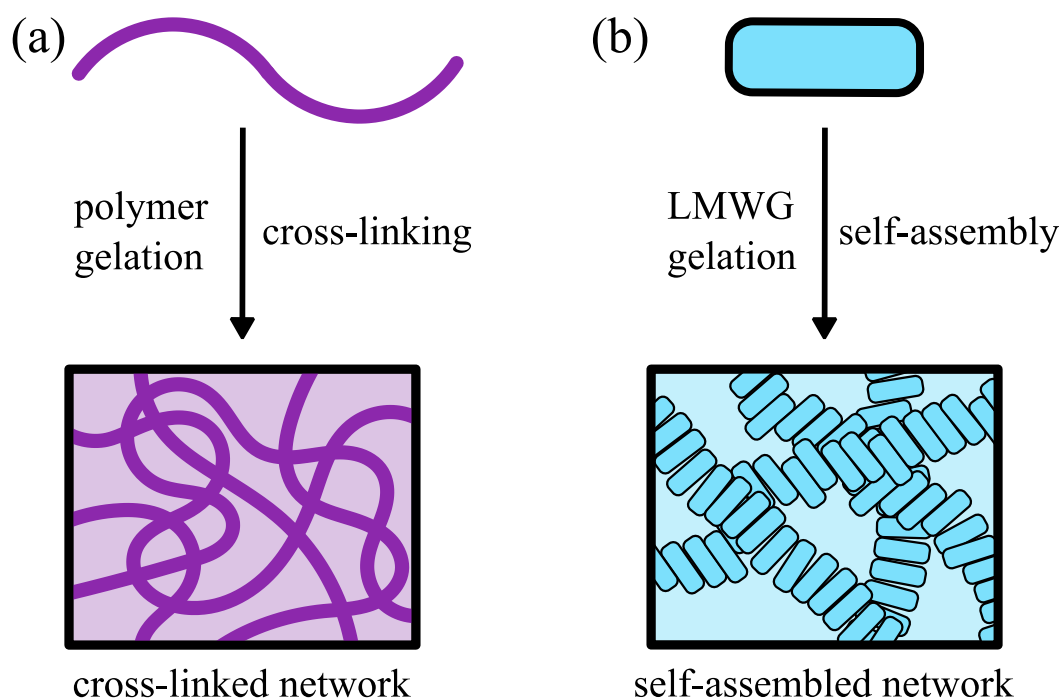
Figure 1.1. Scheme illustrating the typical formation mechanisms of hydrogels using (a) polymers and (b) LMWGs. The network formed immobilises water, giving a hydrogel.

1.2. Low Molecular Weight Gelators

Hydrogels formed from LMWGs tend to have less mechanical stability compared to polymeric hydrogels.[17] Other solvents can also be immobilised to form gels; for example, the immobilisation of an organic solvent produces organogels.[16] To form a hydrogel from LMWGs, initially the LMWG molecules are suspended in water (Figure 1.2a). Next, a stimulus or trigger is applied to the solution containing the LMWG. This trigger must be such that the solubility of the LMWG decreases when the trigger is applied. This encourages interactions between the LMWG molecules, resulting in aggregation and formation of 1D structures (Figure 1.2b). Further interactions occur between the 1D structures and thus entanglement and association occur resulting in a 3D network. The immobilisation of water by this LMWG network produces a self-supporting hydrogel (Figure 1.2c).[18, 19] Various types of 1D structures are possible including fibres formed by β-sheet peptides,[20] and helical/coiled ribbons.[21] Shorter fibres are less favourable for gelation since long, thin and flexible fibres are better for entanglement and water trapping.[22]
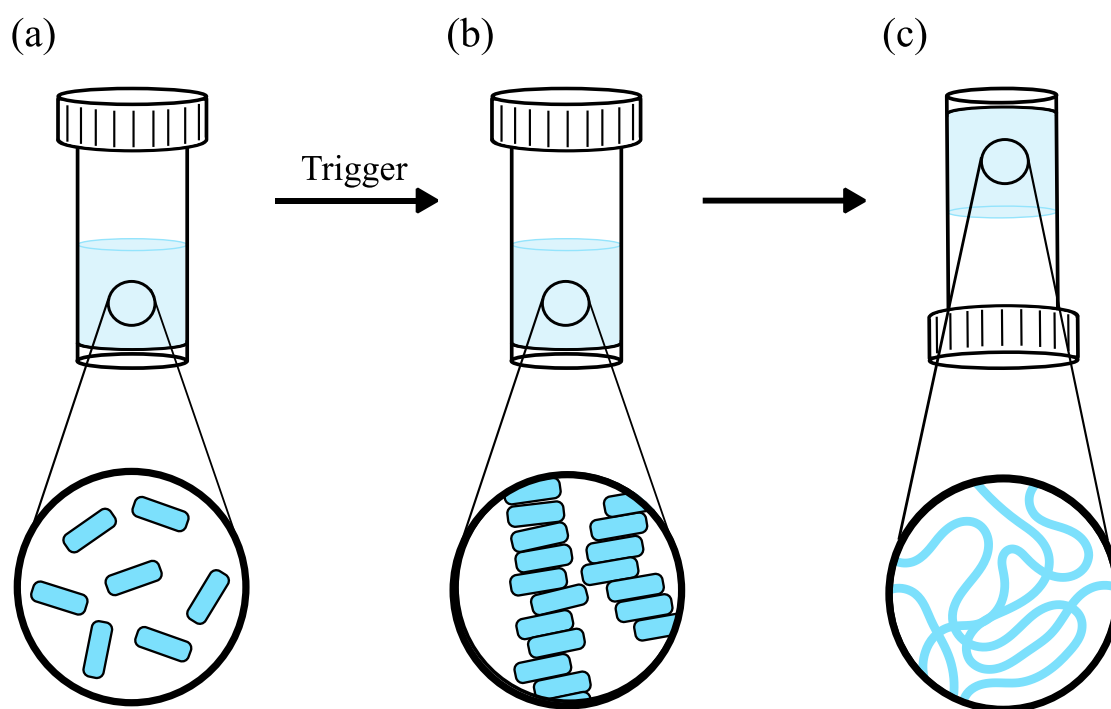
Figure 1.2. Scheme depicting the self-assembly process for LMWGs. (a) Initially LMWG molecules are suspended in water; (b) structure formation begins when a trigger is applied; (c) a self-supporting hydrogel is formed due to water immobilisation by a network of structures.

Crystallisation is an alternative outcome to gelation.[22-24] Crystallisation indicates the phase separation of 3D crystals of solute from solution, instead of a 3D network capable of trapping solution.[24] The transition of a gel to crystals, which happens occasionally, demonstrates the meta-stable nature of these gels and emphasises the strong relationship between the gel and crystal states.[25] Instead of a gel-to-crystal transition occurring, it is also possible for gels and crystals to co-exist.[26] Syneresis, the contraction of a gel and subsequent expulsion of liquid, also shows the partially stable nature of some gels. This property could be exploited for the capture and release of pollutants, drugs, or other small molecules.[25]

1.3. Gelator Design

The design of LMWGs is important for forming hydrogels with desired properties for a particular application. This is challenging, however, because many LMWGs are discovered by trial-and-error.[27] Despite the fact that research into predicting LMWG gelation has been successful,[28-32] no work yet has been able to predict the properties of the gels made from these successful LMWGs; and developing new LMWGs that produce gels with certain properties for specific applications is challenging. Some predictors require the synthesis of the molecules and screening in order to predict if it will gel, making it unfavourable.[29, 30] Limitations also exist when using solely computational predictors, for example, computational limitations and accuracy; and the reliability and robustness of the descriptors used for simulation and prediction.[31]

A small number of exemplar LMWG structures are shown in Figure 1.3. As already noted, LMWGs are frequently discovered through serendipity, making them therefore difficult to design. However, there are common features of many LMWGs. The fragments used to create LMWGs are normally such that they allow for the hydrophobic effect, π–π stacking and hydrogen bonding so self-assembly and gelation can occur.[33, 34] LMWGs are based on many types of molecules such as amino acids,[35] peptide amphiphiles,[36] saccharides,[37] ureas,[38] cholesterols,[39] nucleobases,[40] sugars,[41] perylene bisimides (also called perylene diimides),[42] and naphthalene diimides.[43]

(1)   **(2)**   **(3)**

(4)   **(5)**   **(6)**

(7)   **(8)**   **(9)**

(10)
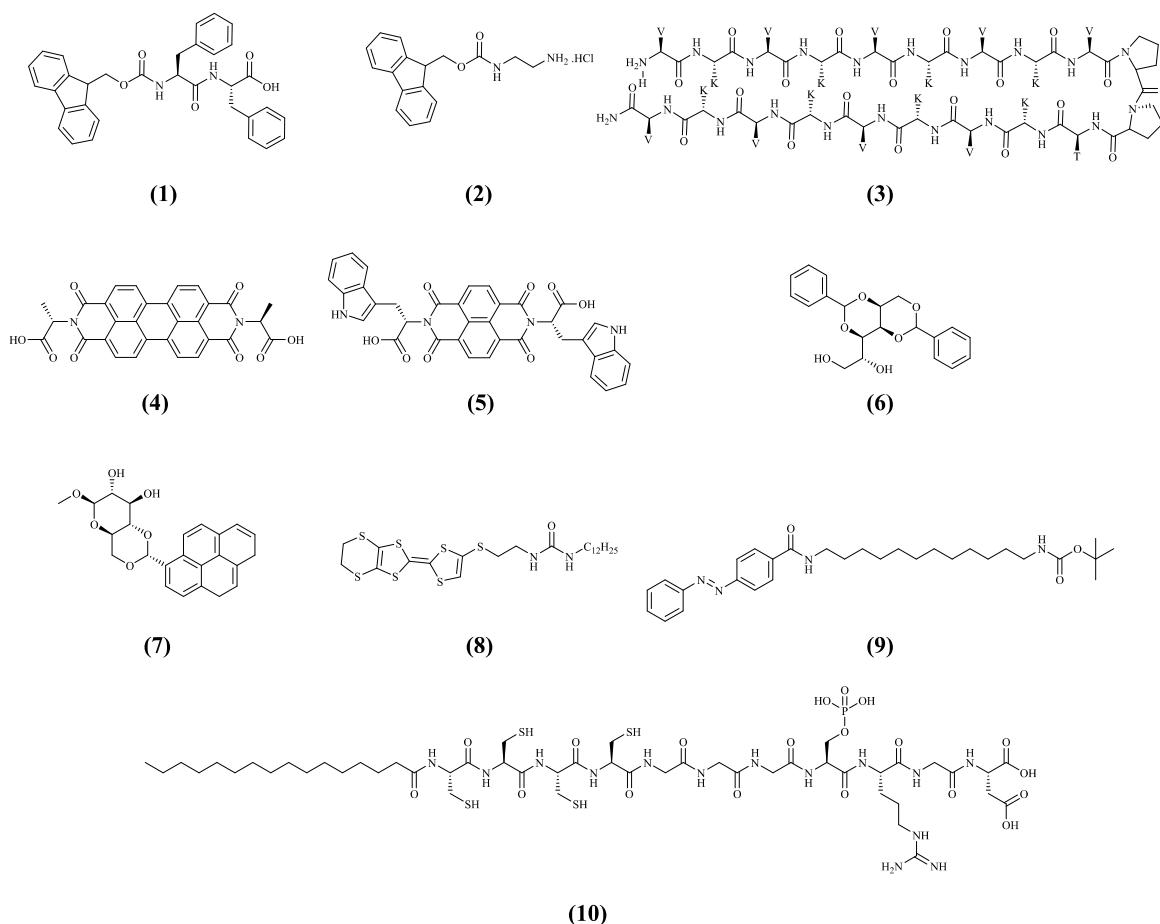
Figure 1.3. A small set of example types of LMWGs showing the structural diversity within this class: (**1**) fluorenylmethoxycarbonyl-dipeptide with free *C*-terminus;[44] (**2**) fluorenylmethoxycarbonyl protecting group with free *N*-terminus;[45] (**3**) MAX1;[46] (**4**) perylene bisimide/perylene diimide;[47] (**5**) naphthalene diimide;[48] (**6**) 1,3:2,4-Dibenzylidene-D-sorbitol;[8] (**7**) saccharide containing LWMG with pyrene protecting group;[37] (**8**) urea-based LMWG;[38] (**9**) azobenzene containing LMWG;[49] (**10**) peptide amphiphile.[50]

Even slight modifications in LMWG structure are known to substantially impact gelation effectiveness. For example, changing the sequence of amino acids within a LMWG can stop gelation.[32] Changing the chirality of amino acids has also been shown to affect gelation.[51] Even changing H_2O for D_2O as the solvent used during gelation can alter gel properties.[52, 53] This is significant as samples are sometimes required to be made in D_2O for techniques such as small-angle neutron scattering and infrared spectrometry.[54, 55] It is almost impossible to change only one parameter of a LMWG at a time. Changing one functional group, for example, will in turn alter sterics, hydrophobicity, packing, solubility and the positions available for hydrogen bonding.[56] Fluorine is commonly incorporated into a

7

LMWG because it can allow for the extensive formation of hydrogen bonds and improves biocompatibility.[57]

To self-assemble in water, LMWGs must contain both hydrophilic and hydrophobic regions which are able to create a balance between solubility and hydrophobicity.[58] If a LMWG is too hydrophobic, there is likely to be precipitation and not gelation. If the LMWG is too soluble in the gelation solvent, there is no self-assembly driving force. A hydrophobic component to the LMWG allows for the hydrophobic effect, which can be added in various ways. An example of this is an alkyl tail, which must be of sufficient length to thermodynamically allow the formation of networks to allow for gelation.[59] Short-chained amino acid-based LMWGs normally have a free *C*-terminus, but protected *N*-terminus. These *N*-terminus protecting groups provide crucial intermolecular π–π stacking interactions due to their aromatic nature.[60] The *N*-terminus can be protected by numerous fragments including a fluorenylmethoxycarbonyl (Fmoc) protecting group (Figure 1.3, **1** and **2**),[44] carboxybenzyl protecting group,[61] anthracene protecting group,[62] and naphthalene protecting group.[63] Naphthalene protecting groups can be decorated with various moieties at different ring positions which can affect the self-assembly process and give different final gel properties.[64, 65] Whilst studying a library of naphthalene dipeptide LMWGs, Chen et al. discovered that altering the substituent on the six-position of the naphthalene protecting group alters gelation.[65] The naphthalene-alanine-valine LMWG with no substituents was found not to form a gel. This was also true when a cyano group was placed on the six-position of the naphthalene group. However, the incorporation of a bromine to the six-position of the naphthalene protecting group allowed gelation to occur. The addition of a linker, and the choice of linker, between the protecting group and the remaining LMWG is also known to affect self-assembly.[66]

The amphiphilic peptide LMWG MAX1 (Figure 1.3, **3**) is capable of fully reversible self-assembly under appropriate conditions. MAX1 forms a β-hairpin secondary structure due to intramolecular folding, which is stabilised by hydrogen bonds and encourages self-assembly. Consisting of high β-sheet propensity amino acids valine (V) and lysine (K), MAX1 is a 20-residue peptide. The central tetrapeptide (-V^DPPT-) was designed to initiate a high type II' β-turn, resulting in the hairpin.[46] At physiological pH, valine is a non-polar amino acid whilst lysine is positively charged and hydrophilic. Therefore, electrostatic forces

(charges on lysine) and the hydrophobic effect (from non-polar valine) can be used to control the folding process.[67] Self-assembly is driven by the increasing of pH or the increasing of the ionic strength of the solution to screen repulsive effects between the cationic functionality. This results in both lateral intramolecular hydrogen bonding and facial hydrophobic interactions. The motif of repeating patterns of alternating polar and non-polar amino acids is common practice for designing LMWGs and is present in various LMWG groups including the MAX, RADA/EAK16, and P11 LMWG groups.[68]

Perylene bisimides or perylene diimides (PBIs or PDIs respectively) are a group of dyes with an aromatic core (Figure 1.3, **4**). The self-assembly process of PBIs is dominated by π–π interactions between the molecules, with contributions from hydrogen bonding and the hydrophobic effect.[69, 70] The π–π stacking abilities of PBIs, however, often means they exhibit poor water solubility. Modifications to the PBI structures are often necessary to change their solubility, assembled structures, and subsequent properties.[71] When functionalised with amino acids, PBIs have been shown to self-assemble into semiconducting and photoconductive gels, which could be used as a PBI-based photodetector and in photovoltaics.[72] The presence of the carboxylic acid functional group from the amino acid allows for the formation of PBI solutions in water above pH 6.[73] The choice of amino acid used to functionalise has been reported to make a difference to the properties (for example, aggregation) of the PBI.[73, 74] Using experimental and computational methods, the self-assembly and gelation process of PBI functionalised with the amino acid alanine has been examined.[47] It was proven that this PBI self-assembles at all pH values with the aggregates growing in size when protonated. Similarly, functionalised naphthalene diimides (NDIs), which also have an aromatic core (Figure 1.3, **5**), have the ability to gel.[48]

1.4. Gelation Triggers

As discussed previously, the self-assembly of LMWGs requires a trigger to begin the process. This section will discuss some of the ways self-assembly can be triggered. LMWG triggers induce a change in solubility to produce gels. A LMWG is first suspended in a solvent and the trigger applied. This reduces the LMWG solubility, leading to the formation of self-assembled aggregates. These aggregates can then entangle, trap the solvent and form a gel.[18, 19, 75]

1.4.1. pH Triggers

A pH trigger can be used when a LMWG has a functional group which can be protonated and de-protonated. Such functional groups include carboxylic acids and amines.[76] For LMWGs with a free carboxylic acid, the LMWG is suspended in water and the pH of the resulting solution is such that it is above the apparent pK_a of the LMWG. This gives the carboxylate form of the LMWG, Figure 1.4a. To trigger this solution into a gel, an acid is added. The free carboxylate form of the carboxylic acid is re-protonated, the solubility of the LMWG is decreased, and the LMWG self-assembles, Figure 1.4b and Figure 1.4c.[65] Work by van Bommel et al. has shown that acidic LMWGs (with free carboxylic acid component) can be gelled using acid and disassembled using base.[77] For comparison, they also examined basic LMWGs containing free nitrogen from an imidazole component of the LMWG which could be readily protonated and de-protonated. These basic gelators could be gelled by the addition of base and disassembled by the addition of acid. The self-assembly process using protonation and de-protonation can be reversible, however this cyclic assembly/disassembly process is not always possible.[50, 77]
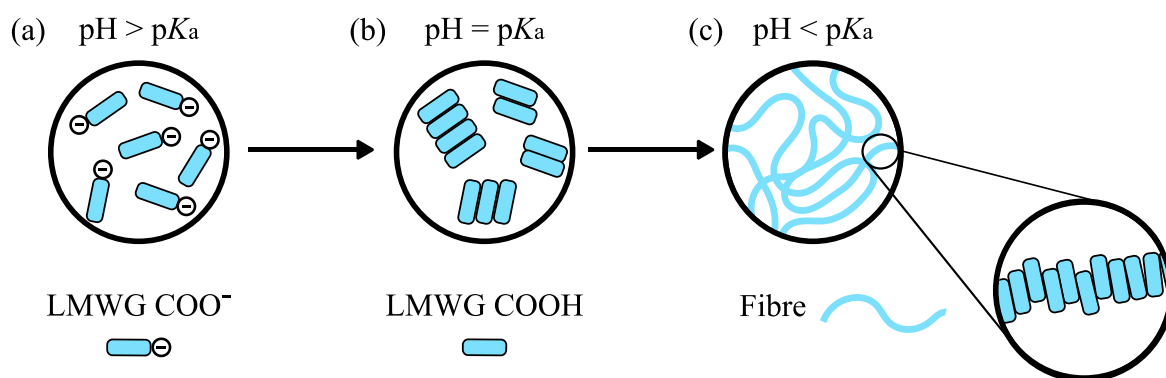

Figure 1.4. Schematic of the self-assembly process using a pH trigger for a LMWG containing a free *C*-terminus. (a) At high pH, the LMWG is soluble in water when in the carboxylate form; (b) when the pH is lowered to the pK_a value, self-assembly begins; (c) decreasing in pH beyond the pK_a value results in fibre formation which can then trap water to form a gel.

Different acids can be used as pH triggers. Aqueous hydrochloric acid (HCl) can be utilised in the gelation process, but since the rate of protonation is faster than the rate of diffusion, this method does not give reproducible gels.[63, 78] Gaseous HCl can also be used to trigger gelation.[75] Glucono-δ-lactone (GdL) is now commonly also used as a pH trigger.[78-81] Unlike HCl, which normally does not give homogeneous gels, GdL slowly produces acid to give homogeneous gels. GdL hydrolyses in water and releases protons. These protons can then re-protonate the LMWG. There is an even distribution of protons throughout the sample due to the rate of hydrolysis being slower than the rate of GdL mixing in the solution, resulting in homogeneous and reproducible gels.[78] Similar small molecules such as sultones (the cyclic esters of sulfonic acid), can also be used as a pH trigger through the slow hydrolysis and breakdown of the cyclic structure to release acid.[82]

Photoacid generators (PAGs) are another method used to form gels via pH. PAGs produce protons when exposed to light. This can then re-protonate a LMWG in the carboxylate form, decreasing the solubility to give a gel. A commonly used PAG for gelation is diphenyliodonium nitrate (DPIN).[83-85] Using a PAG to trigger gelation is advantageous as the gelation can be selective. By introducing a photomask and blocking light exposure to sections of a sample, it is possible to control where gelation occurs.[85] However, not all LMWGs can be triggered using this method. For example, the LMWG 2NapFF (a diphenylalanine-based LMWG with naphthalene protecting group) could not be gelled with DPIN, but other similar LMWGs could be triggered using this PAG.[86]

It is possible to release protons to trigger gelation using electrochemistry. An electrode is placed into a solution containing both LMWG and a molecule capable of releasing protons during redox reaction. This creates a pH gradient starting from the electrode surface.[87] An example of such a molecule is hydroquinone which is oxidised, producing protons. This reduces the solubility of the LMWG at the electrode surface.[88] The thickness of a gel can be tuned as required by altering the reaction time at the electrode.[89] Gels formed using an electrochemical pH trigger are advantageous as they are able to show spatiotemporal control as they are formed without a container.[88]

1.4.2. Metal/Salt Trigger

Using chelation, metal ions from salts can be used to trigger self-assembly. LMWGs containing amino acids are able to chelate metal ions through the carboxylate terminus (Figure 1.5a) or through both the amine and carbonyl groups (Figure 1.5b), as well as utilising extra chelation sites on specific amino acids such as histidine or cysteine (Figure 1.5c).[90] The effect of salts correlates to the Hofmeister series.[91] Triggering gels using metal ions is advantageous because they are capable of forming gels at biological pH and above.[92] Many groups use Ca^{2+} ions to form gels.[92-94]
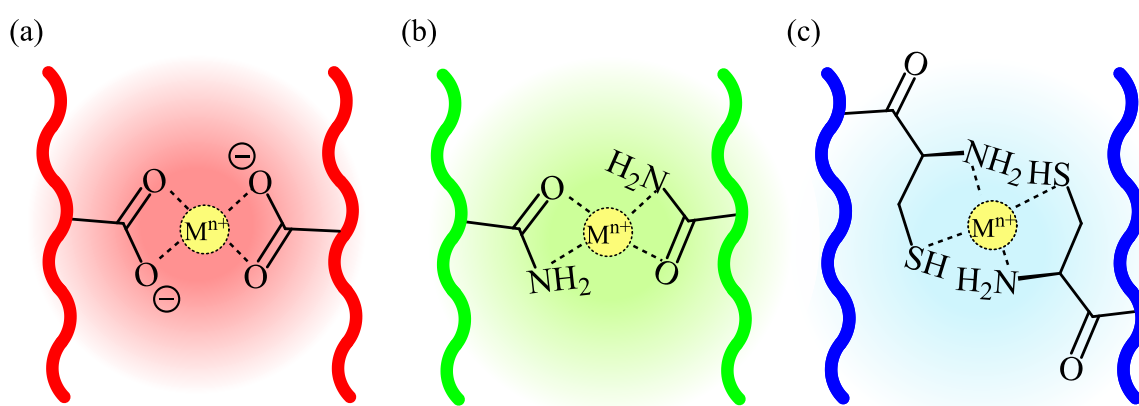
Figure 1.5. Possible sites of metal chelation through (a) carboxylate groups; (b) amides; (c) cysteines.

Self-assembly using metal ions can be altered by both the valence and quantity of the metal ion.[95] By varying the metal ions used, formation of chiral and non-chiral fibres using phenylalanine-based LMWGs can be formed.[96] The handedness of the fibres, along with the diameter, were tuned using a library of 16 different metal ions. These differences were attributed to the intermolecular hydrogen bonding between the amide groups and coordination between the carbonyl groups and metal ions during self-assembly.

1.4.3. Solvent Trigger

A solvent triggered hydrogel requires a water-miscible organic solvent that the LMWG is soluble in, and water (an anti-solvent). A high concentration stock solution of LMWG in organic solvent is diluted using water. This dilution starts the self-assembly

process. Again, this trigger method uses changes in solubility to produce hydrogels.[97, 98] Solvent triggered gels form quickly, with Menger et al. reporting gel formation using a solvent trigger in less than 30 seconds.[99]

Examples of organic solvents suitable for this trigger method include dimethyl sulfoxide,[100] hexafluoroisopropanol,[101] and acetonitrile.[102] The ratio of solvent to anti-solvent can be varied. This can alter the final stiffness and microstructure of the gels, and whether or not a gel will form at all.[103] As interactions between the LMWG and the solvent can affect the stacking of the LMWG molecules, the self-assembled structures can be altered. This has been reported for chiral self-assembled nanostructures due to solvent polarity affecting hydrogen bonding and solvent-LMWG interactions.[104]

1.4.4. Temperature Trigger

Again, this trigger utilises changes in solubility to trigger self-assembly and gelation. When heated, the solubility of the LMWG in the chosen solvent increases. The solubility of the LMWG begins to decrease as the temperature is lowered, which begins the self-assembly process.[22, 105] When lowered to the gelation temperature, T_{gel}, the solvent is immobilised and a gel is formed.[22] The critical temperature points (dissolution and gelation temperatures) are LMWG concentration dependent.[106] This method is very common for organogels,[49, 107-109] and also possible with hydrogels.[110, 111] Rheological properties of gels are affected by temperature,[106] as are fibre dimensions which depend upon the rate of cooling.[112]

1.4.5. Light Trigger

Photo-responsive LMWGs use light to trigger gelation. Different wavelengths of light can be used to reversibly change between the isomers of photo-responsive LMWG fragments and hence create sol-gel-sol transitions.[113-115] Examples of such photo-responsive fragments include azobenzene,[49] stilbene,[116] and arylazopyrazole.[117] These sol-gel-sol transitions occur when switching between the cis- and trans- isomers because of resulting changes in conformation and length; and changes in dipole moment that can disturb the network.[118] Irradiation of a cholesterol-based LMWG by Murata et al. varied the configuration of the LMWG between the cis- and trans- isomers.[113] Here, the trans- form of

the LMWG successfully formed gels while the cis-isomer did not. Cycles of isomerisation could be repeated, thus giving numerous sol-gel-sol transitions. Introducing a template selectively gelled part of a system, and so reversible patterns were created.

Isomerisation can also be triggered, accompanied by the opening and closing of rings, allowing for the gelation and breakdown of gels. Using a photo-responsive spiropyran fragment, isomerisation (via the making and breaking of bonds) between the non-planar and planar forms of the LMWG were controlled by irradiation of various wavelengths, Figure 1.6.[119] The planar isomer was found to form an aggregate-like structure due to π–π stacking, and was capable of forming a gel. This was not possible with the non-planar form of the LMWG, and hence no resulting hydrogels were produced. Coumarin-based LMWGs are known to breakdown from gel to solution due to cleavage when exposed to UV light; such a transition can be utilised for photo-sensitive drug delivery.[120] Reversible photo-dimerisation is also possible with coumarin-based LMWGs.[121] When irradiated with 365 nm light, dimerisation of the LMWG occurs which increases the number of cross-links, subsequently increasing the mechanical properties of the gel.

(a)   (b)
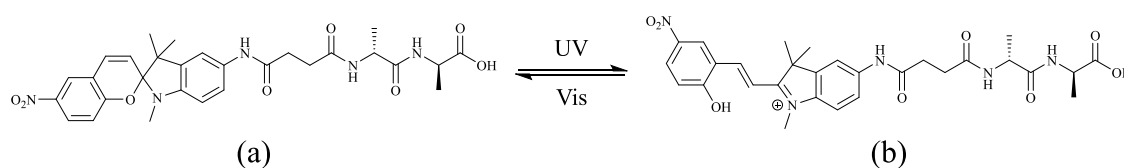
Figure 1.6. Molecular structures of the spiropyran dipeptide used by Qiu et al. in (a) the closed form and (b) the open form.[119]

1.4.6. Enzyme Trigger

Advantageous due to their use in biological systems and highly specific nature, enzymatic triggers are used to make and break bonds and therefore trigger gelation. An example of this is reported by Yang et al. where, by using a peptide-based LMWG and a tyrosine kinase/alkali phosphatase enzyme switch, they control hydrogel assembly and disassembly.[122] The LMWG was found to form gels. However, upon the addition of adenosine triphosphate (ATP) and the kinase enzyme, disassembly occurred due to the phosphorylation of the tyrosine fragment of the LMWG. This increased repulsion between molecules, and overall resulted in the LMWG becoming more hydrophilic after

phosphorylation. Self-assembly can be triggered again by adding phosphatase to the resulting solution of the phosphorylated version of the LMWG which dephosphorylates it, reforming the gel.

Similarly, a simple visual assay for screening enzyme inhibitors of acid phosphatase was created using LMWG formation.[123] The LMWG precursor is considered as a substrate for the enzyme and forms a gel when dephosphorylation of the LMWG precursor occurs using acid phosphatase enzyme. If an inhibitor is present, it can block the conversion of the precursor. Therefore, no hydrogel is formed. The gelation is visible by eye so this simple and inexpensive method could be used to screen for inhibitors and detect the presence of enzymes without the use of a spectrometer.[123] Having a visual assay for detection and diagnosis is advantageous because many diseases are related to overactive and overexpressed enzymes.[124]

1.4.7. Multiple Triggers

It is possible to initiate gelation of the same LMWG with different trigger methods. The final properties of the gels vary depending upon the trigger applied,[94, 105, 125] with self-assembly kinetics also a significant factor in determining the final properties of a gel.[18] Multiple triggers methods have been reported to successfully gel *N*-capped tripeptides which are capable of forming gels by pH trigger, salt trigger, and by the addition of cell culture media.[125] By altering the trigger method, features such as gel stiffness, minimum gelation concentration and biocompatibility can be fine-tuned. Similarly, work by the Stupp group has demonstrated that their amphiphilic oligopeptide LMWGs can be triggered by pH and by addition of salt.[50, 59] A single LMWG can also be used to form both hydrogels and organogels.[126]

It is also possible to simultaneously use two trigger methods at once. The release of protons using a PAG which has been exposed to UV light has been reported to cause Ca^{2+} ions to be freed from an insoluble salt ($CaCO_3$). The freed Ca^{2+} allows for cross-linking between fibres and a gel is formed using a salt trigger, via a PAG pH trigger.[85]

1.5. LMWG Structures

As already discussed previously, LMWGs form hydrogels via self-assembly, where a trigger begins the fibre formation and entanglement. Various structures and length scales are involved in this process and hence different techniques are required to examine all these length scales and gain a detailed understanding of the material under investigation. This is summarised in the following sections. The overall mechanical properties of a gel are affected by the properties of the LMWG structures, including the fibre thickness and how the fibres are arranged in the gel network.[105] We discuss this further in Chapter 4 where we selectively control where gelation occurs and examine the resulting bulk properties using rheology.

1.5.1. Examining LMWG Structures over Multiple Length Scales

Since various length scales are associated with the self-assembly process, it is important to be able to examine LMWG solutions and their corresponding gels at these different length scales, Figure 1.7.[1] Initially and crudely, the bulk gel sample is examined by eye with the vial inversion test, Figure 1.7a.[1, 127] The inversion of the sample vial is a simple method to look for a self-supporting material (a condition for gelation) and gives an indication as to whether or not the sample is a gel, viscous liquid or solution. To confirm the presence of a gel and not a viscous liquid, rheology is utilised.[1, 16, 128-131] Rheology gives information regarding the mechanical properties of the bulk gel. Over the time scale of an experiment, a gel will have a storage modulus (G', an indication of how "solid-like" a sample is) one order of magnitude larger than the loss modulus (G'', an indication of how "liquid-like" a sample is). This is also known as $\tan \delta = G''/G' = 0.1$. Gels are also frequency independent over a large frequency range when the strain imposed on the sample is within the linear viscoelastic region.
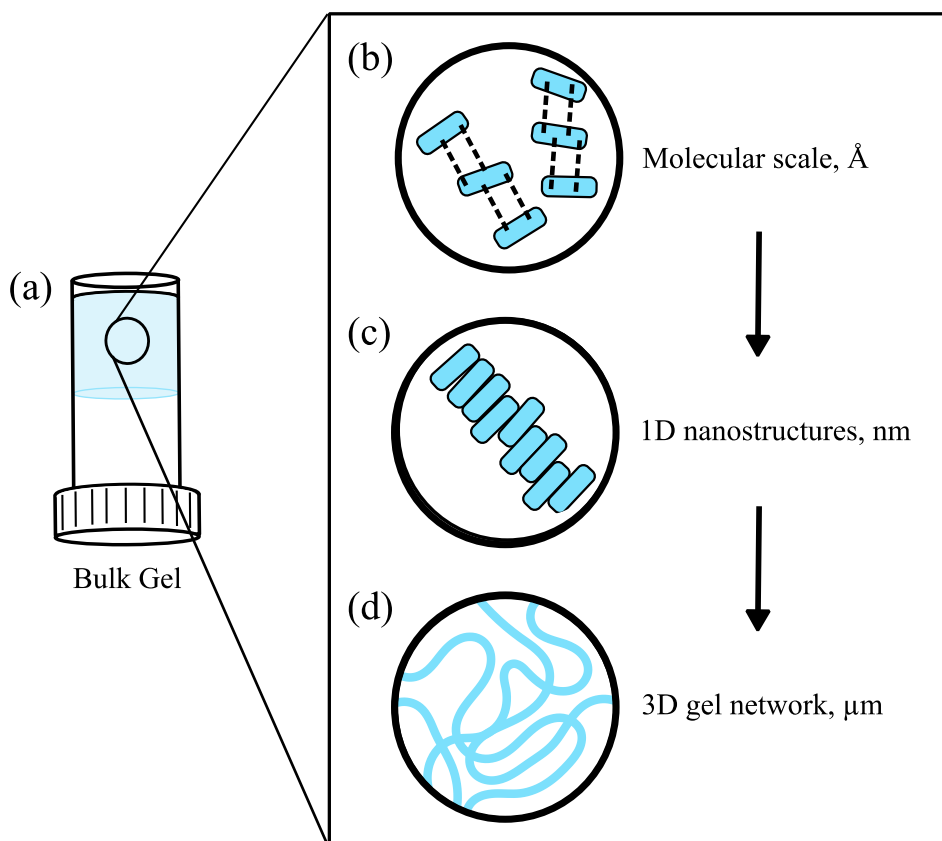
Figure 1.7. Schematic representing the various length scales associated with LMWG self-assembly and gelation showing (a) the completed bulk gel; (b) the angstrom length scale which incorporates free LMWG molecules and the interactions between them; (c) the 1D nanostructures formed by the self-assembly of the LMWG; (d) the 3D gel network, created by the 1D nanoscale structures.

To understand gels at the molecular scale, Figure 1.7b, techniques including infrared (IR) spectroscopy and nuclear magnetic resonance (NMR) spectroscopy are used.[15] Understanding the molecular scale and knowing which interactions are present is helpful as it is these interactions that drive the formation of larger structures. IR spectroscopy indicates which non-covalent interactions are present, whilst studying NMR spectra can give information about aggregates, show the regions participating in the interactions, and can also be used to provide kinetic information about the gelation process.[15, 132]

At the next hierarchal level, 1D nanostructures form, Figure 1.7c. These structures include fibres, spheres, tubes and sheets.[133] Structures at this length scare are commonly studied by microscopy and by small-angle X-ray/neutron scattering. These are

complementary methods and commonly used together since scattering data alone can be ambiguous.[134-136] There can be many models and values which can all seem to fit the data well, but only one will be a true representation of a sample.[136, 137] An advantage of using scattering to examine structures at this length scale is that experiments can be performed in situ, without drying the sample, since drying has been shown to not always give an accurate representation of the structures formed.[138]

The next length scale (Figure 1.7d) allows for the gel network to be analysed. This occurs when the 1D nanostructures form microstructures through, for example, fibre entanglement or fibre branching.[139] Our group has previously shown that the same LMWG can form different microstructures depending on the gelation trigger used.[140] Techniques such as electron and confocal microscopy can effectively image gels at this length scale.[56]

1.5.2. Micellar Structures formed by LMWGs

Before the gelation self-assembly process occurs, it is possible for micellar aggregates to form in the solution phase.[141-143] Micelles, formed by aggregation, can only form above the critical micelle concentration (CMC) and above the Krafft temperature (the minimum temperature at which micelles can occur).[144, 145] The driving force behind micelle formation in water is such that the hydrophobic micellar core and the dispersion medium, water, are separated. Micelles usually exhibit polymorphism and polydispersity; varying in size due to the different numbers of molecules making up each micelle.[146] Micelles can pack together to give mesomorphs, also known as liquid crystals.[144, 146]

Worm-like micelles are a type of cylindrical rod-like micelle which are flexible. These types of micelle are viscoelastic.[147] Worm-like micelles are considered as "living" systems,[148-151] with transient and unique viscoelastic behaviour.[148] Under shear, these micelles can continuously break and reform.[149, 152] Many factors are known to influence micellar growth and properties such as pH,[151, 153] the addition of salt,[154-156] and temperature.[128, 157] In Chapter 2, we examine the effects of these factors on a dipeptide-based LMWG system known to form structures which behave like worm-like micelles at high pH in order to generate the most reproducible data possible from this living system.

Our group has previously examined the transitions from spherical to worm-like micelles.[158] The transition from spherical to worm-like micelles was found to be concentration dependent. At low LMWG concentration, spherical aggregates were found. Increasing the LMWG concentration leads to a second CMC where worm-like micelles were present. In Chapter 3, we examine the effects of increasing the concentration of the LMWGs further in the solution phase.

1.6. Applications

Many industries use polymer gels with examples already located in the food,[159] and pharmaceutical industries, including in diagnostics and drug release devices.[160] Novel, synthetic polymers can be unfavourable because of toxicity and other incompatibilities.[161] There are many reasons LMWG hydrogels are favourable. There are already examples of LMWGs in some industrial applications including lubricating engine greases, glue sticks and personal care products.[162, 163] Hydrogels are predominantly made from water (approximately 99% water to 1% gelator).[15] This is ideal as the water accounting for the bulk of the sample is a readily available, benign compound. Also, as LMWGs are famously reversible (unlike polymer hydrogels),[10] there is the ability to recycle and reuse the gel, reducing the need for constant preparation, synthesis and new materials, saving both time and money. LMWGs show great versatility because they offer a vast array of mechanical properties, and a single LMWG can be responsive to multiple stimuli.[10, 18] Therefore, LMWGs display potential in a wide range of applications. Many reviews examine applications of LMWGs in detail;[6, 164-166] the follow sections provide a few specific examples.

1.6.1. Waste Management

In recent years, LMWG gels have started to attract attention as potential materials for water purification, capable of removing contaminates such as oils, solvents, dyes and heavy metals.[162] The release of such contaminants from industrial processes has greatly affected the global water supply quality, therefore damaging aquatic life and the food chain. People who use the contaminated water are therefore negatively affected, resulting in various

health problems such as vomiting, cancer and neurological damage. It is therefore essential to find methods of removing waste materials.

There are already numerous examples of LMWG gels with the ability to remove small waste molecules from water.[167-170] For example, Kar et al. reported the rapid removal of crystal violet dye from water using phase-selective gelation.[169] Here, the LMWG is capable of gelling both organic solvents and water depending on the form of the LMWG present. When the LMWG has a free carboxylic acid group, it is only able to selectively gel the organic phase in a biphasic system of water and organic solvent. The sodium salt form of the LMWG has the ability to gel both organic solvents and water but was found to only gel the aqueous phase in a mix of water and organic solvent. By adjusting the pH of the system, the free carboxylic acid form or salt form of the LMWG can exist, and therefore selectively gel only part of the water and organic solvent system. To prove this phase-selective gelation can remove dyes from water, a temperature-triggered hydrogel was prepared using the LMWG and 0.1 mM crystal violet dye in 1 mL of water (Figure 1.8a). To this gel, 1 mL of organic solvent (toluene) was added (Figure 1.8b) followed by 1.1 equivalents of HCl (Figure 1.8c). The addition of acid forms the free carboxylic acid form of the LMWG which is not able to form hydrogels, resulting in the almost instantaneous breakdown of the hydrogel to solution. Next, the system is gently heated, shaken and cooled to room temperature. The toluene layer forms a gel, simultaneously trapping the crystal violet dye, whilst the water layer is in a fluid state (Figure 1.8d). The movement of the dye was monitored using ultraviolet–visible spectroscopy (Figure 1.8e), showing the dye was almost completely removed from the water layer within a few minutes. Phase-selective gelation experiments have also been successful in removing other dyes from water, such as rhodamine B.[49]
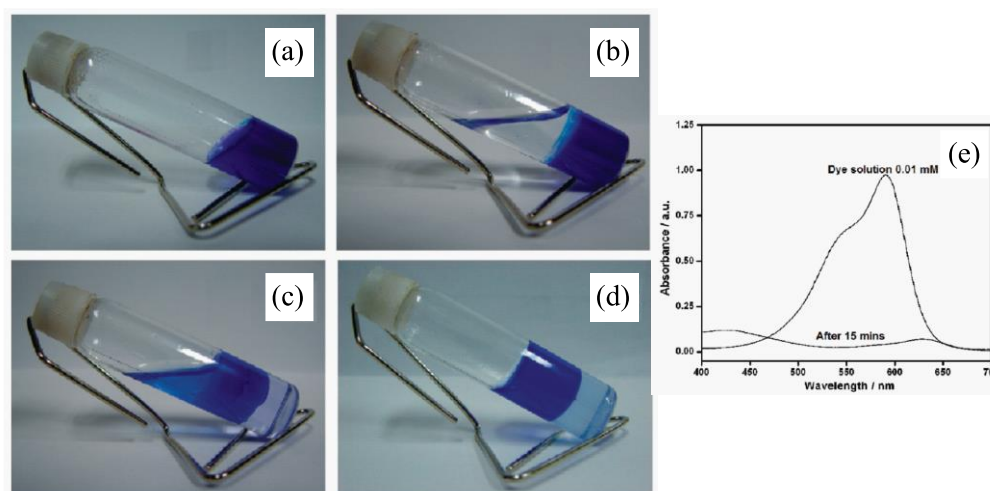
Figure 1.8. (a) Hydrogel containing 0.1 mM of crystal violet dye; (b) toluene (top layer) added to the dye-containing hydrogel (bottom layer); (c) addition of HCl disassembles the dye-containing hydrogel (bottom layer); (d) dye-containing organogel (top layer) formed after heating, leaving the aqueous (bottom) layer clear of dye within minutes; (e) ultraviolet–visible spectroscopy spectrum of an aqueous solution of crystal violet dye indicating the pH-dependent rapid removal of the dye from water. Figure adapted and reprinted with permission.[169] Copyright 2009 American Chemical Society.

Syneresis, the contraction of the gel network and simultaneous expulsion of water, can also be used for purification.[168] Using a LMWG with a photo-responsive azobenzene fragment, syneresis occurred when the LMWG was changed from the trans- to the cis- form using light. The trans- isomer of the LMWG could form hydrogels, trapping dyes and other small molecules, and releasing purified water upon exposure to light. In this study, six different dyes were prepared with the trans- form of the LMWG to form hydrogels. Syneresis was then activated due to the irradiation of the hydrogels with UV light for 2 hours. The expelled water (analysed using ultraviolet–visible spectroscopy) was found to be free of all dyes. Therefore, the syneresis process was successfully exploited to remove dyes from water.

Similarly, a tripeptide composed of three phenylalanine amino acids also uses syneresis to remove water-soluble pollutants such as toxic organic dyes and toxic Pb^{2+} ions from waste-water.[170] Here, syneresis naturally occurs due to the very hydrophobic nature of the LMWG which becomes even more hydrophobic with time. This causes more contraction of the fibres. After 7 days the volume of the hydrogel contracts to approximately 75% of its original volume by releasing about 80% purified water from 2 mL of hydrogel. The

shrinkage behaviour of this hydrogel was found to be thermal, pH and pressure dependent. Using this LMWG, 98.4% of Pb^{2+} ions could be removed.

Additionally, LMWGs have been found to gel various organic liquids including commercial fuels such as petrol and diesel.[171-173] This is significant as it may be used to contain solvent/oil spills, and for the safe transportation of non-flammable fluids.[171]

1.6.2. 3D Printing

The development of 3D tissue scaffolds can be used as an alternative method for organ transplantation in regenerative medicine and in drug discovery assays.[174] Due to recent advances in tissue engineering, 3D printing can now produce detailed 3D tissue structures using the printer's high level of spatial precision. The printability of the material, in this case hydrogels, is determined by both the properties of solutions and the gelation process. Hydrogels have great potential in biomedical applications because they have features that are similar to the extracellular matrix (the natural environment of cells) and allow for homogeneous cell growth, delivering cells to damaged tissues.[175] These materials are ideal for 3D printing because they can retain their shape after printing due to the reversibility of the physical cross-links used to form hydrogels from LMWGs.

The 3D printing of polymer hydrogels has been discussed in numerous review articles.[176-178] The use of LMWGs is less discussed, but there are still some examples.[179-184] Using the extrusion method of 3D printing, Nolan et al. have previously reported the printing of dipeptide-based LMWG hydrogels,[182] where gels were prepared inside syringes and then extruded, with the gels reforming after printing. A small library of LMWGs (triggered by various methods) was studied to determine the properties required for 3D printing. LMWGs which were found to form spherulitic structures printed better compared to those which formed fibrous networks since the spherulitic structures were not as strongly affected by the shearing process when being extruded. This work was continued and recently reported by Fuentes Caparrós et al. who printed 3D multi-layer hydrogels using a solvent trigger, Figure 1.9a.[183] In this work, multiple layers of hydrogels of varying stiffness were printed and stacked, and the rheology examined to evaluate the contribution of each layer to the overall properties of the multi-layered systems. Preparing multi-layered hydrogel systems of

varying stiffness is advantageous for tissue engineering because these layers mimic the various stiffnesses of various organs, healthy tissues and cancerous tissues in the body.[185] We examine multi-stiffness gels in Chapter 4. The gels reported in this work were also studied by rheology before and after printing, showing that the final properties of the gels after printing are affected by the printing process (Figure 1.9b and Figure 1.9c).[183] This is important for biological applications, where the final mechanical properties of the gels are critical to allow for cell growth.
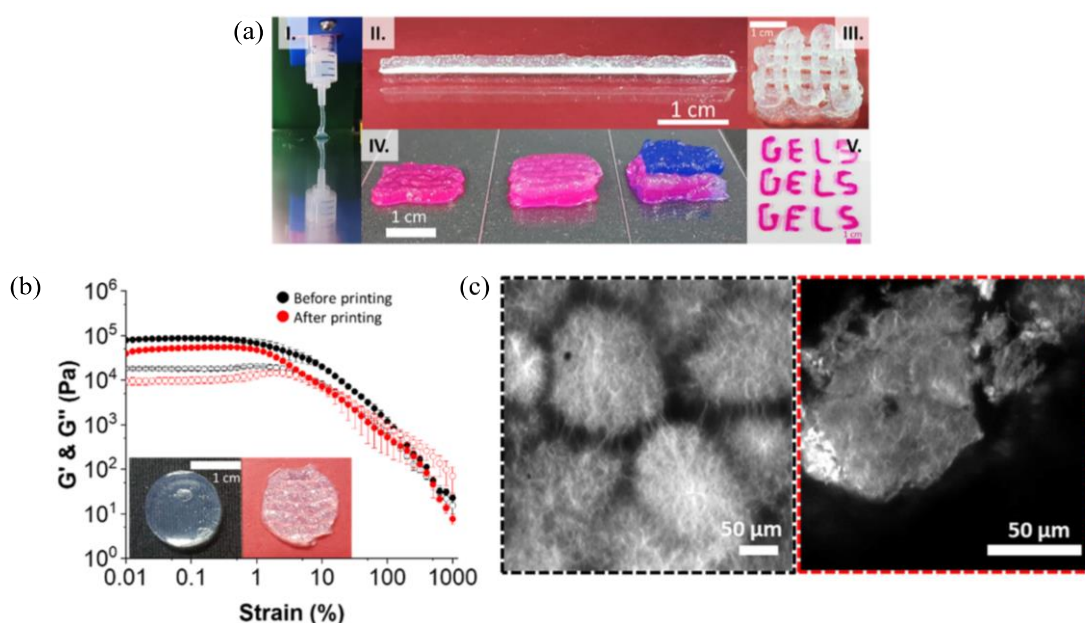

Figure 1.9. (a) Photographs of 3D printed LMWG hydrogels: (I) printing of a gel filament onto the printing bed; (II) a 50 mm printed line; (III) scaffold of three printed layers; (IV) (left to right) one-layer, two-layer, and three-layer systems dyed with Rose Bengal (layer 1), no dye (layer 2), and Nile Blue A (layer 3); (V) printed text; (b) rheology strain sweep for a single-layer before printing (black data) and after printing (red data) with insets showing pictures of gels (left) before and (right) after printing; (c) confocal microscopy images for a gel (left) before and (right) after printing. Figure adapted and reprinted with permission;[183] https://pubs.acs.org/doi/abs/10.1021/acs.biomac.1c00078. Copyright 2021 American Chemical Society (ACS). Further permissions related to the material excerpted should be directed to the ACS.

Additionally, organic solutions containing LMWG molecules can be 3D printed into a liquid coagulation bath to quickly form gel filaments via solvent trigger, allowing for the formation of well-defined patterns.[184] This allows for the 3D printing of LMWGs which are

not thixotropic and cannot be extruded by the 3D printer once gelled because of mechanical fragility. In the study of a sugar-based LMWG, dimethyl sulfoxide (DMSO) and water as the coagulation agent, the DMSO used to initially dissolve the LMWG molecules was highly diluted in the coagulation bath. It was so diluted that it is not detectable within the hydrogel, therefore allowing for the possibility of being used for cell culturing scaffolds. A crucial factor for the 3D printing of gels is that the gel must adhere to the surface it is being printed onto. Here, it was found that hydrogel adhesion to a surface was best when the surface was a polycarbonate membrane. Factors such as LMWG concentration, surface to 3D printer needle distance, needle diameter and flow rate were all found to affect the surface adhesion.

1.6.3. Smart Materials

"Smart" materials are those which are stimuli-responsive and have potential in many areas.[186] These include, but are not limited to, conversion of self-assembling prodrugs,[187] and dissolution-on-demand wound dressings.[188] Smart LMWG hydrogels can be used for controlled drug delivery systems.[189-192] The development of such materials would allow for the smart tissue-specific release of drugs. Due to the targeted release, the potency of the drug increases whilst reducing related side effects. Systems which are responsive to physiological conditions (for example, metal ions and enzymes) are useful for controlled, smart drug release.

As responsive materials, hydrogels have a great potential to be used as sensors. One example uses pyrene-based LMWGs as a sensor for the biological molecule insulin.[193] In a library of LMWGs containing both pyrene and monosaccharide fragments, one LMWG (Figure 1.10a) showed a gradual decrease in emission intensity at 393 nm when the concentration of insulin increased (Figure 1.10b). This resulted in the gel changing colour under UV light (Figure 1.10c). Scanning electron microscopy images (Figure 1.10d) showed the addition of insulin altered the structures of the LMWG fibres. We discuss the incorporation of additives into LMWG structures in Chapter 4. The fibre thickness increased when insulin was incorporated into the system. It is thought that the interaction between the sugar fragment of the LMWG and insulin alters the gel fibres and hence the pyrene fragment of the LMWG is dislocated, meaning less aggregation of the pyrene fragments as the concentration of insulin increases, resulting in quenching at 393 nm.
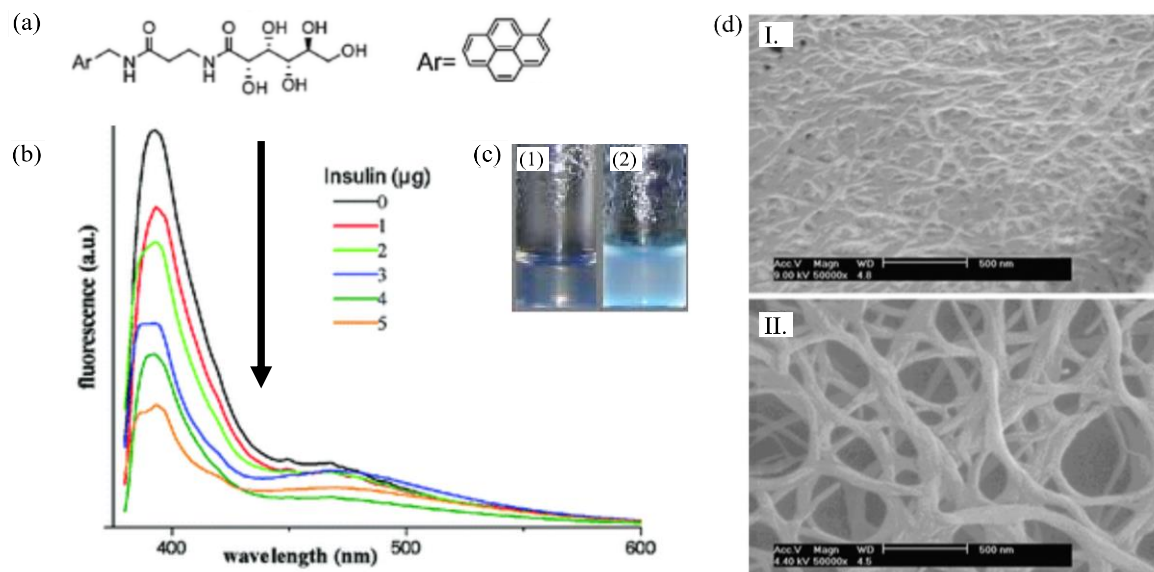
Figure 1.10. (a) Structure of the LMWG used here as an insulin sensor; (b) emission spectra of the LMWG at 0.15% w/w in the presence of various insulin concentrations, with an arrow showing the decrease in emission intensity when increasing the concentration of insulin (excitation λ maximum intensity at 370 nm); (c) pictures of the hydrogel formed by the LMWG without insulin (1) and with 5 µg of insulin (2); (d) scanning electron microscopy images of the corresponding xerogels without insulin (I) and with 5 µg of insulin (II). Figure adapted with permission from The Royal Society of Chemistry.[193]

Other LMWGs are also capable of sensing. For example, the LMWG diphenylalanine with zinc oxide is a highly selective luminescent biosensor for trypsin;[194] a bis-sugar-triazole-based LMWG is capable of sensing mercury ions;[195] and various LMWGs are capable of sensing selected ions in the presence of other ions, showing a selective gel-sol transition or colour change.[196, 197]

1.6.4. Other Applications

Very recently, the use of LMWGs for molecular oxygen trapping has been reported.[198] Molecular oxygen (O_2) is a highly reactive oxidising agent and is harmful to many systems. Here, a dipeptide-based LMWG is shown to trap O_2 and limit diffusion through the hydrogel. Molecular dynamics simulations suggested that the O_2 binding mechanism is controlled by pockets formed between the LMWG aromatic rings, binding the

O_2 through the hydrophobic effect. Therefore, the gels could be used for the storage of the hydrogen producing enzyme [FeFe]-hydrogenase, which is a catalyst for the generation and oxidation of molecular hydrogen (H_2), used in energy conversion devices. The enzyme is irreversibly inhibited by O_2, reducing its activity, hence the need for storage without O_2. The residual activity of the encapsulated enzyme was found to be 68.1% when stored in the dipeptide-based hydrogel. When stored in the hydrogel, the time taken for the enzyme activity to drop by 50% is reported to be 30 minutes, compared to without which takes only seconds for the activity to drop by 50%. It is hoped this work will be transferrable to other O_2-sensitive reactions and applications in the future.

Similarly, hydrogels can be used as a growth media for the growing of crystals, protecting the crystals against degradation.[199] The crystals here were of the enzyme lysozyme which has sensitive cysteine and methionine groups. The dipeptide-based LMWG (consisting of cysteine and phenylalanine amino acids) showed protection of these most sensitive lysozyme groups, giving increased protection from degradation caused by X-ray exposure because of the long LMWG fibres. The crystals grown here were found to be of high quality and compared well with those grown in other media.

1.7. Aims of this Thesis

LMWGs are advantageous for numerous reasons, including their ability to form reversible gels. There are many different fragments and functional groups which can be used to form LMWGs, hence giving a wide variety of LMWG molecules. The aim of this Thesis is to understand and control the structures formed by dipeptide-based LMWGs in both high pH solutions and low pH hydrogels, and examine how these structures can affect the overall properties of the solution or gel. To do this, we focus on one exemplar LMWG, 2NapFF, which comprises of a naphthalene group and two phenylalanine amino acids. Understanding the LMWG formulation structures, self-assembly and gelation will greatly help to improve LMWG construction. Having the ability to alter formulation structures and hence structure packing and resulting bulk properties, could result in a single LWMG being able to give a variety of structures and resulting properties, which could be tuned with a specific application in mind. This would limit the need for new LMWG molecules.

In Chapter 2, we show that sample preparation is key when forming solutions of LMWGs at various LMWG concentrations. These solutions can contain worm-like micelles, which are regarded as "living" systems. We therefore aim to produce a robust protocol for solution preparation to reduce the chances of structure variation within samples which in turn affect the overall properties of the solutions. To create our robust protocol, we examine many factors including pH and stirring methods to show the sensitivity of the solutions.

In Chapter 3, we use our robust protocol from Chapter 2. We aim to show the versatile nature of a single LMWG by varying the LMWG concentration and the counterion used to form the solutions to show a range of structures formed by a single LMWG. These different structures packing together differently and hence the overall bulk properties of the solutions change too. We show that these different properties can be utilised with specific applications in mind.

Finally, in Chapter 4, we show that we can control structures and gelation by selectively gelling. To show we can control the self-assembly of our hydrogels, we aim to form gels with gradient stiffness within a single sample. The gradient stiffness gels are formed using a PAG and exposure to UV light, allowing for selective gelation by managing UV exposure. The addition of the PAG causes structural changes to the solution phase. We aim to form gradients which are both steep and gradual to fully show the extent we can control the structures and gelation process.

1.8. References

1. R. G. Weiss, *J. Am. Chem. Soc.*, 2014, **136**, 7519-7530.
2. R. V. Ulijn, N. Bibi, V. Jayawarna, P. D. Thornton, S. J. Todd, R. J. Mart, A. M. Smith and J. E. Gough, *Mater. Today*, 2007, **10**, 40-48.
3. Z.-X. Zhang, D. J. Young, Z. Li and X. J. Loh, *Small Methods*, 2019, **3**, 1800270.
4. R. A. Batista, P. J. P. Espitia, J. d. S. S. Quintans, M. M. Freitas, M. Â. Cerqueira, J. A. Teixeira and J. C. Cardoso, *Carbohydr. Polym.*, 2019, **205**, 106-116.
5. S. Cascone and G. Lamberti, *Int. J. Pharm.*, 2020, **573**, 118803.
6. N. M. Sangeetha and U. Maitra, *Chem. Soc. Rev.*, 2005, **34**, 821-836.
7. A. J. Holder, N. Badiei, K. Hawkins, C. Wright, P. R. Williams and D. J. Curtis, *Soft Matter*, 2018, **14**, 574-580.
8. B. O. Okesola, V. M. P. Vieira, D. J. Cornwell, N. K. Whitelaw and D. K. Smith, *Soft Matter*, 2015, **11**, 4768-4787.
9. S. R. Raghavan and J. F. Douglas, *Soft Matter*, 2012, **8**, 8539-8546.

10. M. de Loos, B. L. Feringa and J. H. van Esch, *Eur. J. Org. Chem.*, 2005, **17**, 3615-3631.
11. M. Žinic, F. Vögtle and F. Fages, in *Low Molecular Mass Gelator*, Springer Berlin Heidelberg, Berlin, Heidelberg, 2005, pp. 39-76.
12. X. N. Zhang, Y. J. Wang, S. Sun, L. Hou, P. Wu, Z. L. Wu and Q. Zheng, *Macromolecules*, 2018, **51**, 8136-8146.
13. A. Dawn, T. Shiraki, S. Haraguchi, S.-i. Tamaru and S. Shinkai *Chem. Asian J.*, 2011, **6**, 266-282.
14. D. J. Abdallah and R. G. Weiss, *Langmuir*, 2000, **16**, 352-355.
15. G. Yu, X. Yan, C. Han and F. Huang, *Chem. Soc. Rev.*, 2013, **42**, 6697-6722.
16. P. Terech and R. G. Weiss, *Chem. Rev.*, 1997, **97**, 3133-3160.
17. B. P. Nowak and B. J. Ravoo, *Soft Matter*, 2020, **16**, 7299-7304.
18. B. Ding, Y. Li, M. Qin, Y. Ding, Y. Cao and W. Wang, *Soft Matter*, 2013, **9**, 4672-4680.
19. Y. Qiao, Y. Lin, Z. Yang, H. Chen, S. Zhang, Y. Yan and J. Huang, *J. Phys. Chem. B.*, 2010, **114**, 11725-11730.
20. C. Tang, A. M. Smith, R. F. Collins, R. V. Ulijn and A. Saiani, *Langmuir*, 2009, **25**, 9447-9453.
21. L. A. Estroff, L. Leiserowitz, L. Addadi, S. Weiner and A. D. Hamilton, *Adv. Mater.*, 2003, **15**, 38-42.
22. L. A. Estroff and A. D. Hamilton, *Chem. Rev.*, 2004, **104**, 1201-1218.
23. D. K. Kumar and J. W. Steed, *Chem. Soc. Rev.*, 2014, **43**, 2080-2088.
24. K. Hanabusa and M. Suzuki, *Polym. J.*, 2014, **46**, 776.
25. S. Kralj, O. Bellotto, E. Parisi, A. M. Garcia, D. Iglesias, S. Semeraro, C. Deganutti, P. D'Andrea, A. V. Vargiu, S. Geremia, R. De Zorzi and S. Marchesan, *ACS Nano*, 2020, **14**, 16951-16961.
26. A. D. Martin, J. P. Wojciechowski, M. M. Bhadbhade and P. Thordarson, *Langmuir*, 2016, **32**, 2245-2250.
27. P. Dastidar, *Chem. Soc. Rev.*, 2008, **37**, 2699-2715.
28. J. K. Gupta, D. J. Adams and N. G. Berry, *Chem. Sci.*, 2016, **7**, 4713-4719.
29. M. Raynal and L. Bouteiller, *Chem. Comm.*, 2011, **47**, 8271-8273.
30. D. Rosa Nunes, M. Raynal, B. Isare, P.-A. Albouy and L. Bouteiller, *Soft Matter*, 2018, **14**, 4805-4809.
31. R. Van Lommel, J. Zhao, W. M. De Borggraeve, F. De Proft and M. Alonso, *Chem. Sci.*, 2020, **11**, 4226-4238.
32. P. W. J. M. Frederix, G. G. Scott, Y. M. Abul-Haija, D. Kalafatovic, C. G. Pappas, N. Javid, N. T. Hunt, R. V. Ulijn and T. Tuttle, *Nat. Chem.*, 2015, **7**, 30-37.
33. X. Yang, G. Zhang and D. Zhang, *J. Mater. Chem.*, 2012, **22**, 38-50.
34. X. Yu, L. Chen, M. Zhang and T. Yi, *Chem. Soc. Rev.*, 2014, **43**, 5346-5371.
35. C. Tomasini and N. Castellucci, *Chem. Soc. Rev.*, 2013, **42**, 156-172.
36. P. Berndt, G. B. Fields and M. Tirrell, *J. Am. Chem. Soc.*, 1995, **117**, 9515-9522.
37. Q. Chen, Y. Lv, D. Zhang, G. Zhang, C. Liu and D. Zhu, *Langmuir*, 2010, **26**, 3165-3168.
38. M. Yamanaka, *J Incl Phenom Macrocycl Chem.*, 2013, **77**, 33-48.
39. C. Yu, M. Xue, K. Liu, G. Wang and Y. Fang, *Langmuir*, 2014, **30**, 1257-1265.
40. K. Araki and I. Yoshikawa, in *Low Molecular Mass Gelator*, Springer Berlin Heidelberg, Berlin, Heidelberg, 2005, pp. 133-165.
41. O. Gronwald and S. Shinkai, *Chem. Eur. J.* , 2001, **7**, 4328-4334.
42. E. Krieg, E. Shirman, H. Weissman, E. Shimoni, S. G. Wolf, I. Pinkas and B. Rybtchinski, *J. Am. Chem. Soc.*, 2009, **131**, 14365-14373.

43. M. Al Kobaisi, S. V. Bhosale, K. Latham, A. M. Raynor and S. V. Bhosale, *Chem. Rev.*, 2016, **116**, 11685-11796.
44. V. Jayawarna, M. Ali, T. A. Jowitt, A. F. Miller, A. Saiani, J. E. Gough and R. V. Ulijn, *Adv. Mater.*, 2006, **18**, 611-614.
45. S. Panja and D. J. Adams, *Chem. Comm.*, 2019, **55**, 47-50.
46. J. P. Schneider, D. J. Pochan, B. Ozbas, K. Rajagopal, L. Pakstis and J. Kretsinger, *J. Am. Chem. Soc.*, 2002, **124**, 15030-15037.
47. E. R. Draper, L. Wilbraham, D. J. Adams, M. Wallace, R. Schweins and M. A. Zwijnenburg, *Nanoscale*, 2019, **11**, 15917-15928.
48. A. Das and S. Ghosh, *Chem. Comm.*, 2016, **52**, 6860-6872.
49. Z. Zhang, S. Zhang, J. Zhang, L. Zhu and D. Qu, *Tetrahedron*, 2017, **73**, 4891-4895.
50. J. D. Hartgerink, E. Beniash and S. I. Stupp, *Science*, 2001, **294**, 1684.
51. A. Brizard, R. Oda and I. Huc, in *Low Molecular Mass Gelator*, Springer Berlin Heidelberg, Berlin, Heidelberg, 2005, pp. 167-218.
52. C. A. Grant, P. C. Twigg, M. D. Savage, W. H. Woon and D. Greig, *Macromol. Mater. Eng.*, 2012, **297**, 214-218.
53. K. McAulay, H. Wang, A. M. Fuentes-Caparrós, L. Thomson, N. Khunti, N. Cowieson, H. Cui, A. Seddon and D. J. Adams, *Langmuir*, 2020, **36**, 8626-8631.
54. Y. B. Melnichenko and G. D. Wignall, *J. Appl. Phys.*, 2007, **102**, 021101.
55. P. I. Haris and D. Chapman, *Biopolymers*, 1995, **37**, 251-263.
56. E. R. Draper and D. J. Adams, *Chem*, 2017, **3**, 390-410.
57. S. Maity, P. Das and M. Reches, *Sci. Rep.*, 2015, **5**, 16365.
58. D. M. Ryan, T. M. Doran, S. B. Anderson and B. L. Nilsson, *Langmuir*, 2011, **27**, 4029-4039.
59. J. D. Hartgerink, E. Beniash and S. I. Stupp, *PNAS*, 2002, **99**, 5133.
60. S. M. M. Reddy, P. Dorishetty, G. Augustine, A. P. Deshpande, N. Ayyadurai and G. Shanmugam, *Langmuir*, 2017, **33**, 13504-13514.
61. S. R. S. Veloso, P. J. Jervis, J. F. G. Silva, L. Hilliou, C. Moura, D. M. Pereira, P. J. G. Coutinho, J. A. Martins, E. M. S. Castanheira and P. M. T. Ferreira, *Mater. Sci. Eng. C.*, 2021, **122**, 111869.
62. P. R. A. Chivers, R. S. Dookie, J. E. Gough and S. J. Webb, *Chem. Comm.*, 2020, **56**, 13792-13795.
63. Z. Yang, G. Liang, M. Ma, Y. Gao and B. Xu, *J. Mater. Chem.*, 2007, **17**, 850-854.
64. L. Chen, T. O. McDonald and D. J. Adams, *RSC Adv.*, 2013, **3**, 8714-8720.
65. L. Chen, S. Revel, K. Morris, L. C. Serpell and D. J. Adams, *Langmuir*, 2010, **26**, 13466-13471.
66. S. Fleming, S. Debnath, P. W. J. M. Frederix, T. Tuttle and R. V. Ulijn, *Chem. Comm.*, 2013, **49**, 10587-10589.
67. B. Ozbas, J. Kretsinger, K. Rajagopal, J. P. Schneider and D. J. Pochan, *Macromolecules*, 2004, **37**, 7331-7337.
68. G. A. Braun, B. E. Ary, A. J. Dear, M. C. H. Rohn, A. M. Payson, D. S. M. Lee, R. C. Parry, C. Friedman, T. P. J. Knowles, S. Linse and K. S. Åkerfeldt, *Biomacromolecules*, 2020, **21**, 4781-4794.
69. Y. Chen, Y. Feng, J. Gao and M. Bouvet, *J. Colloid Interface Sci.*, 2012, **368**, 387-394.
70. F. Würthner, *Chem. Comm.*, 2004, 1564-1579.
71. Z. Guo, X. Zhang, Y. Wang and Z. Li, *Langmuir*, 2019, **35**, 342-358.
72. S. Roy, D. Kumar Maiti, S. Panigrahi, D. Basak and A. Banerjee, *RSC Adv.*, 2012, **2**, 11053-11060.

73. E. Kozma, G. Grisci, W. Mróz, M. Catellani, A. Eckstein-Andicsovà, K. Pagano and F. Galeotti, *Dyes and Pigments*, 2016, **125**, 201-209.
74. J. G. Egan, G. Brodie, D. McDowall, A. J. Smith, C. J. C. Edwards-Gayle and E. R. Draper, *Mater. Adv.*, 2021, **2**, 5248-5253.
75. R. C. Claussen, B. M. Rabatic and S. I. Stupp, *J. Am. Chem. Soc.*, 2003, **125**, 12680-12681.
76. A. Aggeli, M. Bell, L. M. Carrick, C. W. G. Fishwick, R. Harding, P. J. Mawer, S. E. Radford, A. E. Strong and N. Boden, *J. Am. Chem. Soc.*, 2003, **125**, 9619-9628.
77. K. J. C. van Bommel, C. van der Pol, I. Muizebelt, A. Friggeri, A. Heeres, A. Meetsma, B. L. Feringa and J. van Esch, *Angew. Chem. Int. Ed.*, 2004, **43**, 1663-1667.
78. D. J. Adams, M. F. Butler, W. J. Frith, M. Kirkland, L. Mullen and P. Sanderson, *Soft Matter*, 2009, **5**, 1856-1862.
79. B. P. Nowak, M. Niehues and B. J. Ravoo, *Soft Matter*, 2021, **17**, 2857-2864.
80. A. Sharma, J. P. Wojciechowski, Y. Liu, T. Pelras, C. M. Wallace, M. Müllner, A. Widmer-Cooper, P. Thordarson and G. Lakhwani, *Cell Rep. Physical Science*, 2020, **1**, 100148.
81. B. L. Abraham, E. S. Toriki, N. D. J. Tucker and B. L. Nilsson, *J. Mater. Chem. B.*, 2020, **8**, 6366-6377.
82. G. Panzarasa, T. Sai, A. L. Torzynski, K. Smith-Mannschott and E. R. Dufresne, *Mol. Syst. Des. Eng.*, 2020, **5**, 445-448.
83. D. J. Cornwell, O. J. Daubney and D. K. Smith, *J. Am. Chem. Soc.*, 2015, **137**, 15486-15492.
84. A. L. Fameau, A. Arnould, M. Lehmann and R. von Klitzing, *Chem. Comm.*, 2015, **51**, 2907-2910.
85. V. Javvaji, A. G. Baradwaj, G. F. Payne and S. R. Raghavan, *Langmuir*, 2011, **27**, 12591-12596.
86. J. Raeburn, T. O. McDonald and D. J. Adams, *Chem. Comm.*, 2012, **48**, 9355-9357.
87. R. Fernandes, L.-Q. Wu, T. Chen, H. Yi, G. W. Rubloff, R. Ghodssi, W. E. Bentley and G. F. Payne, *Langmuir*, 2003, **19**, 4058-4062.
88. E. K. Johnson, D. J. Adams and P. J. Cameron, *J. Am. Chem. Soc.*, 2010, **132**, 5130-5136.
89. J. E. Bressner, B. Marelli, G. Qin, L. E. Klinker, Y. Zhang, D. L. Kaplan and F. G. Omenetto, *J. Mater. Chem. B.*, 2014, **2**, 4983-4987.
90. T. Shao, N. Falcone and H.-B. Kraatz, *ACS Omega*, 2020, **5**, 1312-1317.
91. S. Roy, N. Javid, P. W. J. M. Frederix, D. A. Lamprou, A. J. Urquhart, N. T. Hunt, P. J. Halling and R. V. Ulijn, *Chem. Eur. J.*, 2012, **18**, 11723-11731.
92. L. Chen, G. Pont, K. Morris, G. Lotze, A. Squires, L. C. Serpell and D. J. Adams, *Chem. Comm.*, 2011, **47**, 12071-12073.
93. J. Shi, Y. Gao, Y. Zhang, Y. Pan and B. Xu, *Langmuir*, 2011, **27**, 14425-14431.
94. M. A. Greenfield, J. R. Hoffman, M. Olvera de la Cruz and S. I. Stupp, *Langmuir*, 2010, **26**, 3641-3647.
95. W. Ji, C. Yuan, S. Zilberzwige-Tal, R. Xing, P. Chakraborty, K. Tao, S. Gilead, X. Yan and E. Gazit, *ACS Nano*, 2019, **13**, 7300-7309.
96. F. Wang and C.-L. Feng, *Angew. Chem. Int. Ed.*, 2018, **57**, 5655-5659.
97. R. Orbach, L. Adler-Abramovich, S. Zigerson, I. Mironi-Harpaz, D. Seliktar and E. Gazit, *Biomacromolecules*, 2009, **10**, 2646-2651.
98. A. Rajbhandary, D. M. Raymond and B. L. Nilsson, *Langmuir*, 2017, **33**, 5803-5813.
99. F. M. Menger and K. L. Caran, *J. Am. Chem. Soc.*, 2000, **122**, 11679-11691.

100. J. H. Kim, S. Y. Lim, D. H. Nam, J. Ryu, S. H. Ku and C. B. Park, *Biosens. Bioelectron.*, 2011, **26**, 1860-1865.
101. J. Ryu, S.-W. Kim, K. Kang and C. B. Park, *Adv. Mater.*, 2010, **22**, 5537-5541.
102. R. Jain and S. Roy, *Mater. Sci. Eng. C.*, 2020, **108**, 110483.
103. J. Raeburn, C. Mendoza-Cuenca, B. N. Cattoz, M. A. Little, A. E. Terry, A. Zamith Cardoso, P. C. Griffiths and D. J. Adams, *Soft Matter*, 2015, **11**, 927-935.
104. X. Dou, N. Mehwish, C. Zhao, J. Liu, C. Xing and C. Feng, *Acc. Chem. Res.*, 2020, **53**, 852-862.
105. J. Raeburn, A. Zamith Cardoso and D. J. Adams, *Chem. Soc. Rev.*, 2013, **42**, 5143-5156.
106. S. Liu, W. Yu and C. Zhou, *Soft Matter*, 2013, **9**, 864-874.
107. P. Terech, in *Specialist Surfactants*, ed. I. D. Robb, Springer Netherlands, Dordrecht, 1997, pp. 208-268.
108. S. Debnath, A. Shome, S. Dutta and P. K. Das, *Chem. Eur. J.* , 2008, **14**, 6870-6881.
109. W. J. Peveler, H. Packman, S. Alexander, R. R. Chauhan, L. M. Hayes, T. J. Macdonald, J. K. Cockcroft, S. Rogers, D. G. A. L. Aarts, C. J. Carmalt, I. P. Parkin and J. C. Bear, *Soft Matter*, 2018, **14**, 8821-8827.
110. Y. Song, S. R. Challa, C. J. Medforth, Y. Qiu, R. K. Watt, D. Peña, J. E. Miller, F. v. Swol and J. A. Shelnutt, *Chem. Comm.*, 2004, 1044-1045.
111. A. Friggeri, B. L. Feringa and J. van Esch, *J. Controlled Release*, 2004, **97**, 241-248.
112. M. Moniruzzaman and P. R. Sundararajan, *Langmuir*, 2005, **21**, 3802-3807.
113. K. Murata, M. Aoki, T. Nishi, A. Ikeda and S. Shinkai, *J. Chem. Soc., Chem. Commun.*, 1991, 1715-1718.
114. F. A. Larik, L. L. Fillbrook, S. S. Nurttila, A. D. Martin, R. P. Kuchel, K. Al Taief, M. Bhadbhade, J. E. Beves and P. Thordarson, *Angew. Chem. Int. Ed.*, 2021, **60**, 6764-6770.
115. N. Koumura, M. Kudo and N. Tamaoki, *Langmuir*, 2004, **20**, 9897-9900.
116. S. Miljanić, L. Frkanec, Z. Meić and M. Žinić, *Langmuir*, 2005, **21**, 2754-2760.
117. C.-W. Chu, L. Stricker, T. M. Kirse, M. Hayduk and B. J. Ravoo, *Chem. Eur. J.* , 2019, **25**, 6131-6140.
118. S. Samai, C. Sapsanis, S. P. Patil, A. Ezzeddine, B. A. Moosa, H. Omran, A.-H. Emwas, K. N. Salama and N. M. Khashab, *Soft Matter*, 2016, **12**, 2842-2845.
119. Z. Qiu, H. Yu, J. Li, Y. Wang and Y. Zhang, *Chem. Comm.*, 2009, 3342-3344.
120. Q. Liu, H. Wang, G. Li, M. Liu, J. Ding, X. Huang, W. Gao and W. Huayue, *Chin. Chem. Lett.*, 2019, **30**, 485-488.
121. S. H. Kim, Y. Sun, J. A. Kaplan, M. W. Grinstaff and J. R. Parquette, *New J. Chem.*, 2015, **39**, 3225-3228.
122. Z. Yang, G. Liang, L. Wang and B. Xu, *J. Am. Chem. Soc.*, 2006, **128**, 3038-3043.
123. Z. Yang and B. Xu, *Chem. Comm.*, 2004, 2424-2425.
124. S. C. Bremmer, J. Chen, A. J. McNeil and M. B. Soellner, *Chem. Comm.*, 2012, **48**, 5482-5484.
125. H. McEwen, E. Y. Du, J. P. Mata, P. Thordarson and A. D. Martin, *J. Mater. Chem. B.*, 2017, **5**, 9412-9417.
126. P. Duan and M. Liu, *Langmuir*, 2009, **25**, 8706-8713.
127. X. Du, J. Zhou, J. Shi and B. Xu, *Chem. Rev.*, 2015, **115**, 13165-13307.
128. E. R. Draper, H. Su, C. Brasnett, R. J. Poole, S. Rogers, H. Cui, A. Seddon and D. J. Adams, *Angew. Chemie Int. Ed.*, 2017, **56**, 10467-10470.
129. K. Almdal, J. Dyre, S. Hvidt and O. Kramer, *Polymer Gels and Networks*, 1993, **1**, 5-17.

130. F. Del Giudice, M. Tassieri, C. Oelschlaeger and A. Q. Shen, *Macromolecules*, 2017, **50**, 2951-2963.
131. C. Yan and D. J. Pochan, *Chem. Soc. Rev.*, 2010, **39**, 3528-3540.
132. M. Wallace, J. A. Iggo and D. J. Adams, *Soft Matter*, 2015, **11**, 7739-7747.
133. M. Zelzer and R. V. Ulijn, *Chem. Soc. Rev.*, 2010, **39**, 3351-3357.
134. A. F. Craievich, *Mater. Res.*, 2002, **5**, 1-11.
135. D. A. Jacques and J. Trewhella, *Protein Sci.*, 2010, **19**, 642-657.
136. B. R. Pauw, *J. Phys.: Condens. Matter*, 2013, **25**, 383201.
137. J. Pérez and Y. Nishino, *Curr. Opin. Struct. Biol.*, 2012, **22**, 670-678.
138. L. L. E. Mears, E. R. Draper, A. M. Castilla, H. Su, Zhuola, B. Dietrich, M. C. Nolan, G. N. Smith, J. Doutch, S. Rogers, R. Akhtar, H. Cui and D. J. Adams, *Biomacromolecules*, 2017, **18**, 3531-3540.
139. J.-L. Li and X.-Y. Liu, *Adv. Funct. Mater.*, 2010, **20**, 3196-3216.
140. A. M. Fuentes-Caparrós, B. Dietrich, L. Thomson, C. Chauveau and D. J. Adams, *Soft Matter*, 2019, **15**, 6340-6347.
141. S. Tsonchev, K. L. Niece, G. C. Schatz, M. A. Ratner and S. I. Stupp, *J. Phys. Chem. B.*, 2008, **112**, 441-447.
142. T. Shimada, N. Sakamoto, R. Motokawa, S. Koizumi and M. Tirrell, *J. Phys. Chem. B.*, 2012, **116**, 240-243.
143. S. R. Raghavan and Y. Feng, in *Wormlike Micelles: Advances in Systems, Characterisation and Applications*, The Royal Society of Chemistry, 2017, pp. 9-30.
144. P. W. Atkins, J. De Paula and J. Keeler, in *Atkins' Physical Chemistry*, Oxford University Press, Oxford, 10th edn., 2014, pp. 696-735.
145. F. E.-T. Heakal and A. E. Elkholy, *J. Mol. Liq.*, 2017, **230**, 395-407.
146. C. Tanford, *J. Phys. Chem.*, 1974, **78**, 2469-2479.
147. J.-F. Berret, in *Molecular Gels: Materials with Self-Assembled Fibrillar Networks*, eds. R. G. Weiss and P. Terech, Springer Netherlands, Dordrecht, 1st edn., 2006, pp. 667-720.
148. C. A. Dreiss, *Soft Matter*, 2007, **3**, 956-970.
149. J. Yang, *COCIS*, 2002, **7**, 276-281.
150. S. A. Rogers, M. A. Calabrese and N. J. Wagner, *COCIS*, 2014, **19**, 530-535.
151. X. Wu, Y. Wu, S. Yang, M. Zhao, M. Gao, H. Li and C. Dai, *Soft Matter*, 2016, **12**, 4549-4556.
152. H. Mohammadigoushki, A. Dalili, L. Zhou and P. Cook, *Soft Matter*, 2019, **15**, 5483-5494.
153. K. Sakai, K. Nomura, R. G. Shrestha, T. Endo, K. Sakamoto, H. Sakai and M. Abe, *Langmuir*, 2012, **28**, 17617-17622.
154. T. Shikata, H. Hirata and T. Kotaka, *Langmuir*, 1988, **4**, 354-359.
155. J. Narayanan, C. Manohar, F. Kern, F. Lequeux and S. J. Candau, *Langmuir*, 1997, **13**, 5235-5243.
156. P. A. Hassan, S. J. Candau, F. Kern and C. Manohar, *Langmuir*, 1998, **14**, 6025-6029.
157. N. R. Agrawal, X. Yue, Y. Feng and S. R. Raghavan, *Langmuir*, 2019, **35**, 12782-12791.
158. A. Z. Cardoso, L. L. E. Mears, B. N. Cattoz, P. C. Griffiths, R. Schweins and D. J. Adams, *Soft Matter*, 2016, **12**, 3612-3621.
159. H. Zhang, F. Zhang and R. Yuan, in *Hydrogels Based on Natural Polymers*, ed. Y. Chen, Elsevier, 2020, pp. 357-410.
160. W. A. Laftah, S. Hashim and A. N. Ibrahim, *Polym. Plast. Technol. Eng.*, 2011, **50**, 1475-1486.

161. V. G. Kadajji and G. V. Betageri, *Polymers*, 2011, **3**, 1972-2009.
162. B. O. Okesola and D. K. Smith, *Chem. Soc. Rev.*, 2016, **45**, 4226-4251.
163. C. J. Donahue, *Journal of Chemical Education*, 2006, **83**, 862.
164. S. Banerjee, R. K. Das and U. Maitra, *Journal of Materials Chemistry*, 2009, **19**, 6649-6687.
165. E. R. Draper and D. J. Adams, in *Chemoresponsive Materials*, 2015, pp. 332-363.
166. D. K. Smith, in *Molecular Gels: Structure and Dynamics*, The Royal Society of Chemistry, 2018, DOI: 10.1039/9781788013147-00300, pp. 300-371.
167. V. Castelletto, I. W. Hamley, C. Stain and C. Connon, *Langmuir*, 2012, **28**, 12575-12580.
168. B. K. Das, B. Pramanik, S. Chowdhuri, O. A. Scherman and D. Das, *Chem. Comm.*, 2020, **56**, 3393-3396.
169. T. Kar, S. Debnath, D. Das, A. Shome and P. K. Das, *Langmuir*, 2009, **25**, 8639-8648.
170. S. Basak, N. Nandi, S. Paul, I. W. Hamley and A. Banerjee, *Chem. Comm.*, 2017, **53**, 5910-5913.
171. D. R. Trivedi and P. Dastidar, *Chem. Mater.*, 2006, **18**, 1470-1478.
172. D. R. Trivedi, A. Ballabh and P. Dastidar, *Chem. Mater.*, 2003, **15**, 3971-3973.
173. S. Bhattacharya and Y. Krishnan-Ghosh, *Chem. Comm.*, 2001, 185-186.
174. F. Yanagawa, S. Sugiura and T. Kanamori, *Regenerative Therapy*, 2016, **3**, 45-57.
175. T. Jungst, W. Smolan, K. Schacht, T. Scheibel and J. Groll, *Chem. Rev.*, 2016, **116**, 1496-1539.
176. L. Ning and X. Chen, *Biotechnol. J.*, 2017, **12**, 1600671.
177. D. J. Richards, Y. Tan, J. Jia, H. Yao and Y. Mei, *Isr. J. Chem*, 2013, **53**, 805-814.
178. T. Billiet, M. Vandenhaute, J. Schelfhout, S. Van Vlierberghe and P. Dubruel, *Biomaterials*, 2012, **33**, 6020-6041.
179. B. Raphael, T. Khalil, V. L. Workman, A. Smith, C. P. Brown, C. Streuli, A. Saiani and M. Domingos, *Materials Lett.*, 2017, **190**, 103-106.
180. H. Jian, M. Wang, Q. Dong, J. Li, A. Wang, X. Li, P. Ren and S. Bai, *ACS Appl. Mater. Interfaces*, 2019, **11**, 46419-46426.
181. B. Dessane, R. Smirani, G. Bouguéon, T. Kauss, E. Ribot, R. Devillard, P. Barthélémy, A. Naveau and S. Crauste-Manciet, *Sci. Rep.*, 2020, **10**, 2850.
182. M. C. Nolan, A. M. Fuentes Caparrós, B. Dietrich, M. Barrow, E. R. Cross, M. Bleuel, S. M. King and D. J. Adams, *Soft Matter*, 2017, **13**, 8426-8432.
183. A. M. Fuentes-Caparrós, Z. Canales-Galarza, M. Barrow, B. Dietrich, J. Läuger, M. Nemeth, E. R. Draper and D. J. Adams, *Biomacromolecules*, 2021, **22**, 1625-1638.
184. A. Chalard, M. Mauduit, S. Souleille, P. Joseph, L. Malaquin and J. Fitremann, *Addit. Manuf*, 2020, **33**, 101162.
185. R. Sunyer, A. J. Jin, R. Nossal and D. L. Sackett, *PLOS ONE*, 2012, **7**, e46107.
186. P. J. Jervis, L. Hilliou, R. B. Pereira, D. M. Pereira, J. A. Martins and P. M. Ferreira, *Nanomaterials*, 2021, **11**, 704.
187. A. G. Cheetham, R. W. Chakroun, W. Ma and H. Cui, *Chem. Soc. Rev.*, 2017, **46**, 6638-6663.
188. H. Lu, L. Yuan, X. Yu, C. Wu, D. He and J. Deng, *Burns Trauma*, 2018, **6**, https://doi.org/10.1186/s41038-41018-40138-41038.
189. S. He, L. Mei, C. Wu, M. Tao, Z. Zhai, K. Xu and W. Zhong, *Nanoscale*, 2019, **11**, 5030-5037.
190. C. A. Dreiss, *Curr Opin Colloid Interface Sci.*, 2020, **48**, 1-17.

191. A. Shah, M. S. Malik, G. S. Khan, E. Nosheen, F. J. Iftikhar, F. A. Khan, S. S. Shukla, M. S. Akhter, H.-B. Kraatz and T. M. Aminabhavi, *Chem. Eng. J.*, 2018, **353**, 559-583.

192. M. E. Roth-Konforti, M. Comune, M. Halperin-Sternfeld, I. Grigoriants, D. Shabat and L. Adler-Abramovich, *Macromol. Rapid Commun.*, 2018, **39**, 1800588.

193. S. Bhuniya and B. H. Kim, *Chem. Comm.*, 2006, 1842-1844.

194. N. Swaminathan, N. Sharma, Y. Nerthigan and H.-F. Wu, *Appl. Surf. Sci.*, 2021, **554**, 149600.

195. A. Hemamalini and T. Mohan Das, *New J. Chem.*, 2013, **37**, 2419-2425.

196. Z. Khayat and H. Zali-Boeini, *Dyes and Pigments*, 2018, **159**, 337-344.

197. F. Mandegani, H. Zali-Boeini, Z. Khayat and R. Scopelliti, *Talanta*, 2020, **219**, 121237.

198. O. Ben-Zvi, I. Grinberg, A. A. Orr, D. Noy, P. Tamamis, I. Yacoby and L. Adler-Abramovich, *ACS Nano*, 2021, **15**, 6530-6539.

199. R. Contreras-Montoya, A. Castellví, G. Escolano-Casado, J. Juanhuix, M. Conejero-Muriel, M. T. Lopez-Lopez, J. M. Cuerva, L. Álvarez de Cienfuegos and J. A. Gavira, *Cryst. Growth Des.*, 2019, **19**, 4229-4233.

Chapter 2. Examining the Reproducibility of Low Molecular Weight Gelator Precursor Solutions

This Chapter is adapted from the following publication:

"Transferring molecular level changes to bulk properties via tunable self-assembly and hierarchical ordering"

L. Thomson, D. McDowall, L.J. Marshall, O. Marshall, H. Ng, W.J.A. Homer, E. Theodosiou, P.D. Topham, L.C. Serpell, R.J. Poole, A. Seddon, D.J. Adams, submitted.

LT was responsible for the synthesis of the gelator molecule used, methodology, collecting and analysing all experimental data found in this Chapter. RJP contributed to rheological experimental design and analysis. AS and DJA conceptualised and supervised the project. LT, AS and DJA wrote the initial draft of the manuscript, to which all authors contributed for the final publication. All other authors listed above contributed to the paper this Chapter is adapted from, but their work is not shown in this Chapter.

2.1 Introduction

In Chapter 1, we discussed the self-assembly process and trigger methods regarding gelation. For many trigger methods, the LMWG is first suspended in water at high pH.[1, 2] This gives a solution containing the carboxylate form of the LMWG, which can then be gelled by applying the trigger and reducing the LMWGs solubility. For gels triggered by the addition of metal ions, it is reported that the existence of worm-like micellar structures in these solutions is a prerequisite for gelation to occur.[3] Although considerations about gel reproducibility are common in literature,[2, 4-6] for example, reproducible rheological data or transition temperatures,[2, 4] discussions and protocols regarding these precursor solutions are usually very limited.

Many groups, however, have reported the presence of self-assembled structures in these LMWG precursor solutions, or solutions containing similar molecules. It is well reported that peptides in particular are able to self-assemble into various nanostructures.[7-10] We hypothesis that our peptide-based LMWG precursor solution structures should also be reproducibly created in order to therefore gain the most reproducible data possible when examining the solutions, or when gelling these solutions.

Our group commonly reports the existence of micelles in our precursor solutions of various dipeptide LMWGs.[3, 11-15] We have encountered both spherical and worm-like micelles. The LMWG chemical structure, LMWG concentration and counterions used to deprotonate the LMWG are known to make a difference to the micellar structures present. In recent work utilising small-angle X-ray and neutron scattering, we were able to show how the molecules of a dipeptide-based LMWG, known as 2NapFF, (Figure 2.1a) packed together to form nanotubes with a hollow core.[16] It was established that deprotonated carboxylic acids can be found at the interior and exterior of the elongated structures with naphthalene located in between, Figure 2.1b. Traditionally, however, these worm-like micelles have a hydrophobic core rather than a hollow one,[17, 18] but we have previously shown that these structures behave in a similar way to worm-like micelles,[3, 11-14] and so will be considered as such in this Thesis. When using a pH trigger to induce gelation, the hollow core disappears first, protonating the free carboxylic acids found in the core, causing a structural change. As the pH is decreased further, the cylinders become more elliptical.
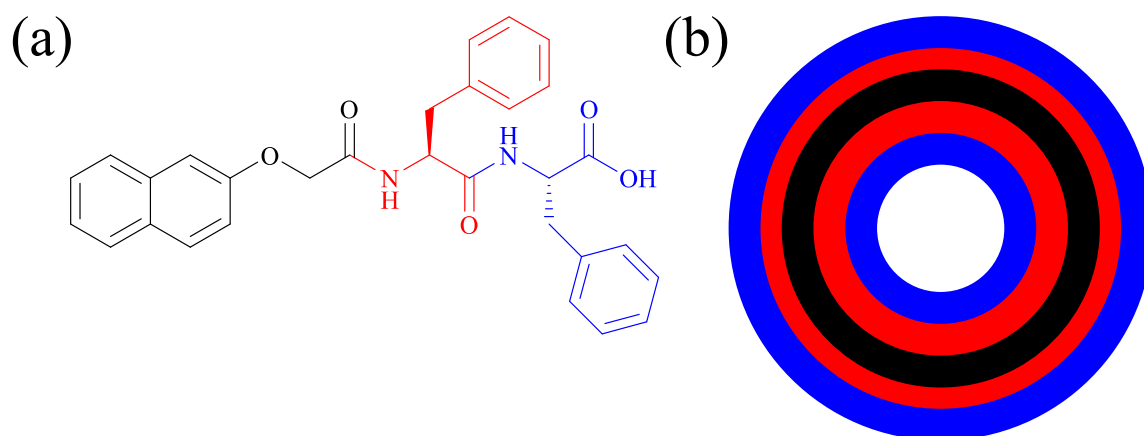
Figure 2.1. (a) Structure of the LMWG 2NapFF; (b) end on schematic of a hollow worm-like micelle formed by 2NapFF in solution, with colour coding showing the different sections of the structure highlighted in (a).

Worm-like micelles are considered a dynamic "living" system.[18-21] The micelles are capable of continuous breaking and reforming, and exhibit unique viscoelastic behaviour.[18, 19] The micelles are long and polymer-like; normally nanometres in diameter and several micrometres in length.[22, 23] The micelles however are also normally polydisperse in length.[24] This is not always the case however as recently, work has shown that the self-assembly of polymer worm-like micelles can be controlled by sonification time.[25] By adjusting the sonification time, the authors were able to control the aspect ratio of the micelles with very good monodispersity. Micellar growth can be affected by pH,[21, 26] the addition of salt,[27-29] and temperature.[13, 30]

Raghavan and co-workers focus extensively on worm-like micelles.[22, 24] The micelles studied by these researchers are not always in water, with solvents such as glycerol and formaldehyde also capable of allowing worm-like micelles to form.[30] In these solvents, the micelles persisted at temperatures as low as -20 °C. It is proposed that they could be used for applications such as anti-freeze coatings or lubricants. Other systems containing worm-like micelles which have been researched by the group are light responsive with the lengths of the micelles changed upon irradiation with light.[31, 32]

As well as dipeptide-based structures, peptide amphiphiles (PAs) are another class of molecule which form nanostructures. The Hamley research group commonly utilise a

combination of techniques, including small-angle X-ray scattering (SAXS) and complementary imaging methods, which can be used to look at structures in both the solution and hydrogel phases.[33-36] For example, when examining PAs, the group reported that pH affected the dimensions of the fibril structures formed, and the alignment of the structures.[35] It was also found that the PA solutions could spontaneously gel at pH 8, and gel at pH 12 when subjected to a heat-cool cycle. This paper, however, does not give many details with regards to how the solutions are formed. Other groups also use similar methods to examine PA self-assembly and structures.[37, 38] Another example examines a self-assembly process where spherical micelles are initially formed, followed by worm-like micelles as incubation time is increased, showing the transient nature of these strucutres.[38]

In this Chapter, we aim to establish a robust protocol for solutions containing a dipeptide LMWG which is known to form worm-like micelles at high pH. This protocol will give solutions of both reproducible rheological data and visibly similar samples. We will examine a number of factors which could alter the structures present in the solution, and the physical appearance of the samples; and discuss the challenges of reproducibility associated with these "living" materials.

2.2 Results and Discussion

We focus here on forming solutions of the functionalised dipeptide LMWG, 2NapFF, Figure 2.1a, which is used as an exemplar material selected from our group's library of LMWGs. Our group has previously shown this LMWG has two critical micelle concentrations (CMCs) up to a 2NapFF concentration of 10 mg/mL.[12] Whilst increasing the concentration of 2NapFF, it was found that spherical aggregates formed at the first CMC. At a second CMC, approximately 5 mg/mL 2NapFF, worm-like micelles were found to exist. We continue on from this work and examine solutions up to a 2NapFF concentration of 100 mg/mL. Above this LMWG concentration, it is difficult to form homogeneous solutions. In this Chapter, we investigate three concentrations of 2NapFF: 10, 40 and 100 mg/mL. These concentrations were chosen since previously, 10 mg/mL was the upper concentration limit studied; 100 mg/mL is the highest LMWG concentration we can use which still produces homogeneous solutions; and 40 mg/mL was chosen as an intermediate between these two concentrations. 40 mg/mL was chosen as the intermediate here because we wanted a concentration approximately halfway between our lower and upper limits. In initial tests, 40 mg/mL appeared to behave similarly to 45 and 50

mg/mL but using 40 mg/mL saved on material. A 2NapFF concentration of 100 mg/mL is the equivalent of 10 wt% which is a high loading volume and has the potential to form lyotropic liquid crystals. This is discussed in detail in Chapter 3, but briefly, lyotropic liquid crystals form when the concentration of an amphiphile is increased such that the structures interact and pack together into a more ordered mesophase.[39, 40]

2.2.1 Stirring Effects and Sample Aging

As a "living" system, worm-like micelles continuously break and reform when shear is applied,[19] and rheological properties (for example, as previously shown by a self-assembled flavonoid liquid crystal system)[41] have been reported to show a shear history dependence. When preparing our samples, we must stir to produce a homogeneous solution. This applies shear to the solution. Hence, we investigate the rate of stirring and time of stirring on our 2NapFF samples.

Samples were stirred at three different rates, whilst the container and stirrer bar size were kept constant. For stirring method 1, samples were stirred continuously at 400 rpm (set by stirrer plate) for seven days. For method 2, samples were stirred continuously at 1000 rpm (set by stirrer plate) for seven days. For method 3, samples were stirred overnight at 400 rpm (set by stirrer plate) to create a homogeneous solution and were then left undisturbed to stand for the remaining six day period. The data collected are shown in Figure 2.2. Using stirring method 1 (400 rpm) we see, in general, a gradual decrease in viscosity over the seven-day period. Using a higher shear rate, stirring method 2 (1000 rpm), we see 2NapFF solutions at concentrations of 10 and 40 mg/mL come to equilibrium viscosity after only one day stirring. This is shown very obviously when comparing the two shear rates of solutions at a concentration of 40 mg/mL 2NapFF (Figure 2.2d-e).

Fluid properties are known to be time-dependent; this is due to entanglement rates.[42] The rate of entanglement (based on Brownian-motion) is slow. Disentanglement, however, is driven by strain/shear and is therefore quicker.[42, 43] Hence, when our samples are allowed to stand undisturbed on the bench, we remove the shear which would be responsible for the continuous breaking of the micelles, allowing the worm-like micelles to slowly entangle, allowing the viscoelasticity of the solutions to increase.[44] We see this in Figure 2.2 where

shear history impacts the rheological properties for 2NapFF concentrations of 10 and 40 mg/mL. The viscosity gradually increases over the seven day period when left undisturbed.

For 100 mg/mL, however, we see a gradual decrease in viscosity over the seven-day period when left undisturbed. We hypothesis that this is due to the samples being both very viscous and very concentrated. Solutions at a concentration of 100 mg/mL were visibly very viscous, and we hypothesise that loading the samples onto the rheometer may have disturbed the entangled structures, as could the force applied to the structures when lowering the rheometer geometry for measurement.
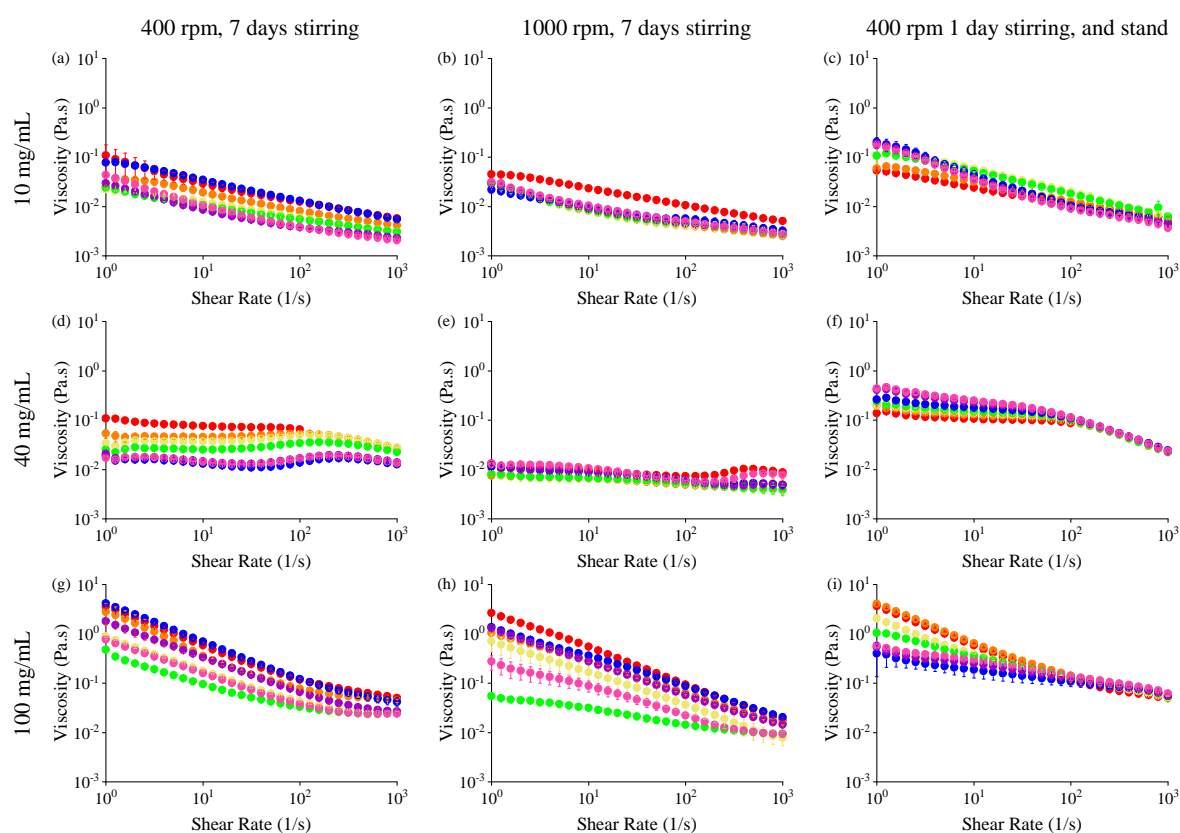
Figure 2.2. Viscosity data for solutions of 2NapFF at (a)-(c) 10 mg/mL; (d)-(f) 40 mg/mL; (g)-(i) 100 mg/mL at pH 10.5 whilst varying stirring over a seven-day period. Plots show viscosity after day 1 (red, the day following the creation of the samples), day 2 (orange), day 3 (yellow), day 4 (green), day 5 (blue), day 6 (purple) and day 7 (pink). Samples were: (a), (d), (g) stirred continuously at 400 rpm for seven days; (b), (e), (h) stirred continuously at 1000 rpm for seven days; (c), (f), (i) stirred overnight at 400 rpm, then left undisturbed to stand for the remaining six days.

The containers and stirrer bars used to prepare the samples also affects the sample viscosity, Figure 2.3. Choice of container is already known to make a difference to some samples. Our group has recently shown that the choice of container can affect gelling.[45] In this example, a flavin-based LMWG cannot be gelled using a solvent trigger when using a plastic 7 mL Sterilin vial, but can be gelled in metal cups of the same size and can also be gelled in glass containers of various dimensions. This is due to differences in capillary forces and surface chemistry. Here, we select a 50 mL Falcon tube (inner diameter of 27 mm) with a stirrer bar of dimensions 25 x 8 mm and compare this to a Sterilin vial (inner diameter 15 mm) with a stirrer bar of dimensions 13 x 3 mm. Keeping the stirring rate set to 1000 rpm for both sample containers, we observe clear differences in the viscosity trend over the seven-day monitoring period. When samples are prepared in Falcon tubes and stirred with 25x8 mm stirrer bars, Figure 2.3a, the viscosity comes to a steady state equilibrium after only one day of stirring at 1000 rpm. However, when stirring in a smaller container (Sterilin vial) and using a smaller stirrer bar (13 x 3 mm), we see, in general, a decreasing trend in viscosity as stirring time is increased. It is therefore important to consistently prepare the samples by stirring at the same rates, but also by stirring in the same containers.
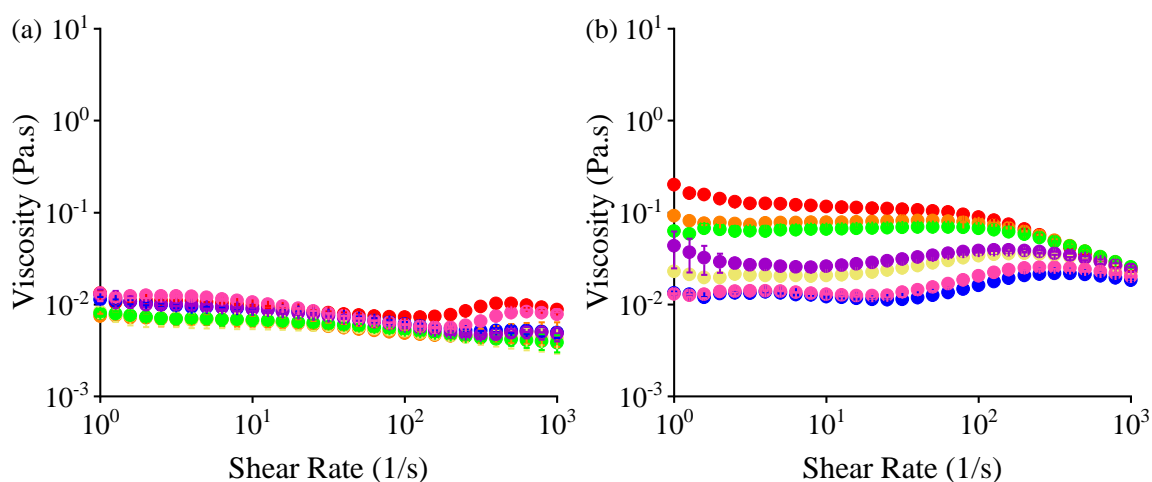
Figure 2.3. Viscosity data for solutions of 2NapFF at 40 mg/mL at pH 10.5, keeping a constant stirring rate of 1000 rpm over a seven-day period, prepared in (a) a falcon tube with 25x8 mm stirrer bar and (b) a 7 mL Sterilin vial with 13x3 mm stirrer bar. Plots show viscosity after day 1 (red, the day following the creation of the samples), day 2 (orange), day 3 (yellow), day 4 (green), day 5 (blue), day 6 (purple) and day 7 (pink).

Additional stirring experiments – denoted as "recovery experiments" – were also examined. Here, we examine our 40 mg/mL 2NapFF concentration solutions whilst combining stirring methods. Initially, we stir samples at either 400 rpm or 1000 rpm continuously for three days, before leaving to stand undisturbed for the remaining four days (Figure 2.4). Combining the stirring and standing methods for these samples, we see a combination of the effects seen in Figure 2.2. When stirring at the lower stirring rate of 400 rpm, the viscosity increases and comes to equilibrium after day 5. This same viscosity equilibrium does not occur until day 6 when initially stirring at the higher stirring rate of 1000 rpm.
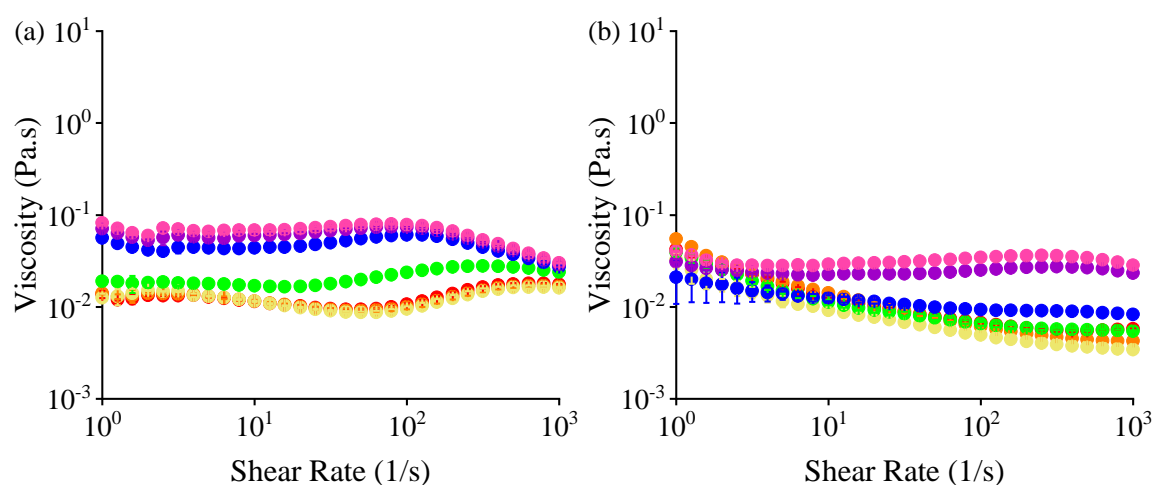
Figure 2.4. Viscosity data for solutions of 2NapFF at 40 mg/mL at pH 10.5 whilst varying stirring over a seven-day period; showing day 1 (red, the day following the creation of the samples), day 2 (orange), day 3 (yellow), day 4 (green), day 5 (blue), day 6 (purple) and day 7 (pink). Samples were (a) stirred for 3 days at 400 rpm, then left undisturbed to stand for the remaining four days; (b) stirred for 3 days at 1000 rpm, then left undisturbed to stand for the remaining four days.

To further examine the effects of combined stirring methods and viscosity steady state equilibrium, we performed additional "recovery experiments." 2NapFF at a concentration of 40 mg/mL were stirred at 400 rpm or 1000 rpm for either one day or seven days. All samples were then left to stand undisturbed on the bench for an additional seven days. We aimed to establish the effects of different stirring rates and times on the viscosity increases we have already noted when samples are left undisturbed after stirring. Combining the 400 rpm stirring rate and resting, Figure 2.5a, we see similar viscosity plot shapes to

those seen in Figure 2.2d. We also see the viscosity increase like that shown in Figure 2.2f. The increase in viscosity over the seven day standing period is approximately half an order of magnitude greater, regardless if samples were originally stirred at 400 rpm for one day or for seven days. However, when at the greater stirring rate of 1000 rpm followed by resting, Figure 2.5b, we see that like Figure 2.2e, the viscosity of samples stirred at 1000 rpm comes to equilibrium after one day. Unlike when stirring at 400 rpm, we do not see an increase in viscosity once stirring has stopped. As the micelles have been disturbed more at 1000 rpm compared to 400 rpm, we assume they have been broken more by the larger shear applied and hence in the same stand time, we do not see the micelles entangle as quickly to increase the viscosity when the shear is removed. We note that although there are visible changes and rheological changes in viscosity, there is no indication of sedimentation (which can occur in colloidal suspensions)[46] in any of the examples described in this section.
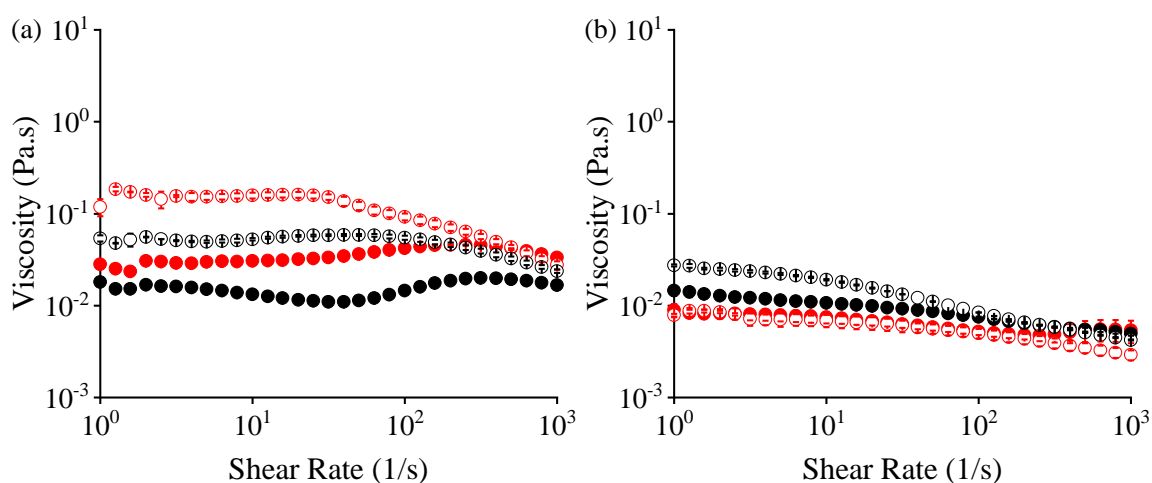
Figure 2.5. Viscosity data for solutions of 2NapFF at 40 mg/mL at pH 10.5 to examine the effects of stirring at different rates and then removing shear. Samples were stirred at (a) 400 rpm and (b) 1000 rpm for one day (filled red circles, the day following the creation of the samples); and seven days (filled black circles), and then left undisturbed for seven days following stirring. Viscosity measured after the seven-day rest period are represented by hollow red circles for samples stirred for one day before the rest period and hollow black circles for samples stirred for seven days before the rest period.

2.2.2 Effects of pH

Previously, it has been reported that both worm-like micelles and liquid crystal phases can be altered by variations in pH.[21, 26, 47] Our group has reported that in order to form solutions of 2NapFF, the solutions must be at high pH.[1] At high pH, the LMWG free carboxylic acid group is deprotonated which increases the LMWG solubility in water. Adding excess base increases the number of charges present in the system, increasing electrostatic screening, and could affect how the 2NapFF molecules can aggregate and hence affect the solution properties. Lowering to pH 9 could mean a change in structures or packing due to an apparent pK_a found near this pH in 2NapFF solutions at concentrations of 5 and 10 mg/mL.[13, 48] Viscosity data collected whilst varying pH are shown in Figure 2.6. At 2NapFF concentrations of 10 mg/mL and 100 mg/mL, there is no variation in viscosity as the pH is varied between pH 9 and pH 12. At a 2NapFF concentration of 40 mg/mL, we see a pH dependence. The viscosity of 2NapFF at 40 mg/mL is lower at pH 9 and pH 9.5 compared to when at pH 10-12. We attribute this to an apparent pK_a found near this pH region. 2NapFF at a concentration of 40 mg/mL and pH 10.5 shows a slight increase in viscosity at low shear rate compared to pH 10 and pH 11-12. This could suggest a potential change in morphology at this concentration and pH. To confirm this, further investigation with other techniques such as small-angle neutron or X-ray scattering, and imaging methods would be required. Overall, these data highlight again the sensitivity of these systems to small changes. Care should be taken when adjusting the pH to the desired value. To do this, we always use a calibrated pH probe and allow ample stirring time between the addition of acid/base and the pH measurement to ensure the pH is uniform throughout the sample. Examining our samples by eye, we can see turbidity differences depending on the 2NapFF concentration and pH of the samples (Figure 2.7). Examining polarised optical microscopy (POM) images, Figure 2.8, we see differences in the images collected below pH 10 at 2NapFF concentrations of 10 and 40 mg/mL. We again attribute this to the apparent pK_a located near this pH. For 100 mg/mL, the POM images do not show an obvious difference at any pH, consistent with the viscosity measurements collected at various pH values.
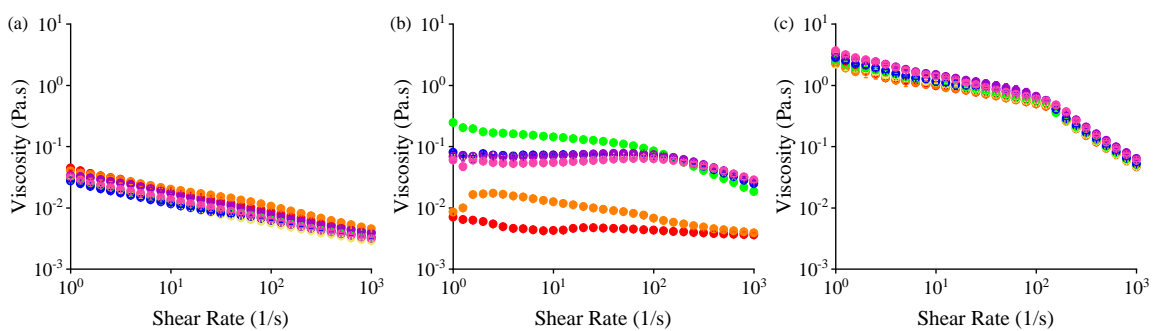
Figure 2.6. Viscosity data for (a) 10 mg/mL; (b) 40 mg/mL; (c) 100 mg/mL 2NapFF solutions at pH 9 (red); 9.5 (orange); 10 (yellow); 10.5 (green); 11 (blue); 11.5 (purple); 12 (pink).
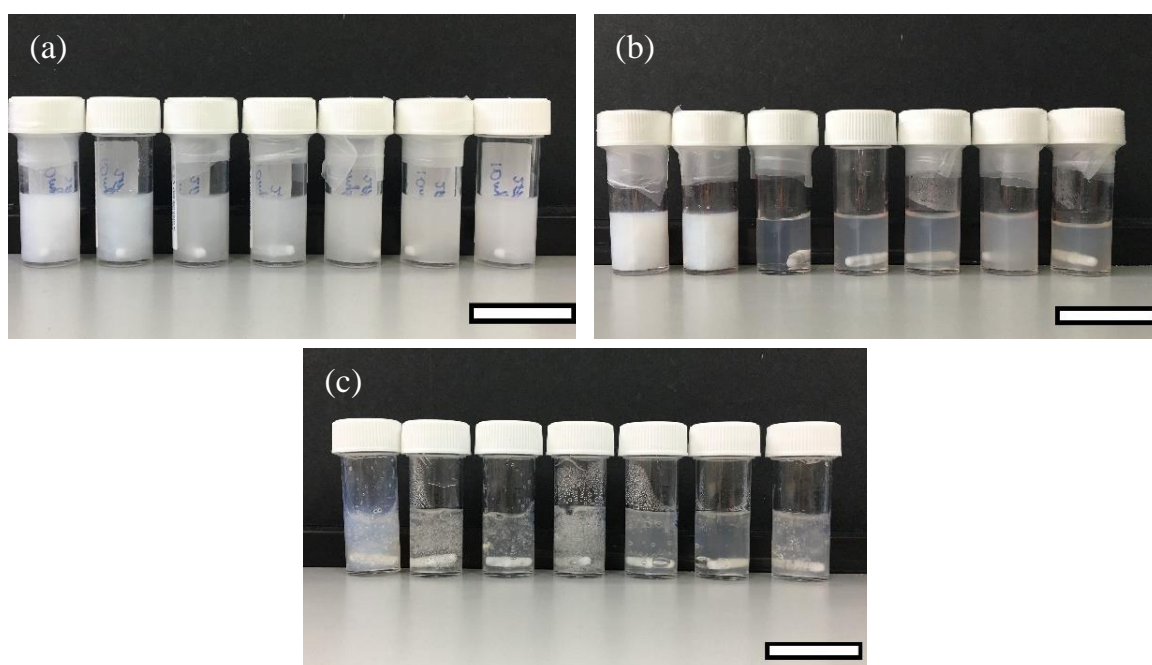

Figure 2.7. Photographs of (a) 10 mg/mL; (b) 40 mg/mL; (c) 100 mg/mL 2NapFF concentration solutions when varying pH. From left to right: pH 9, pH 9.5, pH 10, pH 10.5, pH 11, pH 11.5, pH 12. Scale bars represent 3 cm.
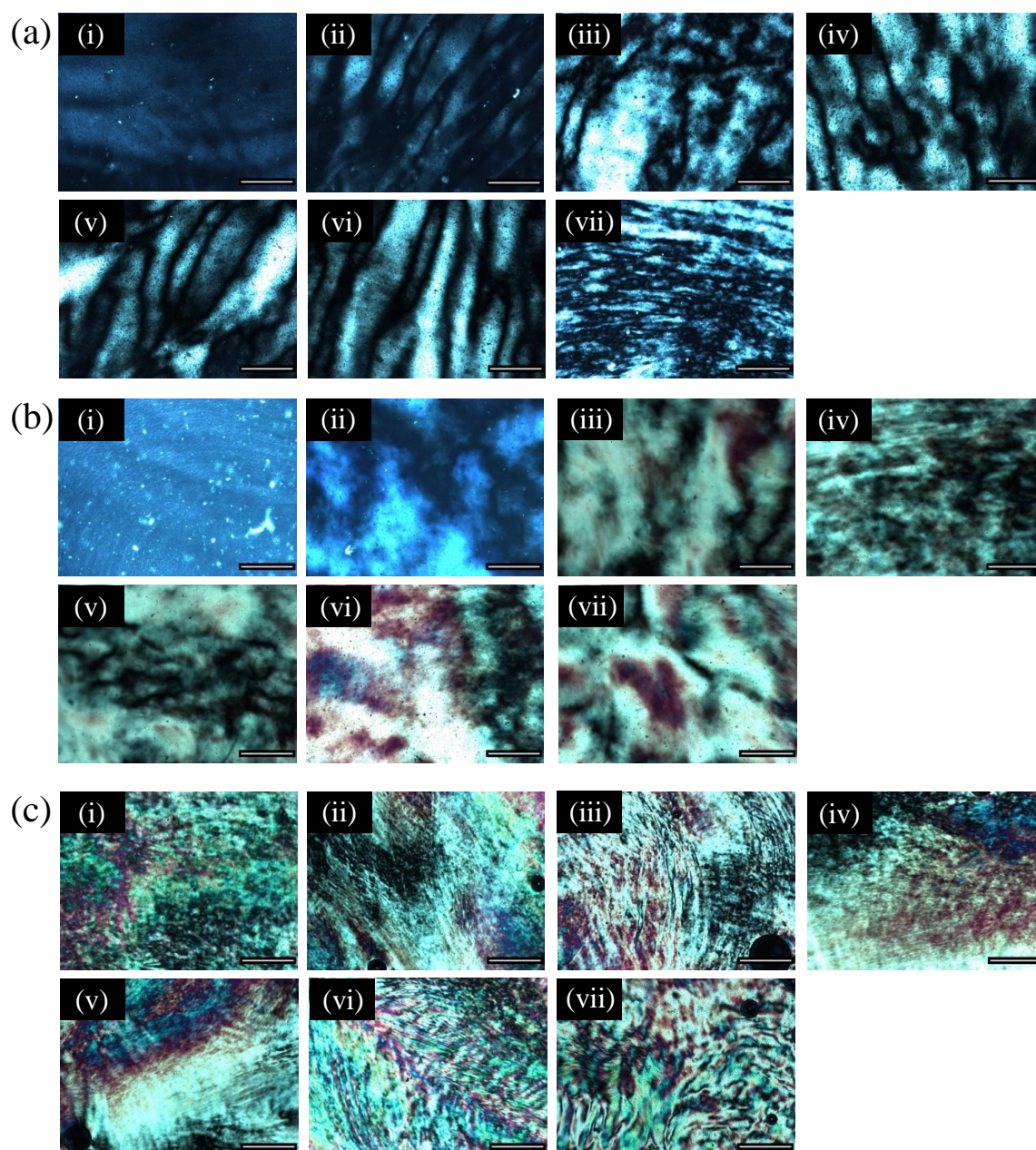
Figure 2.8. POM images for 2NapFF solutions at concentrations of (a) 10 mg/mL; (b) 40 mg/mL; (c) 100 mg/mL at (i) pH 9; (ii) 9.5; (iii) 10; (iv) 10.5; (v) 11; (vi) 11.5; (vii) 12. Scale bars represent 500 μm.

2.2.3 Addition of NaCl

The effects of salts on micellar and liquid crystal phases are commonly reported in literature.[18, 30, 40, 49] Salts can encourage micelle growth due to electrostatic screening.[18] For example, in a study of a cationic surfactant in organic solvents, binding salts (salts with large

organic counterions) increased the viscosity of the samples. However, simple salts (such as sodium chloride) showed no effect on viscosity.[30] We investigate this concept with our 2NapFF system because we have previously shown that solutions of 2NapFF can gel when various salts, including NaCl, are added.[3, 11, 12]

Hence, using 10, 40 and 100 mg/mL 2NapFF solutions, we examined the effect of adding NaCl to 2NapFF during the preparation process, Figure 2.9. For 2NapFF solutions at a concentration of 10 mg/mL, no differences in viscosity are observed until a 1:1 NaCl:2NapFF molar ratio. For 2NapFF solutions at a concentration of 40 mg/mL, there is a small increase in viscosity between 0.001 and 0.01 NaCl:1 2NapFF molar ratios. For 2NapFF solutions at a concentration of 100 mg/mL, there is a small increase in viscosity between 0 and 0.1 NaCl:1 2NapFF molar ratios. This however is much more pronounced at 1:1 NaCl;2NapFF where there is approximately an increase in viscosity which spans two orders of magnitude. Since NaCl can be used to trigger 2NapFF gelation,[3] the increase in viscosity with a 1:1 molar ratio could be due to the beginning of cross-links forming between the worm-like micelles. This would signify the beginning of a network forming, which would increase the viscosity. Increasing the salt ratio again to 10:1 NaCl:2NapFF in 100 mg/mL 2NapFF solutions, there is a drop of an order of magnitude in viscosity compared to the 1:1 NaCl:2NapFF sample. We suggest this is due to charge screening, or because of the breakdown of the gel by stirring which would have been formed if left undisturbed. Overall, the viscosity changes caused by the addition of salt are more obvious when the concentration of 2NapFF is increased. We attribute this increase in viscosity occurring at lower salt ratios as the 2NapFF concentration increases because the system is more concentrated, amplifying any changes.

At salt ratios of 1:1 NaCl:2NapFF or 10:1 NaCl:2NapFF, we also observe changes in visible appearance (Figure 2.10) and in POM images (Figure 2.11). At these increased salt ratios, samples are more turbid. Examining using POM, solutions containing a 10:1 salt to 2NapFF molar ratio are so turbid that they cannot be imaged effectively in this way. All POM images, except the 10:1 NaCl:2NapFF molar ratio at concentrations of 40 and 100 mg/mL, show interaction with the cross-polarised light.
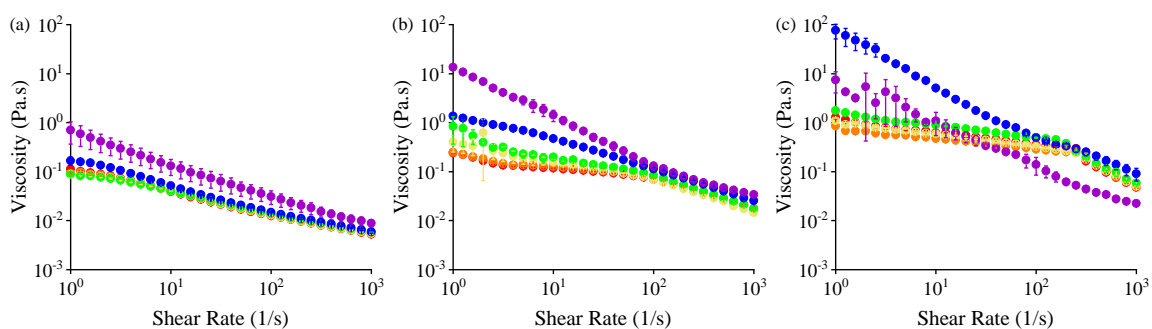
Figure 2.9. Viscosity data for 2NapFF solutions at pH 10.5 at concentrations of (a) 10 mg/mL; (b) 40 mg/mL; (c) 100 mg/mL with added NaCl of molar ratios: 0:1 NaCl:2NapFF (red); 0.001:1 NaCl:2NapFF (orange); 0.01:1 NaCl:2NapFF (yellow); 0.1:1 NaCl:2NapFF (green); 1:1 NaCl:2NapFF (blue); 10:1 NaCl:2NapFF (purple).
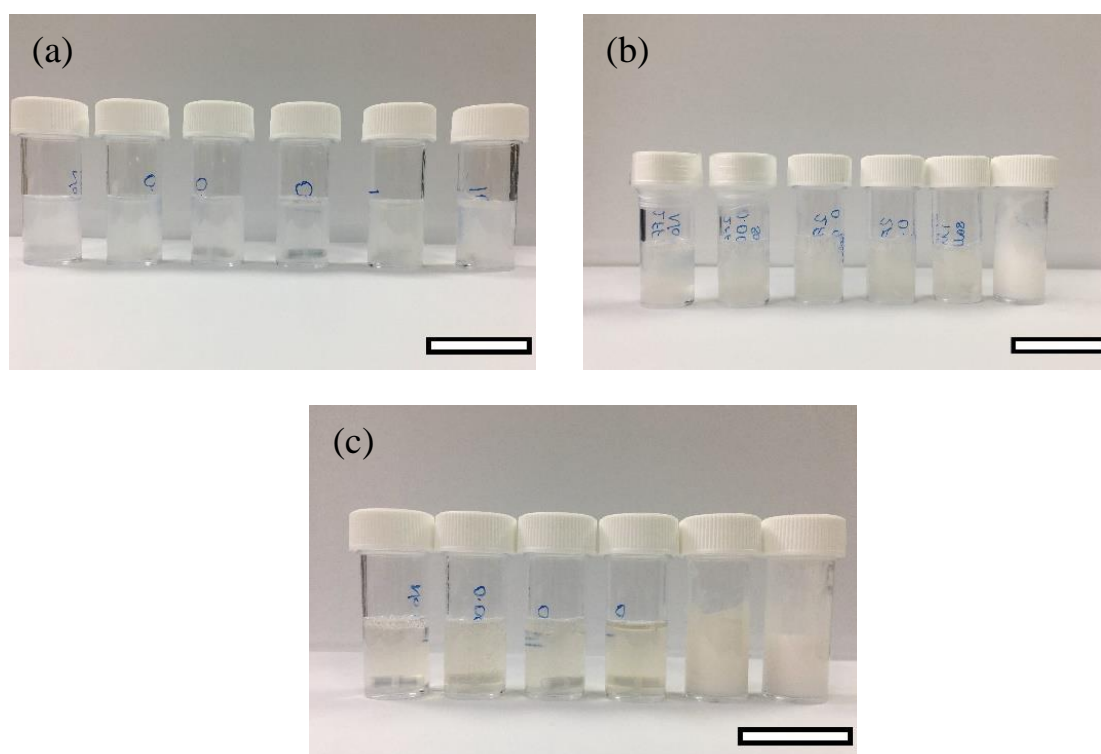

Figure 2.10. Photographs of solutions containing added NaCl at 2NapFF concentrations of (a) 10 mg/mL; (b) 40 mg/mL; (c) 100 mg/mL. From left to right contain no NaCl; 0.001:1 NaCl:2NapFF; 0.01:1 NaCl:2NapFF; 0.1:1 NaCl:2NapFF; 1:1 NaCl:2NapFF; 10:1 NaCl:2NapFF. Scale bars represent 3 cm.
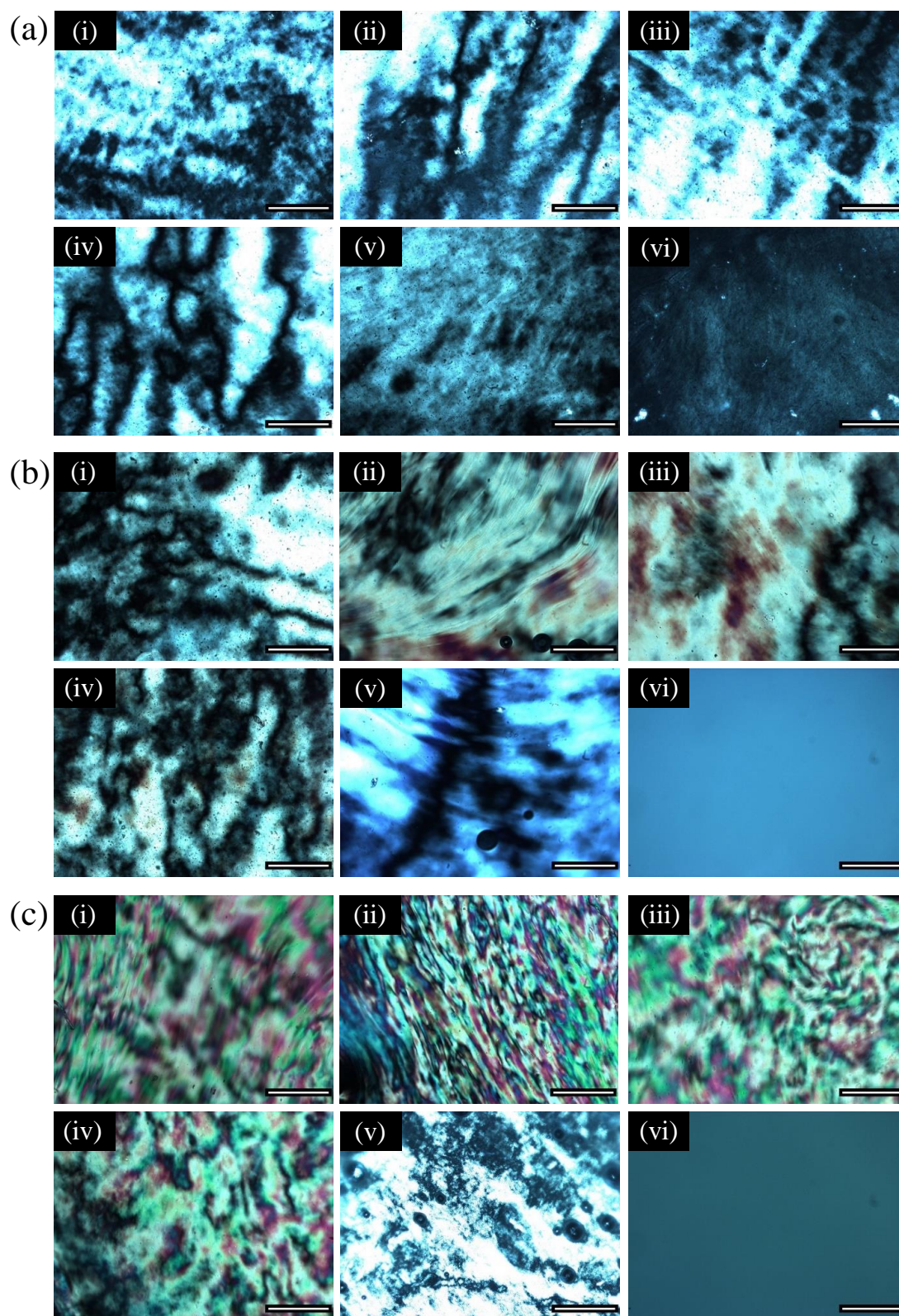
Figure 2.11. POM images for 2NapFF solutions at concentrations of (a) 10 mg/mL; (b) 40 mg/mL; (c) 100 mg/mL with (i) no NaCl; (ii) 0.001:1 NaCl:2NapFF; (iii) 0.01:1 NaCl:2NapFF; (iv) 0.1:1 NaCl:2NapFF; (v) 1:1 NaCl:2NapFF; (vi) 10:1 NaCl:2NapFF. Scale bars represent 500 μm.

2.2.4 Sample Stability

We have previously shown that the viscosity of 2NapFF solutions at concentrations of 10 mg/mL or lower show shear thinning behaviour.[50] To test for any sample artefacts when examining 2NapFF solutions at higher concentrations, we checked for any time dependency and instability within our 40 mg/mL 2NapFF sample, setting the rheometer to hold constant shear rate values of 1, 5, 10, 50, 100, 500 and 1000 s^{-1} for 10 minutes before moving to the next value (Figure 2.12). We see that compared to our original viscosity data (Figure 2.12b, red), there is no considerable change in viscosity when the shear rate is held for 10 minutes. This suggests that any features shown are not simply due to a time dependence or instability.
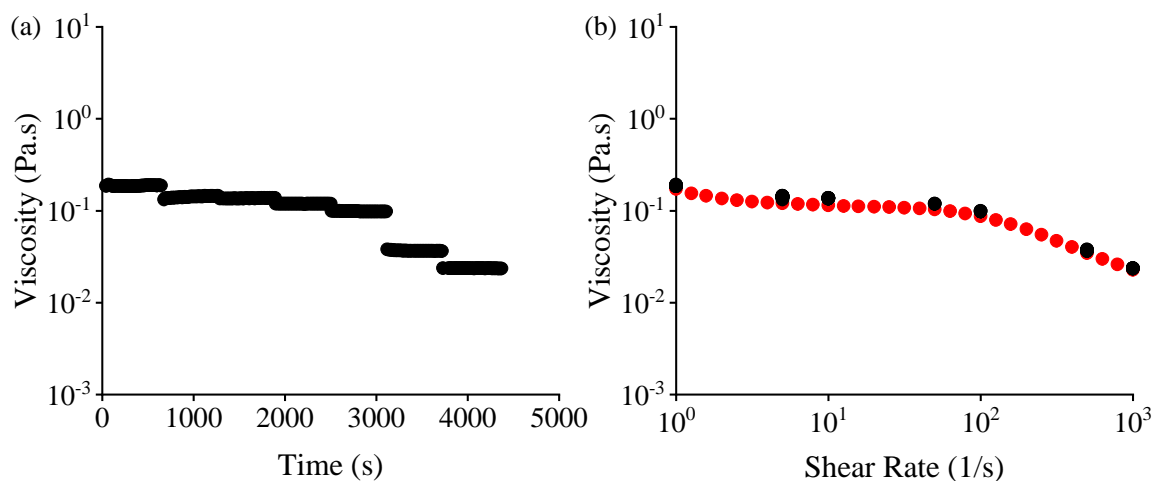
Figure 2.12. Viscosity time sweep for 2NapFF solutions at a concentration of 40 mg/mL and pH 10.5, stirred for 2 days before measurement. (a) Full viscosity data collected when shear rate was held constant for 10 minutes at 1, 5, 10, 50, 100, 500 and 1000 s^{-1}. (b) Original viscosity run of 2NapFF at pH 10.5 (red) at a concentration of 40 mg/mL and viscosity data, taken from (a), when holding the shear rate constant (black), to compare.

Additionally, we pre-sheared our 2NapFF solutions. As described previously, worm-like micelles break and reform when shear is applied.[19] Hence, to check for instability, sample memory and history, we used the rheometer to pre-shear our samples. Here, we used the same solution to perform two consecutive viscosity sweeps at each investigated concentration. From our data in Figure 2.13, solutions at a concentration of 100 mg/mL 2NapFF show a small decrease in viscosity caused by pre-shearing. Again, we suggest that

changes are visible at this 2NapFF concentration because the solutions are very concentrated, which amplifies any changes in the viscosity data.
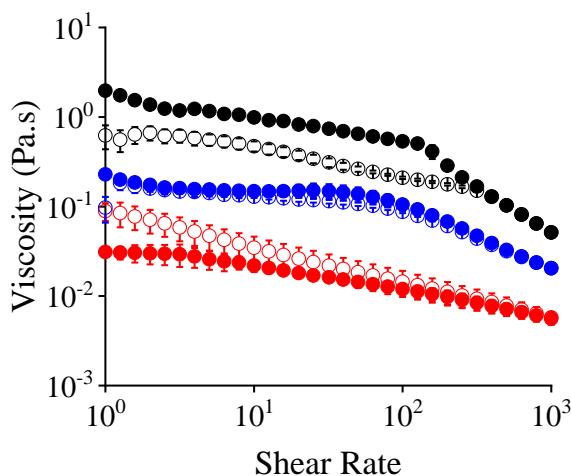

Figure 2.13. Viscosity data for 2NapFF solutions at pH 10.5 at a concentration of 10 mg/mL (red); 40 mg/mL (blue); 100 mg/mL (black) which have been pre-sheared using a rheometer. Filled circles represent the first viscosity measurement and empty circles represent the second viscosity measurement of the same sample. The geometry was not lifted between the first and second viscosity measurements and samples were left to sit for two minutes undisturbed between measurements.

2.3 Conclusions and Future Work

In this Chapter, we aim to find a sample preparation method for solutions of the LMWG, 2NapFF, which is known to form worm-like micelles. Although many LMWG hydrogels are formed from precursor solutions, there is usually not the same attention given to the precursor solutions as the gels. This is surprising, as there are examples of similar structures, including short-chain peptides and PAs, which are known to self-assemble into nanostructures in the solution phase. There are also numerous reports studying the effects of various properties (such as pH and addition of salt) on micellar structures, however there is little cross-over between this and LMWG precursor solutions.

We have shown many different factors affect our solutions, including stirring methods, pH and addition of NaCl. We show here that the micelles present in these 2NapFF solutions are "living" with the constant making and breaking of micelles altering the viscosity as the

stirring methods are altered. Higher shear rates affect the micelles more compared to lower shear rates. Here, we suggest that by removing shear, micelles are allowed the chance to reform and the viscosity increases. To confirm this is the case, rheo-SANS or rheo-SAXS could be utilised. These techniques allow scattering to be measured simultaneously alongside rheology so that changes in structure which arise due to shear can be monitored. We have also showed that we are able to check the stability of our samples by applying shear for an extended period of time using a rheometer and monitoring the viscosity for any changes with time. Factors such as changing the pH of the solutions and adding NaCl during the sample preparation stage can also affect viscosity, POM images and the appearance of the sample by eye. It is therefore important to keep a detailed account of the preparation method and to keep the method as consistent as possible.

We have shown that although 2NapFF is a LMWG, it is acting here as a surfactant. Over a range of 2NapFF concentrations studied, many factors affect the viscosity of the solutions. The concentrations of 2NapFF solutions chosen for examination in this Chapter were based on the maximum concentration already examined by our group, the maximum concentration we were able to form a homogenous solution with during this work, and an intermediate concentration. It was found that each concentration behaved differently during the sample preparation process depending on the factor being investigated. We hypothesise that solutions at the highest LMWG concentration studied, 100 mg/mL, shows changes more obviously than the more dilute solutions due to the amount of LMWG present.

In future work, Chapter 3, we use our findings here to prepare solutions of 2NapFF in a consistent way in order to investigate the structures and packing of 2NapFF present in the solutions.

2.4 Experimental

2.4.1 Synthesis of LMWG

Synthesis of the LMWG used in this chapter, 2NapFF, can be found in Chapter 6, Section 1.

2.4.2 2NapFF Solution Preparations

To produce a solution of 2NapFF at concentrations of 10, 40 and 100 mg/mL requires a predetermined mass of solid 2NapFF, 1 molar equivalent of sodium hydroxide with respect to 2NapFF and deionised water to make up the final volume.[51] Based on calculations to have a 1:1 molar ratio of 2NapFF to hydroxide, solutions of concentration 10 and 40 mg/mL required 0.1 M sodium hydroxide, whereas 2NapFF at a concentration of 100 mg/mL required 1 M sodium hydroxide. Water was always added to the solid 2NapFF first, followed by the addition of NaOH. All solutions were formed at room temperature (normally between 22 and 25 °C). Further preparation conditions were altered as described in the rest of Section 2.4.2 depending on the factors under investigation.

Preparation of Solutions to Examine Stirring Effects and Aging. 17 mL of solution of 2NapFF at a concentration of 40 mg/mL and 9 mL of 2NapFF solutions prepared at concentrations of 10 and 100 mg/mL were prepared using predetermined quantities as described in Section 2.4.2. Solutions were made in 50 mL Falcon tubes, stirred with the same (25 x 8 mm) stirrer bars, and wrapped in Parafilm. Three different stirring methods were used on each sample over a seven-day period to establish if sample preparation history could affect the samples. Solutions were either stirred continuously at 400 rpm for seven days; stirred at 1000 rpm for seven days; or stirred overnight at 400 rpm and then left to stand undisturbed for the remaining six days of the seven-day period. Viscosity measurements were performed every day for seven days, with day 1 representing the day following the creation of the samples. Any used sample was discarded after viscosity measurement. The pH was adjusted every day to 10.5 ± 0.1 using 0.1, 1 M and 2M NaOH; or 1 M and 2 M HCl as required for each solution. This did not affect the overall concentration of the solutions as no more than 3 µL of base was added each day.

Preparation of Solutions to Examine Container Size. For 2NapFF solutions prepared at a concentration of 40 mg/mL, solutions were also examined over a seven-day period but prepared in 7 mL Sterilin vials instead of 50 mL Falcon tubes to establish if the containers used to prepare samples could also affect stirring and therefore sample viscosity. Seven lots of 3 mL 2NapFF samples at a concentration of 40 mg/mL prepared using the predetermined quantities as described in Section 2.4.2. Solutions were made in 7 mL Sterilin

vials, stirred with the same (13 x 3 mm) stirrer bars, and wrapped in Parafilm. Samples were then stirred at 1000 rpm for seven days. Viscosity measurements were performed every day for seven days, with day 1 representing the day following the creation of the samples. Any used sample was discarded after viscosity measurement. The pH was adjusted daily to 10.5 $\pm$ 0.1 using 0.1 M, 1 M and 2M NaOH; or 1 M and 2 M HCl as required for each solution.

Preparation of Solutions for "Recovery" Experiments. For 2NapFF solutions prepared at a concentration of 40 mg/mL, additional stirring effects samples were created – denoted as "recovery experiments". 9 mL of 2NapFF solution at a concentration of 40 mg/mL were prepared using the predetermined quantities as described in Section 2.4.2. Solutions were made in 50 mL Falcon tubes, stirred with the same (25 x 8 mm) stirrer bars, and wrapped in Parafilm. Two different stirring methods were used on each sample over a seven-day period. This was to establish if any sample preparation history could affect the data collected. Samples were either stirred at 400 rpm or 1000 rpm for three days, and then both left to stand undisturbed for the remaining four days of the seven-day period. Viscosity measurements were performed every day for seven days, with day 1 representing the day following the creation of the samples. Any used sample was discarded after viscosity measurement. The pH was adjusted daily to 10.5 $\pm$ 0.1 using 0.1 M, 1 M and 2M NaOH; or 1 M and 2 M HCl as required for each solution.

Preparation of Solutions for Additional "Recovery" Experiments. A second "recovery experiment" using 2NapFF at a concentration of 40 mg/mL was performed with the aim to establish the effects of combined stirring and resting on viscosity. Four lots of 9 mL of 2NapFF solution at a concentration of 40 mg/mL were prepared using the predetermined quantities as described in Section 2.4.2. Solutions were made in 50 mL Falcon tubes, stirred with the same (25 x 8 mm) stirrer bars, and wrapped in Parafilm. Solutions were either stirred at 400 rpm for one day; stirred at 400 rpm for seven days; stirred at 1000 rpm for 1 day; or stirred at 1000 rpm for seven days. After these initial different stir periods, viscosity was measured. Solutions were then left undisturbed for a seven-day period. Viscosity measurements were then taken after this seven-day rest period. Any used sample was discarded after viscosity measurement. The pH was adjusted to pH 10.5 $\pm$ 0.1 using 0.1M, 1 M and 2M NaOH; or 1 M and 2 M HCl as required for each solution before each viscosity measurement was performed.

Preparation of Solutions to Examine pH Effects. 3 mL of 2NapFF solutions at concentrations of 10, 40 and 100 mg/mL were prepared using the predetermined quantities as described in Section 2.4.2. Solutions were made in Sterilin vials, wrapped in Parafilm, and left to stir for 3 days at 1000 rpm using 13x3 mm stirrer bars. After three days of stirring, the pH was adjusted to 9.0, 9.5, 10.0, 10.5, 11.0, 11.5 or 12.0 ± 0.1 using 0.1 M, 1 M and 2M NaOH; or 1 M and 2 M HCl as required.

Preparation of Solutions to Examine Effects of Adding NaCl. The volumes and concentrations of NaOH and NaCl solutions were calculated such that the molar ratio of NaOH:2NapFF was 0.8:1 and molar ratio of NaCl:2NapFF varied between 0.001-10:1. Solutions containing no added NaCl were also prepared. The adding of components was kept consistent with solid 2NapFF first being weighed into a 7 mL Sterilin vial, followed by water, NaCl solution (if applicable) and finally NaOH to give a total volume of 3 mL. Solutions were wrapped in Parafilm and stirred overnight at 1000 rpm using 13x3 mm stirrer bars. The pH was adjusted to 10.5 ± 0.1 using 0.1 M, 1 M and 2M NaOH as required. The pH of the solutions was adjusted using NaOH only to avoid altering the ratio of NaCl:2NapFF which would be altered in HCl was also used.

Preparation of Solutions for Viscosity Time Sweep. 3 x 4 mL of 2NapFF solution at a concentration of 40 mg/mL were prepared using the predetermined quantities as described in Section 2.4.2. Solutions were made in Sterilin vials, wrapped in Parafilm, and left to stir for 2 days at 400 rpm using 13x3 mm stirrer bars. The pH was adjusted to pH 10.5 ± 0.1 using 0.1 M, 1 M and 2M NaOH; or 1 M and 2 M HCl as required.

2.4.3 Instruments and Methodologies

Rheology - Viscosity. Viscosity measurements were carried out using an Anton Paar Physica MCR101 rheometer. Measurements were performed using a 50 mm cone geometry (CP50) with gap distance between the geometry and the plate set to 0.101 mm and temperature set to 25 °C. To minimise shearing which could be induced by pipetting, all samples were poured onto the rheometer plate. Fresh solution was used for all runs, unless otherwise stated. All viscosity measurements were performed in duplicate, and values averaged. Error bars represent the standard deviation between the replicates.

Rheology - Viscosity Time Sweep. In addition to regular viscosity measurements (as described previously in this Section) additional viscosity measurements were performed using a CP50 geometry and 0.101 mm gap at 25 °C. For these additional viscosity measurements, the shear rate was held constant for 10 minutes at 1, 5, 10, 50, 100, 500 and 1000 s^{-1} before moving to the next shear rate to look for instability within the sample.

Rheology - Pre-shear of Solutions using a Rheometer. In addition to regular viscosity measurements (as described previously in this Section) additional viscosity measurements were performed using a CP50 geometry and 0.101 mm gap at 25 °C. Two identical viscosity measurements were performed immediately one after the other on a single solution with the geometry remaining in the measuring position between the first and second viscosity measurements. Samples were left to sit under the CP50 geometry for about two minutes undisturbed between measurements.

pH Measurements. A calibrated FC2020 Hanna pH probe was used to measure the pH of all solutions. The accuracy of the measurements stated by the supplier is ± 0.1. The probe was calibrated with pH 4, 7 and 10 buffers with an additional buffer at pH 12.45 used when measuring the pH above pH 11. Measurements were carried out at room temperature (normally between 22 and 25 °C).

POM. POM images were collected using a Nikon Eclipse LV100 microscope at 5x magnification. Solutions were transferred to a microscope slide by a cut plastic Pasteur pipette for imaging. The plastic Pasteur pipette was cut to widen the pipette to try and reduce any shearing. Scale bars were added to images using the software ImageJ.

2.5 References

1. L. Chen, S. Revel, K. Morris, L. C. Serpell and D. J. Adams, *Langmuir*, 2010, **26**, 13466-13471.
2. D. J. Adams, M. F. Butler, W. J. Frith, M. Kirkland, L. Mullen and P. Sanderson, *Soft Matter*, 2009, **5**, 1856-1862.
3. L. Chen, G. Pont, K. Morris, G. Lotze, A. Squires, L. C. Serpell and D. J. Adams, *Chem. Comm.*, 2011, **47**, 12071-12073.
4. C. Rizzo, P. Cancemi, L. Mattiello, S. Marullo and F. D'Anna, *ACS Applied Materials & Interfaces*, 2020, **12**, 48442-48457.
5. Y. Lyu and H. S. Azevedo, *Molecules*, 2021, **26**, 873.

6. S. Panja and D. J. Adams, *Chem. Eur. J.*, 2021, **27**, 8928.
7. M. R. Ghadiri, J. R. Granja, R. A. Milligan, D. E. McRee and N. Khazanovich, *Nature*, 1993, **366**, 324-327.
8. M. Reches and E. Gazit, *Science*, 2003, **300**, 625-627.
9. M. Reches and E. Gazit, *Nano Letters*, 2004, **4**, 581-585.
10. R. V. Ulijn and A. M. Smith, *Chem. Soc. Rev.*, 2008, **37**, 664-675.
11. L. Chen, T. O. McDonald and D. J. Adams, *RSC Adv.*, 2013, **3**, 8714-8720.
12. A. Z. Cardoso, L. L. E. Mears, B. N. Cattoz, P. C. Griffiths, R. Schweins and D. J. Adams, *Soft Matter*, 2016, **12**, 3612-3621.
13. E. R. Draper, H. Su, C. Brasnett, R. J. Poole, S. Rogers, H. Cui, A. Seddon and D. J. Adams, *Angew. Chemie Int. Ed.*, 2017, **56**, 10467-10470.
14. K. McAulay, P. A. Ucha, H. Wang, A. M. Fuentes-Caparrós, L. Thomson, O. Maklad, N. Khunti, N. Cowieson, M. Wallace, H. Cui, R. J. Poole, A. Seddon and D. J. Adams, *Chem. Comm.*, 2020, **56**, 4094-4097.
15. K. McAulay, L. Thomson, L. Porcar, R. Schweins, N. Mahmoudi, D. J. Adams and E. R. Draper, *Organic Materials*, 2020, **2**, 108-115.
16. E. R. Draper, B. Dietrich, K. McAulay, C. Brasnett, H. Abdizadeh, I. Patmanidis, S. J. Marrink, H. Su, H. Cui, R. Schweins, A. Seddon and D. J. Adams, *Matter*, 2020, **2**, 764-778.
17. C. Tanford, *J. Phys. Chem.*, 1974, **78**, 2469-2479.
18. C. A. Dreiss, *Soft Matter*, 2007, **3**, 956-970.
19. J. Yang, *COCIS*, 2002, **7**, 276-281.
20. S. A. Rogers, M. A. Calabrese and N. J. Wagner, *COCIS*, 2014, **19**, 530-535.
21. X. Wu, Y. Wu, S. Yang, M. Zhao, M. Gao, H. Li and C. Dai, *Soft Matter*, 2016, **12**, 4549-4556.
22. S. R. Raghavan and Y. Feng, in *Wormlike Micelles: Advances in Systems, Characterisation and Applications*, The Royal Society of Chemistry, 2017, pp. 9-30.
23. M. Z. Jora, E. Sabadini and S. R. Raghavan, *Langmuir*, 2020, **36**, 13408-13414.
24. S. R. Raghavan and J. F. Douglas, *Soft Matter*, 2012, **8**, 8539-8546.
25. O. Nahi, O. J. Cayre, Y.-Y. Kim, A. J. Smith, N. J. Warren and F. C. Meldrum, *Chem. Comm.*, 2020, **56**, 7463-7466.
26. K. Sakai, K. Nomura, R. G. Shrestha, T. Endo, K. Sakamoto, H. Sakai and M. Abe, *Langmuir*, 2012, **28**, 17617-17622.
27. T. Shikata, H. Hirata and T. Kotaka, *Langmuir*, 1988, **4**, 354-359.
28. J. Narayanan, C. Manohar, F. Kern, F. Lequeux and S. J. Candau, *Langmuir*, 1997, **13**, 5235-5243.
29. P. A. Hassan, S. J. Candau, F. Kern and C. Manohar, *Langmuir*, 1998, **14**, 6025-6029.
30. N. R. Agrawal, X. Yue, Y. Feng and S. R. Raghavan, *Langmuir*, 2019, **35**, 12782-12791.
31. R. Kumar and S. R. Raghavan, *Soft Matter*, 2009, **5**, 797-803.
32. H. Shi, Y. Wang, B. Fang, Y. Talmon, W. Ge, S. R. Raghavan and J. L. Zakin, *Langmuir*, 2011, **27**, 5806-5813.
33. J. A. Hutchinson, S. Burholt, I. W. Hamley, A.-K. Lundback, S. Uddin, A. Gomes dos Santos, M. Reza, J. Seitsonen and J. Ruokolainen, *Bioconjugate Chem.*, 2018, **29**, 2296-2308.
34. J. N. B. D. Pelin, B. B. Gerbelli, C. J. C. Edwards-Gayle, A. M. Aguilar, V. Castelletto, I. W. Hamley and W. A. Alves, *Langmuir*, 2020, **36**, 2767-2774.

35. J. N. B. D. Pelin, C. J. C. Edwards-Gayle, V. Castelletto, A. M. Aguilar, W. A. Alves, J. Seitsonen, J. Ruokolainen and I. W. Hamley, *ACS Applied Materials & Interfaces*, 2020, **12**, 13671-13679.

36. I. W. Hamley and V. Castelletto, in *Peptide-based Biomaterials*, The Royal Society of Chemistry, 2021, pp. 19-46.

37. H. Cui, M. J. Webber and S. I. Stupp, *Peptide Science*, 2010, **94**, 1-18.

38. T. Shimada, N. Sakamoto, R. Motokawa, S. Koizumi and M. Tirrell, *J. Phys. Chem. B.*, 2012, **116**, 240-243.

39. M. Holmes and J. Charvolin, *J. Phys. Chem.*, 1984, **88**, 810-818.

40. G. J. T. Tiddy, *Phys. Rep.*, 1980, **57**, 1-46.

41. J. Fan, F. Liu and Z. Wang, *Int. J. Pharm.*, 2016, **497**, 248-254.

42. J. M. Dealy and T. K. P. Vu, *J. Non-Newton Fluid*, 1977, **3**, 127-140.

43. R. A. Stratton and A. F. Butcher, *J. Polym. Sci. Pol. Phys.*, 1973, **11**, 1747-1758.

44. J.-F. Berret, in *Molecular Gels: Materials with Self-Assembled Fibrillar Networks*, eds. R. G. Weiss and P. Terech, Springer Netherlands, Dordrecht, 1st edn., 2006, pp. 667-720.

45. M. Cariello, B. Dietrich, L. Thomson, V. Gauci, A. Boyer, S. Sproules, G. Cooke, A. Seddon and D. J. Adams, *Chemistry – A European Journal*, 2022, **28**, e202201725.

46. C. Allain, M. Cloitre and M. Wafra, *Physical Review Letters*, 1995, **74**, 1478-1481.

47. R. Negrini and R. Mezzenga, *Langmuir*, 2011, **27**, 5296-5303.

48. L. Thomson, R. Schweins, E. R. Draper and D. J. Adams, *Macromol. Rapid Commun.*, 2020, **41**, 2000093.

49. Z. Xu and C. Gao, *ACS Nano*, 2011, **5**, 2908-2915.

50. K. McAulay, B. Dietrich, H. Su, M. T. Scott, S. Rogers, Y. K. Al-Hilaly, H. Cui, L. C. Serpell, Annela M. Seddon, E. R. Draper and D. J. Adams, *Chem. Sci.*, 2019, **10**, 7801-7806.

51. C. Colquhoun, E. R. Draper, R. Schweins, M. Marcello, D. Vadukul, L. C. Serpell and D. J. Adams, *Soft Matter*, 2017, **13**, 1914-1919.

Chapter 3. Transferring Molecular Level Changes to Bulk Properties of Low Molecular Weight Gelators

This Chapter is adapted from the following publication:

"Transferring molecular level changes to bulk properties via tunable self-assembly and hierarchical ordering"

L. Thomson, D. McDowall, L.J. Marshall, O. Marshall, H. Ng, W.J.A. Homer, E. Theodosiou, P.D. Topham, L.C. Serpell, R.J. Poole, A. Seddon, D.J. Adams, submitted.

LT was responsible for the synthesis of the gelator molecule used. AS was responsible for the collection and analysis of all small-angle X-ray scattering data. LT was responsible for all other methodology, collection of data and analysis, with contributions from DM and OM highlighted when discussed in the text of this Chapter. HN contributed the software used for data analysis. AS and DJA conceptualised and supervised the project. LT, AS and DJA wrote the initial draft of the manuscript, to which all authors contributed for the final publication. All other authors listed above contributed to the paper this Chapter is adapted from, but their work is not shown in this Chapter.

3.1. Introduction

Functionalised dipeptides are interesting molecules that can be used to form useful and exciting materials.[1-3] Many LMWGs are functionalised peptides,[4-6], capable of forming hydrogels via self-assembly.[7] These hydrogels are formed from precursor solutions of LMWGs made by first suspending the LMWG in water at high pH.[6, 8] We discuss the structures, such as worm-like micelles, found in these precursor solutions in Chapter 2. Additionally in Chapter 2, we focus on the worm-like micelles formed by the LMWG 2NapFF in detail, alongside the factors such as shear dependence and addition of salt during the solution preparation stage in order produce a robust protocol to make these "living" micellar solutions as reproducible as possible.

For amphiphilic molecules such as 2NapFF at high pH, the carboxylate form of the LMWG exists and our group has shown that worm-like micelles form at concentrations of 5-10 mg/mL 2NapFF.[9] We commonly examine LMWG solutions and gels around these low concentrations values, since gels are easily formed at these concentrations.[9-11] Increasing the concentration of amphiphilic molecules in water to a sufficiently high concentration, however, can result in interactions between the anisotropic structures, leading to the structures packing together into a more ordered mesophase.[12-14]

Liquid crystals represent the intermediate state between the conventional states of liquid and solid.[15-17] Applications of liquid crystals include displays (for example, computers or watches),[14, 16] thermometers,[16] and drug delivery systems.[18, 19] Different phases of liquid crystals exist depending on the arrangements of the anisotropic molecules and can be accessed by varying temperature (thermotropic liquid crystals) or concentration (lyotropic liquid crystals).[16, 17, 20] In liquid crystal systems, the solvent is responsible for the liquid crystal fluidity and the amphiphilic molecules provide the structure and elastic properties.[18, 20] Most of the mathematics and theory behind liquid crystals stands true for both thermotropic and lyotropic liquid crystals.[16]

To form lyotropic liquid crystals, the concentration of the amphiphile in water is increased. Above a certain amphiphile concentration, the micelles repel each other and the free energy required to force the micelles together is more than the free energy required to

form a different phase.[14] Factors which influence the formation of lyotropic liquid crystals include the contact between the hydrophobic section of the amphiphile and water, the size of the repulsion forces between head groups, steric effects, and charge present on other nearby molecules.[14]

Examples of liquid phases include nematic, lamellar, cubic and hexagonal.[12, 14, 18, 20] A selection of examples of liquid crystal phases are shown in Figure 3.1. Solids have both positional and orientational order; liquids have neither positional nor orientational order.[17] If molecules have orientational order, but no positional order they are said to be in the nematic phase.[16, 17] Orientational order means the molecules have a preferred direction ($\vec{n}$, the liquid crystal director).[16, 17] The smectic liquid crystal phases also exhibit orientational order, but now we additionally have partial positional order.[17] Smectic structures are layered and parallel to each other but not spaced regularly within the layers. It is this irregular spacing of molecules which allows the material to still flow.[15] Different smectic phases exist and use Friedel indices (e.g. A, B, C) to differentiate between them.[21] For example, smectic A (SmA) is layered with all molecules essentially pointing in the same direction, perpendicular to the formed layers. However, in the smectic C (SmC) phase, although layered similarly to SmA, $\vec{n}$ is no longer perpendicular to the layers as the molecules become tilted.[16, 17, 21, 22] Due to their orientational order, liquid crystals respond to external stimuli such as magnetic and electric fields, and shear.[17]
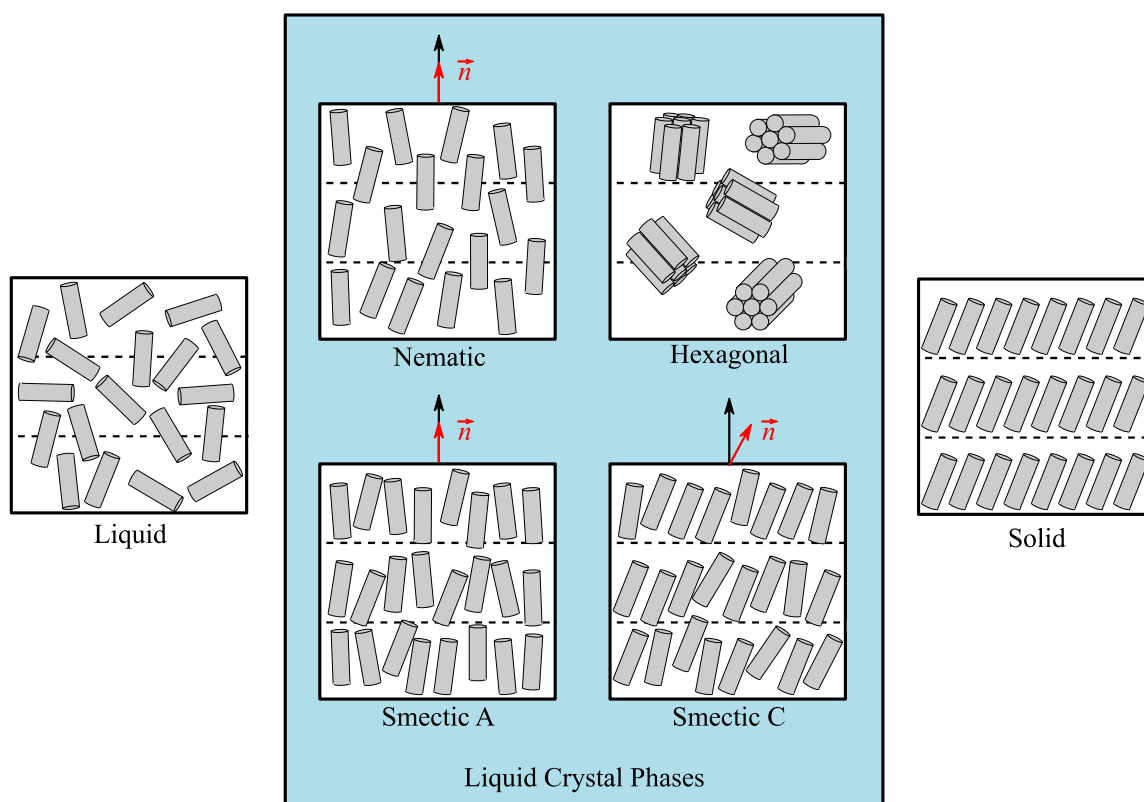
Figure 3.1. Exemplar liquid crystal phases, with liquid and solid phases shown for comparison. $\vec{n}$ represents the liquid crystal director and is shown in red.

Using polarised optical microscopy (POM), it is possible to observe different textures which can be used to identify the different liquid crystal phases, with defects (which occur naturally in liquid crystals) responsible for these identifying textures.[15, 16, 23] The types of textures observed can vary based on thermal and phase history of a sample.[23] In nematic liquid crystal phases, there are two types of defects responsible for creating different patterns under cross-polarised light; these are point and line defects.[16] For a nematic liquid crystal phase placed between two microscope slides, the molecules can orientate parallel (homogenous) or perpendicular (homeotropic) to the slides.[23] If aligned homogeneously a schlieren defect texture can be observed; this is indicative of nematic liquid crystals. However, if homeotropic alignment occurs, dark sections will appear because of the sudden, but continuous, change in molecule orientation. Other distinct textures are also known to identify other liquid crystal phases.[16, 23, 24] Different colours can be observed due to sample thickness and birefringence.[16, 25]

To design useful materials from solutions containing micellar aggregates or liquid crystal phases, we need to understand and control the structures present. This must be considered across various length scales; taking into account the individual structures, the packing of these structures and how this affects the bulk properties of the solutions. As discussed in Chapter 1, rationally designing LMWGs with properties for a specific application is a challenge, and commonly new LMWGs are designed in order to achieve desired properties.

With this approach in mind, in this Chapter we demonstrate that a single LMWG (acting here as a surfactant) can be used to create a hierarchy of self-assembled structures that can be understood using the theories applied to liquid crystals. This allows us to prepare materials with hierarchical order, controlled across multiple length scales. We show that the molecular packing of a single building block can be tuned by carefully altering selected parameters, which results in materials with different bulk properties, reducing the need to design a new LMWG from scratch.

3.2.   Results and Discussion

This Chapter follows on from Chapter 2 where we describe a robust preparation method for solutions of the dipeptide-based LMWG, 2NapFF, at concentrations up to and including 100 mg/mL. Our group has previously reported that at low concentrations, changes in structure from free molecules to spherical aggregates to worm-like micelles occur as LMWG concentration is increased.[9] Our group has also shown that for this LMWG, again at low concentrations, different self-assembled structures form in solution when different counterions are used to de-protonate the LMWG to form the solutions.[26] In this Chapter, we examine the structures formed by 2NapFF with two different counterions (NaOH and TBAOH, denoted as 2NapFF-Na and 2NapFF-TBA respectively) at various LMWG concentrations to examine changes in structure, and the resulting properties of these self-assembled solutions.

Initially, there are obvious differences between dispersions of 2NapFF prepared at high pH with NaOH and TBAOH. First, it is possible to form solutions of concentrations up to 100 mg/mL of 2NapFF with NaOH. This is not true of 2NapFF-TBA which does not form

homogeneous solutions after overnight stirring at 100 mg/mL. Therefore, a concentration series discussed in this Chapter for 2NapFF-Na ranges from 5-100 mg/mL, but for 2NapFF-TBA only ranges from 5-75 mg/mL. Another very obvious difference between the solutions made with the different counterions is the viscosity. Visibly, 2NapFF-TBA produces solutions which are visibly much more viscous than 2NapFF-Na, Figure 3.2. At a concentration of 10 mg/mL 2NapFF (Figure 3.2a), 2NapFF-TBA is stable enough to self-support for approximately 1 minute. This is not true of 2NapFF-Na at the same LMWG concentration which is unstable to inversion. This is similar for 2NapFF-Na at a concentration of 75 mg/mL which cannot self-support, but 2NapFF-TBA at the same concentration is stable to inversion (Figure 3.2b). The rheology of these samples (to confirm the presence of gels or viscous liquids) is discussed later in this Chapter.
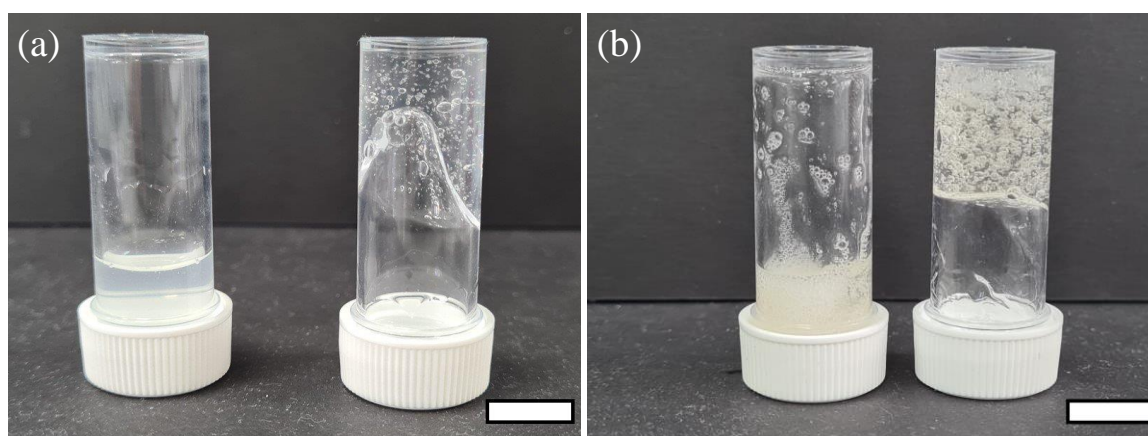
Figure 3.2. Photographs of 2NapFF-Na (left) and 2NapFF-TBA (right) at LMWG concentrations of (a) 10 mg/mL and (b) 75 mg/mL. Scale bars represent 1 cm.

To quantify the differences in viscosity and to give an indication as to where potential structural or packing changes occur, we use rheological measurements. Previously in polymer systems, plotting viscosity versus concentration showed where changes in structure occur by studying the positions of maxima and minima.[27, 28] A new phase occurs when the structures repel each other and the energy required to force the micelles together is more than the energy required to form a different phase.[14] We show our viscosity vs concentration plots for 2NapFF-TBA and 2NapFF-Na, alongside full viscosity data, in Figure 3.3. Examining 2NapFF-TBA, Figure 3.3a, we see that as the concentration of 2NapFF is increased, the viscosity also increases, with no maxima in the data. This contrasts with 2NapFF-Na (Figure 3.3b) where maxima and minima appear in the viscosity data when

plotted against concentration. Minima in the viscosity vs concentration data occur at 15 mg/mL, 50 mg/mL and 75 mg/mL 2NapFF-Na, suggesting that these concentrations could be the concentrations at which a new phase exists. Overall, we show 2NapFF-TBA is more viscous than 2NapFF-Na with 10 mg/mL 2NapFF-TBA showing a similar viscosity at 1 s^{-1} to 2NapFF-Na at 100 mg/mL.
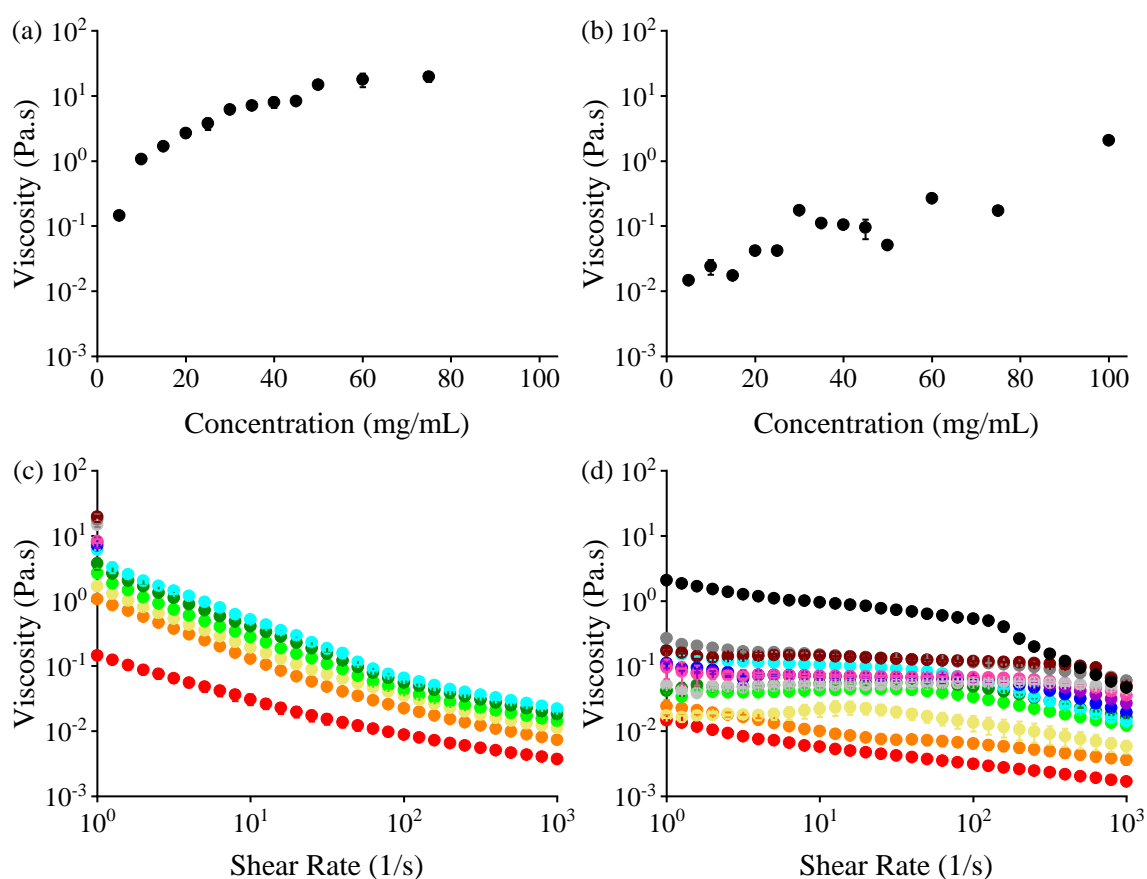

Figure 3.3. Viscosity data for 2NapFF-Na and 2NapFF-TBA. Summary of (a) 2NapFF-TBA and (b) 2NapFF-Na viscosity with increasing concentration taken at 1 s^{-1}. Full viscosity data for (c) 2NapFF-TBA and (d) 2NapFF-Na at concentrations of 5 (red); 10 (orange); 15 (yellow); 20 (light green); 25 (dark green); 30 (light blue); 35 (dark blue); 40 (purple); 45 (pink); 50 (light grey); 60 (dark grey); 75 (brown); 100 (black) mg/mL of 2NapFF.

Examining the viscosity data in full (Figure 3.3c and Figure 3.3d), we see different behaviours depending on which counterion is used. For 2NapFF-TBA, Figure 3.3c, all the data are shear thinning at each concentration of 2NapFF. We have shown this before and suggest it is due to the presence of worm-like micelles.[26] We only plot in full 2NapFF-TBA

concentrations up to and including 30 mg/mL. At higher 2NapFF-TBA concentrations, it was possible to see the sample get pulled from under the rheometer geometry and continue to rotate with solution being pulled onto the top of the geometry. This makes the data invalid and so only the first data point is considered since we know for sure no solution is on the top of the geometry at this point. One possible reason for this observation could be due to the Weissenberg effect.[29] Solutions of worm-like micelles can align when exposed to shear. A restoring force occurs which is greater than the force used to induce flow. Therefore, there is a build-up of perpendicular forces and the fluid appears to climb. This resulting perpendicular force could explain why the fluid was sucked from under the rheometer geometry, if we consider the geometry as a rotating rod. The full viscosity of 2NapFF-Na, Figure 3.3d, however, shows more complex behaviour than just the shear thinning we see with 2NapFF-TBA. For example, 2NapFF-Na at a concentration of 15 mg/mL (Figure 3.3d, yellow data), we see initially that the viscosity is shear independent, followed by shear thickening and then shear thinning. Although this behaviour has not been reported before in our group with our dipeptide-based systems, previous research reported using polymer systems have shown similar plots with a combination of shear thickening and shear thinning present in a single sample.[30-32]

Using POM images, it is possible to observe different textures which can be used to help identify different phases, including micellar and liquid crystal phases.[15, 16, 23] Micellar and cubic liquid crystal phases show no textures under cross-polarised light,[24] whereas other liquid crystal phases show birefringence under polarised light,[33-36] with alignment defects (which occur naturally in liquid crystals) responsible for the identifying textures.[23] POM images for both 2NapFF-Na and 2NapFF-TBA at all LMWG concentrations are shown in Figure 3.4. All concentrations of 2NapFF with both counterions, with the exception of 2NapFF-TBA at 5 mg/mL, exhibit interaction with the cross-polarised light which suggest anisotropic structures are present. Since 5 mg/mL 2NapFF-TBA appears dark under polarised light it suggests no direction preference.[15] Some bubbles (dark circles) can be seen in some of the 2NapFF-TBA samples at higher concentration. These bubbles occur due to the stirring of the viscous samples, but do not affect the POM images overall.
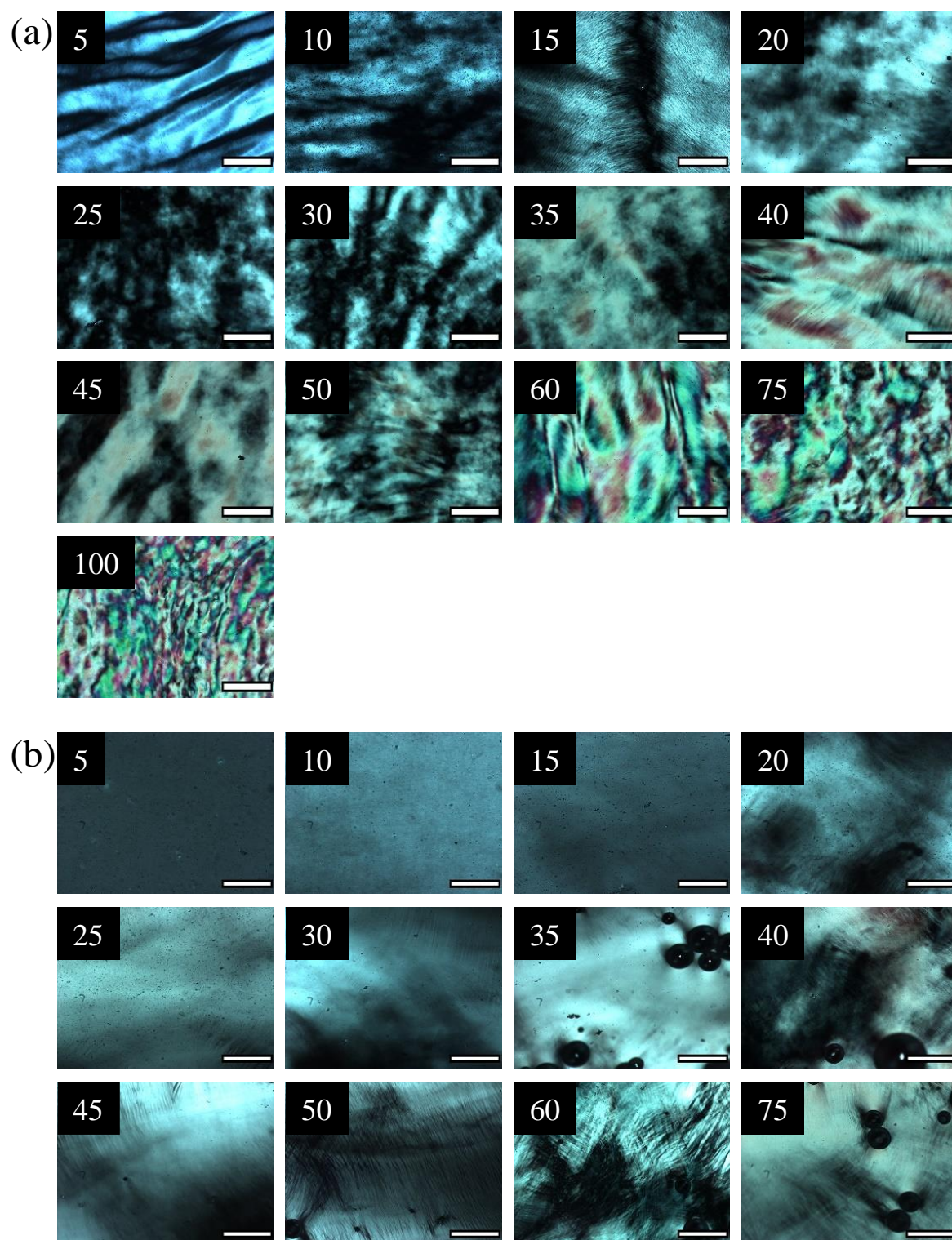
Figure 3.4. POM images for (a) 2NapFF-Na and (b) 2NapFF-TBA (concentration is shown as an inset in top left of each image). Scale bars represent 500 µm.

To confirm what structures and packing are present at each concentration of 2NapFF, and for each counterion series, we turn to small-angle X-ray scattering (SAXS). All SAXS samples were prepared by Lisa Thomson (University of Glasgow) and all SAXS data were collected, processed and analysed by Annela Seddon (University of Bristol). From the 2D SAXS data, it is possible to see alignment in the 2NapFF-Na series where the alignment is parallel to the long axis of the capillary in which they are measured (Figure 3.5). This occurs at 2NapFF-Na concentrations of 15 mg/mL and greater. The 2D SAXS patterns for 2NapFF-TBA, however, show very little ordering (Figure 3.6).
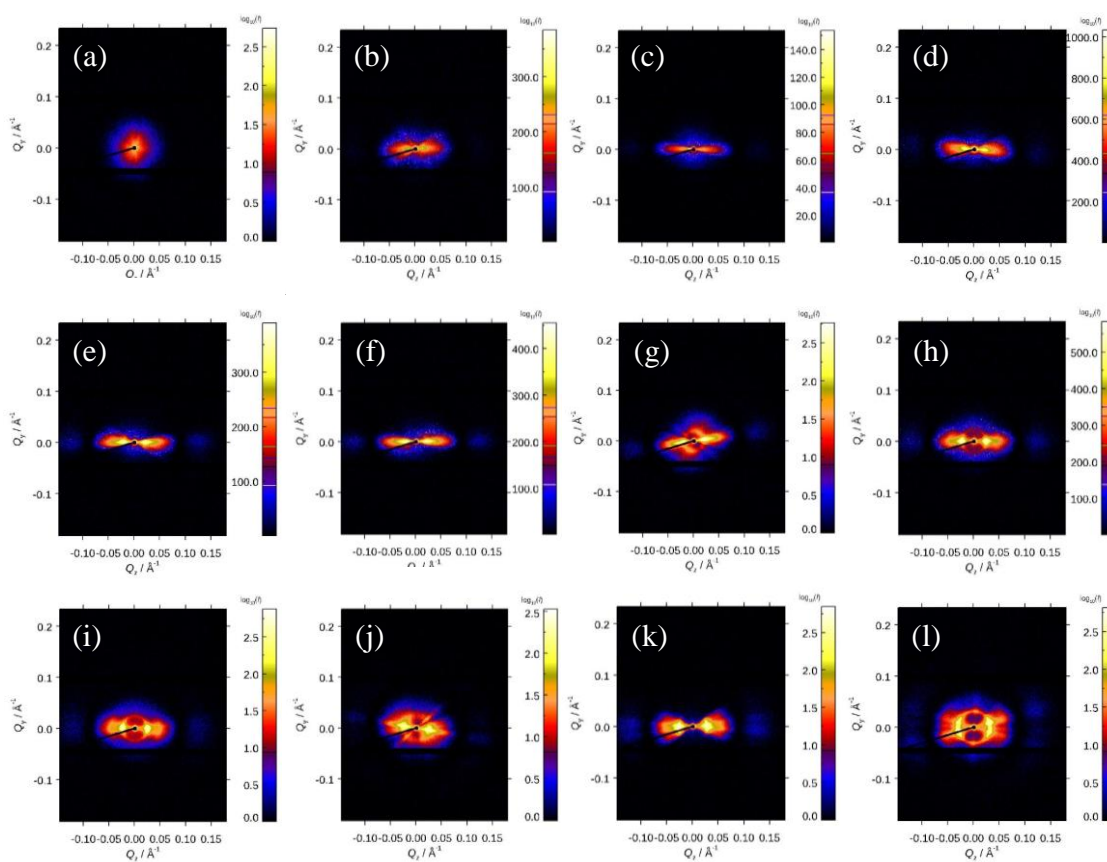
Figure 3.5. 2D SAXS patterns for 2NapFF-Na at concentrations of (a) 10 mg/mL; (b) 15 mg/mL; (c) 20 mg/mL; (d) 25 mg/mL; (e) 30 mg/mL; (f) 35 mg/mL; (g) 40 mg/mL; (h) 45 mg/mL; (i) 50 mg/mL; (j) 60 mg/mL; (k) 75 mg/mL; (l) 100 mg/mL.
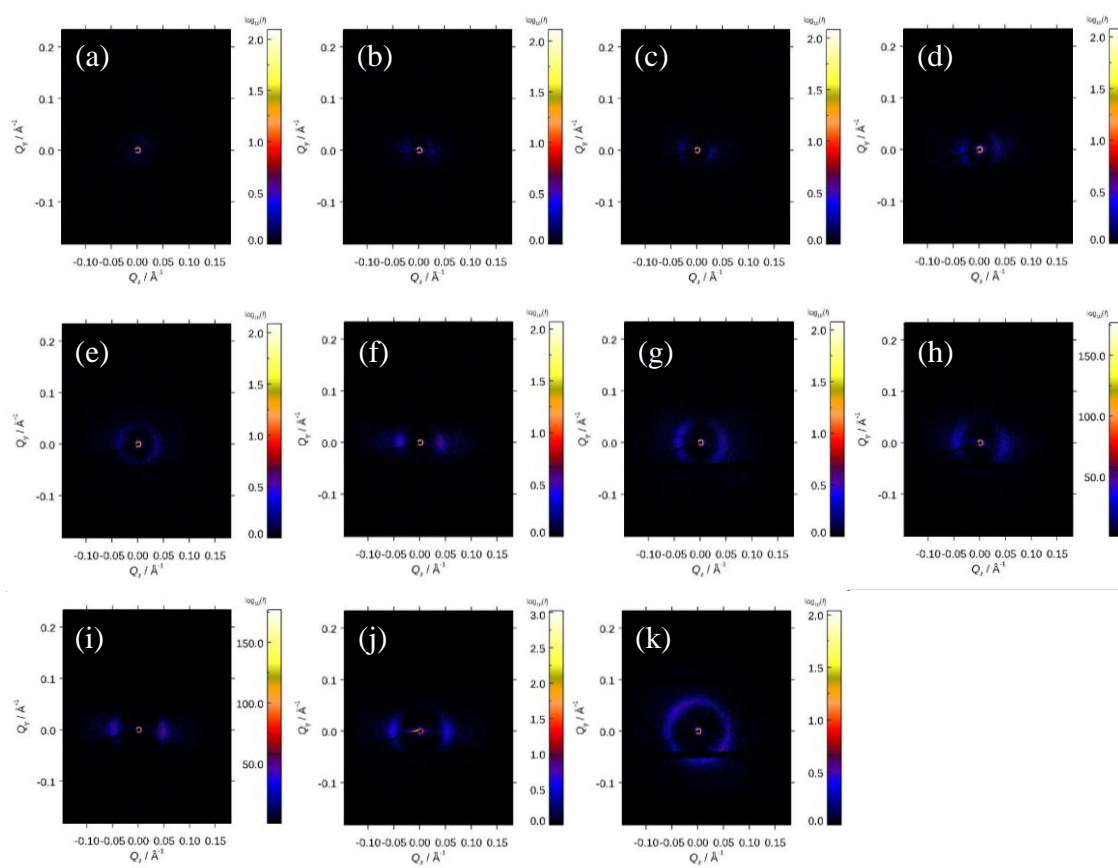
Figure 3.6. 2D SAXS patterns for 2NapFF-TBA at concentrations of (a) 10 mg/mL; (b) 15 mg/mL; (c) 20 mg/mL; (d) 25 mg/mL; (e) 30 mg/mL; (f) 35 mg/mL; (g) 40 mg/mL; (h) 45 mg/mL; (i) 50 mg/mL; (j) 60 mg/mL; (k) 75 mg/mL.

The 1D SAXS data for the 2NapFF-Na series can be fitted to a flexible cylinder model with a radius of approximately 4.2 nm, which is similar across all 2NapFF-Na concentrations (Table 3.1). The exceptions to this are at 2NapFF-Na concentrations of 60 mg/mL and greater. Here, the flexibility is lost with the preferred model for fitting now being a rigid cylinder model. This change corresponds with a change in POM images where more colours are observed. The structures are actually hollow tubes which can be demonstrated by small angle neutron scattering;[37] however, using SAXS, the contrast from the hollow core cannot be detected and so fitting to a flexible cylinder or rigid cylinder is most appropriate. The length of the cylinders is outside that of the Q range of this technique (greater than 100 nm) and so cannot be fitted. The scale parameter obtained during fitting indicates the volume fraction of scattering material in the sample.[38] For 2NapFF-Na, we show that this value increases with increasing 2NapFF-Na concentration, suggesting there are a greater number of cylinders formed as the concentration of 2NapFF-Na is increased.

Table 3.1. SAXS best fit parameters for 2NapFF-Na.

Concentration	100 mg/mL	75 mg/mL	60 mg/mL	50 mg/mL	45 mg/mL	40 mg/mL
Model	Cylinder	Cylinder	Cylinder	Flexible cylinder	Flexible cylinder	Flexible cylinder
Background (cm^{-1})	0.0008 ± 0.0001	0.0034 ± 0.0002	0.015 ± 0.0002	0.0063 ± 0.0002	0.0097 ± 0.0002	0.0118 ± 0.0002
Scale	$0.006 \pm 2.6 \times 10^{-5}$	$0.005 \pm 5.8 \times 10^{-5}$	$0.005 \pm 3.0 \times 10^{-5}$	$0.004 \pm 7.2 \times 10^{-5}$	$0.004 \pm 7.5 \times 10^{-5}$	$0.004 \pm 6.4 \times 10^{-5}$
Length (Å)	>1000	>1000	>1000	>1000	>1000	>1000
Kuhn Length (Å)	NA	NA	53 ± 2	66 ± 4	70 ± 5	130 ± 16
Radius (Å)	42.7 ± 0.04	42.7 ± 0.04	42.7 ± 0.05	43.1 ± 0.05	43.1 ± 0.06	42.8 ± 0.07
χ^2	13.65	8.17	5.91	11.79	10.81	6.18
Concentration	35 mg/mL	30 mg/mL	25 mg/mL	20 mg/mL	15 mg/mL	10 mg/mL
Model	Flexible cylinder	Flexible cylinder	Flexible cylinder	Flexible cylinder	Flexible cylinder	Flexible cylinder
Background (cm^{-1})	0.0103 ± 0.0002	0.0036 ± 0.0001	0.0040 ± 0.0001	0.0026 ± 0.0001	0.0024 ± 0.0001	0.0084 ± 0.0001
Scale	$0.003 \pm 5.1 \times 10^{-5}$	$0.003 \pm 4.5 \times 10^{-5}$	$0.002 \pm 1.52 \times 10^{-5}$	$0.001 \pm 3.2 \times 10^{-6}$	$0.001 \pm 4.5 \times 10^{-6}$	$0.001 \pm 3.2 \times 10^{-6}$
Length (Å)	>1000	>1000	>1000	144 ± 23	250 ± 3	>1000
Kuhn Length (Å)	97.7 ± 11.8	53.9 ± 0.6	209.3 ± 155.5	382.9 ± 18.6	196 ± 5.6572	760.5 ± 121.1
Radius (Å)	42.7 ± 0.07	42.2 ± 0.07	41.0 ± 0.09	41.8 ± 0.09	41.2 ± 0.1	43.5 ± 0.1
χ^2	6.92	4.15	16.76	12.85	5.45	2.15

Collecting a similar SAXS data series for 2NapFF-TBA, the data can again be fitted to a flexible cylinder model with a radius of approximately 1.5 nm (Table 3.2). Similar to 2NapFF-Na, this value remains similar for all concentrations of 2NapFF-TBA. It is not possible to fit the Kuhn length at 2NapFF-TBA at concentrations above 30 mg/mL, indicating that the samples are now behaving as rigid cylinders. This change at 30 mg/mL is consistent with changes in our viscosity data at the same concentration, at which we saw solutions being pulled from under the rheometer geometry during rotation at this concentration and above. For 2NapFF-TBA, and unlike 2NapFF-Na, the scaling parameter does not increase drastically with increasing 2NapFF concentration. This shows that the addition of more 2NapFF molecules to the system does not simply result in more cylinders in solution, but rather adds length to the existing cylinders. This increase in length can encourage the formation of branched micelles. Branched micelles form when the energy required to form a micellar end cap is greater than the energy for branch formation and so instead of breaking into other shorter micelles, micelles tend to fuse and form junctions.[39] Scattering alone cannot confirm this and requires the complementary technique of cryogenic-transmission electron microscopy (cryo-TEM).[40] Cryo-TEM, however, is limited to dilute solutions and is difficult to use to examine high viscosity solutions.[41]

Table 3.2. SAXS best fit parameters for 2NapFF-TBA.

Concentration	75 mg/mL	60 mg/mL	50 mg/mL	45 mg/mL	40 mg/mL	35 mg/mL
Model	Cylinder	Flexible Cylinder	Cylinder	Cylinder	Cylinder	Flexible Cylinder
Background (cm^{-1})	0.02 ± 0.0002	0.001 ± 7.3 x 10^{-5}	0.01± 0.0002	0.01 ± 0.0003	0.002 ± 8.8x10^{-5}	0.002 ± 5.5x10^{-5}
Scale	0.02 ± 0.0008	0.06 ± 0.0003	0.007 (fixed)	0.01 ± 0.0009	0.01 ± 0.0005	0.002 ± 0.0002
Length (Å)	>1000	>1000	>1000	>1000	>1000	>1000
Kuhn Length (Å)	NA	4 ± 0.1	NA	NA	NA	>1000
Radius (Å)	15.3 ± 0.2	16.7 ± 0.2	16.0 ± 0.2	13.6 ± 0.3	16.6 ± 0.3	14.6 ± 0.3
χ^2	2.50	1.85	34.6	2.73	1.84	2.17
Concentration	30 mg/mL	25 mg/mL	20 mg/mL	15 mg/mL	10 mg/mL	
Model	Flexible Cylinder	Flexible Cylinder	Flexible Cylinder	Flexible Cylinder	Flexible Cylinder	
Background (cm^{-1})	0.002 ± 0.0002	0.002 ± 7.0x10^{-5}	0.002 ± 4.4x10^{-5}	0.001 ± 2.5x10^{-5}	0.0009 ± 2.8x10^{-5}	
Scale	0.01 ± 0.0004	0.01 ± 0.0003	0.009 ± 0.0004	0.005 ± 0.0003	0.005 ± 0.0003	
Length (Å)	>1000	>1000	>1000	316 ± 123	197 ± 11	
Kuhn Length (Å)	38 ± 7	54 ± 2	70 ± 4	110 ± 13	112 ± 11	
Radius (Å)	13.8 ± 0.4	15.9 ± 0.3	14.3 ± 0.3	15.3 ± 0.3	14.1 ± 0.4	
χ^2	2.79	2.37	2.40	2.41	2.33	

A peak in the 1D SAXS patterns of 2NapFF-Na appears at concentrations of 20 mg/mL and greater (Figure 3.7). This is the structure factor peak (Q*) and represents interactions between particles in a densely packed system.[38, 42] This suggests an isotropic to nematic transition at 20 mg/mL 2NapFF-Na occurs due to the appearance of Q* and the alignment seen in the 2D SAXS patterns. Classic liquid crystal behaviour of small molecules requires that the molecules (or particles) be anisotropic to form a liquid crystal phase and these molecules are often rigid.[16] We treat each of our 2NapFF cylinders as a cylindrical particle, so that anisotropy is present. Until a concentration of greater than 60 mg/mL 2NapFF-Na our cylinders are flexible but still form a nematic phase. Whilst the onset of the Q* peak can be linked to the ordering of the cylinders in 2NapFF-Na, the situation is different for 2NapFF-TBA. For 2NapFF-TBA, Q* peaks start to appear at a slightly lower concentration of 15 mg/mL (Figure 3.8) but appears in sample concentrations where no alignment is observed in the 2D scattering patterns. This shows that the cylinders in 2NapFF-TBA are interacting at lower concentration but are unable to align in the manner seen for the 2NapFF-Na analogue. This data confirms observations seen in our POM images. The patterns observed with 2NapFF-Na suggested alignment and the present of the nematic liquid crystal phase. However, the lack of distinct pattern in the images of 2NapFF-TBA is missing which indicated no alignment or liquid crystal phases.
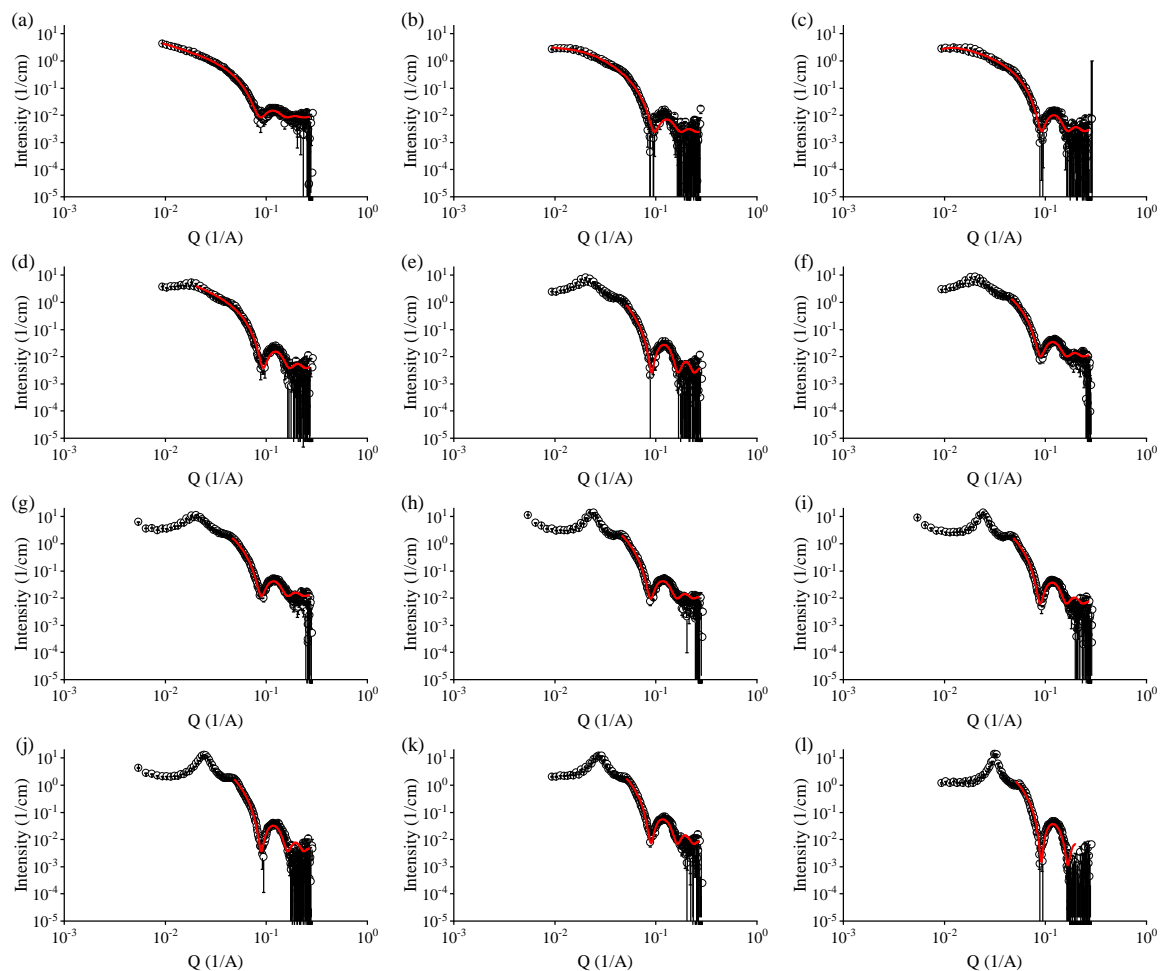
Figure 3.7. 1D SAXS data for 2NapFF-Na at concentrations of (a) 10 mg/mL; (b) 15 mg/mL; (c) 20 mg/mL; (d) 25 mg/mL; (e) 30 mg/mL; (f) 35 mg/mL; (g) 40 mg/mL; (h) 45 mg/mL; (i) 50 mg/mL; (j) 60 mg/mL; (k) 75 mg/mL; (l) 100 mg/mL. Data are shown in black with fits shown in red.
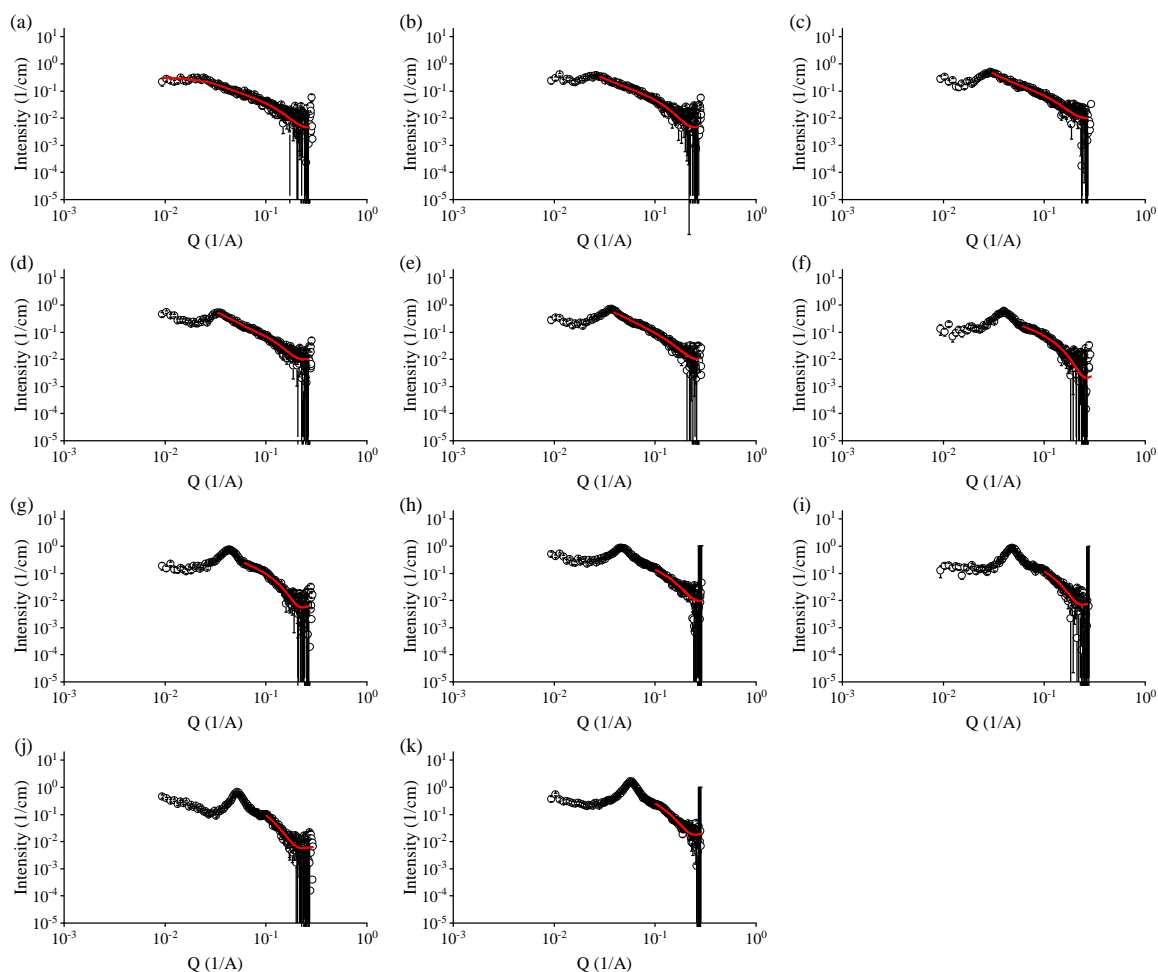
Figure 3.8. 1D SAXS data for 2NapFF-TBA at concentrations of (a) 10 mg/mL; (b) 15 mg/mL; (c) 20 mg/mL; (d) 25 mg/mL; (e) 30 mg/mL; (f) 35 mg/mL; (g) 40 mg/mL; (h) 45 mg/mL; (i) 50 mg/mL; (j) 60 mg/mL; (k) 75 mg/mL. Data are shown in black with fits shown in red.

Knowing now about the variations in structures and packing present in our solutions with different counterions, we examine how the properties of the solutions containing the different structures respond to various stimuli. First, we look at how our solutions respond to a heat-cool cycle. It is well reported that micelles can be affected by temperature.[43, 44] This is also true of liquid crystals with changes in temperature able to unlock liquid crystal phases.[16] Our group has shown before that 2NapFF-Na at a concentration of 10 mg/mL undergoes structural changes when subjected to a heat-cool cycle.[44] We find here that this is also true at higher concentrations of 2NapFF. In this work, a heat-cool cycle involves heating samples in an oven set to 60 °C for one hour and then leaving to cool undisturbed at room

temperature for two hours. This allows the sample ample time to return to room temperature again after heating.

Initially, we study the effects of heat-cool on our structures using SAXS. A summary of the fitting parameters obtained from the fitting of the 1D SAXS data before and after heating for both counterions at 2NapFF concentrations of 10 mg/mL and 75 mg/mL are shown in Table 3.3. In all cases, the radii of the cylinders decrease after heat-cool, and the Kuhn length is also reduced. This is extremely noticeable in the highest concentration samples, which now fit to a flexible cylinder model instead of a rigid cylinder model, showing that the rigidity has been lost after heat-cool cycle. The samples post heating also show a reduced intensity and shifted Q^* (Figure 3.9), reflecting their reduced radii. The orientation in the 2D SAXS patterns is also lost and the samples are now isotropic (Figure 3.9).

Table 3.3. SAXS best fit parameters for 2NapFF-Na and 2NapFF-TBA before and after heat-cool (HC).

2NapFF-Na	10 mg/mL, Before HC	10 mg/mL, After HC	75 mg/mL, Before HC	75 mg/mL, After HC
Model	Flexible Cylinder	Flexible Cylinder	Cylinder	Flexible Cylinder
Background (cm^{-1})	0.0084 ± 0.0001	0.013 ± 0.0002	0.0034 ± 0.0002	0.0084 ± 0.0002
Scale (Cylinder)	$0.001 \pm 3.2 \times 10^{-5}$	$0.001 \pm 5.3 \times 10^{-6}$	$0.005 \pm 5.8 \times 10^{-5}$	0.0023 ± 0.0008
Length (Å)	>1000	>1000	>1000	>1000
Kuhn Length (Å)	761 ± 121	282 ± 5	NA	13 ± 7
Radius (Å)	43.5 ± 0.1	34.0 ± 0.1	42.7 ± 0.04	21.2 ± 0.1
Scale (Power Law)	NA	NA	NA	NA
Power	NA	NA	NA	NA
χ^2	2.15	2.98	8.17	4.65
2NapFF-TBA	**10 mg/mL, Before HC**	**10 mg/mL, After HC**	**75 mg/mL, Before HC**	**75 mg/mL, After HC**
Model	Flexible Cylinder	Cylinder + Power Law	Cylinder	Cylinder
Background (cm^{-1})	$0.0009 \pm 2.8 \times 10^{-5}$	0.009 ± 0.001	0.02 ± 0.0002	0.008 ± 0.0007
Scale (Cylinder)	0.005 ± 0.0003	0.002 ± 0.0003	0.02 ± 0.0008	0.02 ± 0.0002
Length (Å)	197 ± 11	>1000	>1000	>1000
Kuhn Length (Å)	112 ± 11	NA	NA	NA
Radius (Å)	14.1 ± 0.4	14.1 ± 0.2	15.3 ± 0.2	16.8 ± 0.2
Scale (Power Law)	NA	$1.3 \times 10^{-8} \pm 5.4 \times 10^{-9}$	NA	NA
Power	NA	4.0 ± 0.09	NA	NA
χ^2	2.33	1.59	2.50	1.96
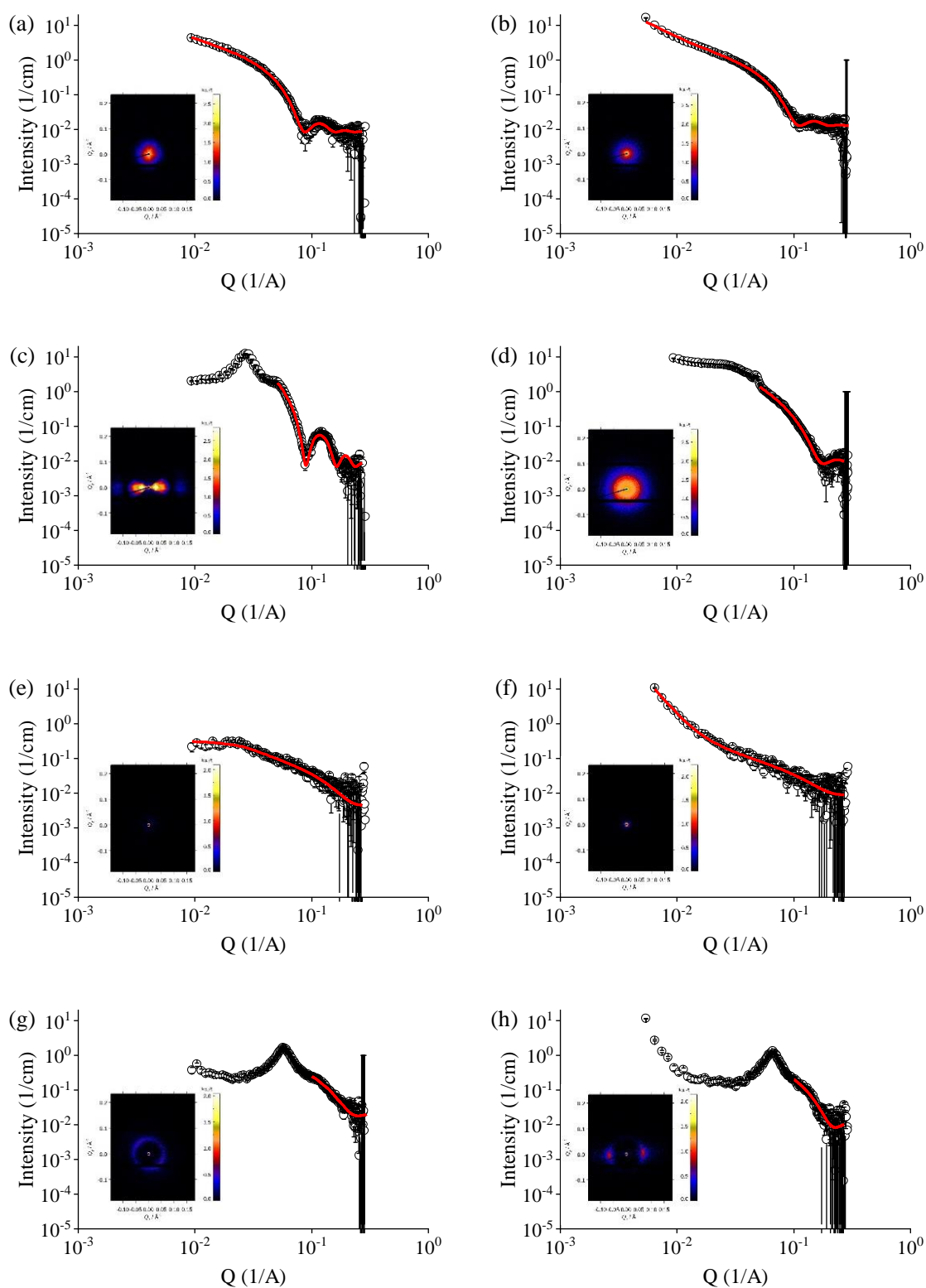
Figure 3.9. 1D SAXS data (and corresponding 2D SAXS data shown as insets) for 10 mg/mL 2NapFF-Na (a) before heat-cool and (b) after heat-cool; 75 mg/mL 2NapFF-Na (c) before heat-cool and (d) after heat-cool; 10 mg/mL 2NapFF-TBA (e) before heat-cool and (f) after heat-cool; 75 mg/mL 2NapFF-TBA (g) before heat-cool and (h) after heat-cool. Data are shown in black with fits shown in red.

Using POM, we can also show the loss of orientation that is observed in the 2D scattering pattern by heating. By locally heating samples of 2NapFF-Na and 2NapFF-TBA through a copper wire under a microscope, the POM images taken during heating show a loss in texture with the images becoming darker (Figure 3.10).[24] This agrees with the SAXS data by also suggesting the samples are now isotropic. Concentration is important here as it is easier to see the changes in the POM images of 2NapFF-Na and 2NapFF-TBA at 75 mg/mL compared to 10 mg/mL. 2NapFF-TBA at 10 mg/mL shows little difference between the control (which is not heated) and the heated sample. This is different compared to 2NapFF-Na 10 mg/mL which shows differences in POM images after 30 minutes of heating compared to the control. In comparison, 2NapFF-Na at 75 mg/mL showed a gradual darkening in the POM images, whilst 2NapFF-TBA showed an almost instant change in image texture which occurred at the same time the solution itself became cloudy.
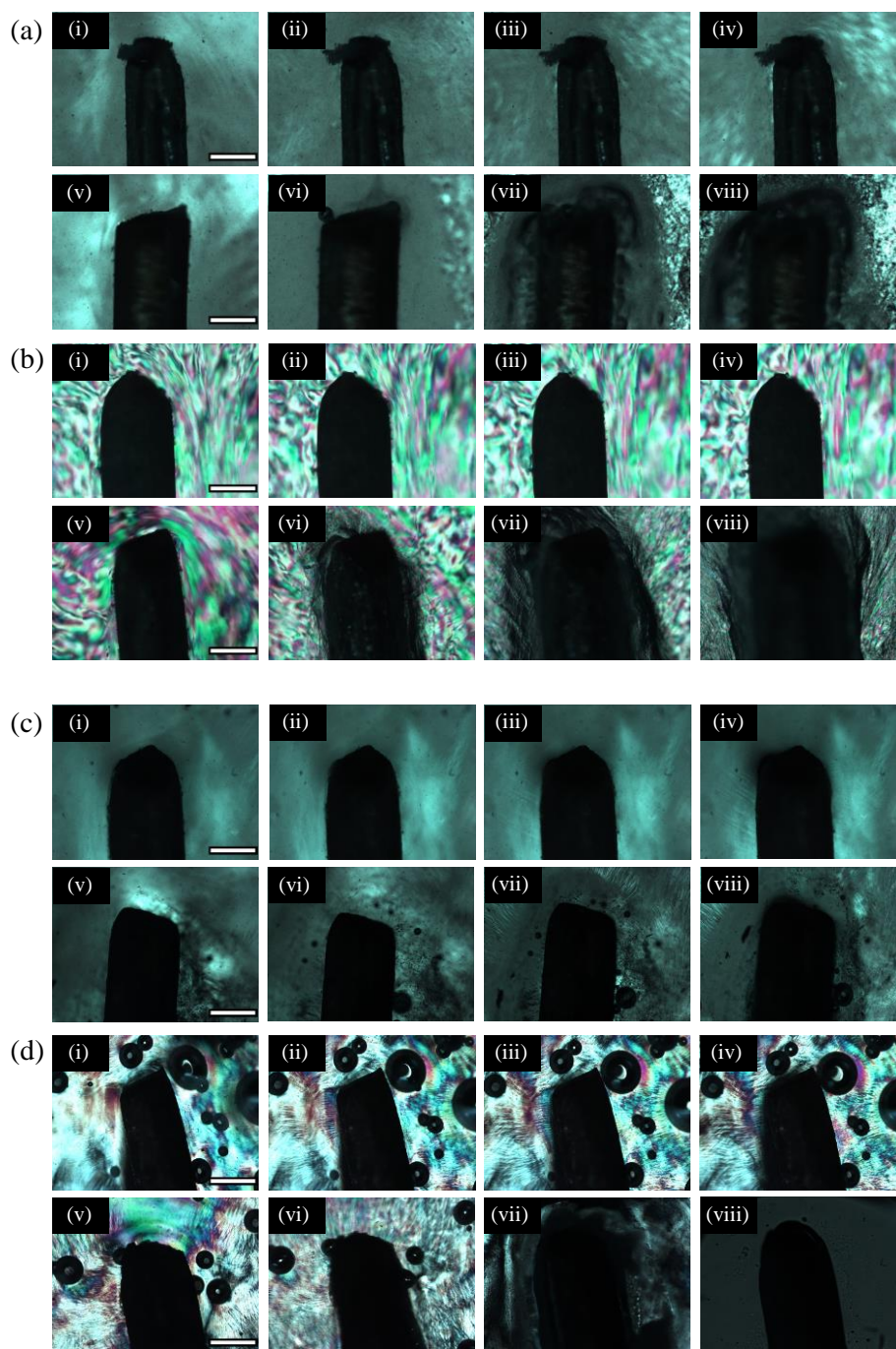
Figure 3.10. Heating of solutions of (a) 10 mg/mL 2NapFF-Na; (b) 75 mg/mL 2NapFF-Na; (c) 10 mg/mL 2NapFF-TBA; (d) 75 mg/mL 2NapFF-TBA using a copper wire, showing (i) control with no heating at 0 minutes; (ii) control with no heating at 10 minutes; (iii) control with no heating at 20 minutes; (iv) control with no heating at 30 minutes; (v) before heating with a copper wire; (vi) after heating with a copper wire for 10 minutes; (vii) after heating with a copper wire for 20 minutes; (viii) after heating with a copper wire for 30 minutes. Scale bar represents 500 μm.

The structural changes which are observed in the SAXS data during heating and cooling are also observed in the bulk properties of 2NapFF-Na and 2NapFF-TBA. To show this we study the full concentration series of 2NapFF-Na and 2NapFF-TBA using strain and frequency sweeps before and after heat-cool cycle. A summary of data collected from the frequency sweeps for both series are shown in Figure 3.11, with full rheological data shown in Chapter 6, Section 2: Supplementary Figures. Before heat-cool, 2NapFF-Na samples exhibit G″ similar to G′ with the exception of 2NapFF-Na at 100 mg/mL. This is consistent with the free-flowing solutions we observe before heat-cool as discussed previously. The frequency sweeps collected show both G′ and G″ are frequency dependent which also correlates with a free-flowing solution. Once a heat-cool cycle is performed, at 2NapFF-Na concentrations of 25 mg/mL and greater, G′ becomes larger than G″, with frequency independent behaviour now observed at concentrations of 50 mg/mL and above. We conclude that between 25-50 mg/mL 2NapFF-Na, these samples are viscoelastic liquids due to their frequency dependent behaviour, but at concentrations of 50 mg/mL 2NapFF-Na and greater these are viscoelastic solids since G′ is approaching an order of magnitude larger than G″, and exhibits frequency independent behaviour over the timescale of an experiment. This, however, could be open to interpretation since gels are difficult to define.[45, 46]
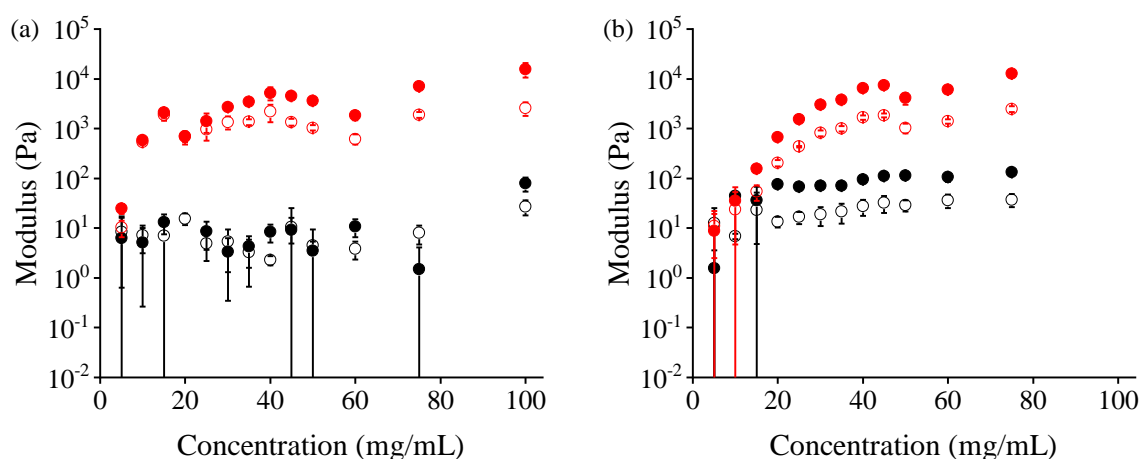
Figure 3.11. Summary of frequency sweep data collected at 10 rad/s for (a) 2NapFF-Na and (b) 2NapFF-TBA measured at room temperature before heat-cool cycle (black) and at room temperature after heat-cool cycle (red). G′ is represented by filled circles and G″ by empty circles.

Before a heat-cool cycle, the 2NapFF-TBA samples are visibly much more viscous compared to 2NapFF-Na. Our rheological data also shows this as without a heat-cool cycle, G′ is greater than G″ for 2NapFF-TBA concentrations of 10 mg/mL and greater, Figure 3.11b. This is consistent with our previous observations which show that 2NapFF-TBA samples are stable to inversion for at least one minute for 2NapFF-TBA concentrations of 10 mg/mL and above. When 2NapFF-TBA samples are subjected to a heat-cool cycle, the samples behave similarly to 2NapFF-Na where both G′ and G″ increase significantly compared to before heat-cool. Again, the frequency sweeps of 2NapFF-TBA at concentrations of 30 mg/mL and greater are frequency independent, with G′ almost an order of magnitude larger than G″ for all concentrations of 2NapFF-TBA after heat-cool (tanδ > 0.2 for all concentrations of 2NapFF-TBA after heat-cool).

Interestingly, however, after a heat-cool cycle, the 2NapFF-TBA samples were less stable to inversion than the 2NapFF-Na samples. All 2NapFF-Na samples are significantly more viscous after the heat-cool cycles; all can now be inverted without flow, and in some cases for at least 14 days (Figure 3.12). After only 1 day of inversion following a heat-cool cycle, 2NapFF-TBA fails vial inversion at concentrations of 30 mg/mL or less compared to 2NapFF-Na which fails at only 10 mg/mL or less (Figure 3.13). This emphasises the importance of using rheology over the vial inversion method to confirm gelation, as although some of the samples here can self-support for a significant amount of time, the rheology does not show the characteristics expected of a true gel.
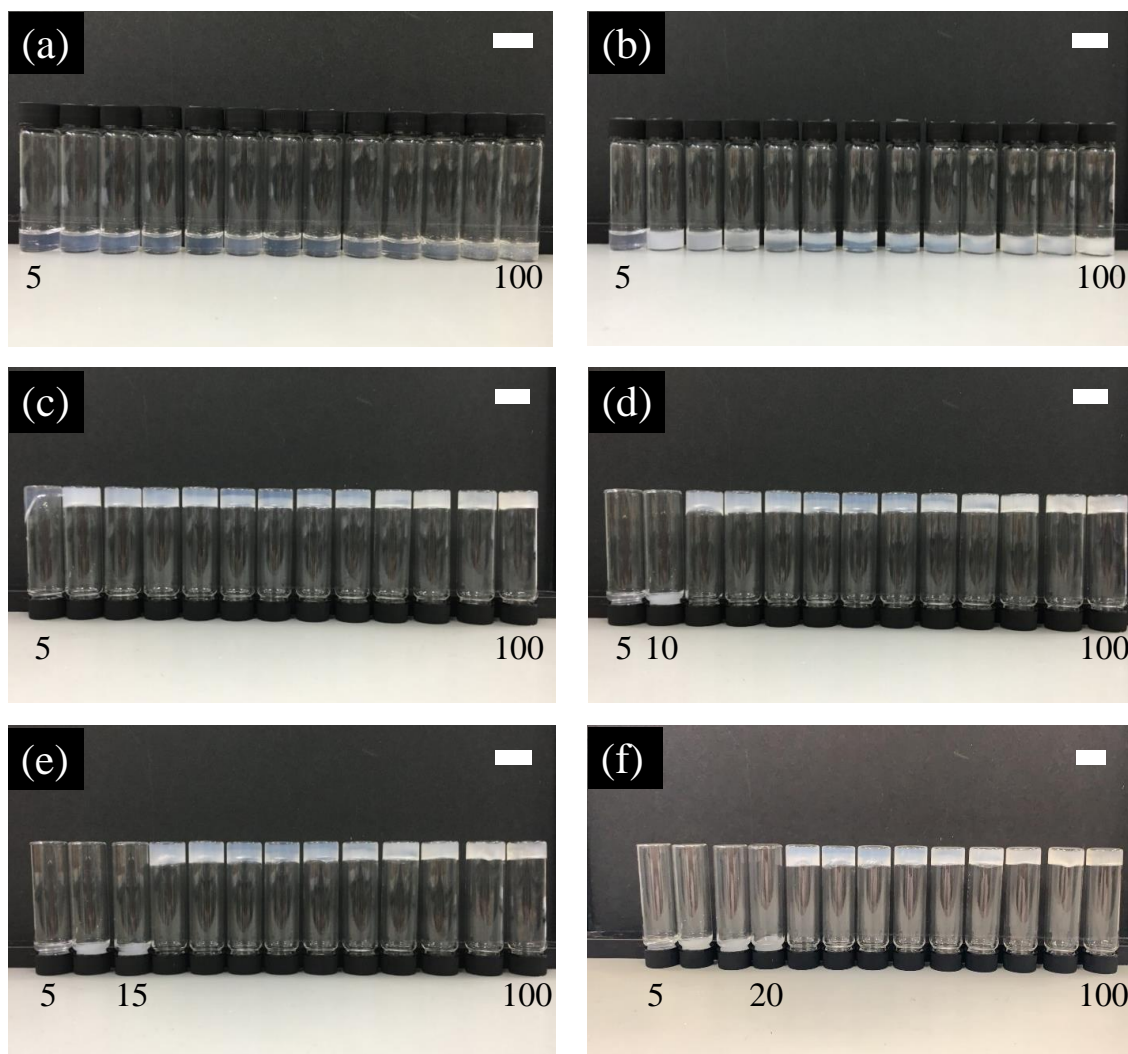
Figure 3.12. Heat-cool of 2NapFF-Na (a) before heating; (b) straight after heating in a 60 °C oven for 1 hour; (c) 2 hours after heating; (d) 1 day after heating; (e) 3 days after heating; (f) 9 days after heating. Vials were left undisturbed and inverted for a 14 day period, after which the experiment was stopped due to potential evaporation issues. Scale bars represent 2 cm.
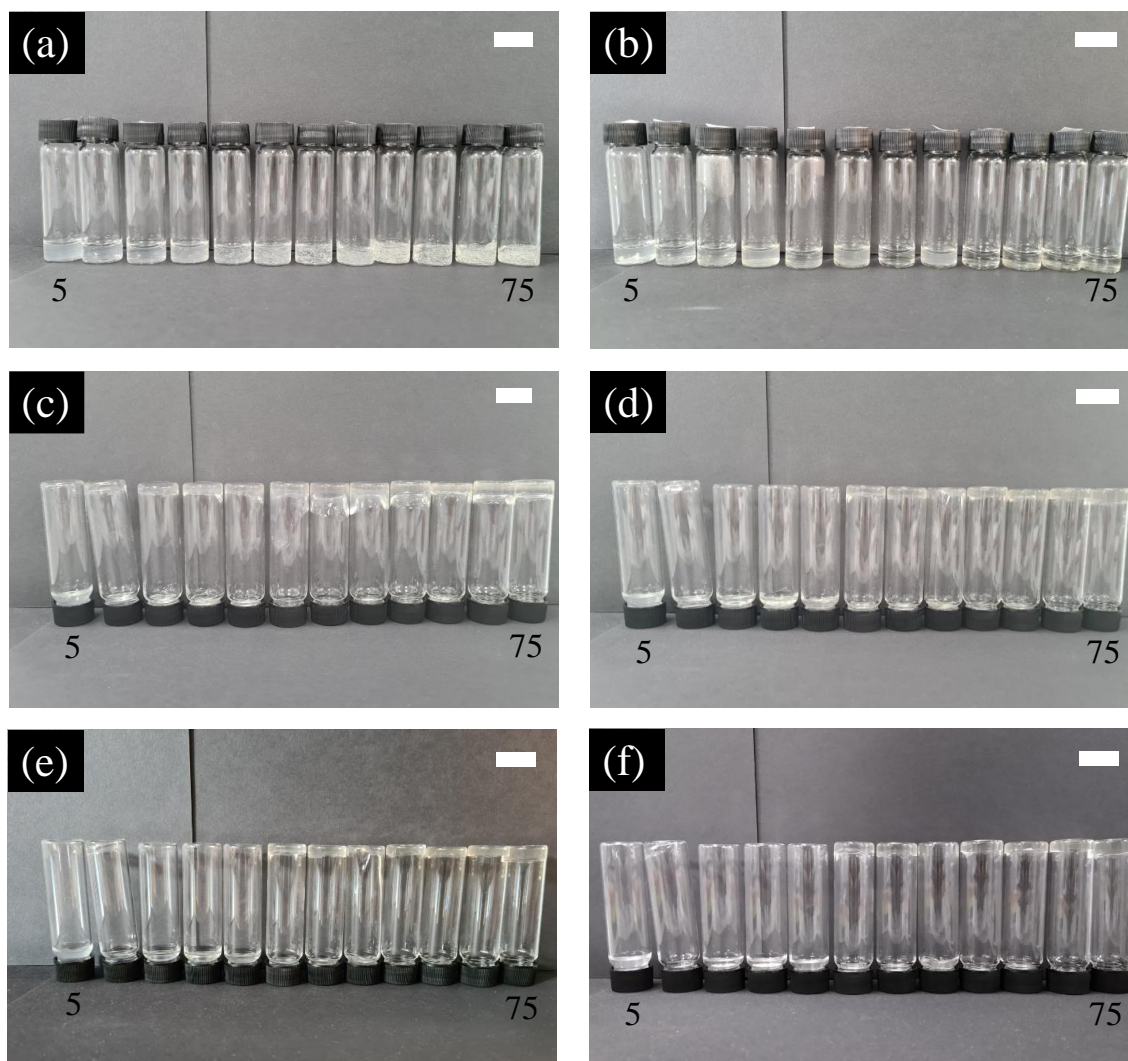
Figure 3.13. Heat-cool of 2NapFF-TBA (a) before heating; (b) straight after heating in a 60 °C oven for 1 hour; (c) 2 hours after heating; (d) 1 day after heating; (e) 3 days after heating; (f) 9 days after heating. Vials were left undisturbed and inverted for a 14 day period, after which the experiment was stopped due to potential evaporation issues. Scale bars represent 2 cm.

Differences in extensional viscosity are also present after a heat-cool cycle. To show this, the extensional relaxation time (λ_E) was studied for both 2NapFF-Na and 2NapFF-TBA at 25 mg/mL before and after heat-cool using the dripping-onto-substrate technique.[47] This technique involves video recordings of the dispensing of a droplet of fluid onto a substrate, which results in the formation of an unstable liquid bridge that subsequently thins and breaks. The speed and shape with which the unstable liquid bridge breaks is analysed to determine the extensional relaxation time. All solutions for examining extensional viscosity were

prepared by Lisa Thomson (University of Glasgow) and all data collected, processed and analysed by Daniel McDowall (University of Glasgow), using a script written by Henry Ng (University of Liverpool) for analysis. For 2NapFF-TBA before heat-cool, λ_E is too large to measure. The filament dries out before it breaks. For 2NapFF-Na, however, $\lambda_E = 14.6 \pm 6.5$ ms. Using the same method to study the λ_E for both 2NapFF-Na and 2NapFF-TBA after heat-cool, the behaviour of the solutions is reversed. After heat-cool 2NapFF-Na was too viscous to measure, whereas 2NapFF-TBA gave $\lambda_E = 346 \pm 110$ ms. These differences in extensional viscosity before and after heat-cool are most clearly shown using frames from the videos taken during the measuring process (Figure 3.14).
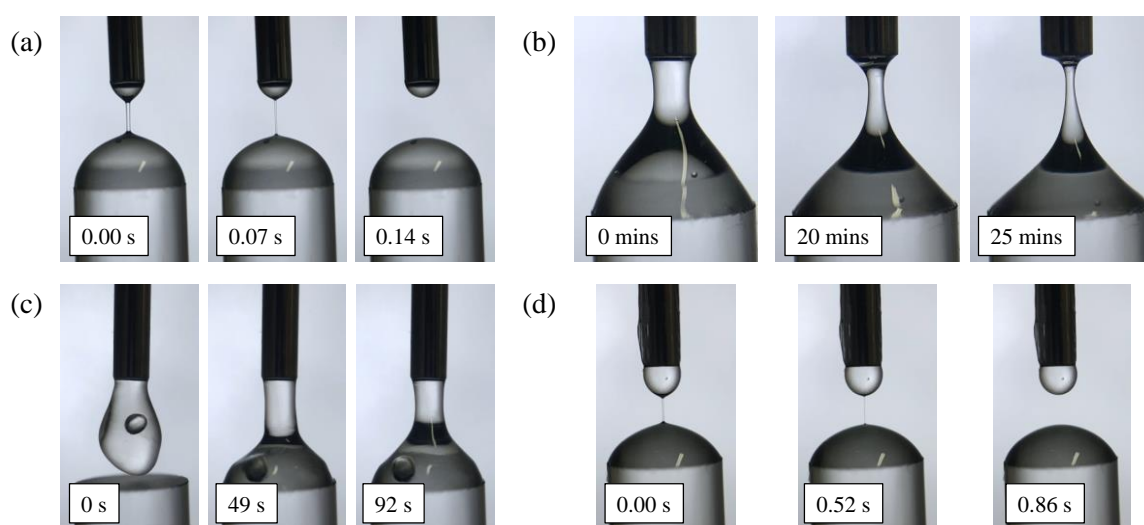
Figure 3.14. Frames from dripping-onto-substrate technique showing (a) 2NapFF-Na; (b) 2NapFF-TBA; (c) 2NapFF-Na after heat-cool; (d) 2NapFF-TBA after heat-cool. For (a) and (d) the timestamps are set to zero at the formation of a slender filament (height = 10 x width). For (b) and (c) timestamps are from the start of droplet touching the substrate.

When 2NapFF-TBA samples are removed from the oven, the viscosity is significantly lower when hot as compared to prior to heating. To quantify this, we monitor the viscosity during the heat-cool cycle. The viscosity of 75 mg/mL 2NapFF-TBA drops approximately 4 orders of magnitude when heating to 60 °C; in comparison, the viscosity of the 75 mg/mL 2NapFF-Na solution under the same conditions does not exhibit a decrease in viscosity when heating (Figure 3.15). This suggests different heating mechanisms are present for each counterion.
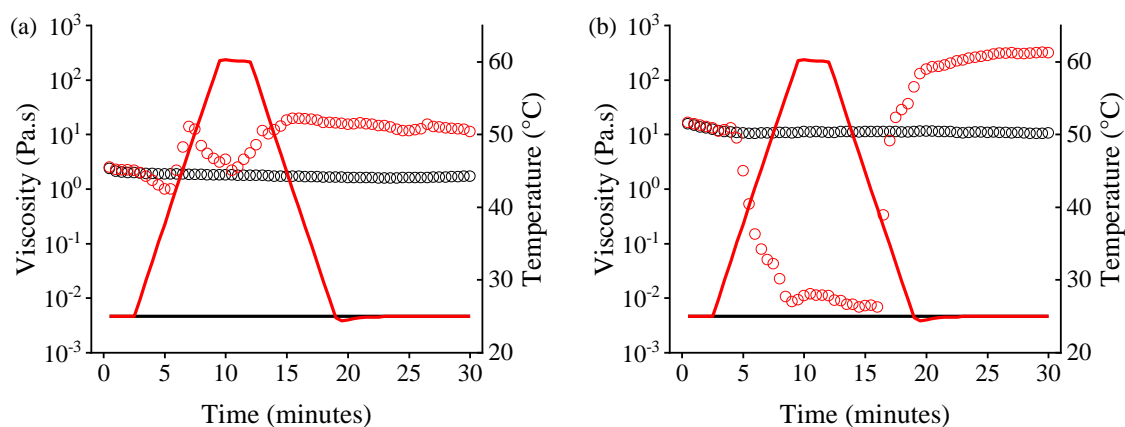
Figure 3.15. Viscosity data at a concentration of 75 mg/mL for (a) 2NapFF-Na and (b) 2NapFF-TBA during heating using a CP50 geometry. Red data points show the viscosity being measured for 2 minutes at 25 °C, then heated at a rate of 5 °C/min from 25 °C to 60 °C before being held at 60 °C for 2 minutes. This was then cooled back to 25 °C at the same rate with the viscosity continuously monitored. Black data points show a control sample which was kept at 25 °C throughout. Line plots show the temperatures during the heat-cool (red) and control (black) viscosity measurements.

In addition to this visible change after heating, 2NapFF-TBA also shows visible changes during heating while 2NapFF-Na does not (Figure 3.16a). Further visible changes also occur as at higher concentrations (greater than 25 mg/mL 2NapFF-TBA), with phase separation occurring on heating, and the samples re-homogenising spontaneously on cooling. This is most obvious with the most concentrated sample, 2NapFF-TBA at 75 mg/mL (Figure 3.16b). Simultaneously, the G′ and G″ of 2NapFF-TBA decreases as it becomes homogeneous again whilst G′ and G″ remains constant for 2NapFF-Na following the 24 hours after heat-cool, Figure 3.16c. 2NapFF-TBA seems to be an example of a small molecule that demonstrates a lower critical solution temperature (LCST). This behaviour has been shown for other similar micellar systems.[48-50] Using NMR spectroscopy, we prove that 2NapFF is found in both layers straight after heating with 1 part 2NapFF-TBA found in the top, more-liquid-like layer, compared to 21 parts 2NapFF-TBA found in the oily bottom layer (Chapter 6, Section 2: Supplementary Figures).
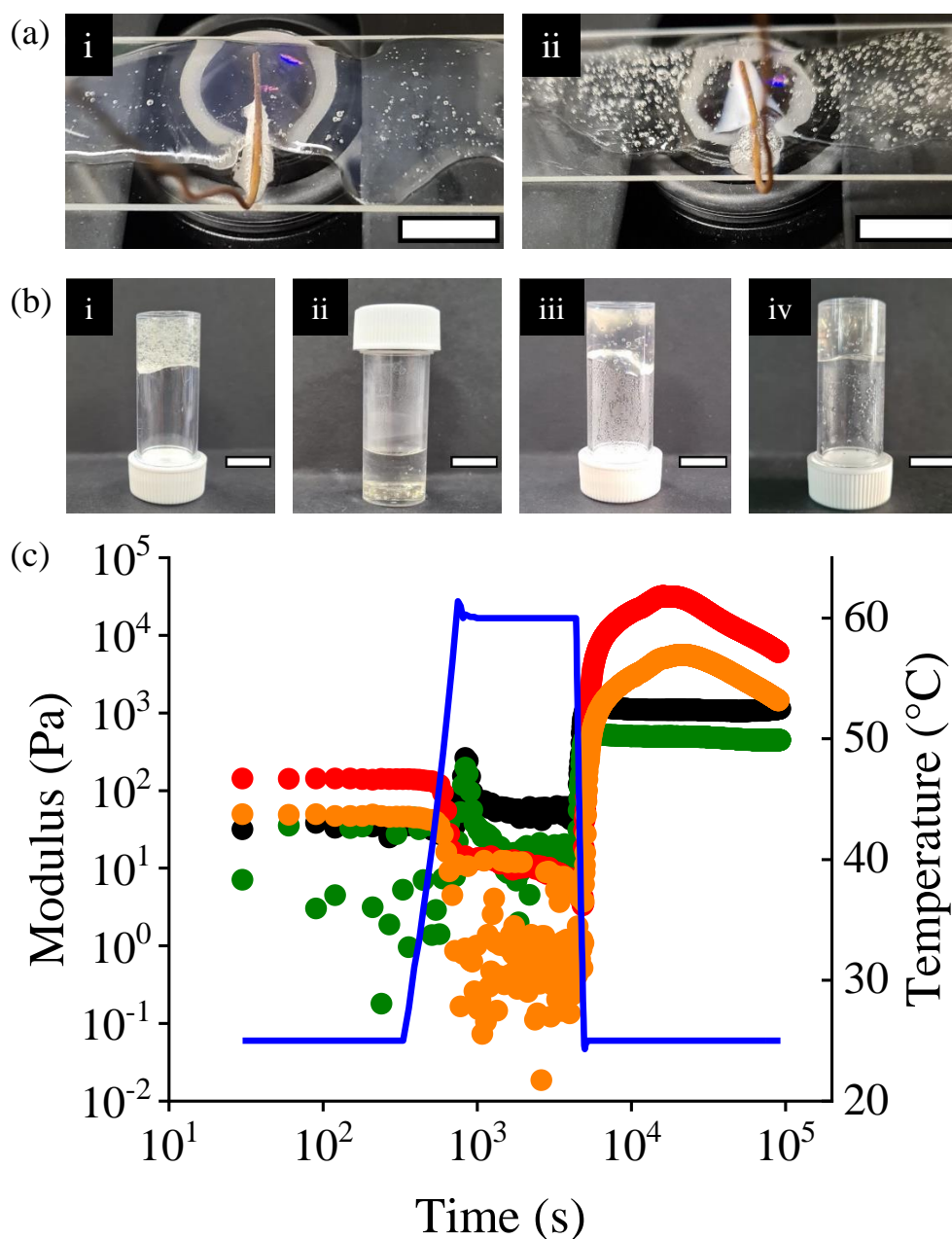
Figure 3.16. (a) Photographs of (i) 2NapFF-Na and (ii) 2NapFF-TBA at a concentration of 75 mg/mL taken during heating with a copper wire. 2NapFF-TBA becomes cloudy compared to 2NapFF-Na which shows no change. Superglue can be seen in both images at the bottom of the slide which has been used to secure the copper wire. Scale bars represent 1 cm. (b) Photographs of 2NapFF-TBA at a concentration of 75 mg/mL taken (i) before heating; (ii) straight after 1 hour heating at 60 °C; (iii) after 2 hours cooling to room temperature; (iv) the day following heating. Scale bars represent 1 cm. (c) Time sweep data at a concentration of 75 mg/mL for 2NapFF-Na (G′ black circles; G″ green circles) and 2NapFF-TBA (G′ red circles; G″ orange circles) during a heat-cool cycle. The blue line shows the temperatures during the heat-cool cycle.

Another stimulus we apply to 2NapFF-Na and 2NapFF-TBA is a magnetic field which can induce alignment of anisotropic structures. To examine alignment, we use deuterium (^{2}H) NMR as previous work by our group shows that when using 2NapFF-Na in D_2O at 5 mg/mL and placing in a 400 MHz NMR spectrometer, the deuterium peak of D_2O exhibits splitting which suggests that the worm-like micellar structures present in the solution align with respect to the magnetic field.[51] Our group has previously added probe molecules to LMWG solutions in order to examine their alignment by NMR spectroscopy.[52] However, as described previously in Chapter 2, the 2NapFF solutions used in this Thesis are very sensitive to even seemingly small changes. Therefore, since we could collect good quality ^{2}H NMR and ^{23}Na NMR data without the addition to another component to the system, the addition of probe molecules was not investigated further here. Exemplar data is shown in Figure 3.17 and all NMR data can be found in Chapter 6, Section 2: Supplementary Figures. For 2NapFF-Na, we see splitting in all concentrations of solution with the exception of 2NapFF-Na at 100 mg/mL. However, solutions of 2NapFF-TBA at all concentrations of LMWG examined, showed no splitting, and hence no alignment, when placed inside the magnetic field. We believe this is due to the increased viscosity of the 2NapFF-TBA solutions. As already discussed, the viscosity of 10 mg/mL 2NapFF-TBA is comparable to 2NapFF-Na at 100 mg/mL, both of which show no splitting in their ^{2}H data. Since 2NapFF-TBA solutions are not free-flowing compared to 2NapFF-Na, we believe the solution state NMR spectrometer cannot collect the ^{2}H data. As discussed previously, there is a significant decrease in viscosity when 2NapFF-TBA is heated. Examining the ^{2}H NMR data for 2NapFF-TBA, exemplar data shown in Figure 3.17 and full ^{2}H NMR data shown in Chapter 6, Section 2: Supplementary Figures, we show that no peaks can be found in the ^{2}H data before heat-cool, Figure 3.17, green data (when the sample is most viscous). Peaks do appear however when recording ^{2}H NMR data at 60 °C and when returning back to 25 °C (Figure 3.17 red and blue data respectively). This also suggests that the viscosity of the samples is a vital property when examining these solutions in this manner.
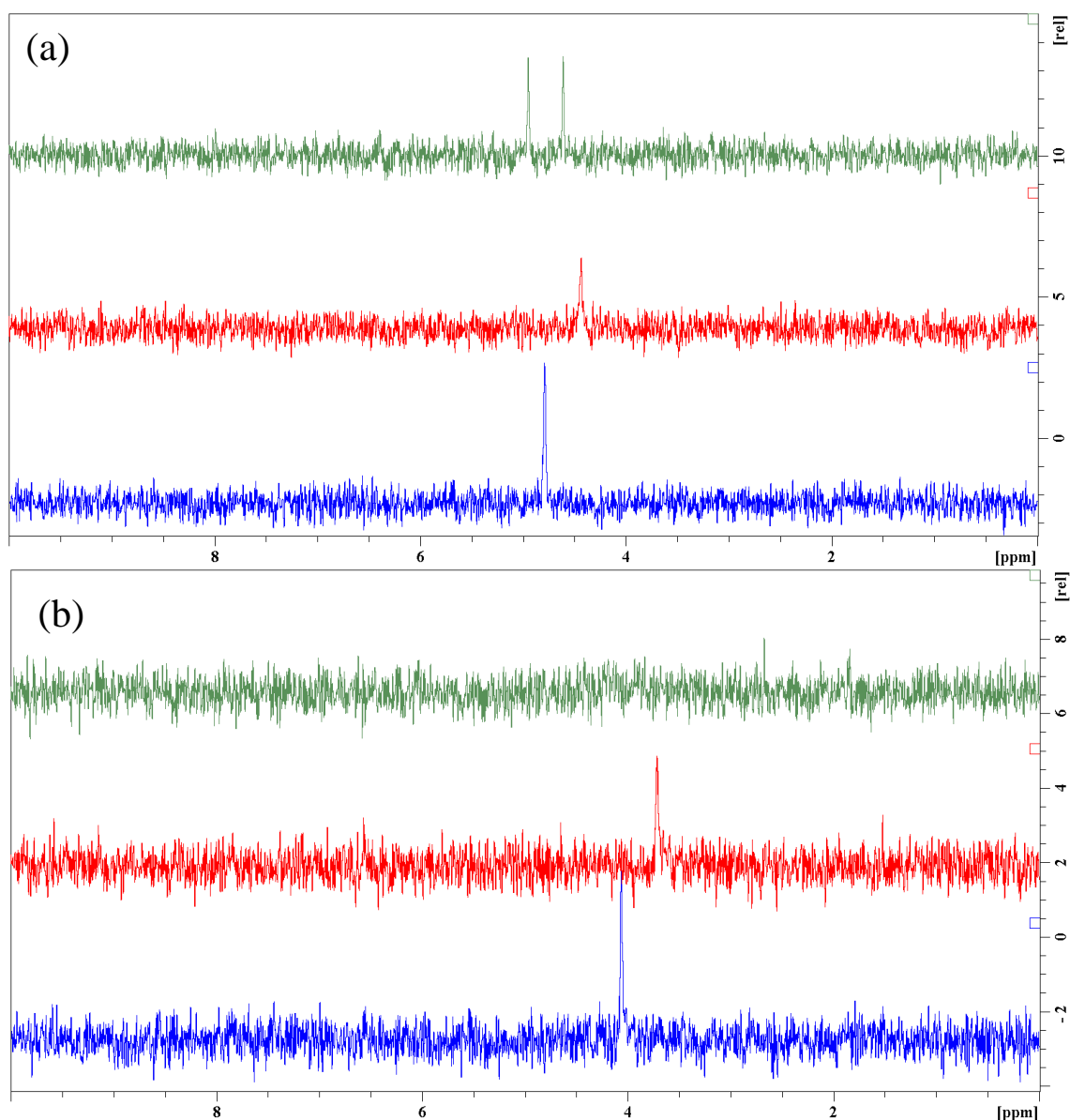
Figure 3.17. Exemplar ^{2}H NMR spectroscopy data for (a) 2NapFF-Na and (b) 2NapFF-TBA at a concentration of 25 mg/mL. Data were collected at 25 °C (green), at 60 °C (red) and then cooled to 25 °C (blue).

We can quantify the alignment of the 2NapFF-Na solutions by examining the [23]Na spectra. Similar to the data collected for ^{2}H, the ^{23}Na NMR data will show splitting if alignment is present in the 2NapFF-Na samples.[26] The magnitude of the splitting observed depends on the relative alignment of the structures present.[51, 52] The worm-like micelles formed by 2NapFF-Na can be aligned in a magnetic field with the degree of alignment being concentration dependent, Figure 3.18. We show, in general, as the concentration of 2NapFF-Na is increased so does the size of splitting and hence the alignment of the structures. We

assume we can collect data for 100 mg/mL 2NapFF-Na using ^{23}Na NMR spectroscopy but not from ^{2}H at the same 2NapFF concentration because of the substantial quantity of ^{23}Na present within the samples.
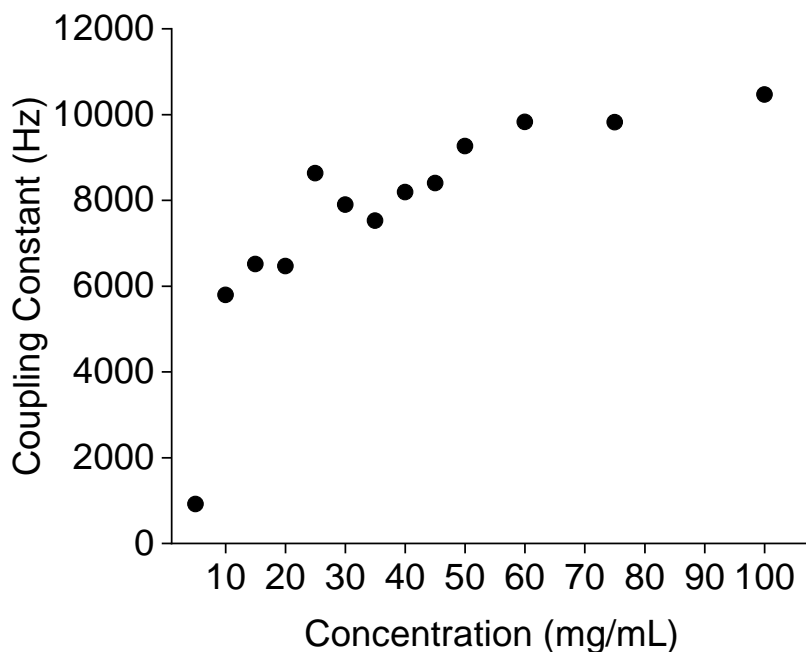
Figure 3.18. Summary of ^{23}Na NMR for 2NapFF-Na.

POM can also be used to show the alignment of our structures in 2NapFF-Na after exposure to a magnetic field. The directions of shear and the magnetic field are shown in Figure 3.19. Exemplar 2NapFF-Na POM images are shown in Figure 3.20 with all concentrations shown in Chapter 6, Section 2: Supplementary Figures. Inside the NMR tube and before placing inside the NMR spectrometer (Figure 3.20i), we see the textures described previously. After exposure to a magnetic field, the textures align in the direction of the magnetic field (Figure 3.20ii). We again see evidence of the textures disappearing when a heat-cool cycle is performed (Figure 3.20iii) as the POM images are now dark.
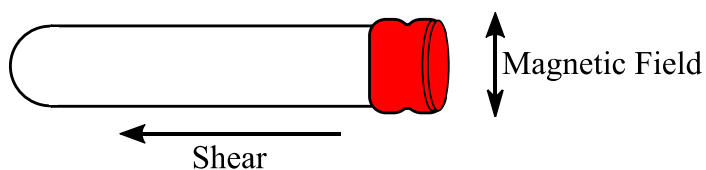
Figure 3.19. Directions of shear and magnetic field within an NMR tube.
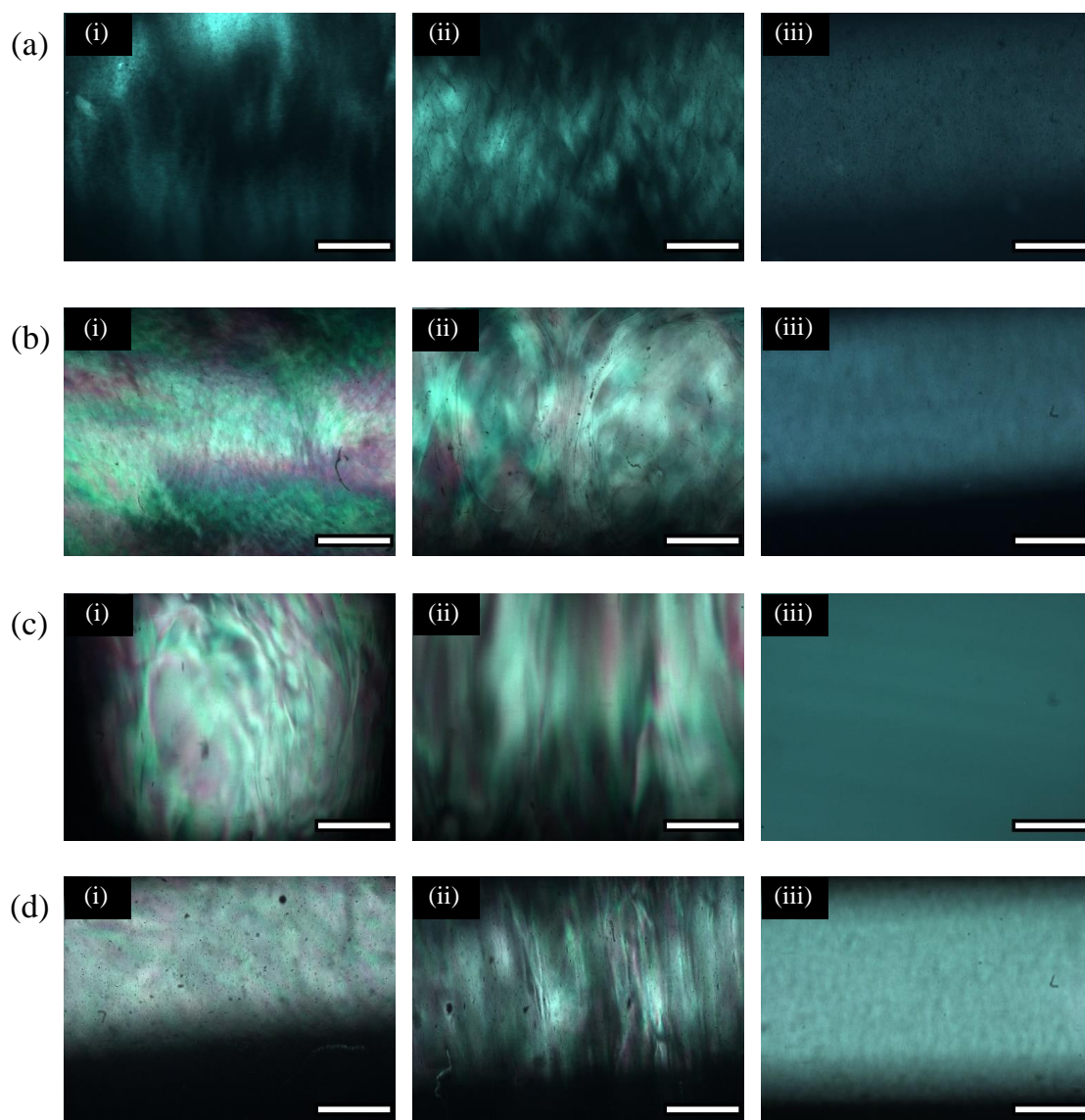
Figure 3.20. POM images of 2NapFF-Na at exemplar concentrations of (a) 10 mg/mL; (b) 25 mg/mL; (c) 40 mg/mL; (d) 75 mg/mL taken (i) before inserting the sample into the NMR spectrometer; (ii) after inserting the sample into the NMR spectrometer; (iii) after heating the sample to 60 °C and cooling back to 25 °C inside the NMR spectrometer. Scale bars represent 500 µm.

Examining POM images of 2NapFF-TBA (Figure 3.21), we see similar images as we did for 2NapFF-Na. Again, the images are similar to those discussed previously for 2NapFF-TBA with little texture present (Figure 3.21i). The texture remains similar after exposure to a magnetic field, Figure 3.21ii. This texture is again lost after heat-cool (Figure 3.21iii). This is consistent with other heat-cool experiments. Overall, these NMR data show that by simply changing the concentration of 2NapFF, the counter ion used to create the solutions, or the temperature of the solutions, we have control over the behaviour and ordering of the 2NapFF worm-like micelles.
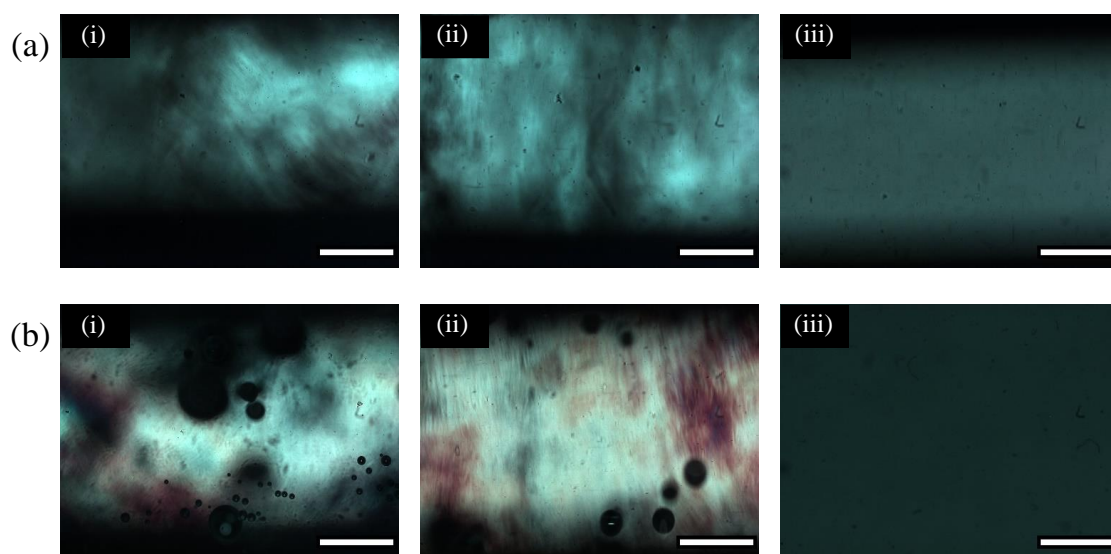
Figure 3.21. POM images of 2NapFF-TBA at exemplar concentrations of (a) 10 mg/mL; (b) 25 mg/mL taken (i) before inserting the sample into the NMR spectrometer; (ii) after inserting the sample into the NMR spectrometer; (iii) after heating the sample to 60 °C and cooling back to 25 °C inside the NMR spectrometer. Scale bars represent 500 µm.

Understanding that the packing, order and alignment of the primary structures can be controlled by counterion, concentration and temperature allows us to rationally determine which systems should be used for different applications. To exemplify this, we have chosen a small number of specific examples.

Gel noodles can often be formed from solutions by extrusion into a bath of a gelling agent, typically a divalent salt.[53, 54] Here, all solutions made in order to form gel noodles were prepared by Lisa Thomson and Olivia Marshall (University of Glasgow) and noodles created and analysed by Olivia Marshall and Daniel McDowall (University of Glasgow). We show that noodles can be formed from both 2NapFF-Na and 2NapFF-TBA (Figure 3.22a). The properties of the gel noodles, however, are affected by the different counterions. 2NapFF-Na gel noodles are far more mechanically robust compared to those of 2NapFF-TBA. They are so much more robust, that these 2NapFF-Na noodles can be lifted out of the gelling bath, which is not possible for 2NapFF-TBA (Figure 3.22b). The 2NapFF-Na gel noodles also show far greater alignment compared to the gel noodles formed by 2NapFF-TBA (Figure 3.22c), which is in agreement with the SAXS, POM and NMR alignment data for 2NapFF-Na compared to 2NapFF-TBA described previously in this Chapter.
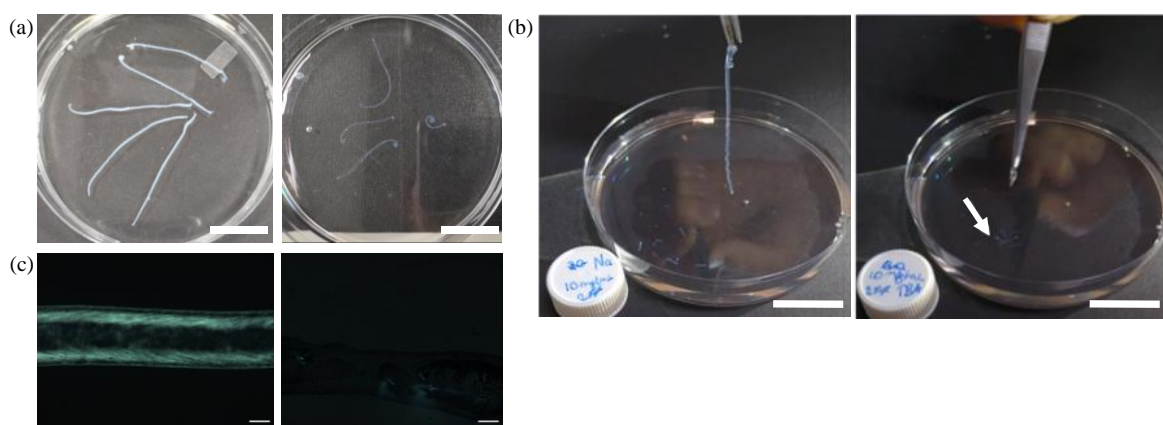
Figure 3.22. (a) Gel noodles made with 2NapFF-Na (left) and 2NapFF-TBA (right) at concentrations of 25 mg/mL. Scale bars represent 2 cm; (b) photographs showing differences in mechanical strength of noodles. The noodles were formed in a dish and then picked up at one end using tweezers and lifted out of the calcium bath. The 2NapFF-Na noodles (left) are robust enough to be picked up. The 2NapFF-TBA noodles (right) break when lifting, even after multiple attempts. The white arrow is added to guide the eye to broken sections of noodles still in the gelling bath. Scale bars represent 2 cm; (c) POM images of a 2NapFF-Na (left) and 2NapFF-TBA (right) noodles. Scale bars represent 200 µm.

In comparison, 2NapFF-TBA is by far the preferred solution for the formation of liquid threads (all solutions made by Lisa Thomson, University of Glasgow, and data collected alongside Daniel McDowall, University of Glasgow, with Daniel McDowall performing image analysis). Whilst threads of 2NapFF-Na break almost immediately over a small size gap (3 cm, Figure 3.23a), the high extensional viscosity of 2NapFF-TBA means that it is possible to anchor the solution to a surface and then drag solution between gaps of various sizes and still form persistent threads (Figure 3.23b and Figure 3.23c). By sequentially adding and joining multiple threads, a web-like structure can be formed and then dried overnight, showing the stability of the threads that they can support themselves whilst drying over a number of hours (Figure 3.23d). Alternatively, once the web-like structure has been formed, concentrated HCl can be added to the bottom of the beaker where the acidic vapour gels the threads, resulting in increased opacity (Figure 3.23e). Instead of trying to string horizontally to form threads, it is possible to form long threads by extruding and allowing the 2NapFF-TBA solution to fall with gravity (Figure 3.23f). This gives threads which are able to reach 77 cm in length before breaking. These webs are similar to those which can be formed by spider silk and silkworm silk.[55] Suggested applications for these types of materials include ligament tissue engineering and in medical devices.
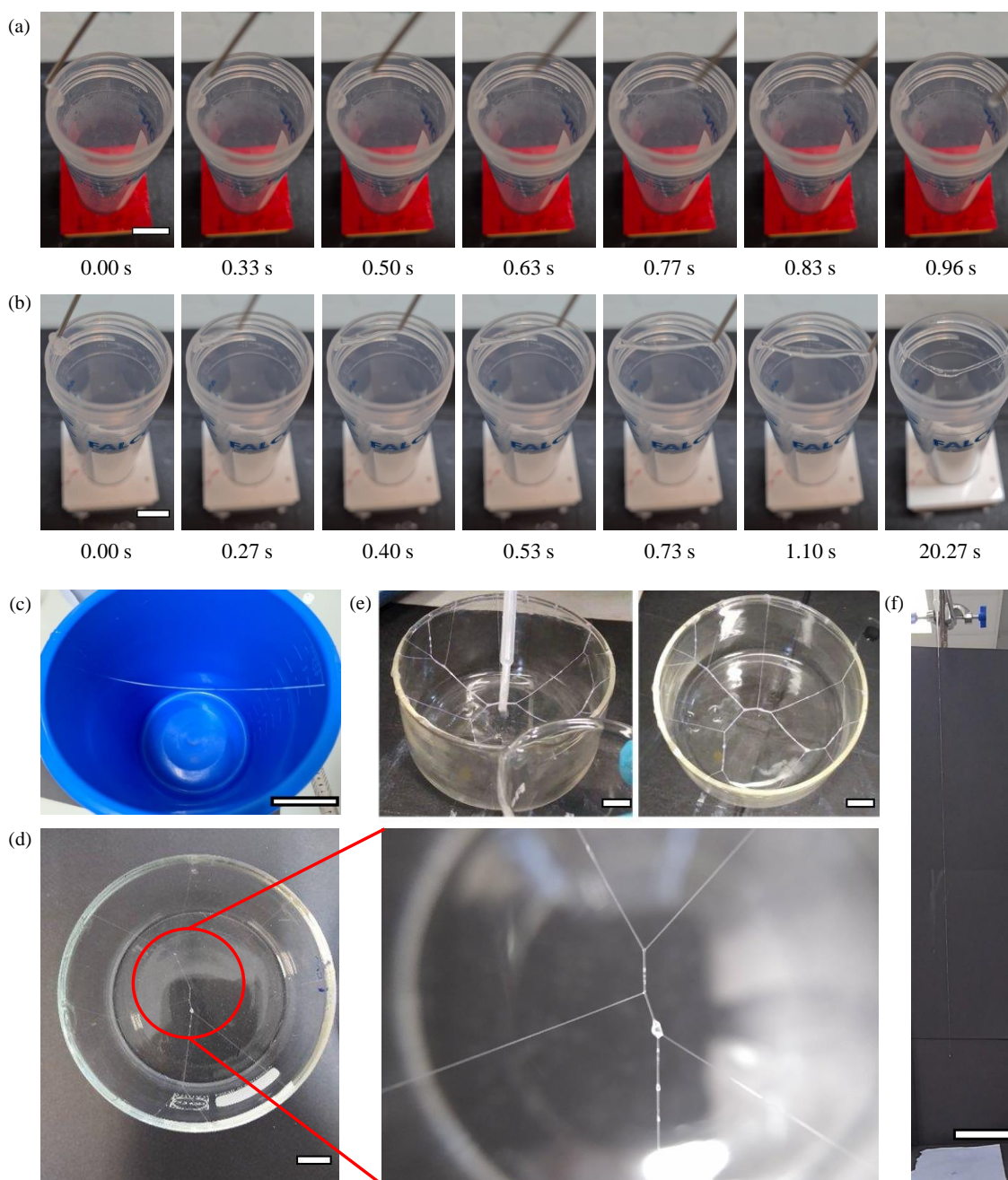
Figure 3.23. Frames (with time stamps) from a video showing the stringing of 75 mg/mL (a) 2NapFF-Na and (b) 2NapFF-TBA across a Falcon tube of gap size 3 cm. Scale bars represent 1 cm in both (a) and (b). (c) Forming a 2NapFF-TBA 75 mg/mL thread over a gap of 24 cm. Scale bar represents 10 cm. (d) Photographs of a 2NapFF-TBA web after drying out overnight. Scale bar represents 1 cm; (e) photographs of 2NapFF-TBA web after gelling with HCl vapour. Scale bar represents 1 cm; (f) examining the length of a string formed when allowed to fall freely with gravity. Using ImageJ the length of the string was calculated to be 77 cm. Scale bars represent 10 cm.

3.3. Conclusions and Future Work

In this Chapter, we aim to control the structures within solutions of the LMWG 2NapFF and hence control the resulting properties of the bulk materials. This is done by carefully altering the concentration of the LMWG and the counterion used to make the solutions, or by temperature. Being able to control the self-assembly process, the structures and resulting bulk properties of a single LMWG by altering these parameters reduces the need to find new LMWGs for certain desired properties and creates a range of interesting materials.

We prepare a range of different materials from a single building block by varying LMWG and counterion used to deprotonate the LWMG to form the solution. This results in changes in viscosity and POM images, which help to suggest the structures present. The structures and interactions between the structures are confirmed by SAXS. From the SAXS data, we are able to show that interactions between 2NapFF molecules occur at different concentrations depending on the counterion used. A micellar to nematic liquid crystal phase occurs at 20 mg/mL 2NapFF-Na. However, no alignment is present in 2NapFF-TBA at any concentration, even although interactions between 2NapFF-TBA structures are present at concentrations of 15 mg/mL and above. By increasing the concentration of 2NapFF, we show that the increased number of 2NapFF molecules self-assemble differently depending on the counterion; 2NapFF-Na forms additional structures when more 2NapFF is added, compared to 2NapFF-TBA which sees the cylindrical structures elongate in length.

The materials created are very susceptible to changes in temperature. This change is unsurprising since temperature is known to affect both micellar structures and can be used to access different liquid crystal phases. We show this temperature dependence in numerous ways, focussing on visual changes, rheological changes and changes in texture when examining POM images and changes in SAXS data. Our work here highlights why simply inverting a vial does not confirm the existence of a gel, and why using rheology to confirm the existence of a gel is always preferable. Future experiments could focus on cycling temperature. This would be interesting to examine since we show that 2NapFF-TBA has an LCST and its rheological properties change with time during heating and cooling.

Using our single LMWG, 2NapFF, we show that 2NapFF-Na is more susceptible to alignment by magnetic field with alignment increasing with 2NapFF-Na concentration. 2NapFF-TBA, however, does not align with magnetic field. Similarly, we show 2NapFF-Na and 2NapFF-TBA can both form gel noodles. However, 2NapFF-TBA forms noodles which are less stable than 2NapFF-Na, which can be easily picked up. We are also able to use the extensional viscosity of 2NapFF-TBA to prepare threads and webs. This is not possible with 2NapFF-Na.

Overall, we show that understanding the structures and packing of LMWG solutions allows the bulk properties to be controlled. Although one specific exemplar LMWG is chosen here, we would look to extend this to other LWMG systems to prove the discussions here are suitable in broader terms. Future work will also focus on finding other parameters which could also influence the structures and hence bulk properties of solutions. We hope this will produce more interesting and diverse materials. Other parameter which could be investigated include changing the chirality of the amino acids of the LMWG, or combining LMWGs into a multi-component system, both of which we have shown before make differences to our materials at low concentrations.[56, 57] We also wish to move this work to include the gel phase. By gelling the solutions discussed here in detail, we hope to find new interesting materials and again diversify the properties obtained by a single LMWG. Also, future work would involve trying to lock in the magnetic alignment of 2NapFF-Na at different 2NapFF concentrations by gelling, and examining if any rheological differences can be identified compared to the non-aligned gels.

3.4. Experimental

3.4.1. Synthesis of LMWG

Synthesis of the LMWG used in this chapter, 2NapFF, can be found in Chapter 6, Section 1.

3.4.2. 2NapFF Solution Preparation

To produce a solution of 2NapFF requires a predetermined mass of 2NapFF, 1 molar equivalent of a hydroxide, either sodium hydroxide (NaOH) or tetrabutylammonium hydroxide (TBAOH), with respect to 2NapFF and deionised water to make up the final volume (Table 3.4).[58] 2NapFF solutions made with NaOH are denoted 2NapFF-Na and those made with TBAOH denoted as 2NapFF-TBA. Based on calculations to have a 1:1 molar ratio of 2NapFF to hydroxide, solutions of concentration 50 mg/mL or greater of 2NapFF required 1 M hydroxide. All others were prepared using 0.1 M hydroxide. All solutions were formed at room temperature (normally between 22 and 25 °C). Based on factors discussed in Chapter 2, such as container size, shearing and pH, it was decided that solutions would always be made in 7 mL Sterilin vials with 3 mL made in a vial at a time. This would be stirred with a 13 x 3 mm stirrer bar at a rate of 1000 rpm overnight. The following day, once a homogeneous solution was obtained, the pH was adjusted to pH 10.5 using the corresponding hydroxide.

Table 3.4. Mass of solid 2NapFF and volumes of hydroxide and water needed to make 3 mL of various concentrations of 2NapFF solutions. Asterisks represent when 1M hydroxide was used to make the 1:1 XOH:2NapFF ratio possible.

Concentration of 2NapFF Solution (mg/mL)	Mass of 2NapFF (mg)	Volume of 0.1 M NaOH or TBAOH solution (mL)	Volume of water (mL)
5	15	0.30	2.70
10	30	0.60	2.40
15	45	0.91	2.09
20	60	2.21	1.79
25	75	1.51	1.49
30	90	1.81	1.19
35	105	2.11	0.89
40	120	2.42	0.58
45	135	2.72	0.28
50	150	0.30*	2.70
60	180	0.36*	2.64
75	225	0.45*	2.55
100	300	0.60*	2.40

3.4.3. Instruments and Methodologies

Rheology - Viscosity. Viscosity measurements were carried out using an Anton Paar Physica MCR101 rheometer. Measurements were performed using a 50 mm cone geometry (CP50) with gap distance between the geometry and the plate set to 0.101 mm and temperature set to 25 °C. To minimise shearing which could be induced by pipetting, all samples were poured onto the rheometer plate. Fresh solution was used for all runs. All viscosity measurements were performed in duplicate, and values averaged. Error bars represent the standard deviation between the replicates.

Rheology – Viscosity Heat-cool. Viscosity measurements carried out during heating and cooling were carried out using an Anton Paar Physica MCR301 rheometer.

Measurements were performed using a 50 mm cone geometry (CP50) with gap distance between the geometry and the plate set to 0.101 mm, shear rate set to 1 s^{-1} and temperature cycled from 25 °C to 60 °C and back to 25 °C. A control sample which was kept at 25 °C was also measured. Samples were poured onto the plate to minimise shearing that would be caused by pipetting the solutions. Fresh solution was used for each run.

Rheology - Bulk. Bulk rheology was carried out using an Anton Paar Physica MCR 101 rheometer. 10 x 3 mL of all concentrations of 2NapFF-Na (5-100 mg/mL) and 2NapFF-TBA (5-75 mg/mL) were formed using the procedure described in Section 3.4.2. 2 mL of each were then pipetted into 7 mL Sterilin vials and then placed into an oven set to 60 °C for 1 hour. After an hour, solutions were allowed to cool undisturbed on the bench at room temperature over two hours. After two hours, samples were examined using rheology using a vane (ST10) and cup geometry. All samples were measured at a constant temperature of 25 °C. Measurements were carried out in triplicate, averaged and standard deviation between the measurements calculated. Strain tests were performed at 10 rad/s from 0.01% to 1000% strain. Frequency sweeps were performed from 1 rad/s to 100 rad/s at 0.1% strain.

Rheology – Time Sweep. Overnight rheological time sweep measurements were performed using an Anton Paar Rhysica MCR301 rheometer. Samples were prepared in 7 mL Sterilin vials using a vane (ST10) and cup geometry to test 2 mL of prepared sample which was pipetted into the vial. Samples were measured at room temperature, before heating at a rate of 5 °C/min to 60 °C. This temperature was maintained for 1 hour, and then cooled at the same rate back to 25 °C. Once cooled measurements were continued for 24 hours.

pH Measurements. A calibrated FC2020 Hanna pH probe was used to measure the pH of all solutions. The accuracy of the measurements stated by the supplier is ± 0.1. The probe was calibrated with pH 4, 7 and 10 buffers. Measurements were carried out at room temperature (normally between 22 and 25 °C).

POM. Optical microscope images were collected using a Nikon Eclipse LV100 microscope under cross-polarised light at 5x magnification. Solutions were transferred to a microscope slide by a cut plastic Pasteur pipette or by scooping for imaging. The plastic

Pasteur pipette was cut to widen the pipette to try and reduce any shearing. Scale bars were added to images using the software ImageJ.

SAXS. To ensure aging was not an issue, samples were always ran on day 7 following the creation of the solutions. Data were collected on a SAXSLAB Ganesha 300XL instrument (Xenocs) at the University of Bristol by Annela Seddon. 70 µL of sample were transferred to a 1.5 mm borosilicate glass capillary (Capillary Tube Supplies Ltd) using a wide bore glass Pasteur pipette. Higher concentration samples (typically over 50 mg/mL) were extremely viscous and required brief centrifugation (1600 rpm, 60 s) to ensure that they were loaded into the capillary without any air bubbles. Capillaries were sealed with UV curable epoxy (Norland) for 30 minutes, and measured for 3600 s in a Q range of 0.007 - 0.25 Å^{-1}. Data were subsequently corrected for capillary and solvent (water) background and fitted using SasView software.[59]

Dripping-onto-Subtrate. Experiments were performed by Daniel McDowall (University of Glasgow) by dispensing 2NapFF-Na and 2NapFF-TBA at a concentration of 25 mg/mL from a 19 G flat-headed needle (connected to a 10 mL syringe) onto a 4 mm diameter cylindrical glass substrate. The fluid was dispensed using an Alaris Carefusion syringe pump at a flow rate of 0.2 mL/hour with the dispensing stopped immediately prior to droplet contact. The thinning process was recorded on an iPhone 8 with a clip-on macrolense using either the Slo-Mo (240 frames per second) or video (30 frames per second) settings. Video recordings were converted from .mov files on the iPhone by default to individual frame-by-frame .tiff files. The conversion process require different software for each step as follows:

1. VLC media player (version 3.0.12)[60] converts .mov to .mp4
2. FFmpeg (2021-04-04 build)[61] converts .mp4 to .avi
3. ImageJ (version 1.52n)[62] converts .avi to .tiff

The .tiff files showing the thinning process were analysed in MatLab (version R2021a)[63] using a script written by Henry Ng (University of Liverpool) to extract the evolution of filament diameter with time.

Heat-cool Methods – Heat-cool vial Inversion Tests. 2 mL of each concentration of 2NapFF-Na and 2NapFF-TBA were pipetted into 14 mL glass vials and then placed into

an oven set to 60 °C for 1 hour. After an hour, solutions were allowed to cool undisturbed on the bench at room temperature over two hours. These were then inverted and monitored for instability every day for a 14 day period.

Heat-cool Methods – Copper Wire Heating. A copper wire (which had been placed in concentrated acid to remove its casing and then washed and dried) was attached to a microscope slide using super glue. The wire was bent and attached to the slide such that solution could fill around and underneath it. Solution was poured/scooped onto the slide and placed under the microscope. The end of the copper wire not attached to the slide was heated with a Bosch heat gun on maximum setting for 30 minutes. Control samples were also prepared in the same way, but without the wire attached to the slide being heated. Images were taken under cross-polarised light during this time to monitor changes.

NMR. 1 mL of each solution was pipetted into a 5 mm NMR tube. Using a 400 MHz Bruker Spectrometer, ^{2}H and ^{23}Na NMR spectra (if appropriate) were collected as described previously,[26, 64] and analysed and phases adjusted using TopSpin 4.0.7. Samples were heated to 60 °C inside the spectrometer and cooled back to 25 °C also in the spectrometer.

Noodles. Gel noodles were formed by Olivia Marshall and Daniel McDowall (both University of Glasgow) by injecting 10 µL of 2NapFF-Na or 2NapFF-TBA solution into 2 mL of trigger medium (50 mM $CaCl_2$ adjusted to pH 10.5 with the corresponding hydroxide) in 3.5 mL glass vials. A 2-20 µL pipette was used to perform a static injection as has been detailed in previously published work.[65]

Threads and Webs. Using a 2-20 µL pipette tip attached to a 1 mL syringe, where the join between the two was sealed with Parafilm, solutions of 2NapFF-Na and 2NapFF-TBA at concentrations of 75 mg/mL 2NapFF were attempted to be drawn and strung across surfaces to create threads and web patterns. A small amount of solution was dispensed over a gap of various sizes by anchoring the solution to the surface and then pulling vertically whilst slowly dispensing the fluid, resulting in a liquid thread being formed. Threads could be gelled by the vapour of 12 M HCl, or they could be dried resulting in dried out threads by leaving overnight undisturbed. By clamping the syringe and allowing solution to flow with gravity, vertical strings could also be formed.

3.5. References

1. S. Fleming and R. V. Ulijn, *Chem. Soc. Rev.*, 2014, **43**, 8150-8177.
2. X. Du, J. Zhou, J. Shi and B. Xu, *Chem. Rev.*, 2015, **115**, 13165-13307.
3. A. Lampel, *Chem*, 2020, **6**, 1222-1236.
4. C. Tomasini and N. Castellucci, *Chem. Soc. Rev.*, 2013, **42**, 156-172.
5. V. Jayawarna, M. Ali, T. A. Jowitt, A. F. Miller, A. Saiani, J. E. Gough and R. V. Ulijn, *Adv. Mater.*, 2006, **18**, 611-614.
6. L. Chen, S. Revel, K. Morris, L. C. Serpell and D. J. Adams, *Langmuir*, 2010, **26**, 13466-13471.
7. B. Ding, Y. Li, M. Qin, Y. Ding, Y. Cao and W. Wang, *Soft Matter*, 2013, **9**, 4672-4680.
8. D. J. Adams, M. F. Butler, W. J. Frith, M. Kirkland, L. Mullen and P. Sanderson, *Soft Matter*, 2009, **5**, 1856-1862.
9. A. Z. Cardoso, L. L. E. Mears, B. N. Cattoz, P. C. Griffiths, R. Schweins and D. J. Adams, *Soft Matter*, 2016, **12**, 3612-3621.
10. K. McAulay, H. Wang, A. M. Fuentes-Caparrós, L. Thomson, N. Khunti, N. Cowieson, H. Cui, A. Seddon and D. J. Adams, *Langmuir*, 2020, **36**, 8626-8631.
11. A. M. Fuentes-Caparrós, K. McAulay, S. E. Rogers, R. M. Dalgliesh and D. J. Adams, *Molecules*, 2019, **24**, 3855.
12. M. Holmes and J. Charvolin, *J. Phys. Chem.*, 1984, **88**, 810-818.
13. J. N. Israelachvili, in *Intermolecular and Surface Forces*, Elsevier, San Diego, 3rd edn., 2011, ch. 20, pp. 535-576.
14. G. J. T. Tiddy, *Phys. Rep.*, 1980, **57**, 1-46.
15. F. Rosevear, *J. Soc. Cosmetic Chemists*, 1968, **19**, 581-594.
16. D. Andrienko, *J. Mol. Liq.*, 2018, **267**, 520-541.
17. D. K. Yang and S. T. Wu, *Fundamentals of Liquid Crystal Devices*, Wiley, New York, 2nd edn., 2014.
18. D.-H. Kim, A. Jahn, S.-J. Cho, J. S. Kim, M.-H. Ki and D.-D. Kim, *J. Pharm. Investig.*, 2015, **45**, 1-11.
19. R. Negrini and R. Mezzenga, *Langmuir*, 2011, **27**, 5296-5303.
20. A. A. Vedenov and E. B. Levchenko, *Sov. Phys. Usp.*, 1983, **26**, 747-774.
21. P. Oswald and P. Pieranski, *Smectic and Columnar Liquid Crystals: Concepts and Physical Properties Illustrated by Experiments*, CRC Press, 2005.
22. C. Tschierske, *Fluorinated Liquid Crystals: Design of Soft Nanostructures and Increased Complexity of Self-Assembly by Perfluorinated Segments*, Springer Berlin Heidelberg, Berlin, Heidelberg, 2012.
23. J. W. Goodby, in *Handbook of Visual Display Technology*, eds. J. Chen, W. Cranton and M. Fihn, Springer International Publishing, Switzerland, 2016, pp. 1897-1924.
24. H. Li, L. Dang, S. Yang, J. Li and H. Wei, *Colloids Surf., A*, 2016, **495**, 221-228.
25. S. R. Restaino and S. W. Teare, in *Introduction to Liquid Crystals for Optical Design and Engineering*, SPIE Press, Washington, 2015, vol. TT100, ch. 3.
26. K. McAulay, P. A. Ucha, H. Wang, A. M. Fuentes-Caparrós, L. Thomson, O. Maklad, N. Khunti, N. Cowieson, M. Wallace, H. Cui, R. J. Poole, A. Seddon and D. J. Adams, *Chem. Comm.*, 2020, **56**, 4094-4097.
27. S. V. G. Menon, P. S. Goyal, B. A. Dasannacharya, S. K. Paranjpe, R. V. Mehta and R. V. Upadhyay, *Physica B: Condens.*, 1995, **213-214**, 604-606.
28. J. M. Buffa, U. Casado, V. Mucci and M. I. Aranguren, *Cellulose*, 2019, **26**, 2317-2332.

29. R. Abdel-Rahem and H. Hoffmann, *Rheol. Acta*, 2006, **45**, 781-792.
30. H. A. Barnes, J. F. Hutton and K. Walters, *An Introduction to Rheology*, Elsevier, 1989.
31. F. J. Galindo-Rosales, F. J. Rubio-Hernández and J. F. Velázquez-Navarro, *Rheol. Acta*, 2009, **48**, 699-708.
32. H. Chen, W. Liu, M. Hong, E. Zhang, X. Dai, Q. Chen, W. Yang, Y. Xue, X. Qiu and X. Ji, *RSC Adv.*, 2019, **9**, 27455-27463.
33. Y. H. Shim, K. E. Lee, T. J. Shin, S. O. Kim and S. Y. Kim, *Mater. Horiz.*, 2017, **4**, 1157-1164.
34. Z. Xu and C. Gao, *ACS Nano*, 2011, **5**, 2908-2915.
35. P. Davidson, C. Penisson, D. Constantin and J.-C. P. Gabriel, *PNAS*, 2018, **115**, 6662-6667.
36. S. Dieterich, T. Sottmann and F. Giesselmann, *Langmuir*, 2019, **35**, 16793-16802.
37. E. R. Draper, B. Dietrich, K. McAulay, C. Brasnett, H. Abdizadeh, I. Patmanidis, S. J. Marrink, H. Su, H. Cui, R. Schweins, A. Seddon and D. J. Adams, *Matter*, 2020, **2**, 764-778.
38. D. McDowall, D. J. Adams and A. M. Seddon, *Soft Matter*, 2022, **18**, 1577-1590.
39. J. K. Riley, J. J. Richards, N. J. Wagner and P. D. Butler, *Soft Matter*, 2018, **14**, 5344-5355.
40. C. A. Dreiss, *Soft Matter*, 2007, **3**, 956-970.
41. M. A. Calabrese, S. A. Rogers, R. P. Murphy and N. J. Wagner, *J. Rheol.*, 2015, **59**, 1299-1328.
42. H. Schnablegger and Y. Singh, *The SAXS Guide*, Anton Paar GmbH, 4th Edition edn., 2017.
43. N. R. Agrawal, X. Yue, Y. Feng and S. R. Raghavan, *Langmuir*, 2019, **35**, 12782-12791.
44. E. R. Draper, H. Su, C. Brasnett, R. J. Poole, S. Rogers, H. Cui, A. Seddon and D. J. Adams, *Angew. Chemie Int. Ed.*, 2017, **56**, 10467-10470.
45. K. Almdal, J. Dyre, S. Hvidt and O. Kramer, *Polymer Gels and Networks*, 1993, **1**, 5-17.
46. R. G. Weiss, *J. Am. Chem. Soc.*, 2014, **136**, 7519-7530.
47. J. Dinic, L. N. Jimenez and V. Sharma, *Lab on a Chip*, 2017, **17**, 460-473.
48. J. E. Betancourt and J. M. Rivera, *J. Am. Chem. Soc.*, 2009, **131**, 16666-16668.
49. Ç. Batıgöç and H. Akbaş, *Fluid Phase Equilibria*, 2011, **303**, 91-95.
50. M. Miyake and Y. Yamashita, in *Cosmetic Science and Technology*, eds. K. Sakamoto, R. Y. Lochhead, H. I. Maibach and Y. Yamashita, Elsevier, Amsterdam, 2017, pp. 389-414.
51. M. Wallace, A. Z. Cardoso, W. J. Frith, J. A. Iggo and D. J. Adams, *Eur. J. Chem.*, 2014, **20**, 16484-16487.
52. M. Wallace, J. A. Iggo and D. J. Adams, *Soft Matter*, 2015, **11**, 7739-7747.
53. S. Zhang, M. A. Greenfield, A. Mata, L. C. Palmer, R. Bitton, J. R. Mantei, C. Aparicio, M. O. de la Cruz and S. I. Stupp, *Nat. Mater.*, 2010, **9**, 594-601.
54. T. Christoff-Tempesta, Y. Cho, D.-Y. Kim, M. Geri, G. Lamour, A. J. Lew, X. Zuo, W. R. Lindemann and J. H. Ortony, *Nat. Nanotechnol.*, 2021, **16**, 447-454.
55. J. A. Kluge, O. Rabotyagova, G. G. Leisk and D. L. Kaplan, *Trends in Biotechnology*, 2008, **26**, 244-251.
56. K. McAulay, B. Dietrich, H. Su, M. T. Scott, S. Rogers, Y. K. Al-Hilaly, H. Cui, L. C. Serpell, Annela M. Seddon, E. R. Draper and D. J. Adams, *Chem. Sci.*, 2019, **10**, 7801-7806.

57. E. R. Draper, M. Wallace, R. Schweins, R. J. Poole and D. J. Adams, *Langmuir*, 2017, **33**, 2387-2395.
58. C. Colquhoun, E. R. Draper, R. Schweins, M. Marcello, D. Vadukul, L. C. Serpell and D. J. Adams, *Soft Matter*, 2017, **13**, 1914-1919.
59. SasView, (http://www.sasview.org/ (accessed 28th November 2019).
60. VideoLAN, https://www.videolan.org/vlc/, (accessed 25th May 2022).
61. FFmpeg, https://ffmpeg.org/, (accessed 25th May 2022).
62. ImageJ, https://imagej.nih.gov/ij/, (accessed 25th May 2022).
63. MATLAB, https://uk.mathworks.com/products/matlab.html, (accessed 25th May 2022).
64. D. Giuri, L. J. Marshall, B. Dietrich, D. McDowall, L. Thomson, J. Y. Newton, C. Wilson, R. Schweins and D. J. Adams, *Chem. Sci.*, 2021, **12**, 9720-9725.
65. D. McDowall, M. Walker, M. Vassalli, M. Cantini, N. Khunti, C. J. C. Edwards-Gayle, N. Cowieson and D. J. Adams, *Chem. Comm.*, 2021, **57**, 8782-8785.

Chapter 4. Creating Transient Gradients in Supramolecular Hydrogels

This Chapter is adapted from the following publication:

"Creating Transient Gradients in Supramolecular Hydrogels"

LT was responsible for methodology, collecting all rheological and ultraviolet-visible (UV-vis) spectroscopy data, synthesis of the gelator molecule used, and preparation of samples for SANS (small-angle neutron scattering) experiments. ERD and DJA carried out the SANS experiments, RS processed the SANS data. LT fitted the SANS data. DJA conceptualised and supervised the project. LT and DJA wrote the initial draft of the manuscript, to which all authors contributed for the final publication.

4.1. Introduction

Supramolecular hydrogels are formed by the trapping of water within a gel network.[1] The network consists of LMWG molecules which self-assemble when a trigger is applied. These networks are held together by physical cross-links created by weak, non-covalent interactions, including hydrogen bonding, the hydrophobic effect and π-π stacking. This leads to reversible gels.[2-4] As the network is formed via self-assembly, it can be hard to control how the structures form and cross-link. Hence, it can be difficult to spatially control the gel structures, which requires that we can manipulate the assembly over the various length scales associated with a network.[5, 6]

Preparing gels with a gradient in properties has potential uses, with controlled heterogeneity leading to many possible applications, such as tissue engineering. It can be advantageous to form gels with a gradient of stiffness, mimicking the various stiffness of tissue present in the body.[7-11] Different organs and tissues vary in stiffness, as do cancerous tissues which are stiffer than healthy tissue.[10, 11] Varying stiffness also affects cell adhesion and morphology.[10]

Similarly, the existence of a gradient stiffness gel could prove useful in the controlled diffusion, or immobilisation, of a component through a gel. The immobilisation of small biomolecules in gels could be used in sensing or biocatalytic flow reactors.[12, 13] In biocatalysis, enzymes can be single use as they are difficult to recover, and hence not cost-effective. The immobilisation of the enzyme in an organic matrix occurs due to hydrophobic or ionic interactions or via the formation of covalent bonds, and hence allows for the enzyme to be recovered more easily, which improves commercial viability.[13] Our group has previously examined network mesh size and its ability to control diffusion in hydrogels.[14] Smith and co-workers have examined diffusion across organogels. In a multi-component system, it was reported that diffusion was possible across a gel-gel interface.[15] In later work, the Smith group showed spatial and temporal control of their gels by the diffusion from components inserted into cut holes within gels which allowed for well-defined patterning within the gels.[16] Fast acidification resulted in sharp shapes, whereas slow acidification still gave the desired patterns, but were less defined overall.

Numerous methods have already been developed to prepare gels with gradients of properties, including gradients of stiffness[9, 10] and of concentration.[17, 18] Light is commonly used to control gelation and form gradients.[19, 20] For example, Murata et al. used a cholesterol-based gelator, which could cycle between the cis- and trans- isomers using light. Since the trans-form resulted in gels while the cis-isomer did not, cycling between the isomers allowed sol-to-gel-to-sol transitions. By introducing a template and selectively gelling only part of a system, reversible patterns were created, showing spatially controlled gel formation.[19] Photomasks and light can also be used to form gradual gradients.[10] By slowly moving the photomask whilst irradiating, different gradients in stiffness of an acrylamide/bis-acrylamide gel could be achieved. The gradient steepness was affected by the speed of the movement of the photomask. Introducing photomasks into multi-component hydrogel systems can create photopattened gels.[21, 22] This shows that spatial control of hydrogel structures in multi-component systems is possible. Here, the spatial control of these multi-gelator systems relies on different pK_a values of each LMWG in the system.[21-23]

Although gradients have been formed within gels, there is generally little discussion as to the timescale over which these gradients persist. There are a few exceptions. When forming gels with a concentration gradient, Karpiak et al. noted a time dependence; the initial gradient in concentration created within the gel became more continuous and gradual with time, instead of having disjointed layers. This was attributed to diffusion between the layers over time.[24] A similar effect was shown when proton diffusion was used to form gels using an acid-triggered gel.[25] By adding drops of acid to one side of a cell containing the gelator solution at high pH and a pH indicator, it was possible to see the change in pH as the acid diffused through the cell.

In this work, we aim to control our LMWG structures and gelation by selectively gelling a single LMWG. To show we can control self-assembly, we aim to form gels with gradient stiffness within a single gel. The gradients we wish to make are both gradual and steep to fully show the extent we can control the gelation process. We aim to use an acid trigger and diffusion to do so, and use rheology to examine the bulk properties of the heterogeneous samples.

4.2. Results and Discussion

In this Chapter, we again use the LMWG 2NapFF which has been used in both Chapter 2 and Chapter 3 already in this Thesis. 2NapFF was chosen due to its formation of worm-like micelles at high pH,[26] which we hypothesised would limit diffusion. This would be required in this work to gain spatial control of gelation, and hence create gradient stiffness gels.

From the high pH solutions of 2NapFF, homogeneous hydrogels are formed at low pH by the hydrolysis of glucono-δ-lactone (GdL) to gluconic acid. GdL forms homogeneous gels due to a faster rate of GdL mixing compared to the rate of GdL hydrolysis, resulting in a uniform pH change to give homogeneous gels.[27-30] The gels are formed by the re-protonation of the LMWG as the pH is decreased, resulting in a network of fibres.[30] Similarly, photoacid generators (PAGs) can also be used to lower pH. Whilst PAGs have been used to trigger self-assembly in other systems,[22, 31-33] the use of diphenyliodonium nitrate (DPIN) as a PAG to trigger gelation of solutions of 2NapFF at high pH was unsuccessful.[33] Here, we show that the PAG 2-(4-methoxystyryl)-4,6-bis(trichloromethyl)-1,3,5-triazine (MBTT, Figure 4.1)[34, 35] can be used to form gels from 2NapFF with controllable transient gradients in stiffness. MBTT produces hydrochloric acid by carbon-chlorine bond cleavage after excitation by UV light.[34] This acid can then be used for gelation as described previously.
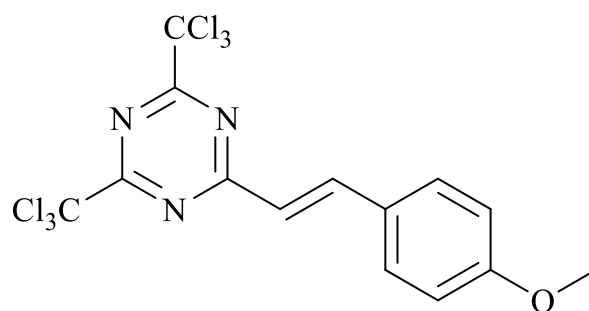
Figure 4.1. Structure of the PAG used in this Chapter, MBTT.

Initially, we focus on the formation of homogeneous gels formed by the hydrolysis of GdL. GdL concentrations of 4, 8 and 16 mg/mL were used to create 2NapFF gels which were analysed using bulk rheology and cavitation rheology. Cavitation rheology is a

localised technique which can probe homogeneous and heterogeneous material at localised points in their native environments.[36-38] Briefly, an air bubble grows within the gel and the mechanical properties can be probed by the pressure that can be withstood before the bubble bursts, known as the critical pressure (P_C) (Figure 4.2). Cavitation rheology allows us to compare the rheological data at localised points within the same gel sample and hence determine gel homogeneity.[36, 38]
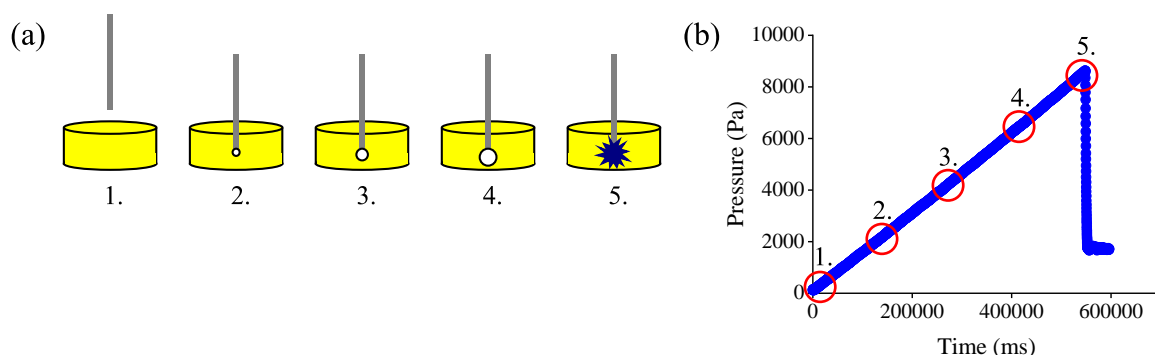
Figure 4.2. (a) Summary of the technique of cavitation rheology: 1. a needle is inserted into the sample at the required depth; 2. air is pushed into the sample causing the formation of a bubble; 3. and 4. air is continually pushed through the sample, resulting in the growth of the bubble; 5. at a critical pressure (P_C) the bubble bursts, indicating the stiffness of the material at the localised point. (b) Exemplar raw data obtained from cavitation rheology, relating to the key stages 1-5 as described in (a).

Here, we use cavitation rheology to probe the gels at different depths. To do this, we use three independent samples of 5 mg/mL 2NapFF and GdL triggered gels for each GdL concentration, and measure the critical pressure of each sample at four different depths. As expected from our previous work using cavitation rheology,[38] the critical pressure increases linearly with depth for these types of gels. Increasing the amount of GdL used to prepare the 2NapFF gels results in a decrease in the final pH (Table 4.1) and an increase in the critical pressure values at each needle depth (Figure 4.3). For gels prepared with 16 mg/mL GdL, no data could be collected at 2.5 mm as the critical pressure values were greater than our cavitation rheometer could measure (above 30,000 Pa; limited by the current pressure sensor in place).

Table 4.1. Final pH of gels formed using different concentrations of GdL. Each pH is the average value taken from three samples with standard deviation quoted in brackets.

GdL Concentration (mg/mL)	Final pH
4	3.9 (0.05)
8	3.5 (0.04)
16	3.1 (0.02)
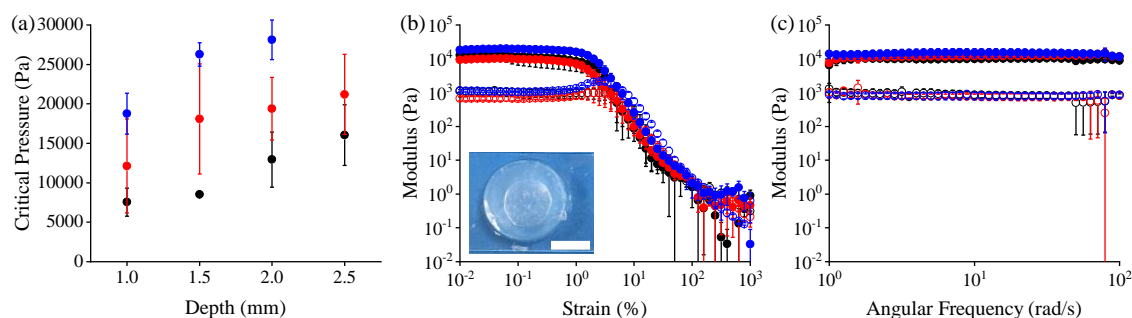
Figure 4.3. Rheology of 5 mg/mL 2NapFF gels triggered using GdL. (a) Cavitation rheology; (b) bulk rheology (strain sweep); (c) bulk rheology (frequency sweep) of 2NapFF gels formed using various GdL concentrations: 4 mg/mL GdL (black), 8 mg/mL GdL (red), and 16 mg/mL GdL (blue). For bulk rheology measurements, G′ is represented by filled circles and G″ by empty circles. Inset - GdL triggered 2NapFF gel. An air bubble can be seen underneath the gel which was formed when moving the gel onto a microscope slide for imaging. Scale bar represents 1 cm.

The bulk rheology data for gels formed using GdL are very similar regardless of the GdL concentration used (Figure 4.3), with no considerable differences in final G′ and G″ values, or strength. This is consistent with previously reported results.[39] Varying the concentration of GdL increases the rate of gelation, with higher concentrations of GdL forming gels quicker.[39, 40] There are small changes in the strain at which the gels break, with the gels becoming slightly stronger as the concentration of GdL increases. The constant values for the bulk rheology but increasing values for the cavitation rheology can be explained by the differences in length scale that are probed by the two rheological methods. Cavitation rheology measures more local properties compared to bulk rheology and so these data imply that there are differences at this length scale which can be detected by cavitation rheology, but not by bulk rheology. The critical pressure values can be linked to cavitation

modulus which relates to modulus collected by bulk rheology as described elsewhere.[36-38] We focus here on the differences in trend instead of absolute values, as we use these homogenous GdL triggered gels as controls to compare to gels triggered by a PAG.

Considering the PAG as a hydrophobic additive, it might be expected that adding it to a solution of hydrophobic 2NapFF at high pH may cause interactions between the two components or affect the self-assembly. Using small-angle neutron scattering, SANS (Figure 4.4 and Table 4.2), we show that at high pH, the addition of MBTT induces a structural change compared to 2NapFF alone. Although both 2NapFF only and 2NapFF with MBTT at high pH both form hollow tubes, the addition of MBTT causes a decrease in radius size compared to that when no MBTT is present.[30] This shows that the presence of the hydrophobic additive affects the LMWG structures at high pH, presumably by being incorporated into the micellar structures at high pH. However, there is no difference in structure when 2NapFF with MBTT is gelled either by using UV irradiation or GdL to lower the pH. In both cases, the data could be fitted to an elliptical cylinder combined with a power law to take into account the scattering at low Q. It is possible that the decomposition products from irradiation of the photoacid could conceptually react with the 2NapFF.[34, 35] However, the similarity in gel state structures when gelled using GdL or by irradiating MBTT implies that this does not happen. Samples for SANS were prepared by Lisa Thomson (University of Glasgow), SANS experiments were performed by Emily Draper and Dave Adams (both University of Glasgow) alongside Ralf Schweins (Institut Laue Langevin), data processing was performed by Ralf Schweins (Institut Laue Langevin) and data fitted by Lisa Thomson (University of Glasgow).
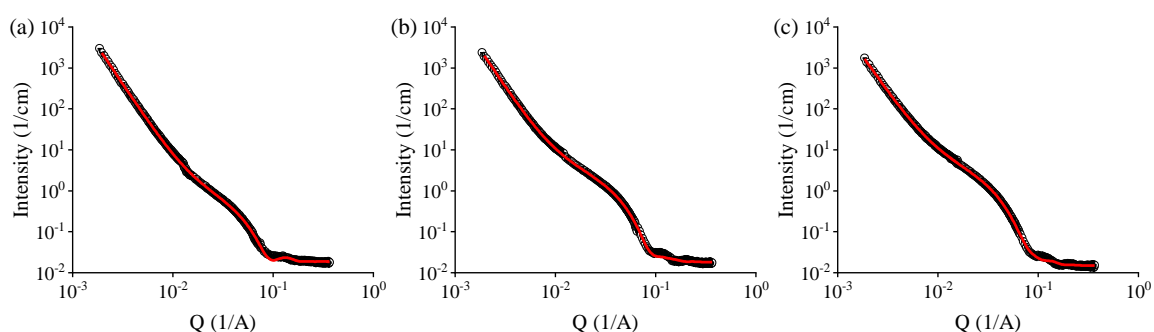
Figure 4.4. SANS for 2NapFF with MBTT. (a) 2NapFF and MBTT solution at high pH; (b) 2NapFF and MBTT gelled using 4 hours of UV irradiation; (c) 2NapFF and MBTT, gelled using GdL. Black circles represent the SANS data and red lines show the best data fits as discussed in the text with parameters shown in Table 4.2.

Table 4.2. SANS best fit values for 2NapFF with MBTT where (a)-(c) correspond to Figure 4.4. Data for 2NapFF solution and gel only are taken from references 30 and 41 respectively.

	2NapFF Solution Only[30]	(a) 2NapFF and MBTT Solution	2NapFF Gel Only[41]	(b) 2NapFF and MBTT gelled by UV exposure	(c) 2NapFF and MBTT gelled by GdL
Model	Hollow Cylinder and Power Law	Hollow Cylinder and Power Law	Flexible Elliptical Cylinder	Elliptical Cylinder and Power Law	Elliptical Cylinder and Power Law
Background (cm^{-1})	0.047 ± 0.000	$0.018639 \pm 3.7342 \times 10^{-5}$	$0.0082 \pm 6.99 \times 10^{-5}$	$0.01817 \pm 4.2416 \times 10^{-5}$	$0.014927 \pm 3.5777 \times 10^{-5}$
Scale (Power Law)	$2.67 \times 10^{-4} \pm 1.27 \times 10^{-5}$	$2.8500 \times 10^{-7} \pm 2.3469^{-10}$	NA	$2.4022 \times 10^{-7} \pm 3.8461 \times 10^{-9}$	$5.0015 \times 10^{-7} \pm 9.2794 \times 10^{-9}$
Power	1.63 ± 0.01	3.7 ± 0.0001	NA	3.7 ± 0.0027	3.5 ± 0.0032
Scale (Cylinder)	$5.34 \times 10^{-3} \pm 1.94 \times 10^{-5}$	$0.0012171 \pm 6.2454 \times 10^{-6}$	$1.40 \times 10^{-3} \pm 5.96 \times 10^{-5}$	$0.002747 \pm 3.7146 \times 10^{-6}$	$0.0024337 \pm 1.8816 \times 10^{-6}$
Radius (Å)	16.5 ± 0.05	6.3 ± 0.2	29.8 ± 0.3	NA	NA
Thickness (Å)	21.3 ± 0.08	31.2 ± 0.3	NA	NA	NA
Minor Radius (Å)	NA	NA	NA	33.1 ± 0.02	35.5 ± 0.01
Axis Ratio (Å)	NA	NA	2.64 ± 0.2	1.5 ± 0.01	1.7 ± 0.01
Kuhn Length (Å)	NA	NA	55 ± 4	NA	NA
Length (Å)	342 ± 2.5	4720 ± 87	2618 ± 124	7524 ± 45	4300 ± 63
χ^2	8.98	9.63	9.35	8.37	5.80

We optimised our 2NapFF and MBTT system (Figure 4.5, full final optimised experimental details can also be found in Section 4.4: Experimental) such that 1.5 molar equivalents of MBTT were used relative to 2NapFF. We initially begin by showing a peak present in the UV-vis data for MBTT in acetonitrile at 376 nm. This is consistent with the quoted λ_{max} value of 379 nm from the supplier in this solvent.[42] The addition of MBTT to a solution of 2NapFF shows absorbance still in this region which is not present in 2NapFF solutions alone (Figure 4.5b). It is unsurprising that the absorbance changes when added to a different solvent with factors including solubility and pH capable of altering the absorbance. Irradiating a solution of the 2NapFF containing MBTT at 365 nm resulted in a change in pH, triggering gelation. Cutting into the gels showed only a colour change at the surface of the gel suggesting the penetration of the UV light is at the surface only. Irradiation for 4 hours or longer resulted in invertible samples. The gels were formed in moulds (created using a syringe of diameter of 2 cm and height of 1 cm), with at least 6 hours of irradiation and 1.5 molar equivalents of MBTT required to form gels of sufficient robustness to be able to remove it from the mould. Even at 6 hours, removal from the mould caused some damage (Figure 4.5d, inset). The addition of the PAG to the LMWG results in slight changes in the apparent pK_a of the 2NapFF. A balance was reached with respect to the distance between the LED and the samples. This distance was such that there was little effect on the temperature of the gels, Figure 4.5e, but also close enough that samples could be irradiated and analysed on the same day. This equated to an LED power of 20 ± 1 mW, which was measured using an intensity sensor.
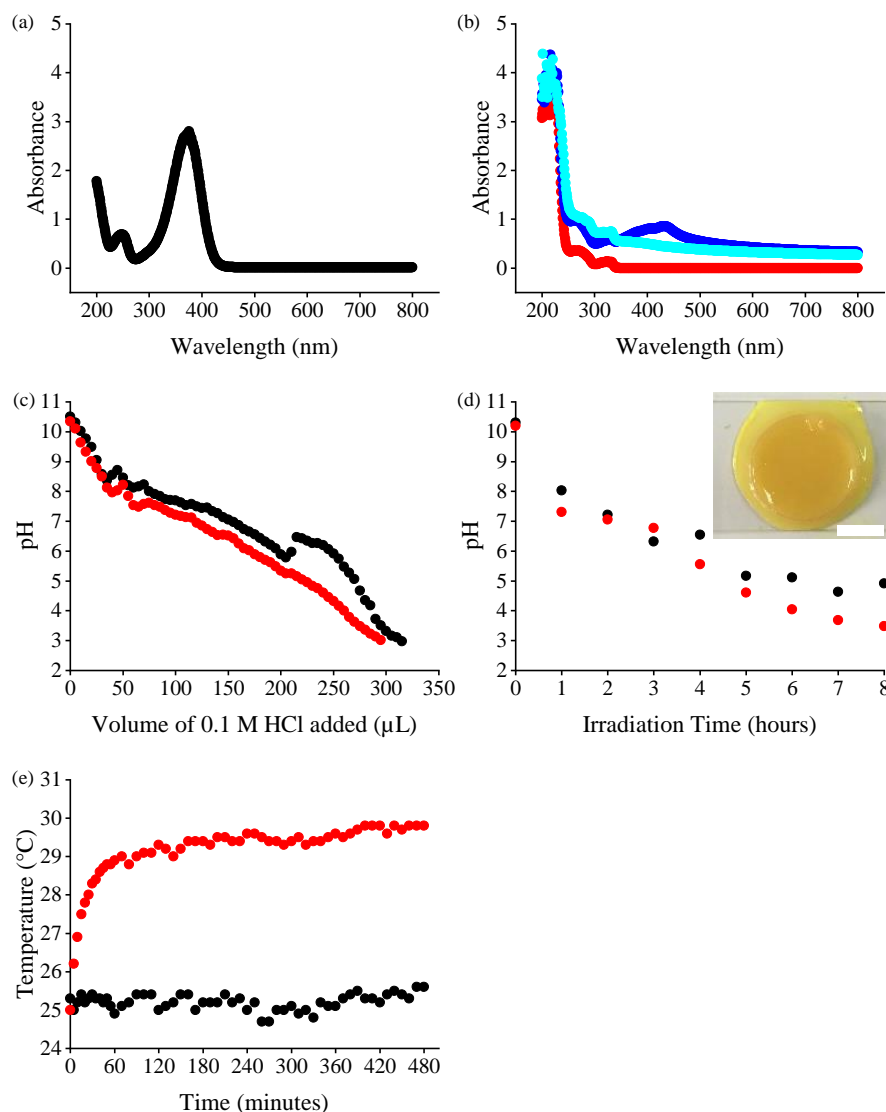
Figure 4.5. Optimisation of our 2NapFF and MBTT system. (a) UV-Vis spectra of 13.5 mg MBTT in 2 mL of acetonitrile; (b) 13.5 mg MBTT in 2 mL of 5 mg/mL 2NapFF solution at high pH before irradiation (blue) and after 20 minutes of irradiation with a 365 nm LED (light blue). Red data shows 5 mg/mL 2NapFF solution only at high pH for comparison. (c) Apparent pK_a titrations for 2NapFF without MBTT (black) and with 1.5 molar equivalents MBTT (red). (d) Comparison of pH changes with irradiation time for 1.0 (black) and 1.5 (red) molar equivalents of MBTT and 5 mg/mL 2NapFF, starting at pH 10.5. Samples were irradiated with a 365 nm LED for the specified time. Inset - Picture of 1.5 molar equivalents MBTT gel removed straight away from its mould after 6 hours UV exposure. Since the gel is very weak at the bottom after this time, damage occurs when removing from the mould, hence the presence of some liquid. Scale bar represents 1 cm. (e) Temperature of a sample under 20 ± 1 mW of UV light over a continuous 8 hours period (red), compared to room temperature (black).

The weaker gels which could not be successfully removed from the mould could still be examined via cavitation rheology without removing from the mould. Gels formed after 4 hours of irradiation show a decreasing critical pressure with increasing needle depth (Figure 4.6a). This is a different trend to that obtained during cavitation rheology of the gels formed with GdL. The change in trend can be explained by the formation of a gradient within the gel. The gels formed with MBTT are done so by irradiating from above. Hence, the change in pH, and therefore gelation, will begin at the top of the gel, with the bottom of the sample receiving less irradiation and will not reach such a low pH. Similarly, for 5 hours of irradiation (Figure 4.6b), the P_C does not increase with increasing depth, again suggesting a gradient in stiffness after this irradiation time.
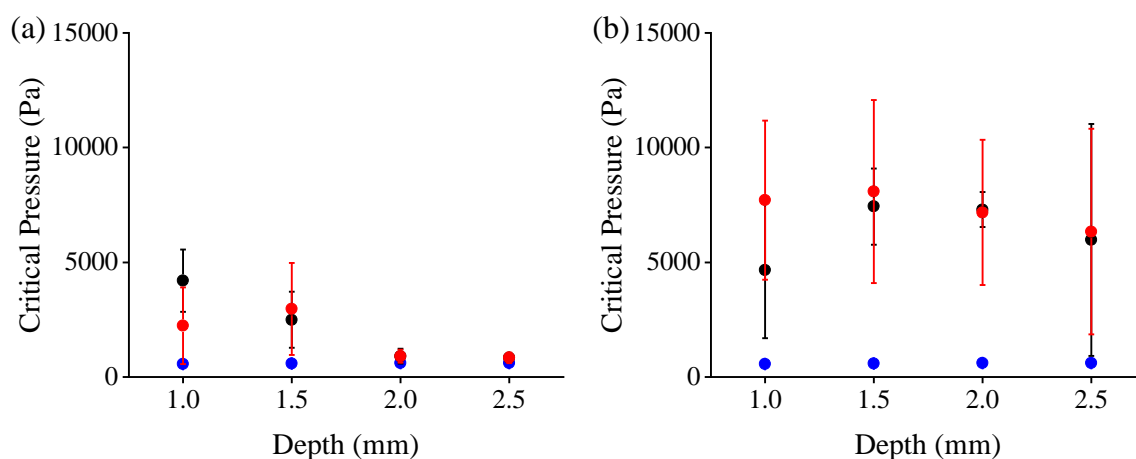
Figure 4.6. Cavitation rheology of 2NapFF gels formed using MBTT after irradiation with a 365 nm LED for (a) 4 hours and (b) 5 hours. Measurements were taken straight after UV exposure (black) and the day following UV exposure (red). For comparison, data for the MBTT and 2NapFF solution with no UV exposure are shown in blue. We explain the large error bars due to the nature of measuring a transient gradient.

At longer irradiation times, for example, 6 hours (Figure 4.7a-c), the critical pressure values measured by cavitation rheology remain relatively constant when increasing needle depth (Figure 4.7a, black data). A homogeneous gel would show an increase in the critical pressure with increasing needle depth as seen for the GdL gels (Figure 4.3). These data therefore show that there is a gradient of stiffness within the gel. These gels formed with 6 hours of irradiation are stiffer than those formed with just 4 hours. After 7 or 8 hours of irradiation, the cavitation rheology data are similar to those for the homogeneous GdL gels,

where again we see an increase in critical pressure as needle depth increases (Figure 4.7d and Figure 4.7g, black data). The critical pressures measured for the gels after 8 hours of irradiation are greater than those for the gel formed after 7 hours. For gels prepared with 8 hours UV exposure, no data could be collected at depths of 1.5 mm or greater as the critical pressure values were greater than our cavitation rheometer could measure (above 30,000 Pa).
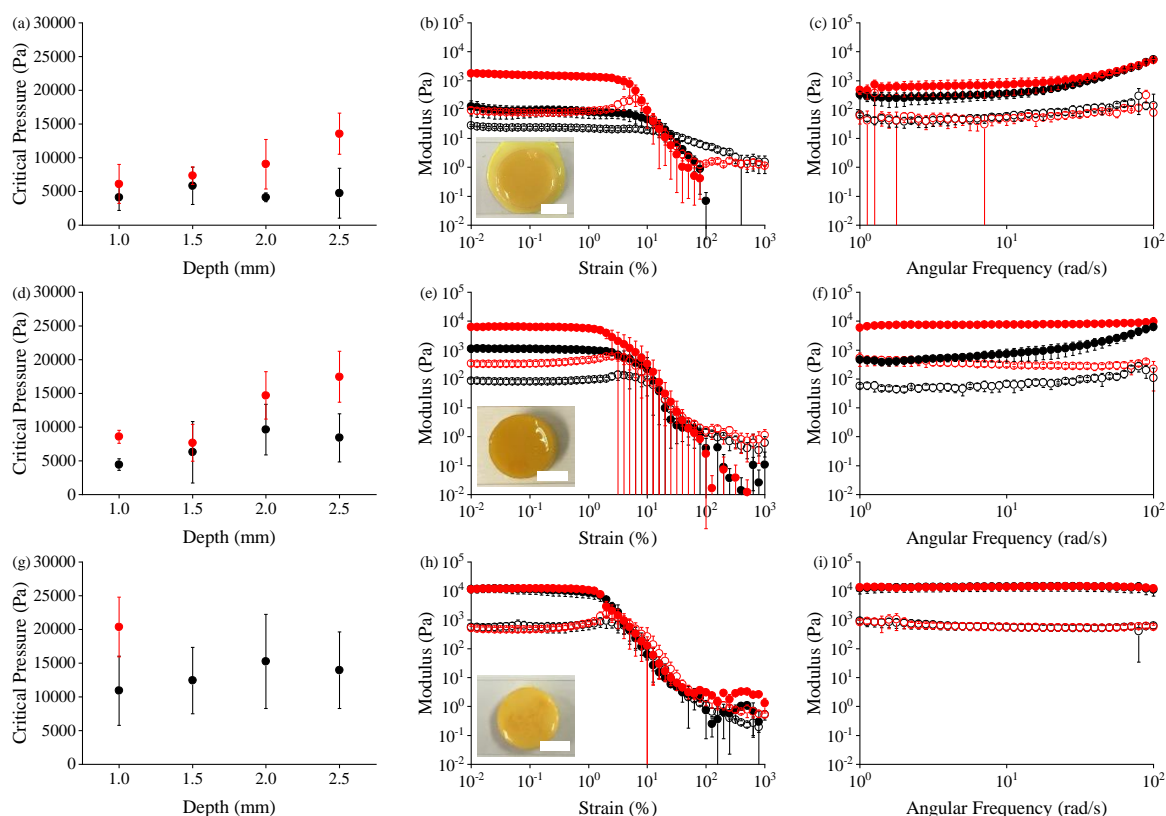
Figure 4.7. Rheology of 2NapFF gels triggered using MBTT and (a)-(c) 6 hours; (d)-(f) 7 hours; (g)-(i) 8 hours UV irradiation, where (a), (d) and (g) show cavitation rheology data; (b), (e) and (h) show bulk rheology (strain sweep) data; (c), (f) and (i) show bulk rheology (frequency sweep) data. For bulk rheology measurements, G′ is represented by filled circles and G″ by empty circles. Experiments were performed straight after UV exposure (black) and the day following UV exposure (red). Insets - MBTT triggered 2NapFF gels straight after each specific irradiation time. Scale bars represent 1 cm.

Interestingly, we observe an aging effect with these gels containing MBTT in both cavitation and bulk rheology. The data described previously are for the measurements on gels immediately after the termination of UV exposure (Figure 4.7, black data). If the gels formed after 6-8 hours of irradiation are allowed to stand overnight before being measured by cavitation rheology, the gels show a trend like that for the homogenous GdL gels, with the critical pressure increasing with depth (Figure 4.7, cavitation rheology, red data). The aging effect is also seen in the bulk rheology data (Figure 4.7, bulk rheology). Examining the bulk rheology data after 6 and 7 hours of UV irradiation, we see an increase in the bulk stiffness with time. This is not true of the 8 hours UV exposure samples, which have very similar bulk rheology data when measured straight away compared to overnight. Again, similar to the GdL only controls described previously, the bulk rheology is unable to display differences in stiffness that the cavitation rheology can. This is again explained by the differences in length scale that are being probed by the two rheological methods. Therefore, we conclude that the stiffness gradients formed by using MBTT and irradiation are only temporary, with the diffusion of protons within the gel eventually leading to a pH equilibrium overnight (Table 4.3), hence losing the initial stiffness gradient. The values in Table 4.3 are the final averaged values for samples as a whole. Measuring the pH at individual depths or localised points during irradiation was not possible due to the size of the pH probe compared to the size of samples, and because the samples were irradiated inside a closed UV-safe box for safety. Monitoring the diffusion of pH during irradiation with a colour changing indicator was also not possible due to the intense yellow colour of the samples and because samples were irradiated inside a closed UV-safe box for safety.

Table 4.3. Final pH of samples formed using 1.5 molar equivalents of PAG and varying UV exposure times. Each pH value is the average value taken from three samples with standard deviation quoted in brackets. The errors associated with samples irradiated for 6 hours is large due to the loss of liquid from the bottom of the samples. This is because although robust enough to be removed from the moulds, the lower parts of the gels, which had not received as much radiation as upper parts of the gel, were visibly weaker and more liquid-like.

Irradiation Time (hours)	Final pH of Samples Straight After UV Exposure	Final pH of Samples Left Overnight Following UV Exposure
0 (solution)	10.1 (0.1)	NA
4	6.7 (0.1)	6.3 (0.4)
5	4.8 (0.3)	4.0 (0.2)
6	5.3 (1.1)	5.0 (0.1)
7	4.4 (0.4)	3.7 (0.2)
8	4.2 (0.6)	3.7 (0.2)

Using a combination of both GdL and MBTT, it is possible to photopattern gels. We consider a photopatterned gel as a gradient gel with a steep gradient between the photopatterned sections. Previous work has described photopatterning of multicomponent systems,[21, 22] where either one, or both, components in the system gel. Here, we show photopatterning using only a single gelator and two pH triggers. To achieve this, we first use the minimum amount of GdL required to gel 2NapFF with MBTT, tuning the amount of GdL used such that a gel is formed, but allows for the gel moduli to still increase significantly when the pH is further decreased by MBTT (Figure 4.8). At this minimum GdL value, a gel network will be formed, and we expect all 2NapFF will be assembled, but there will still be a significant degree of charge on the structures. A further pH decrease will result in the gel becoming stiffer.[39] Using 2.5 mg/mL of GdL results in homogeneous gels where G′ and G″ are different by an order of magnitude. We then utilise MBTT by irradiating sections of the soft GdL triggered gel.
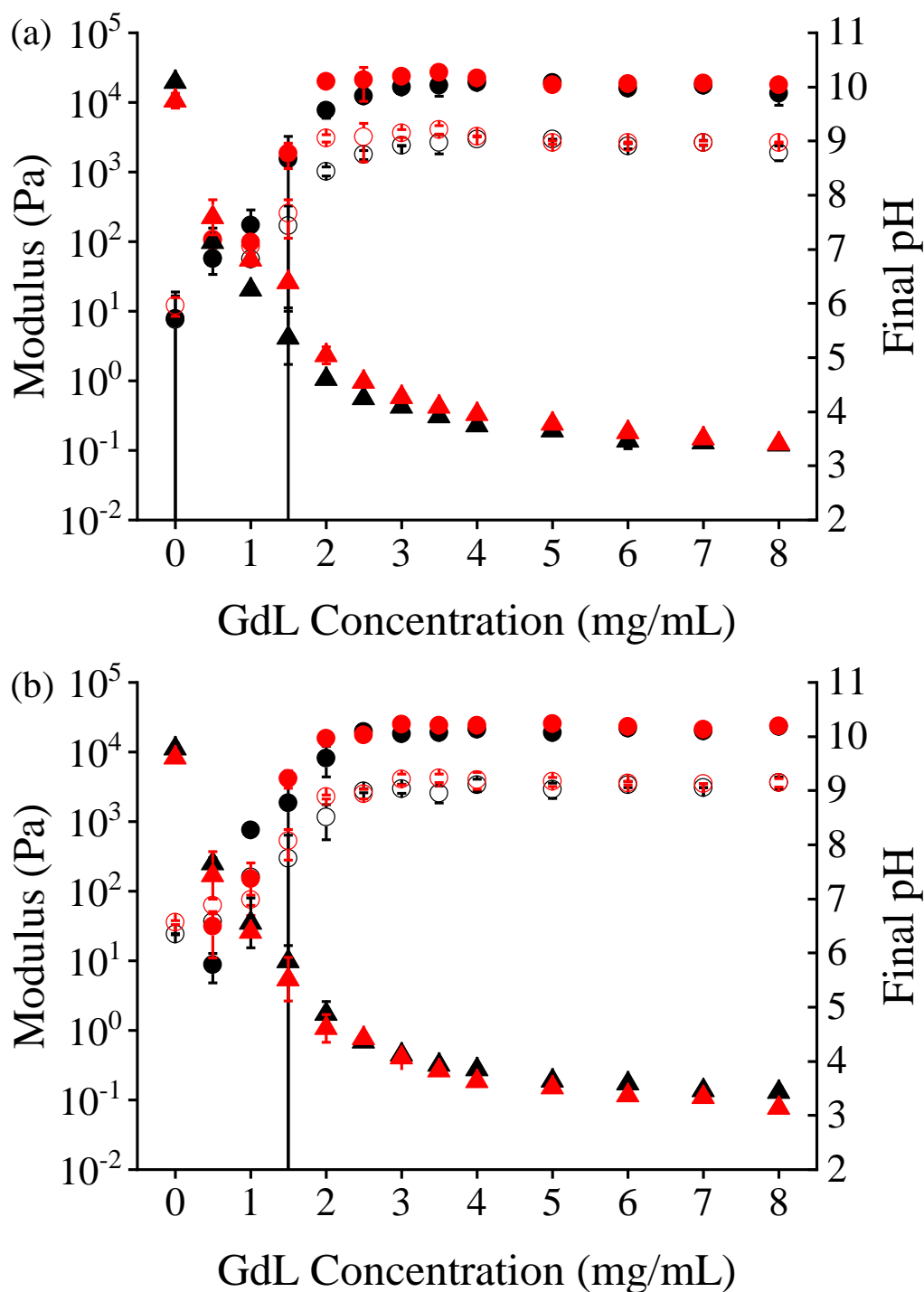
Figure 4.8. (a) Strain and (b) frequency sweeps for samples prepared using varying concentrations of GdL. Black data represents 2NapFF only and red represents 2NapFF with 1.5 molar equivalents of MBTT. Filled circles represent G' values and empty circles represent G'' values (left axis). The triangles show the final pH of the sample (right axis). Experiments were performed in duplicate, with error bars showing the standard deviation between the samples.

To create a pattern, a photomask was used to block radiation to selected regions of the soft gel formed using GdL (patterns shown in Figure 4.9). The sections not covered by the photomask were irradiated for 1 hour and became darker in colour (Figure 4.10). The patterns here are simple, but were chosen since they provide different surface areas that could then be exposed to radiation. More complex patterns have recently been shown in similar work by the Smith group, which shows a greater resolution of photopatterning can be obtained with similar systems.[16] The localised technique of cavitation rheology was used to probe sections of the sample at different points (points 1 and 2 in Figure 4.10, cavitation rheology) with needle depth remaining constant. The cavitation rheology data show the difference in critical pressure values obtained when probing a section of irradiated and non-irradiated gel. For a control gel with no UV radiation (Figure 4.10, pattern **A**), both points measured within this pattern gave very similar critical pressure values. The final pH of these control samples was found to be 4.6. For gels where a section was irradiated, patterns **B**, **C** and **D**, the sections of gel that had been irradiated gave higher critical pressure values than those covered by the mask (Figure 4.10). This shows that the further decrease in the pH leads to the gel becoming stiffer where the gel has been irradiated. As expected from the data using MBTT alone, the pH of the samples became homogeneous over time, as did the rheology, leading to similar critical pressure values at each measurement point after approximately 16 hours (Figure 4.10, cavitation rheology, red data). All patterned samples had an average pH difference of 0.3 pH units across the irradiated and non-irradiated sections and when left overnight, all samples were found to have the same pH throughout, Table 4.4. Again, similar to the GdL only controls described previously in Figure 4.3, the bulk rheology here (Figure 4.10, bulk rheology) is unable to show the differences at the localised points within the irradiated and non-irradiated sections that the cavitation rheology can. This is again explained by the differences in length scale that are being probed by the two rheological methods.

A   B   C   D
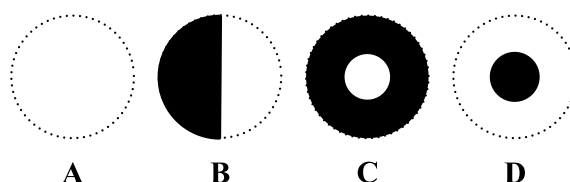
Figure 4.9. Schematic of masks used during photopatterning showing control **A** and patterns **B**, **C** and **D**. Shaded areas represent the areas where the masks were applied which blocked UV radiation to these areas.
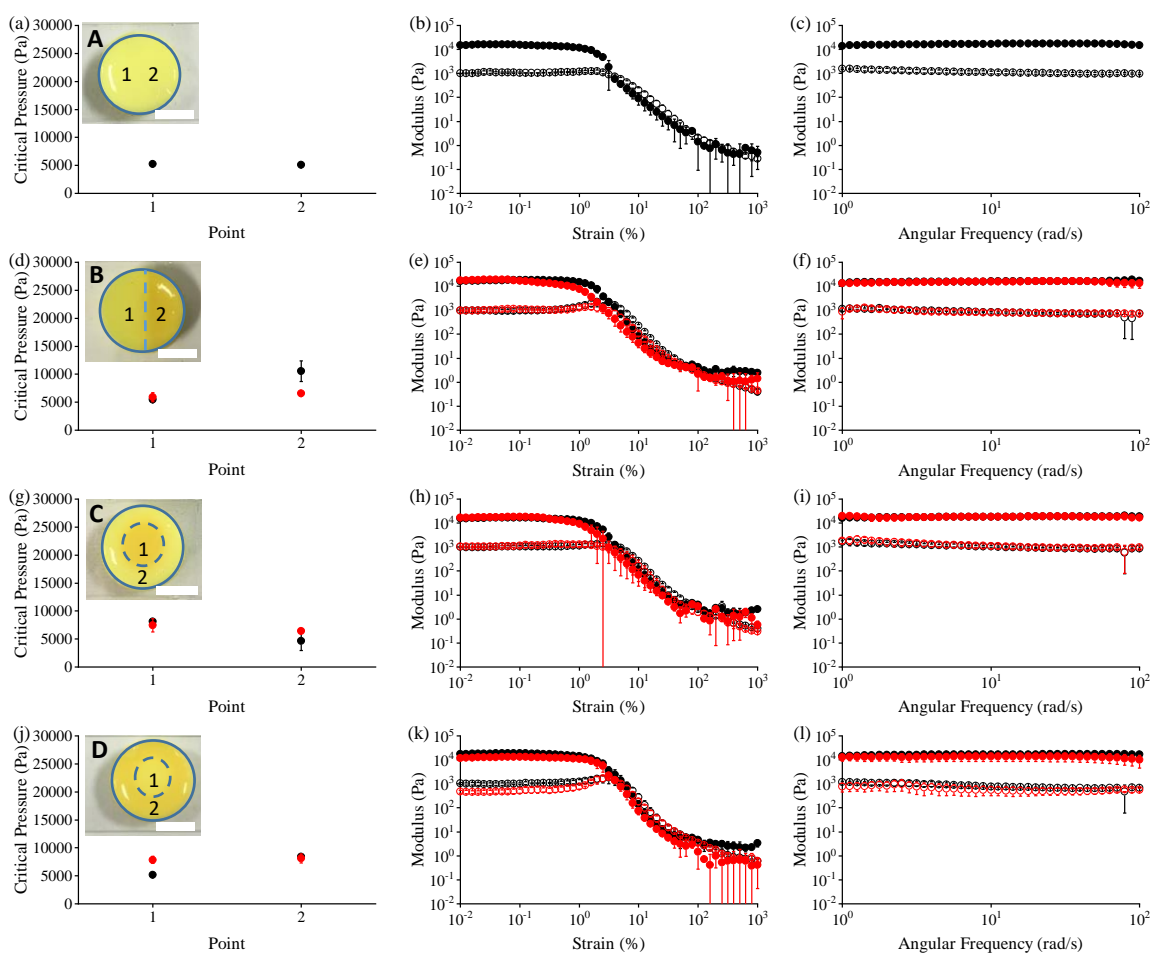
Figure 4.10. Rheology of photopatterned 2NapFF gels (control **A**; and patterns **B**, **C** and **D**), where (a), (d), (g) and (j) show cavitation rheology data; (b), (e) (h) and (k) show bulk rheology (strain sweep) data; (c), (f), (i) and (l) show bulk rheology (frequency sweep) data, with inserts for each photopattern. Scale bars represent 1 cm. Numerical guides are added to differentiate between the areas exposed to UV radiation and those which were not. Numbers indicate the position of the cavitation rheology needle for measurements to be carried out. Experiments were performed straight after UV exposure (black) and the day following UV exposure (red) For bulk rheology measurements, G′ is represented by filled circles and G″ by empty circles.

Table 4.4. Final pH of photopatterned gels formed using 2.5 mg/mL GdL and 1.5 molar equivalents of PAG, irradiated for 1 hour using a photomask. Each pH is the average taken from three samples with standard deviation quoted in brackets.

	Final pH of Samples Straight After UV Exposure		Final pH of Samples Left Overnight Following UV Exposure	
	Non-irradiated Section of Gel	Irradiated Section of Gel	Non-irradiated Section of Gel	Irradiated Section of Gel
Pattern **A**	4.6 (0.1)	NA	NA	NA
Pattern **B**	4.4 (0.0)	4.1 (0.0)	4.3 (0.0)	4.3 (0.1)
Pattern **C**	4.6 (0.2)	4.3 (0.1)	4.3 (0.1)	4.3 (0.1)
Pattern **D**	4.3 (0.1)	4.2 (0.1)	4.1 (0.1)	4.1 (0.1)

4.3. Conclusions and Future Work

In this work, we aim to control our LMWG structures and gelation to form gradient stiffness hydrogels from a single LMWG. There are currently many reports of spatial control of gelation in multi-component systems, but is not well reported in single LMWG component systems. Gradients have previously been formed in different gel systems, with light being a commonly used approach to do so. Although gradients have been reported in literature, there is little comment on the time scale that these gradients last. This is a key examination point when creating gradient stiffness hydrogels from LMWGs, which are well-known for their reversibility due to their formation from non-covalent interactions.

We have shown that we can form supramolecular hydrogels with a tuneable gradient of stiffness. We use the localised technique of cavitation rheology to investigate our heterogeneous gels at a different length scale than traditional bulk rheology can probe. Using this technique, we show our control homogeneous 2NapFF gels (triggered by GdL) have an increasing linear trend in critical pressure as needle depth increases. By comparing this to our gels formed with MBTT, we see different cavitation rheology trends and hence show that gradient stiffness exists within a single gel. The gradients formed using MBTT are gradual and can be tuned by controlling the amount of UV exposure the samples are exposed to. Similarly, we can create photopatterned gels formed using a combination of GdL and MBTT. The boundaries between the patterned sections are considered as steep gradients.

Again, we can use cavitation rheology to show the changes in stiffness between the patterned sections. All the gradients created (gradual or steep) are temporary. When left overnight, our gels become homogeneous. This is due to the diffusion of protons over time, which results in a homogenous pH and stiffness. We show spatial and temporal control of the 2NapFF gel structures.

Using SANS, we show that the incorporation of 1.5 molar equivalents of MBTT to 2NapFF solutions results in changes to the structures found in solution. Although the overall structure with and without MBTT is the same (hollow cylinders) the radius decreases when MBTT is present. There is no difference, however, in gel structure when 2NapFF with MBTT is gelled by UV irradiation or GdL. Future work would look to examine this further. We have shown previously in this Thesis that solutions are susceptible to changes in structure and hence bulk properties. This is true again here in the solution phase, but does not seem as apparent in the gel phase. The addition of hydrophobic, non-LMWG molecules could again open up a range of interesting materials and again reduce the need for new LMWGs to be discovered in order to give certain sought-after properties.

These gelling methods, which allow us to form gradient stiffness gels, could open up opportunities in a number of areas. Whilst we acknowledge that using the current pH range and PAG may not be suitable for biological applications, the concept could be applied to a different system and used to mimic gradient stiffness tissue in a single sample. Other work could use this concept of a gradient stiffness gel to control diffusion across the gel by controlling pH and/or network gradients. This could be used to allow reactions at localised sites and the gradual diffusion of the products across the whole gel. Another potential use for this system could be in 3D printing, where solutions of 2NapFF with MBTT could be printed into a desired pattern and then irradiated to gel.

4.4. Experimental

4.4.1. Synthesis of LMWG

Synthesis of the LMWG used in this chapter, 2NapFF, can be found in Chapter 6, Section 1.

4.4.2. Gel Formation

All gels were formed at a concentration of 5 mg/mL of 2NapFF at room temperature (normally between 22 and 26 °C). To produce a 5 mg/mL stock solution of 2NapFF from which gels were prepared requires 2NapFF, 1 molar equivalent of 0.1 M NaOH with respect to 2NapFF and deionised water; this mixture was stirred overnight using a stirrer bar.[39, 43] Once the 2NapFF had dissolved, the pH was adjusted to pH 10.5 using 1 M NaOH. Gels were prepared from this stock solution by various pH triggers.

GdL Triggered Gels. A pre-weighed amount of GdL (either 4, 8 or 16 mg/mL) was added to a 7 mL Sterilin vial before adding 2 mL of the 2NapFF stock solution and stirring gently with a spatula until the GdL was dissolved. Once dissolved, the resulting solution was transferred to a Fisherbrand 20 mL Luer-Slip Plastic Disposable Syringe (2 cm diameter) with the top cut off and filed using sandpaper. The plunger was set to approximately 3 mL from the top (Figure 4.11). Setting the plunger to this position was calculated using the 2 cm syringe diameter and sample volume of 2 mL to calculate the height of a gel as 0.64 cm. Hence, a mould of diameter 2 cm and 1 cm height was created. This was sealed with Parafilm and left overnight to allow gelation to occur without drying. The gels were removed from the syringe by carefully pushing the plunger and placed onto microscope slides for measurements.

Figure 4.11. UV box setup with syringe mould. The LED is attached to the black-finned heat-sink and placed above the cut-off syringe moulds.

PAG Triggered Gels. The second pH trigger used a PAG, MBTT. Unless otherwise stated, a concentration of 1.5 molar equivalents of PAG (relative molar equivalents to the quantity of LMWG) was added to a 7 mL Sterilin vial before adding 2 mL of 2NapFF stock solution and stirring with a stirrer bar overnight. Note, shorter stirring times of around 30 minutes results in visually homogeneous solutions, but the gelation results were irreproducible. Increasing the stirring time to overnight resulted in both homogeneous solutions as well as reproducible gels when irradiated. The following day, the resulting solution was transferred to a plastic syringe with the top cut off and filed using sandpaper, and plunger set to approximately 3 mL from the top (Figure 4.11). This was sealed with Parafilm and placed underneath a 365 nm LED (0.7 A, RS Components Ltd) inside a UV box and irradiated. Using an intensity sensor (Thorlabs Optical Power Meter PM100D and Thorlabs sensor S/N:16100711) the distance from the LED to the sample was adjusted so that the light intensity always read between 20 ± 1 mW. This distance was such that the sample temperature, when measured with a GM1312 Digital Temperature Indicator Thermometer with Digital Thermocouple, did not rise more than 5 °C over an 8 hour irradiation period (Figure 4.5e). One temperature probe was placed within the sample to record the sample temperature whilst the other probe was placed outside the UV box to monitor room temperature. Once irradiated for a given time, gels were removed from the syringe by pushing the plunger and placed onto microscope slides for measurements.

Mixed pH Triggers for Photopatterning. For photopatterning, a mixture of both GdL (2.5 mg/mL) and MBTT (1.5 molar equivalents) were used. MBTT was added to a 7 mL Sterilin vial before adding 2 mL of LMWG stock solution and stirring with a stirrer bar overnight. The following day, the resulting 2 mL was added to another 7 mL Sterilin vial containing 2.5 mg/mL of GdL and stirred with a spatula until the GdL was dissolved. The resulting mixture was transferred to a plastic syringe with the top cut off and filed using sandpaper, sides wrapped in black card and secured with tape, and plunger set to approximately 3 mL from the top, Figure 4.12a. A photomask (Figure 4.12b) formed from opaque plastic, 2 layers of black card and tape was placed over the syringe and then finally was sealed with Parafilm and left overnight to allow gelation by GdL to occur. Selective radiation using the photomask allowed for the creation of photopattern gel. Gels were removed from the syringe by pushing the plunger and placed onto microscope slides for measurements.
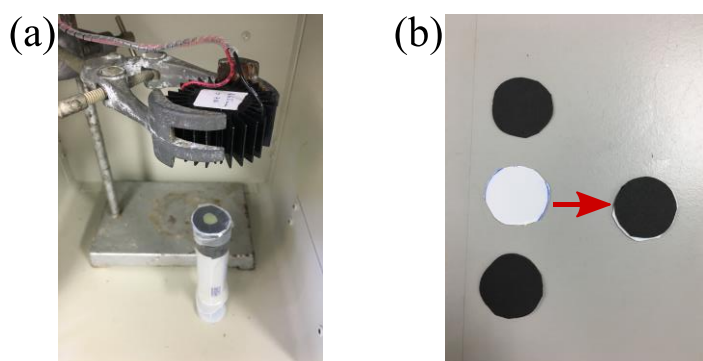
Figure 4.12. (a) UV box setup showing the LED above the syringe mould topped with a photomask for patterned gels. (b) Breakdown of the photomask. Left: component parts of photomask consisting of opaque plastic topped with two pieces of black card. Right: the final photomask, held together with tape, before cutting to give the desired photomask pattern.

4.4.3. Instruments and Methodologies

Bulk Rheology. Bulk rheology was carried out using Anton Paar Physica MCR 101 and 301 rheometers. Samples prepared in 7 mL Sterilin vials were measured using a vane (ST10) and cup geometry to test 2 mL of prepared sample. Samples which were made using the syringe moulds were measured using a PP25/S geometry with sandpaper (80 grit) taped to the flat plate of the rheometer to prevent slippage of the gel during the measurement. All

samples were measured at a constant temperature of 25 °C. Measurements were carried out in triplicate unless otherwise stated, averaged and standard deviation between the measurements calculated. Strain tests were performed at 10 rad/s from 0.01% to 1000% strain. Frequency sweeps were performed from 1 rad/s to 100 rad/s at 0.02% strain. The viscoelastic region was determined from strain tests and ends at the strain value where G′ deviates from linearity, indicating the point at which the gel begins to break.

Cavitation Rheology. Cavitation rheology is a method of analysing gels, first reported by Zimberlin et al.[36] Our cavitation rheometer is custom-built by Bart Dietrich (University of Glasgow) and our setup is fully described in previous work by our group.[38] Briefly, the setup involves a syringe pump (World Precision Instruments Aladdin, AL-1000), 10 mL syringe (Hamilton™ 1000 Series Gastight™ Syringe with Luer-lock attachment), needle of inner diameter 0.41 mm (Fisher Scientific, Hamilton™ Kel-F Hub Blunt Point Needle with Luer-lock attachment), the custom-made Cavitation Rheometer Analyser Box (CRAB), a probe circuit, a 3D printer and a computer with "PuTTY" software to record the output data. All these components were connected using plastic tubing and plastic adapters to allow air to be pushed through the system and create pressure (Figure 4.13). The system was calibrated using a pressure sensor before measurements were recorded. A standard experiment uses the 3D printer and probe circuit to place the needle directly into the sample at the desired location. The needle is stopped precisely on the surface of the sample using the circuit, and once on the surface, the 3D printer can be used to manually lower the needle to the required distance from the surface of the sample. The syringe pump is then turned on, allowing air to flow through the tubing to the sample at a rate of 0.4 mL min^{-1}. A bubble begins to grow within the sample at the end of the needle. The maximum pressure value recorded by the CRAB is known as the critical pressure (P_C). Measurements were carried out in triplicate, averaged and standard deviation between the measurements calculated.
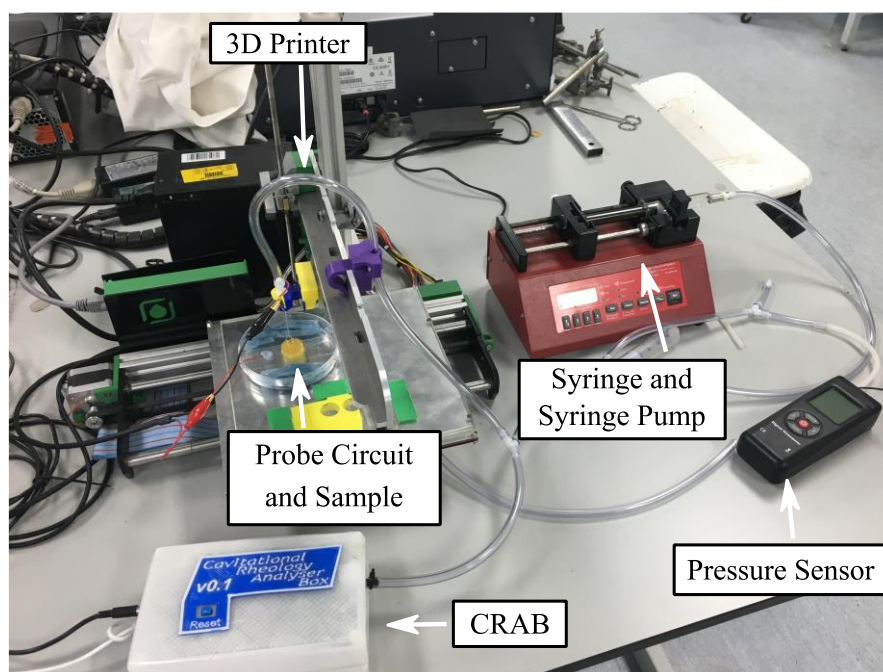
Figure 4.13. Cavitation rheometer setup used in this work.

To avoid the issue of samples drying out during cavitation rheology measurements, samples were placed on microscope slides inside a petri dish (Figure 4.14) where a hydrated atmosphere was created by wet blue roll. A small hole of approximately 1 mm diameter was drilled into the side to allow the cavitation rheometer probe circuit wire to be inserted, and a small cross approximately 22 mm by 5 mm drilled into the lid to allow for the movement of the cavitation rheometer needle.
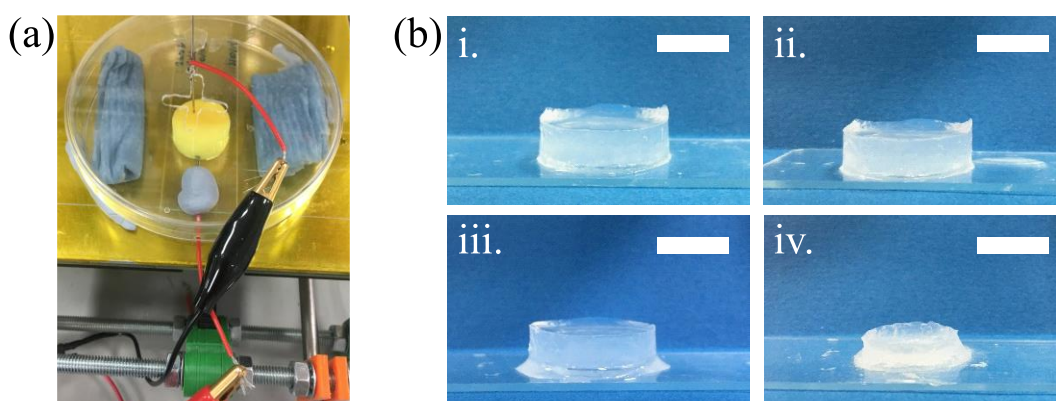
Figure 4.14. (a) Petri dish setup for the cavitation rheometer used to reduce gel drying. (b) Comparison of samples showing visible differences when left for a seven hour period with (ii) and without (iv) the petri dish setup; i. and iii. are the same samples as ii. and iv. respectively, before the start of the drying experiment. Scale bars represent 1 cm.

For samples of 2NapFF and MBTT only with shorter irradiation times (5 hours or less), solutions were placed into a plastic syringe with the top cut off and plunger shortened, Figure 4.15. This allowed samples which were not able to be successfully removed from moulds without breakage to still be measured using cavitation rheology.
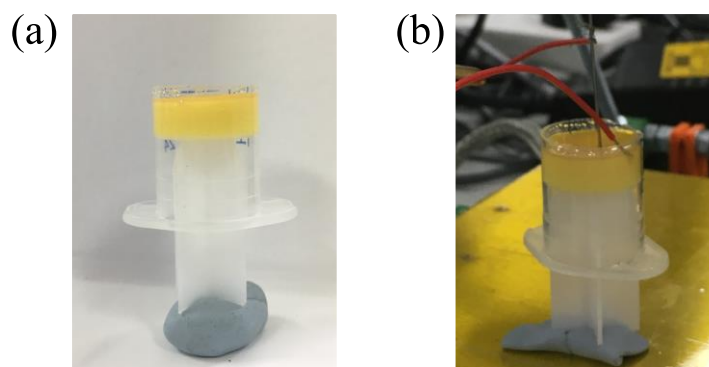
Figure 4.15. (a) Short syringe mould; (b) syringe mould on the cavitation rheometer.

pH Measurements. A FC2020 Hanna pH probe (calibrated to pH 4, pH 7 and pH 10) was used to measure the pH of both stock solutions and gels. The accuracy of the measurements stated by the supplier is $\pm$ 0.1. Measurements were carried out at room temperature (normally between 22 and 26 °C).

Apparent pK_a Titrations. To determine the apparent pK_a of both 5 mg/mL 2NapFF only and 5 mg/mL 2NapFF with 1.5 molar equivalents of MBTT, a titration with 0.1 M HCl was performed. 2 mL of 2NapFF solution at pH 10.5 was titrated with 5 µL portions of 0.1 M HCl until a final pH of 3 was reached. To allow for a homogeneous pH change and to prevent localised gelation upon addition of HCl, the solutions were stirred after the addition of each HCl aliquot until there was no visible gel and the pH came to equilibrium. To add MBTT to the 2NapFF solutions, both were stirred together overnight the day prior to the titration. The sample was titrated in a water bath set to 25 °C to maintain the temperature at which the pH was measured at constant throughout.

Ultraviolet-Visible Absorption Spectrometry. Measurements were carried out using an Agilent Technologies Cary 60 UV-Vis spectrometer. 100 µL of each sample was placed into a quartz slide with path length of 0.1 mm. For irradiated samples, 100 µL of sample was pipetted into the quartz slides then irradiated for 20 minutes at intensity 20 mW.

Deionised water was used to set the baseline. Measurements were carried out at room temperature and using the medium speed setting.

SANS. SANS measurements were performed by Emily Draper and Dave Adams (University of Glasgow) with Ralf Schweins (Institut Laue Langevin, Grenoble, France) using the D11 instrument at the Institut Laue Langevin, Grenoble, France. A neutron beam, with a fixed wavelength of 6 Å and divergence of $\Delta\lambda/\lambda = 9\%$, allowed measurements over a large range (0.001 to 0.3 Å^{-1}) in Q, where $Q = 4\pi\sin(\theta/2)/\lambda$, by using three sample-detector distances of 1.5 m, 8 m, and 39 m. Solutions and gels were measured in UV spectrophotometer grade quartz cuvettes (Hellma) with a 2 mm path length. These were placed in a temperature-controlled sample rack during the measurements. Solutions were prepared as described previously, but now in D_2O (instead of H_2O). Gels formed using GdL were prepared in the cuvettes and then transferred to the rack. The irradiated samples were irradiated ex situ in the cuvettes for a predetermined length of time and then transferred to the rack. Prior to measurement but post irradiation, the samples were wrapped in tinfoil to prevent any further accidental light irradiation. Once collected, the data were then reduced to 1D scattering curves of intensity vs. Q using the facility provided software. The electronic background was subtracted, the full detector images for all data were normalised and scattering from the empty cell was subtracted. The scattering from D_2O was also measured and subtracted from the data. All data processing (background subtractions) was performed by Ralf Schweins (Institut Laue Langevin, Grenoble, France). The instrument-independent data were then fitted to the models discussed in the text using the SasView 4.2.1 software package version.[44] For each data set, the scattering length density (SLD) of each sample was assumed to be 2.73 x 10^{-6} Å^{-2} and SLD for the solvent, 6.39 x 10^{-6} Å^{-2}.[45]

4.5. References

1. N. M. Sangeetha and U. Maitra, *Chem. Soc. Rev.*, 2005, **34**, 821-836.
2. M. de Loos, B. L. Feringa and J. H. van Esch, *Eur. J. Org. Chem.*, 2005, **17**, 3615-3631.
3. P. J. Willcox, D. W. Howie Jr., K. Schmidt-Rohr, D. A. Hoagland, S. P. Gido, S. Pudjijanto, L. W. Kleiner and S. Venkatraman, *J. Polym. Sci. B. Polym. Phys.*, 1999, **37**, 3438-3454.
4. S. Zhang, *Nat. Biotechnol.*, 2003, **21**, 1171.
5. H. Kar and S. Ghosh, *Nat. Chem.*, 2015, **7**, 765-767.
6. R. G. Weiss, *J. Am. Chem. Soc.*, 2014, **136**, 7519-7530.
7. M. Singh, C. Berkland and M. S. Detamore, *Tissue Eng. Part B Rev.*, 2008, **14**, 341-366.
8. L. M. Cross, K. Shah, S. Palani, C. W. Peak and A. K. Gaharwar, *Nanomed.: Nanotechnol. Biol. Med.*, 2018, **14**, 2465-2474.
9. T. H. Kim, D. B. An, S. H. Oh, M. K. Kang, H. H. Song and J. H. Lee, *Biomaterials*, 2015, **40**, 51-60.
10. R. Sunyer, A. J. Jin, R. Nossal and D. L. Sackett, *PLOS ONE*, 2012, **7**, e46107.
11. F. Brandl, F. Sommer and A. Goepferich, *Biomaterials*, 2007, **28**, 134-146.
12. A. Q. Mai, T. Bánsági, A. F. Taylor and J. A. Pojman, *Commun. Chem.*, 2021, **4**, 101.
13. R. A. Sheldon and J. M. Woodley, *Chem. Rev.*, 2018, **118**, 801-838.
14. M. Wallace, D. J. Adams and J. A. Iggo, *Soft Matter*, 2013, **9**, 5483-5491.
15. J. Ruíz-Olles and D. K. Smith, *Chem. Sci.*, 2018, **9**, 5541-5550.
16. H. S. Cooke, L. Schlichter, C. C. Piras and D. K. Smith, *Chem. Sci.*, 2021, **12**, 12156-12164.
17. J. He, Y. Du, J. L. Villa-Uribe, C. Hwang, D. Li and A. Khademhosseini, *Adv. Funct. Mater.*, 2010, **20**, 131-137.
18. P. Liu, C. Mai and K. Zhang, *Front. Chem. Sci. Eng.*, 2018, **12**, 383-389.
19. K. Murata, M. Aoki, T. Nishi, A. Ikeda and S. Shinkai, *J. Chem. Soc., Chem. Commun.*, 1991, 1715-1718.
20. A. R. Hirst, B. Escuder, J. F. Miravet and D. K. Smith, *Angew. Chem. Int. Ed.*, 2008, **47**, 8002-8018.
21. E. R. Draper, E. G. B. Eden, T. O. McDonald and D. J. Adams, *Nat. Chem.*, 2015, **7**, 848.
22. D. J. Cornwell, O. J. Daubney and D. K. Smith, *J. Am. Chem. Soc.*, 2015, **137**, 15486-15492.
23. J. Raeburn, B. Alston, J. Kroeger, T. O. McDonald, J. R. Howse, P. J. Cameron and D. J. Adams, *Mater. Horiz.*, 2014, **1**, 241-246.
24. J. V. Karpiak, Y. Ner and A. Almutairi, *Adv. Mater.*, 2012, **24**, 1466-1470.
25. I. Ziemecka, G. J. M. Koper, A. G. L. Olive and J. H. van Esch, *Soft Matter*, 2013, **9**, 1556-1561.
26. A. Z. Cardoso, L. L. E. Mears, B. N. Cattoz, P. C. Griffiths, R. Schweins and D. J. Adams, *Soft Matter*, 2016, **12**, 3612-3621.
27. Y. Pocker and E. Green, *J. Am. Chem. Soc.*, 1973, **95**, 113-119.
28. D. J. Adams, M. F. Butler, W. J. Frith, M. Kirkland, L. Mullen and P. Sanderson, *Soft Matter*, 2009, **5**, 1856-1862.
29. E. R. Draper, M. Wallace, R. Schweins, R. J. Poole and D. J. Adams, *Langmuir*, 2017, **33**, 2387-2395.

30. E. R. Draper, B. Dietrich, K. McAulay, C. Brasnett, H. Abdizadeh, I. Patmanidis, S. J. Marrink, H. Su, H. Cui, R. Schweins, A. Seddon and D. J. Adams, *Matter*, 2020, **2**, 764-778.

31. A. L. Fameau, A. Arnould, M. Lehmann and R. von Klitzing, *Chem. Comm.*, 2015, **51**, 2907-2910.

32. K. Sun, R. Kumar, D. E. Falvey and S. R. Raghavan, *J. Am. Chem. Soc.*, 2009, **131**, 7135-7141.

33. J. Raeburn, T. O. McDonald and D. J. Adams, *Chem. Comm.*, 2012, **48**, 9355-9357.

34. G. Pohlers, J. C. Scaiano, R. Sinta, R. Brainard and D. Pai, *Chemistry of Materials*, 1997, **9**, 1353-1361.

35. J. Zhang, P. Xiao, F. Morlet-Savary, B. Graff, J. P. Fouassier and J. Lalevée, *Polym. Chem.*, 2014, **5**, 6019-6026.

36. J. A. Zimberlin, N. Sanabria-DeLong, G. N. Tew and A. J. Crosby, *Soft Matter*, 2007, **3**, 763-767.

37. J. A. Zimberlin, J. J. McManus and A. J. Crosby, *Soft Matter*, 2010, **6**, 3632-3635.

38. A. M. Fuentes-Caparrós, B. Dietrich, L. Thomson, C. Chauveau and D. J. Adams, *Soft Matter*, 2019, **15**, 6340-6347.

39. L. Chen, K. Morris, A. Laybourn, D. Elias, M. R. Hicks, A. Rodger, L. Serpell and D. J. Adams, *Langmuir*, 2010, **26**, 5232-5242.

40. M. Wallace, J. A. Iggo and D. J. Adams, *Soft Matter*, 2015, **11**, 7739-7747.

41. K. McAulay, B. Dietrich, H. Su, M. T. Scott, S. Rogers, Y. K. Al-Hilaly, H. Cui, L. C. Serpell, Annela M. Seddon, E. R. Draper and D. J. Adams, *Chem. Sci.*, 2019, **10**, 7801-7806.

42. Sigma-Aldrich, 2-(4-Methoxystyryl)-4,6-bis(trichloromethyl)-1,3,5-triazine, https://www.sigmaaldrich.com/catalog/product/aldrich/530964?lang=en&region=GB, (accessed 31st January 2019).

43. K. McAulay, P. A. Ucha, H. Wang, A. M. Fuentes-Caparrós, L. Thomson, O. Maklad, N. Khunti, N. Cowieson, M. Wallace, H. Cui, R. J. Poole, A. Seddon and D. J. Adams, *Chem. Comm.*, 2020, **56**, 4094-4097.

44. SasView, (http://www.sasview.org/ (accessed 28th November 2019).

45. Neutron activation and scattering calculator, https://www.ncnr.nist.gov/resources/activation/, (accessed 28th November 2019).

Chapter 5. Conclusions and Future Work

The aim of this Thesis was to learn more about how to control LMWG structures in both the solution and gel phase, and investigate how this affects the overall properties of the materials. LMWGs are a very diverse, but not yet fully understood class of materials. LMWG chemical structures can be modified with different fragments and functional groups to alter the final properties of a gel, and if a gel will form or not. Currently, there is little understanding linking the chemical structure of a LMWG, to the formulation structures formed in both LMWG solutions and gels, and how this relates to the final bulk properties of these. The work in this Thesis will enhance our understanding of these systems which means they can be tuned with specific applications in mind. In this Thesis, we utilise one specific LMWG example from our LMWG library, however, the discussions could be applied to other similar systems.

We have shown there is a critical link between the formulation structures formed by our exemplar LMWG (2NapFF) and the resulting bulk properties. Future work would look to examine this further with other LWMG systems to confirm that the formulation method and structures are important for these systems as a whole. We examine precursor solutions (used to make hydrogels) and discuss the sensitivity of these systems to minor changes during sample preparation. Following on from this, we highlight that formulation solution structures can be tuned to give various bulk properties as well as access to liquid crystals. This is the first example of a liquid crystal phase with our LMWG systems. Moving from the solution to gel phase, we demonstrate that we have local control of LMWG structures during gelation to give gradient stiffness hydrogels within a single sample.

Although many gels are formed by the application of a trigger to a precursor LMWG solution, these solutions are usually not given much attention in current literature. This is surprising as structures can form in these solutions. Hence, in Chapter 2 we focus on the preparation of such LMWG solutions. We establish that these solutions are susceptible to many factors, and therefore conclude that care should be taken during solution preparation. Creating a robust preparation method for LMWG solutions reduces the risk of variation in bulk properties between different solution batches caused by variation in LMWG solution structures. Reducing variation between batches would make these solutions more suitable for industrial applications where reproducibility is key.

Currently, it is assumed that to create different, desired bulk properties from LMWGs requires the synthesis of new molecules. In Chapter 3, we use our solution preparation method and further examine the formulation structures present in the solution phase and hence examine the resulting bulk solution properties. Taking a single LMWG, we tune the structures present by altering the LMWG concentration and counterion (NaOH and TBAOH) used to make the solutions. This gives a vast array of structures and hence gives solutions with different bulk properties from one single LMWG. We attribute this difference to the organic alkyl chains of TBAOH which may be incorporated into, and alter, the 2NapFF structures. This would not happen with ionic NaOH. We show that variations of solution composition can be used with specific properties in mind, such as an increase in extensional viscosity. Creating a single, versatile LMWG removes the need to create new molecules. This saves time and resources. To continue this work would involve finding additional parameters to change in order to give even more diverse structures and properties. This could include adding the LMWG to a multi-component system, or by changing the chirality of the amino acids present in the LMWG. Additionally, the corresponding gel phase would also be examined, looking again for changes in bulk properties as the different solution structures are gelled.

Examining different length scales of structures found in hydrogels is of growing interest and is important to understand both localised and bulk properties. In Chapter 4, we examine the gel phase and aim to control the structures during gelation by forming gradient stiffness hydrogels. These gradients are formed by controlling the self-assembly process of a LMWG and PAG system, and by controlling where the gelation can occur. We use traditional bulk rheology to examine the overall bulk properties of the gels and the localised technique of cavitation rheology to prove the existence of gradient stiffnesses within the samples. This research shows that a combination of different techniques are required to fully characterise LMWG hydrogels at various length scales. Future work here would look for applications for these types of gels with varying stiffness; this could include in tissue engineering or as a reaction site with reactions initially localised and then extending as diffusion occurs. Additionally, we show in this Chapter that the addition of a hydrophobic non-gelator molecule (the PAG) causes structural changes to the LMWG solution phase. Future work would examine the effects of adding a hydrophobic non-gelator additive (for example a hydrophobic drug) to both the solution and corresponding gel phases. We expect

this would again increase the versatility of the LMWG systems and give materials with an even wider range of properties.

To conclude, in this Thesis we have examined the link between LMWG formulation structures and overall bulk properties over different length scales in both the LMWG solution and gel phase. Being able to understand this link allows for a more methodical approach to obtain materials with desired properties which is currently lacking in this field.

Chapter 6. Appendix

6.1. Synthesis of LMWG

All materials were purchased from commercial suppliers and used as received. The LMWG 2NapFF was synthesised as described previously,[1-6] using the four-step process summarised in Figure 6.1 (letters and numbers are used to identify each reaction step). All amino acids used throughout were the L-enantiomer.
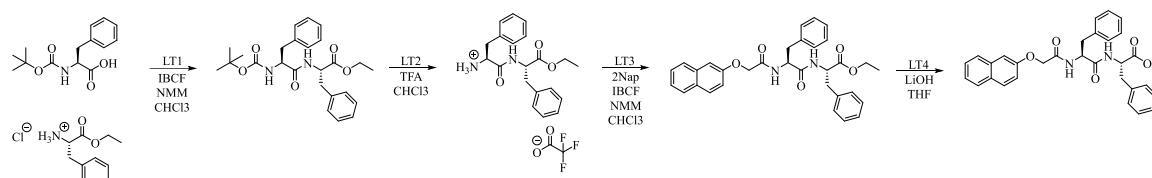
Figure 6.1. Summary of the synthesis of the LMWG 2NapFF.

LT1: Boc-protected phenylalanine (Boc-F, 4.67 g, 17.6 mM) was added to chloroform (approximately 50 mL), N-methylmorpholine (NMM, 1.1 molar equivalents, 2.13 mL) and iso-butyl chloroformate (IBCF, 1.1 molar equivalents, 2.4 mL) and stirred for ten minutes. In a separate container, phenylalanine ethyl ester hydrochloride (F-OEt, 1.1 molar equivalents with respect to Boc-F, 4.45 g) and NMM (1.1 molar equivalents, 2.34 mL) were also stirred together with approximately 50 mL of chloroform for ten minutes. The two mixture were then combined slowly over an ice bath and left to stir overnight. The following day, the reaction was washed twice with water, followed by 1 M hydrochloric acid, and brine, and dried with magnesium sulphate. The solvent was then removed *in vacuo*. The crude compound (Boc-FF-OEt, Figure 6.2) was a yellow solid and was used in the next step without further purification.

^{1}H NMR Boc-FF-OEt (DMSO-d$_6$, 400 Hz) δ 8.33 (1H, NH, doublet J = 8.0 Hz) 8.31 (chloroform); 7.24 (10H, Ph, multiplet); 6.85 (1H, NH, doublet J = 8.0 Hz); 6.41 (impurity); 4.49 (1H, CH, multiplet); 4.20 (1H, CH, multiplet); 4.03 (2H, CH$_2$ ester, quartet, J = 7.1 Hz); 3.87 (impurity); 2.86 (4H, CH$_2$ phenylalanines, multiplet); 1.28 (9H, Boc protecting group, singlet); 1.14 (impurity); 1.10 (3H, CH$_3$ ester, triplet J = 8.0 Hz); 0.88 (impurity).
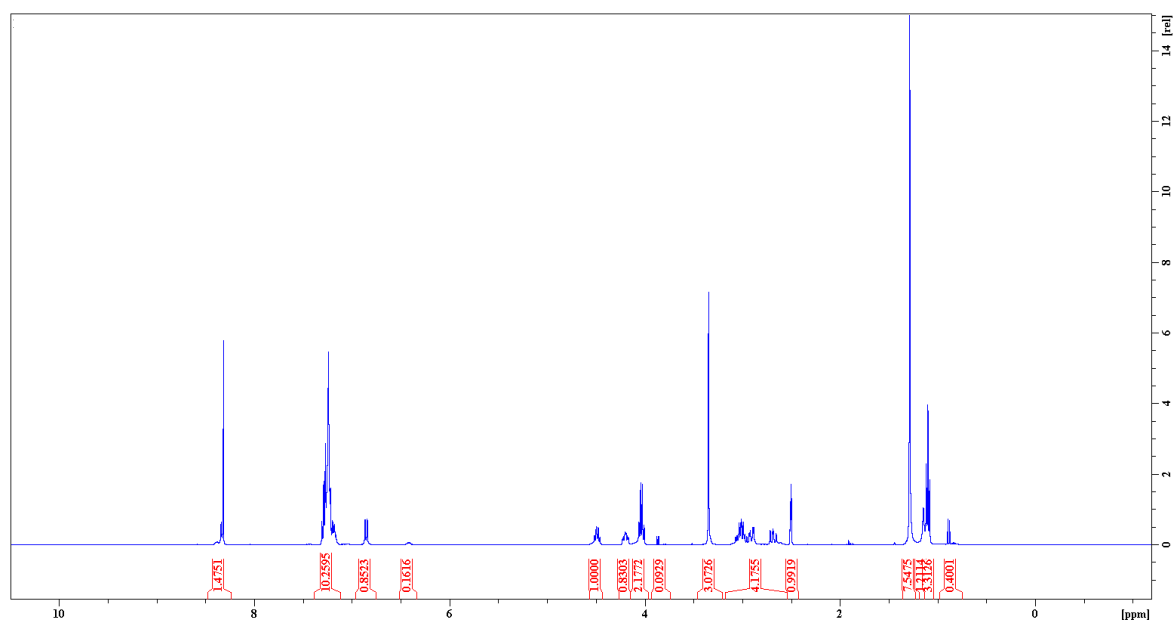
Figure 6.2. ^{1}H NMR of Boc-FF-OEt in DMSO-d$_6$.

LT2: To remove the Boc-protecting group, Boc-FF-OEt was then dissolved in approximately 20 mL of chloroform before adding trifluoroacetic acid (approximately 10 mL, 8 molar equivalents). This was stirred overnight. The following day, diethyl ether (200 mL) was added and stirred for two hours. This gave a white solid, which was collected by vacuum filtration and washed with ether. The product of H$_3$N-FF-OEt.TFA (Figure 6.3) gave an overall yield for the first two steps of 82% (standard deviation of 5.9%) averaged over ten batches.

^{1}H NMR H$_3$N-FF-OEt.TFA (DMSO-d$_6$, 400 Hz) δ 9.01 (1H, NH, doublet J = 7.8 Hz); 8.13 (3H, NH$_3$, singlet); 7.28 (10H, Ph, multiplet); 4.56 (1H, CH, multiplet); 4.05 (3H, CH and CH$_2$ ester, multiplet); 3.02 (4H, CH$_2$ phenylalanines, multiplet); 1.11 (3H, CH$_3$ ester, triplet, J = 7.1 Hz).
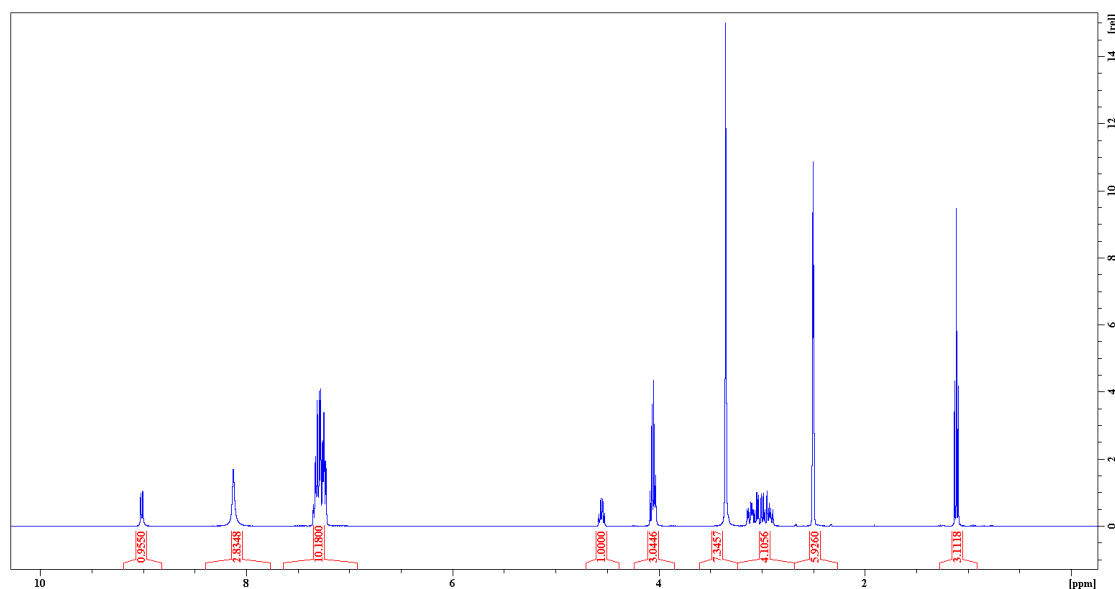
Figure 6.3. ^{1}H NMR of H$_3$N-FF-OEt.TFA in DMSO-d$_6$.

LT3: 2-Naphthoxyacetic acid (2Nap, 1 g, 4.9 mM) was added to chloroform (approximately 50 mL), N-methylmorpholine (NMM, 1.1 molar equivalents, 0.60 mL) and iso-butyl chloroformate (IBCF, 1.1 molar equivalents, 0.68 mL) and stirred for ten minutes. In a separate container, H$_3$N-FF-OEt.TFA (1.1 molar equivalents with respect to 2Nap, 2.47 g) and NMM (1.1 molar equivalents, 0.66 mL) were also stirred together with approximately 50 mL of chloroform for ten minutes. The two mixture were then combined slowly over an ice bath and left to stir overnight. The following day, the reaction was washed twice with water, followed by 1 M hydrochloric acid, and brine, and dried with magnesium sulphate. The solvent was then removed *in vacuo*. The crude compound (2NapFF-OEt, Figure 6.4) was a yellow/brown solid and was used in the next step without further purification.

^{1}H NMR 2NapFF-OEt (DMSO-d$_6$, 400 Hz) δ 8.65 (1H, NH, doublet J = 7.4 Hz); 8.32 (chloroform, singlet); 8.20 (1H, NH, doublet J = 8.6 Hz); 7.84 (2H, Ph, multiplet); 7.73 (1H, Ph, multiplet); 7.64 (1H, Ph, multiplet); 7.36 (1H, Ph, multiplet); 7.20 (12H, Ph, multiplet); 4.67 (1H, CH, multiplet); 4.45 (2H, OCH$_2$, singlet); 4.49 (1H, CH, multiplet); 4.04 (2H, CH$_2$ ester, multiplet); 2.94 (4H, CH$_2$ Ph, multiplet); 1.09 (3H, CH$_3$ ester, triplet J = 7.1 Hz); 0.95-0.68 (impurity).
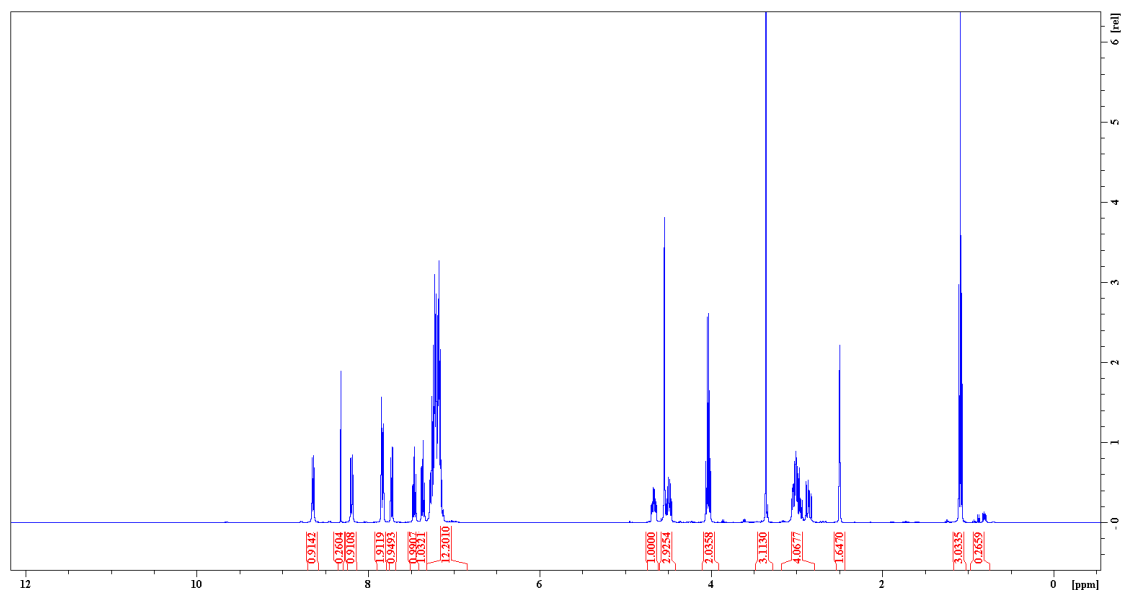
Figure 6.4. ^{1}H NMR of 2NapFF-OEt in DMSO-d$_6$.

LT4: To remove the ester protecting group, 2NapFF-OEt was dissolved in tetrahydrofuran (approximately 100 mL). A solution of lithium hydroxide (4 molar equivalents, 0.48 g) in water (100 mL) was added and left to stir overnight. The next day, 1M hydrochloric acid (approximately 500 mL) was added and stirred overnight to precipitate an off-white solid, 2NapFF. The following day, 2NapFF was collected by vacuum filtration and washed with water. Once washed, 2NapFF was then stirred in diethyl ether overnight, filtered again by vacuum filtration the next day and put in an oven set to 60 °C to remove trace diethyl ether. This gave the white solid 2NapFF (Figure 6.5 and Figure 6.6). The overall yield for steps three and four was 79% (standard deviation of 4.87%) averaged over ten batches.

Mass spectrometry of 2NapFF [M+Na]$^+$ found at 519.1894 and calculated to be 519.1890.

^{1}H NMR 2NapFF (DMSO-d$_6$, 400 Hz) δ 12.861 (1H, COOH, singlet); 8.48 (1H, NH, doublet J=8.4Hz); 8.16 (1H, NH, doublet J=8.8Hz); 7.84 (2H, Ph, multiplet); 7.73 (1H, Ph, multiplet); 7.47 (1H, Ph, multiplet); 7.37 (1H, Ph, multiplet); 7.20 (11H, Ph, multiplet); 4.66 (1H, CH, multiplet); 4.51 (2H, OCH$_2$, singlet); 4.49 (1H, CH, multiplet); 2.99 (4H, CH$_2$ Ph, multiplet).
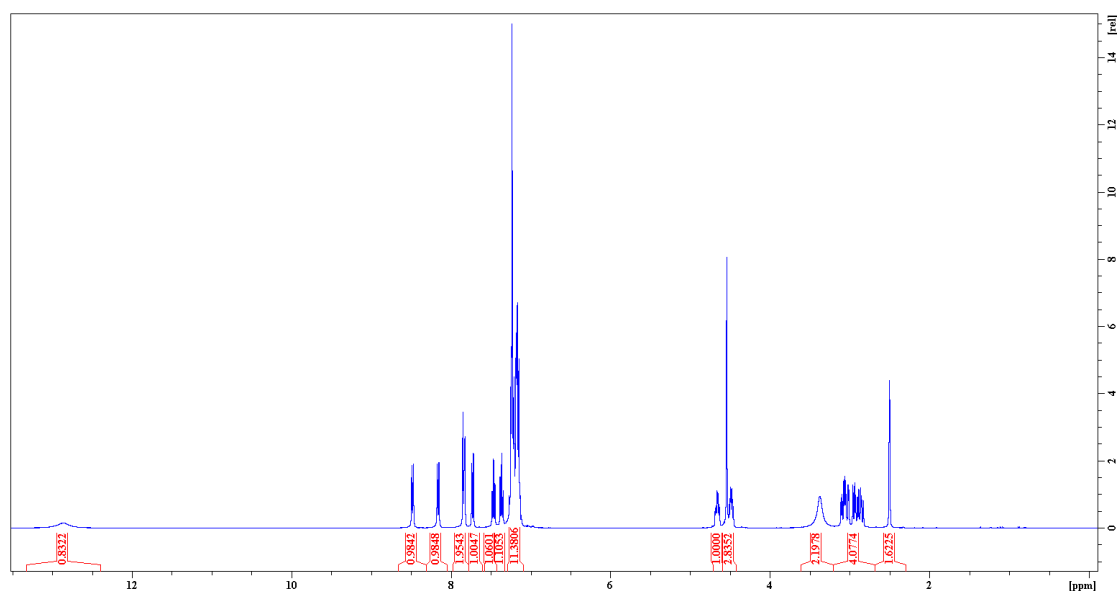
Figure 6.5. ^{1}H NMR of 2NapFF in DMSO-d$_6$.

^{13}C NMR 2NapFF (DMSO-d$_6$, 400 Hz) δ 173.17, 171.28, 167.68 (C=O); 155.97, 137.97, 137.84, 134.50, 129.83, 129.71, 129.59, 129.23, 128.65, 128.44, 127.97, 127.26, 126.90, 126.72, 124.33, 118.91, 107.85 (aromatic C); 67.19 (CH$_2$ from 2Nap); 53.97, 53.71 (CH); 37.90, 37.18 (CH$_2$ Ph).
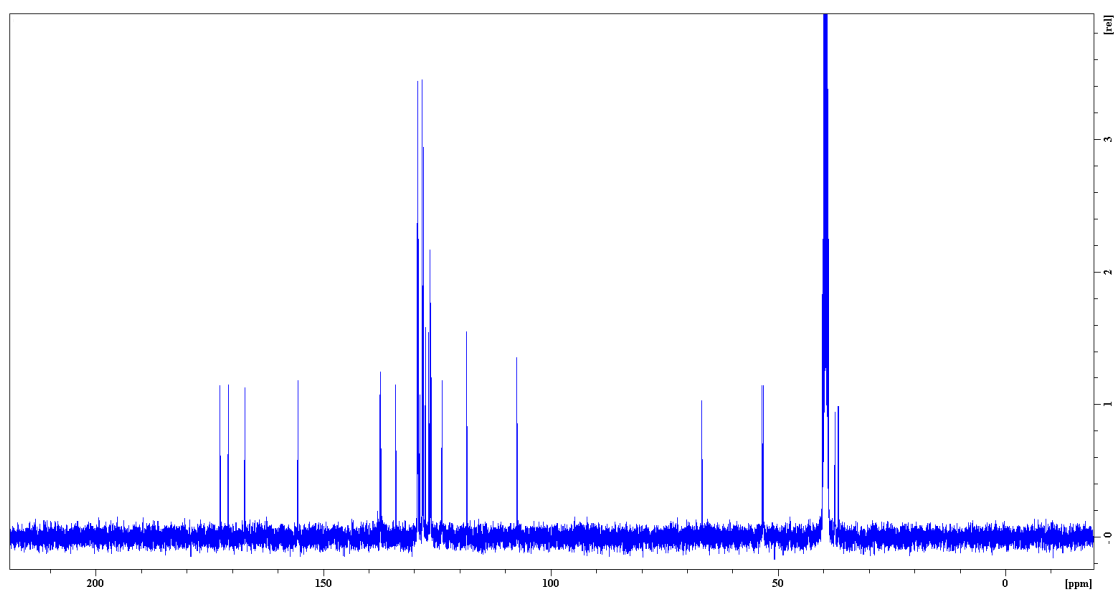
Figure 6.6. ^{13}C NMR of 2NapFF in DMSO-d$_6$.

6.2. Supplementary Figures
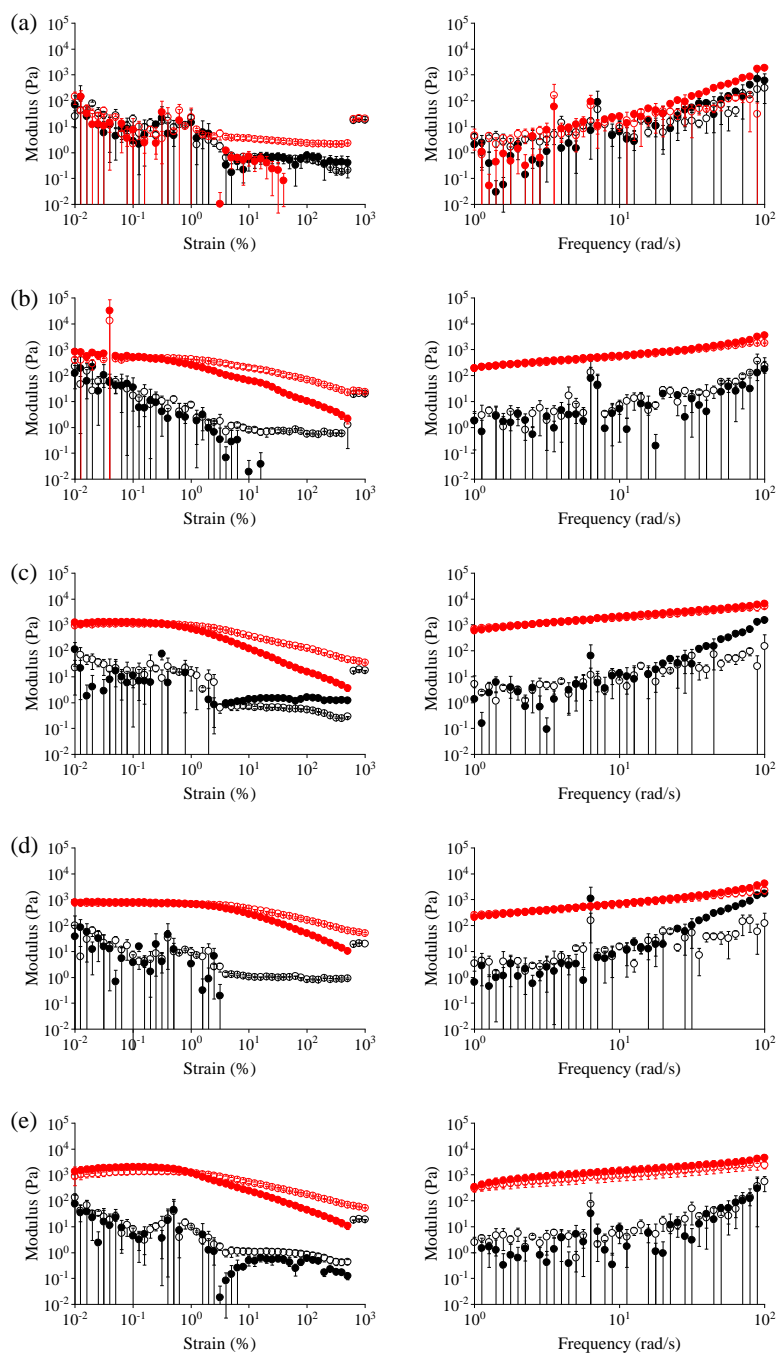
Figure 6.7. Full strain (left) and frequency (right) data for 2NapFF-Na solutions of concentration (a) 5 mg/mL; (b) 10 mg/mL; (c) 15 mg/mL; (d) 20 mg/mL; (e) 25 mg/mL. Black data represents measurements performed at room temperature and red data represents measurements performed at room temperature 2 hours after a heat-cool cycle to 60 ⁰C. G′ is represented by filled circles and G″ by empty circles. Error bars represent the standard deviation between measurements, which were carried out in triplicate.
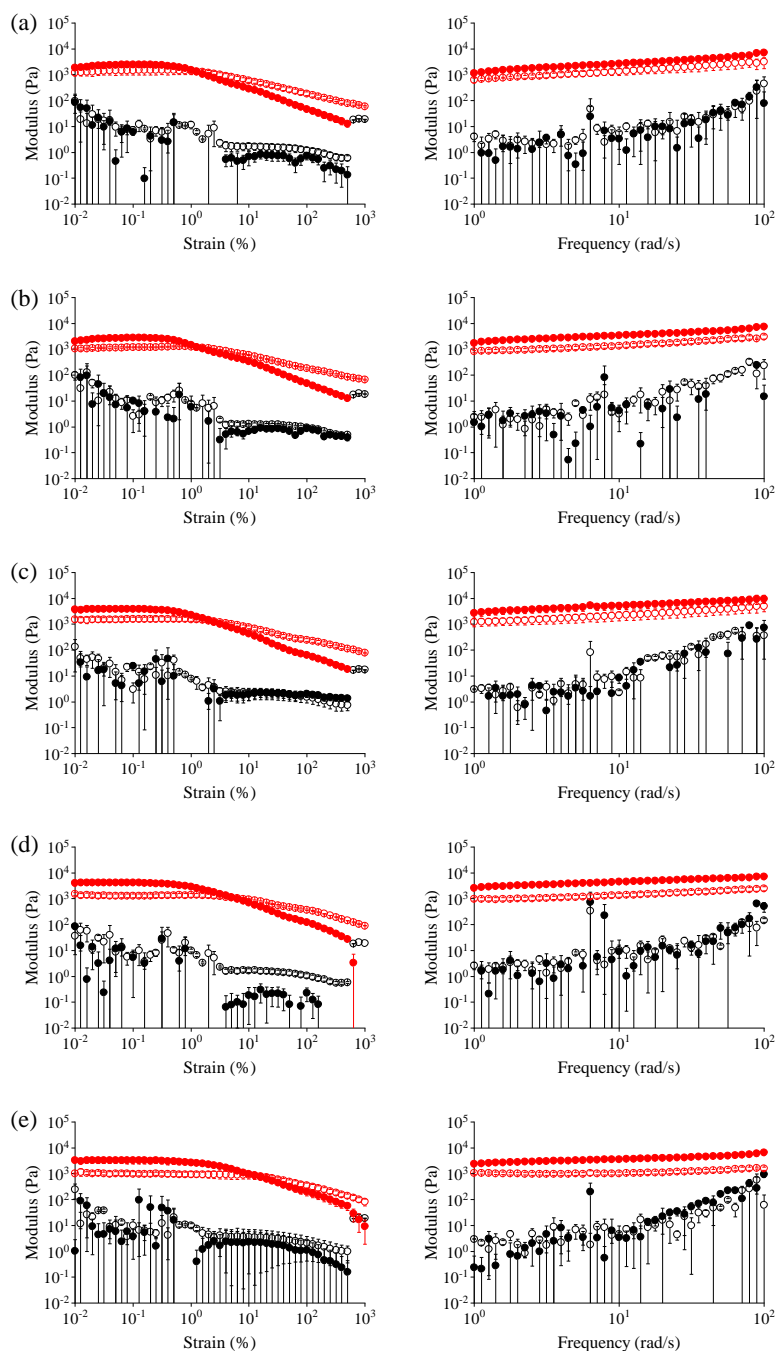
Figure 6.8. Full strain (left) and frequency (right) data for 2NapFF-Na solutions of concentration (a) 30 mg/mL; (b) 35 mg/mL; (c) 40 mg/mL; (d) 45 mg/mL; (e) 50 mg/mL. Black data represents measurements performed at room temperature and red data represents measurements performed at room temperature 2 hours after a heat-cool cycle to 60 ⁰C. G′ is represented by filled circles and G″ by empty circles. Error bars represent the standard deviation between measurements, which were carried out in triplicate.
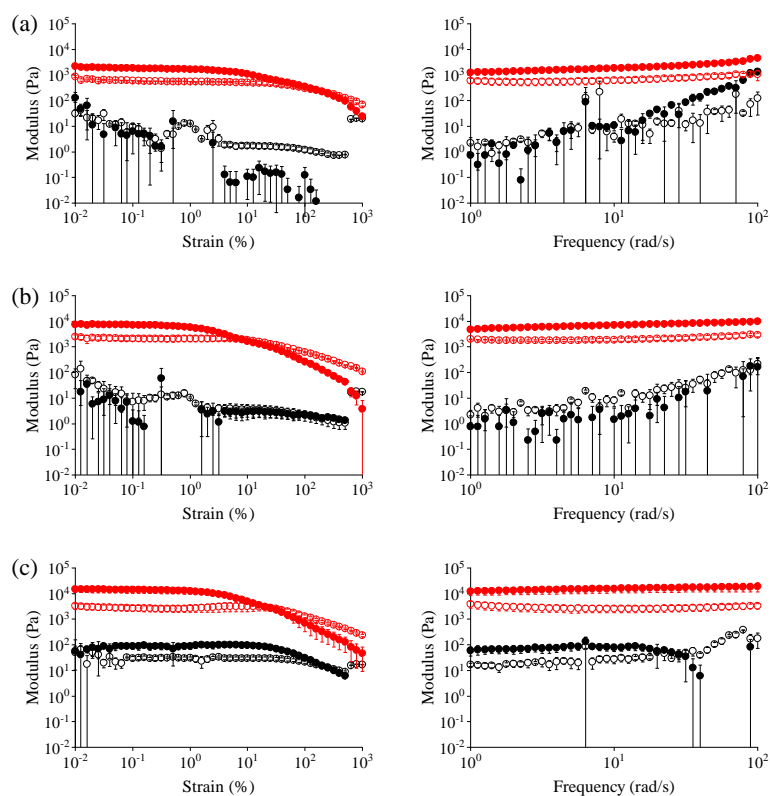
Figure 6.9. Full strain (left) and frequency (right) data for 2NapFF-Na solutions of concentration (a) 60 mg/mL; (b) 75 mg/mL; (c) 100 mg/mL. Black data represents measurements performed at room temperature and red data represents measurements performed at room temperature 2 hours after a heat-cool cycle to 60 ⁰C. G′ is represented by filled circles and G″ by empty circles. Error bars represent the standard deviation between measurements, which were carried out in triplicate.
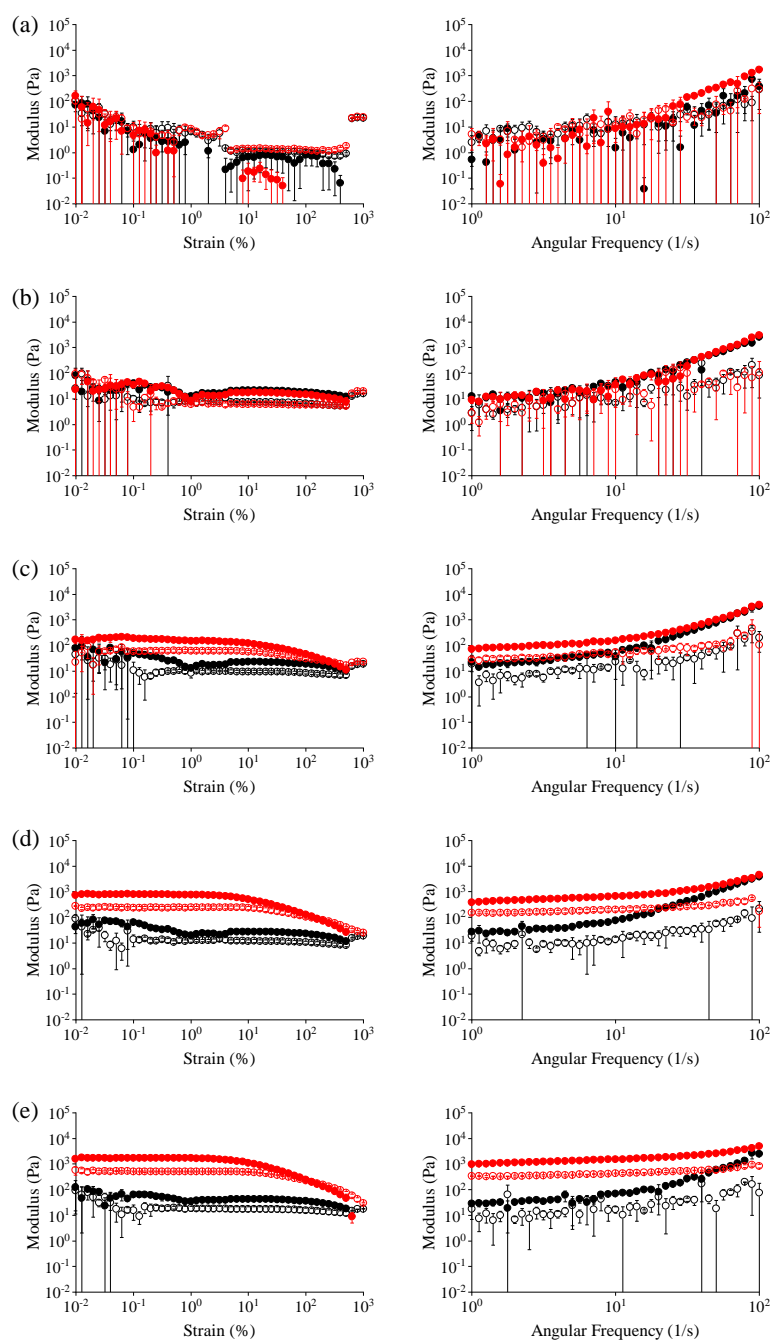
Figure 6.10. Full strain (left) and frequency (right) data for 2NapFF-TBA solutions of concentration (a) 5 mg/mL; (b) 10 mg/mL; (c) 15 mg/mL; (d) 20 mg/mL; (e) 25 mg/mL. Black data represents measurements performed at room temperature and red data represents measurements performed at room temperature 2 hours after a heat-cool cycle to 60 ⁰C. G′ is represented by filled circles and G″ by empty circles. Error bars represent the standard deviation between measurements, which were carried out in triplicate.
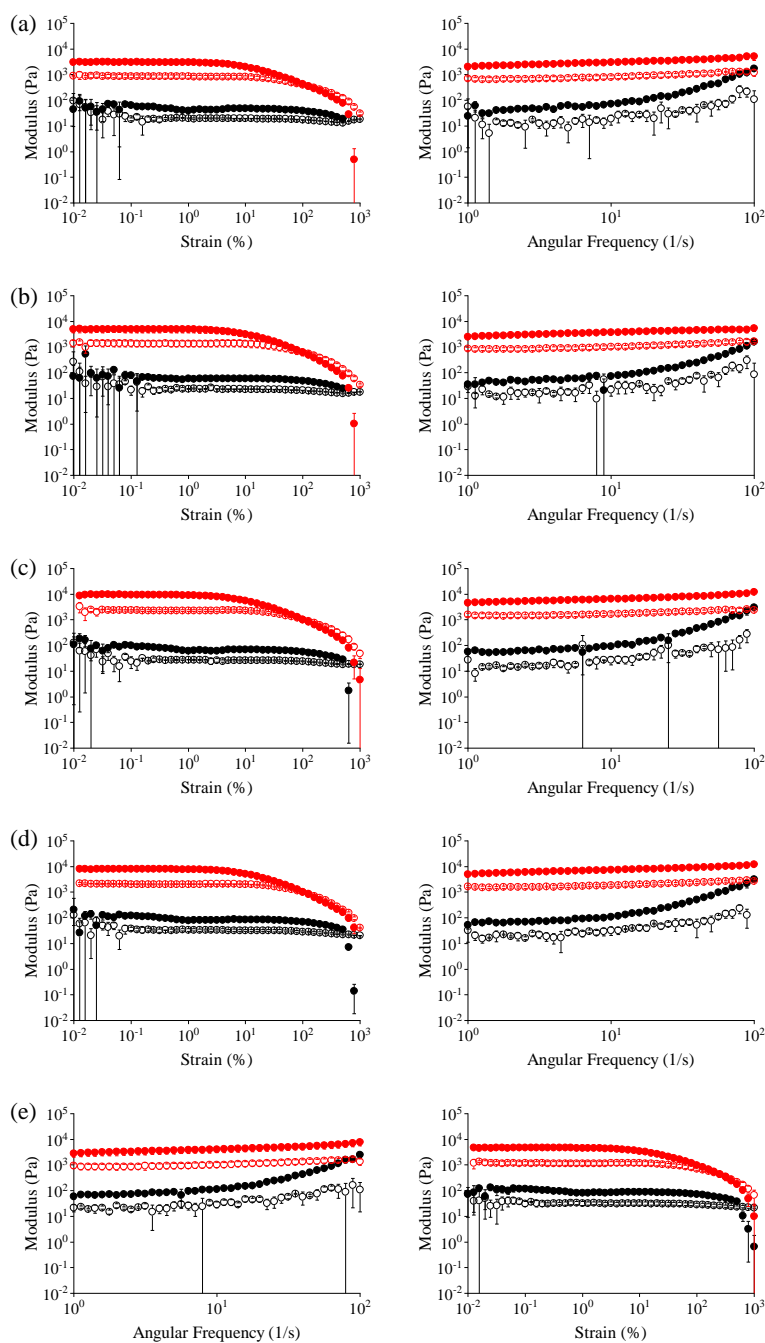
Figure 6.11. Full strain (left) and frequency (right) data for 2NapFF-TBA solutions of concentration (a) 30 mg/mL; (b) 35 mg/mL; (c) 40 mg/mL; (d) 45 mg/mL; (e) 50 mg/mL. Black data represents measurements performed at room temperature and red data represents measurements performed at room temperature 2 hours after a heat-cool cycle to 60 ⁰C. G′ is represented by filled circles and G″ by empty circles. Error bars represent the standard deviation between measurements, which were carried out in triplicate.
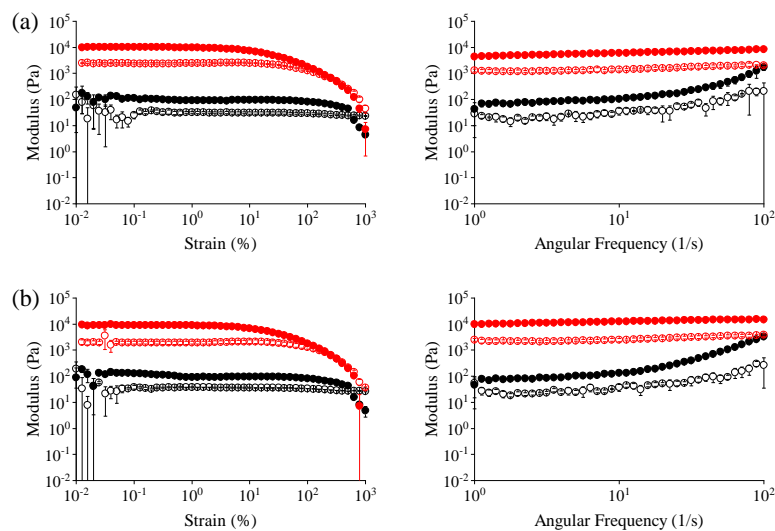
Figure 6.12. Full strain (left) and frequency (right) data for 2NapFF-TBA solutions of concentration (a) 60 mg/mL; (b) 75 mg/mL. Black data represents measurements performed at room temperature and red data represents measurements performed at room temperature 2 hours after a heat-cool cycle to 60 ºC. G′ is represented by filled circles and G″ by empty circles. Error bars represent the standard deviation between measurements, which were carried out in triplicate.
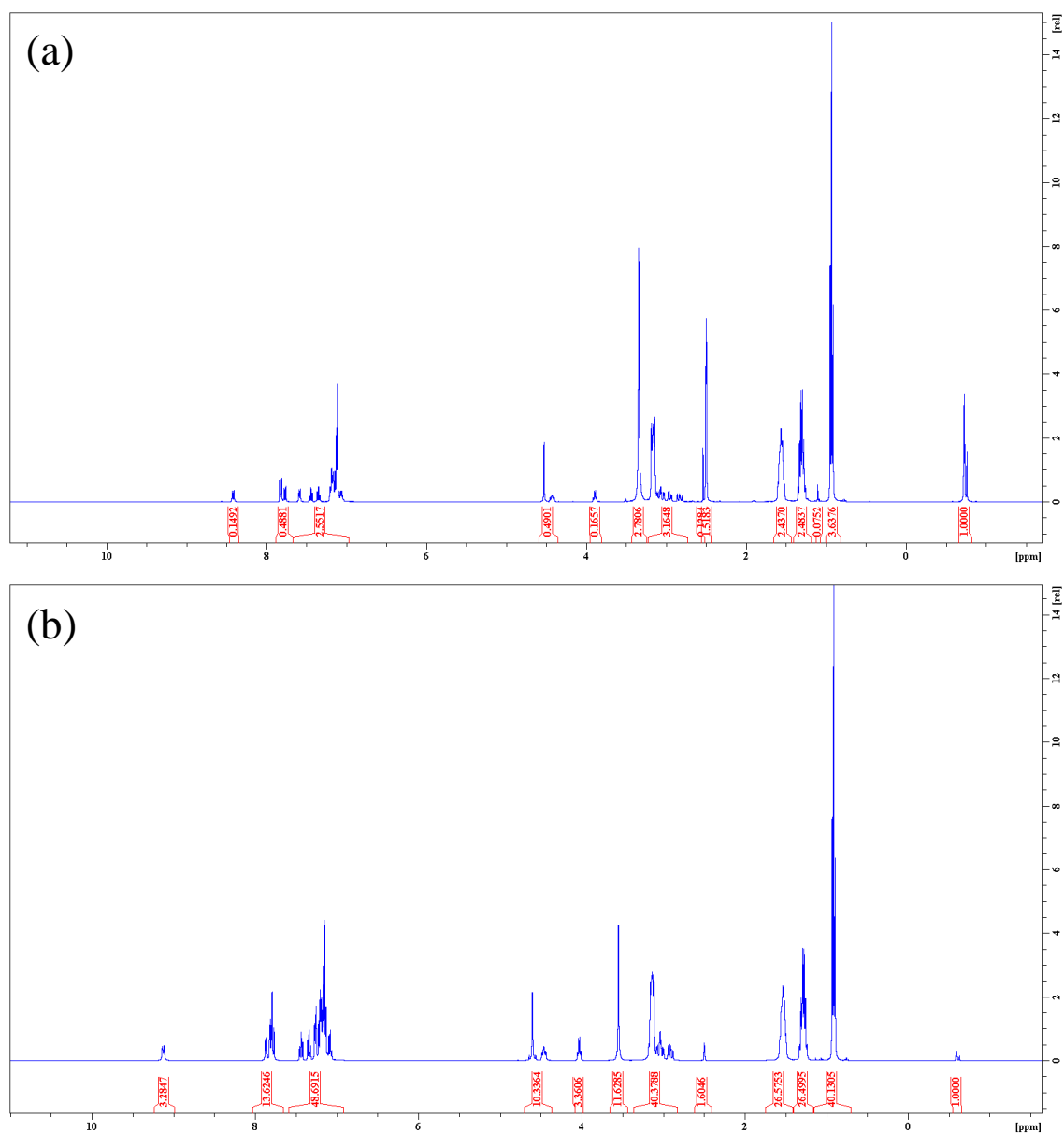
Figure 6.13. Examining the layers of 2NapFF-TBA formed after heat-cool. (a) NMR of top liquid-like layer of 75 mg/mL 2NapFF-TBA formed during heat-cool cycle; (b) NMR of bottom oily layer of 75 mg/mL 2NapFF-TBA formed during heat-cool cycle. Peak at -0.6 ppm is 1% polydimethylsiloxane (PDMS), used to calibrate for integrations.
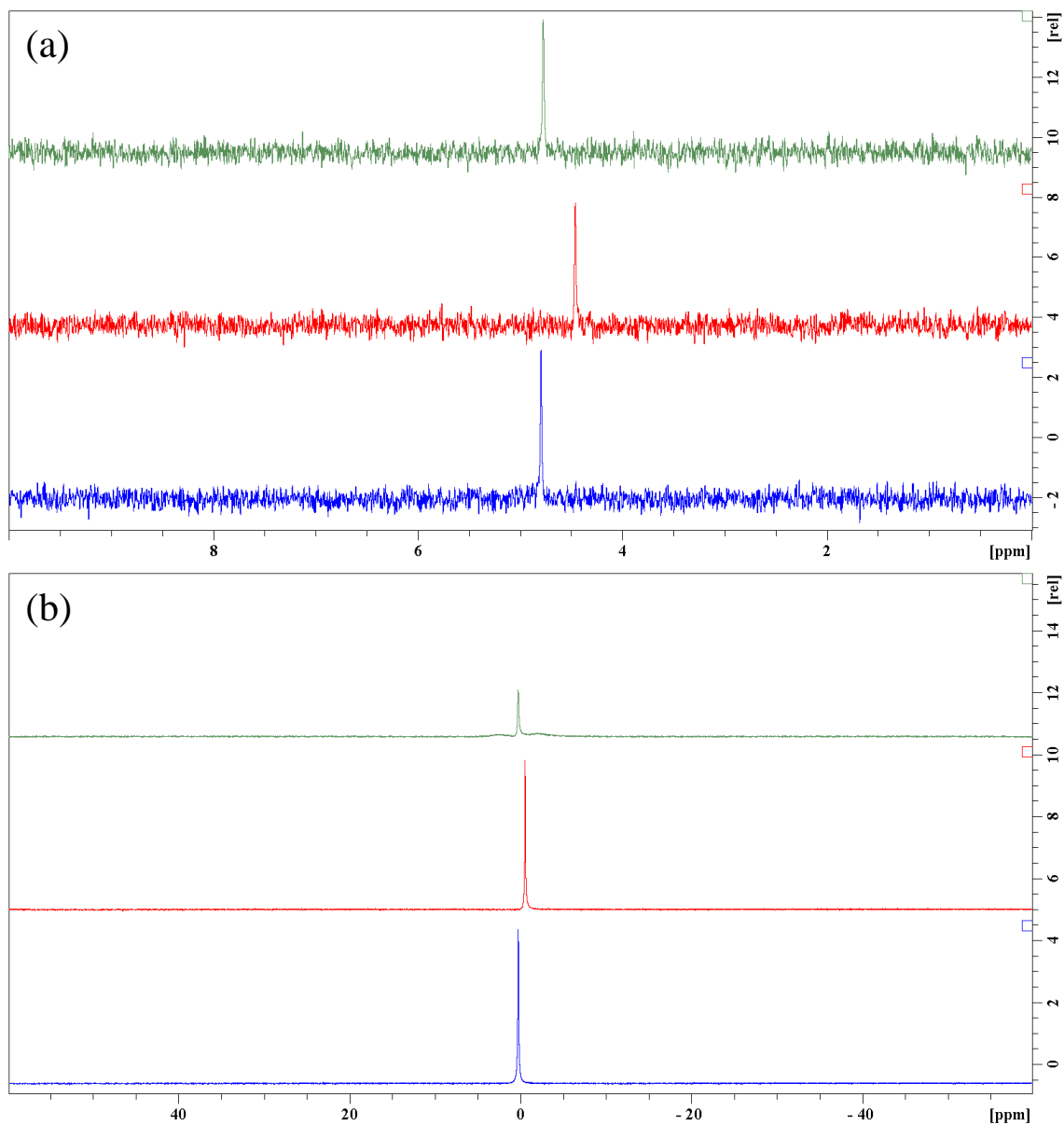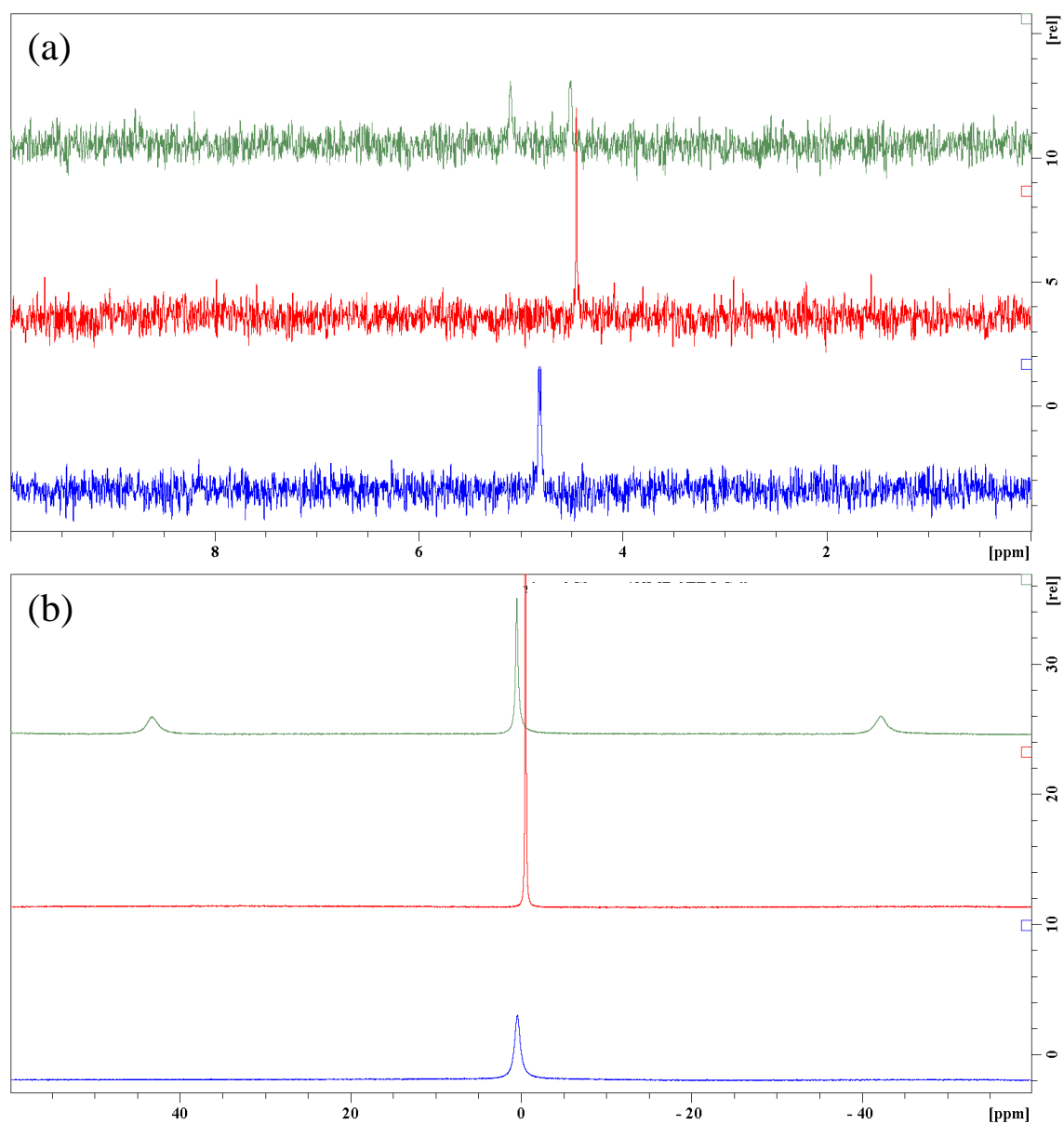
Figure 6.14. (a) ^{2}H and (b) ^{23}Na heat-cool NMR spectroscopy data for 5 mg/mL 2NapFF-Na. Data were collected at 25 °C (green), at 60 °C (red) and then cooled to 25 °C (blue).
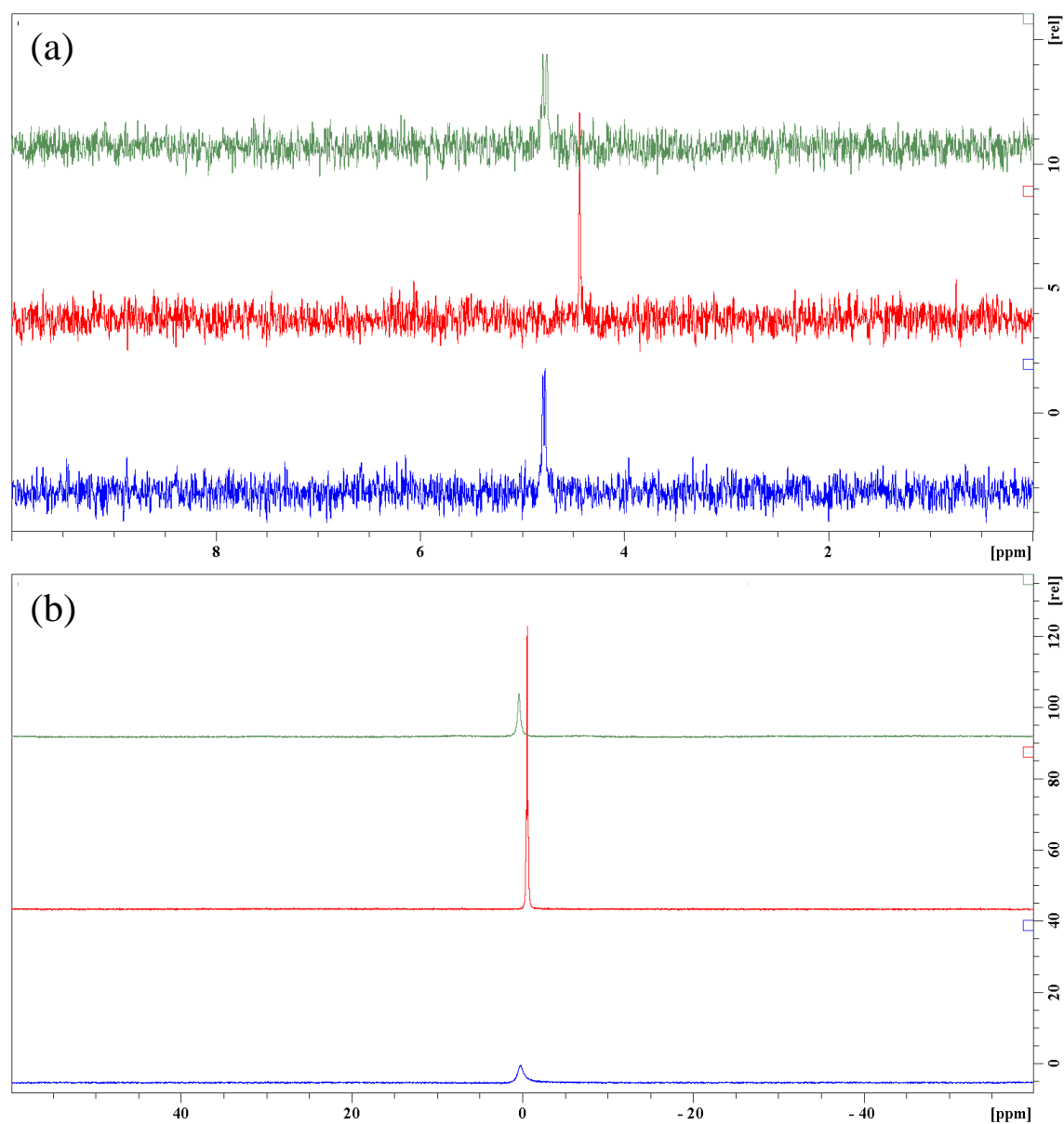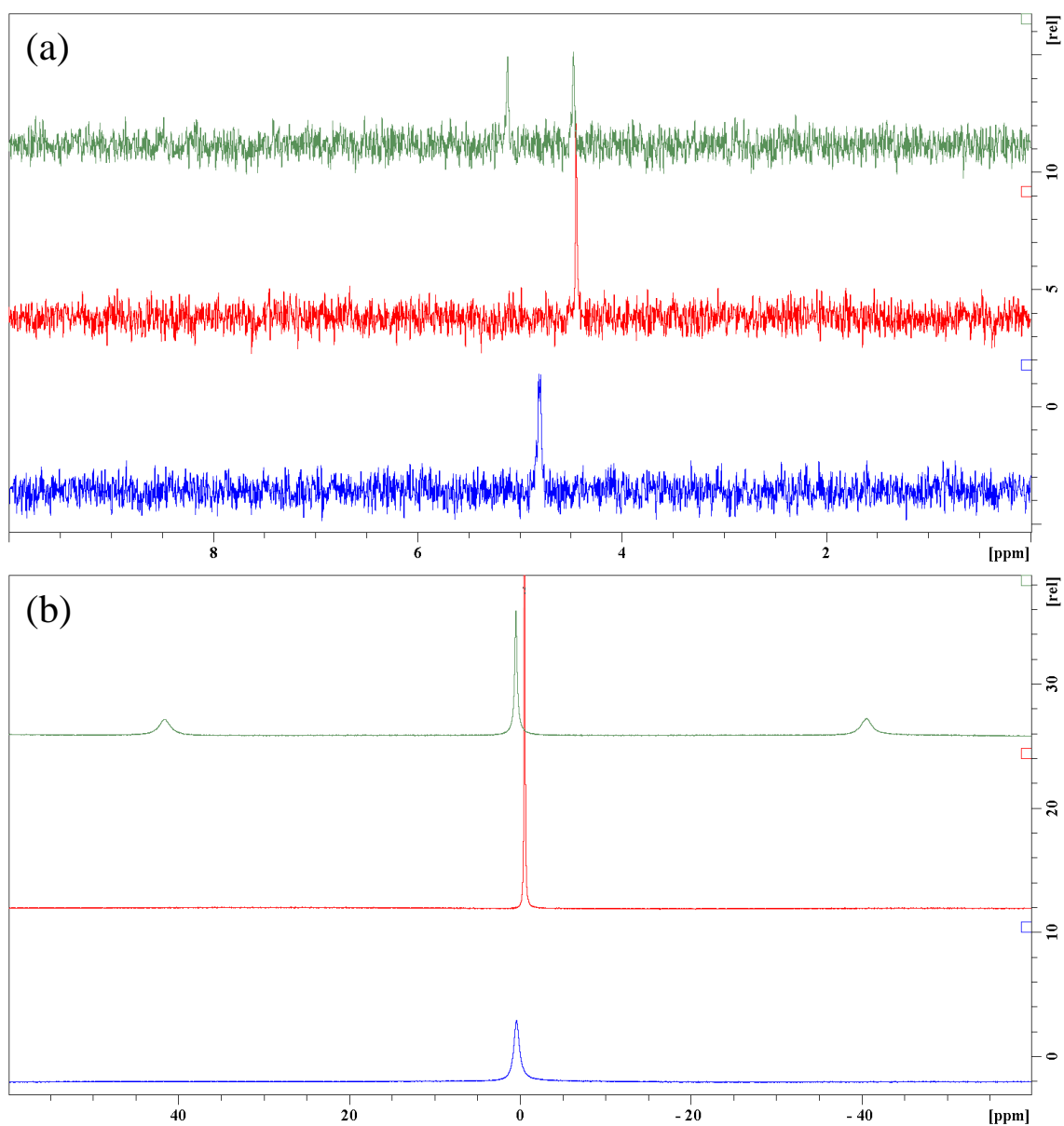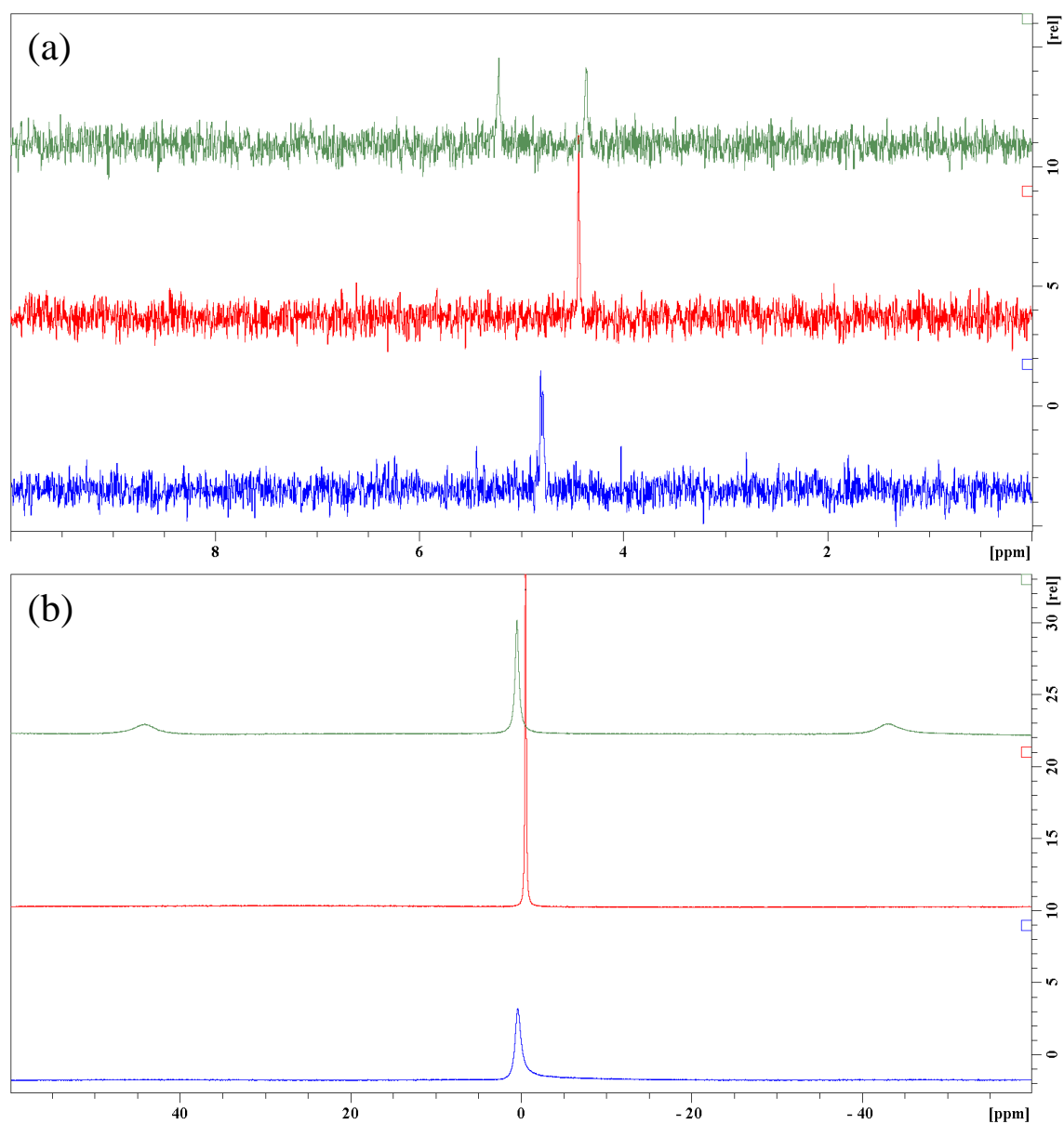
Figure 6.15. (a) ^{2}H and (b) ^{23}Na heat-cool NMR spectroscopy data for 10 mg/mL 2NapFF-Na. Data were collected at 25 °C (green), at 60 °C (red) and then cooled to 25 °C (blue).
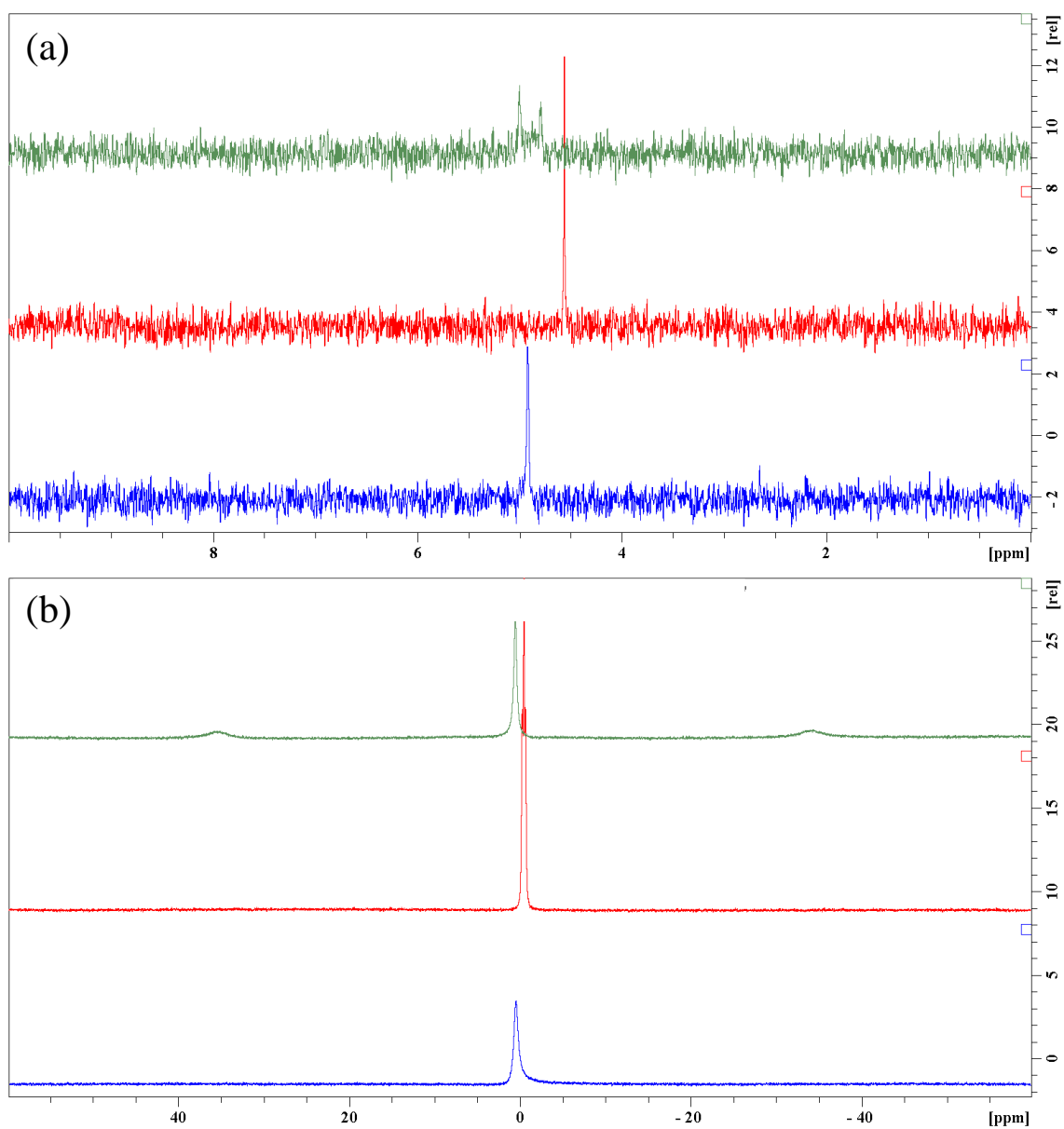
Figure 6.16. (a) ^{2}H and (b) ^{23}Na heat-cool NMR spectroscopy data for 15 mg/mL 2NapFF-Na. Data were collected at 25 °C (green), at 60 °C (red) and then cooled to 25 °C (blue).
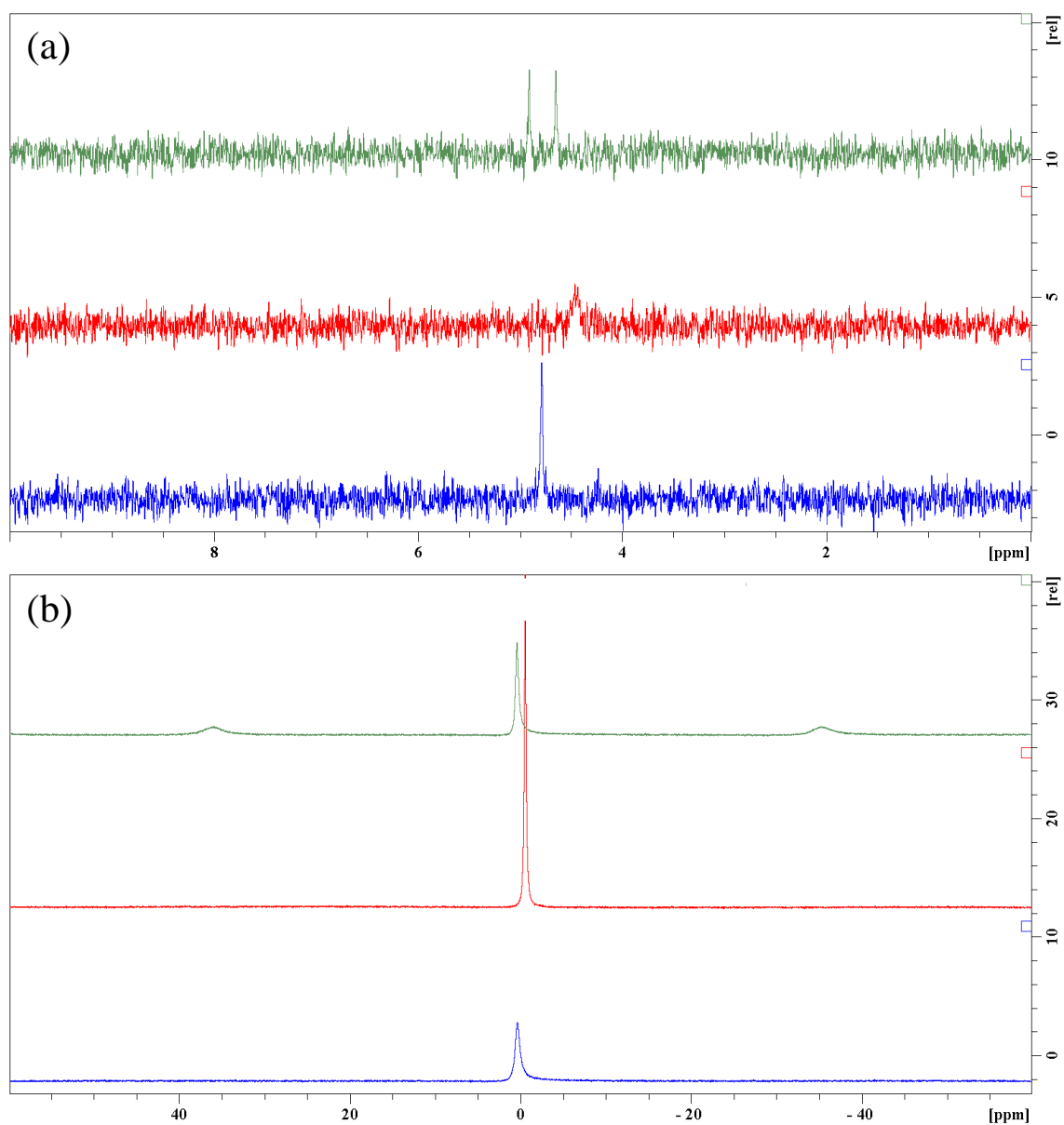
Figure 6.17. (a) ^{2}H and (b) ^{23}Na heat-cool NMR spectroscopy data for 20 mg/mL 2NapFF-Na. Data were collected at 25 °C (green), at 60 °C (red) and then cooled to 25 °C (blue).
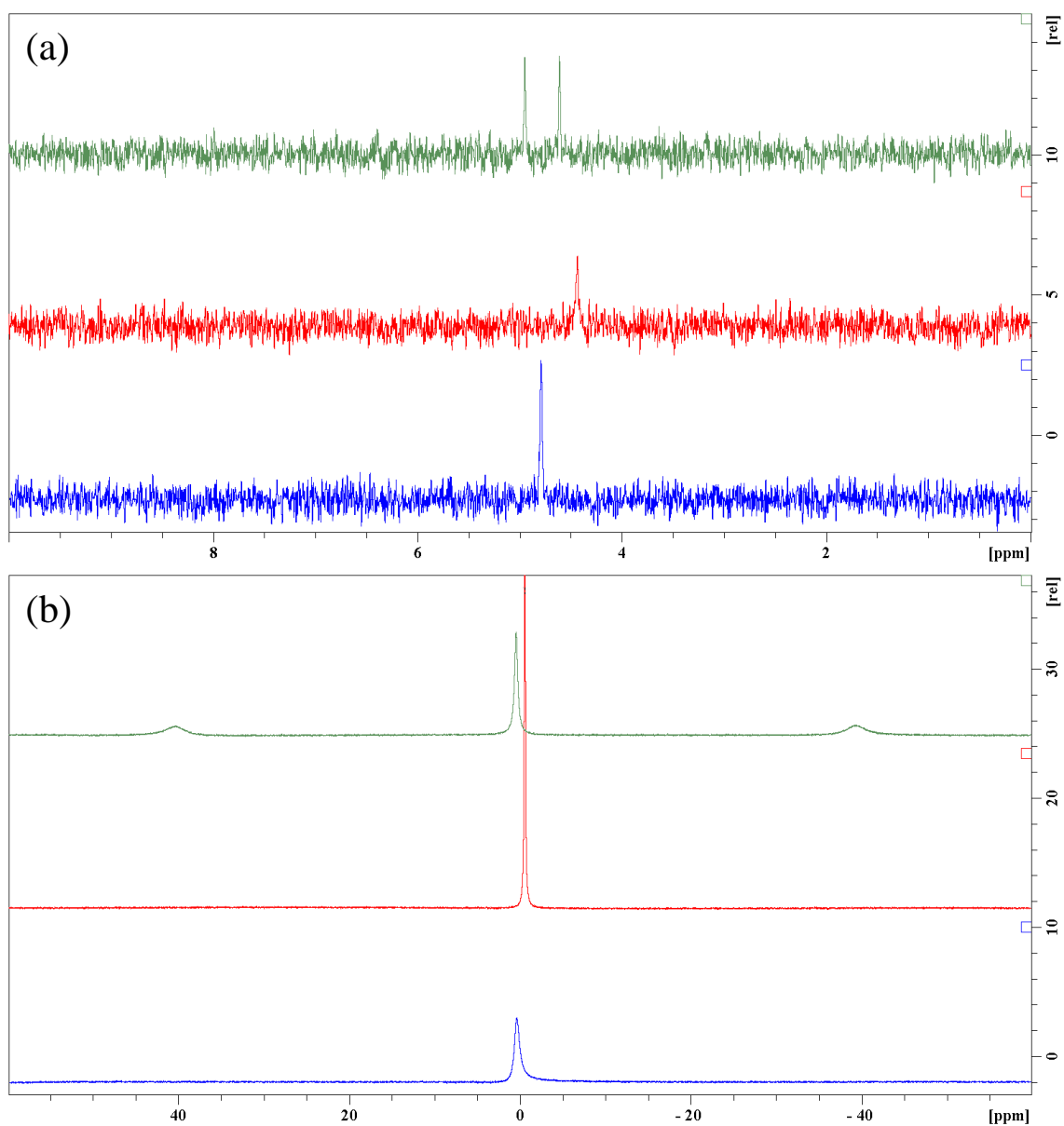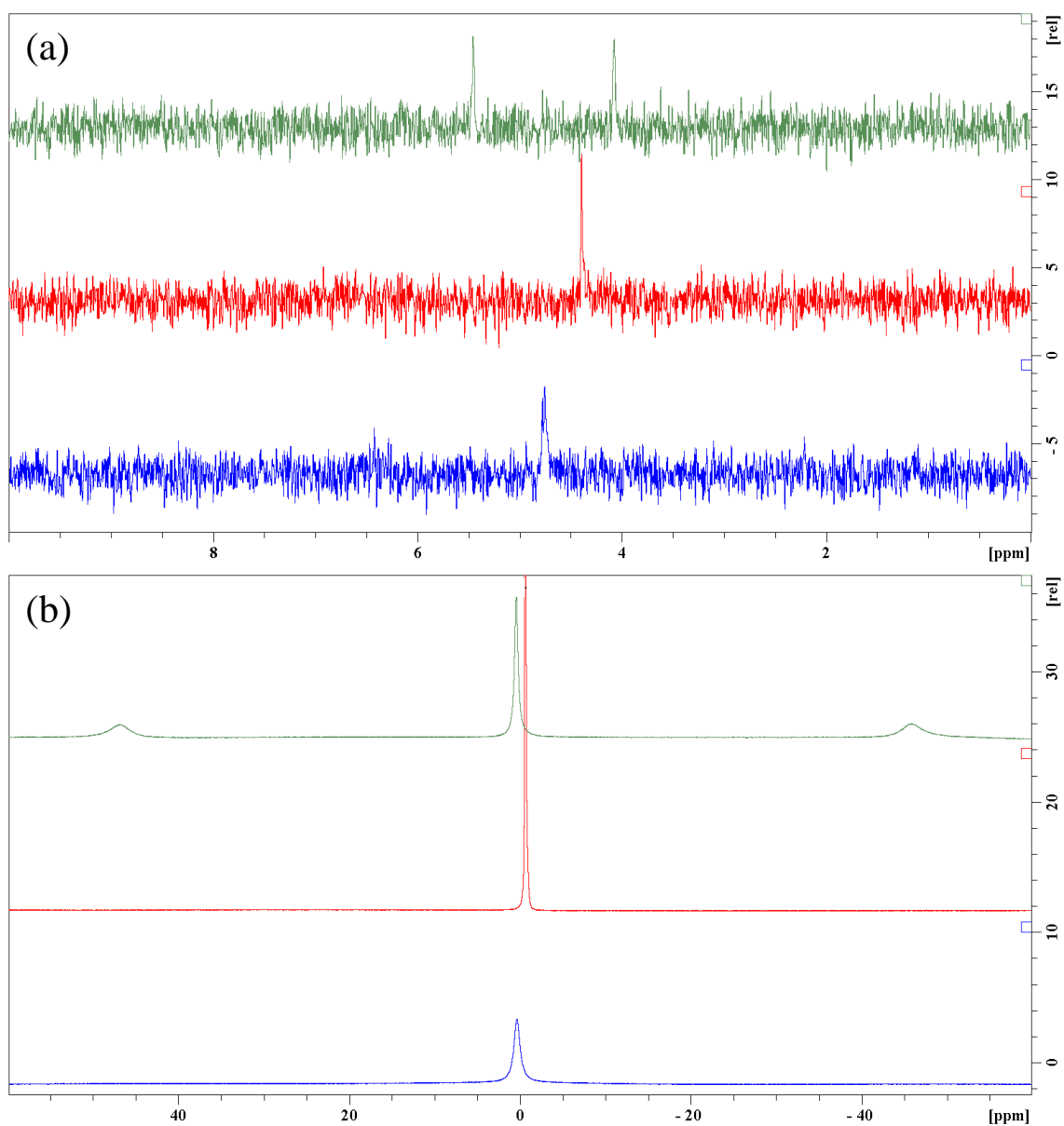
Figure 6.18. (a) ^{2}H and (b) ^{23}Na heat-cool NMR spectroscopy data for 25 mg/mL 2NapFF-Na. Data were collected at 25 °C (green), at 60 °C (red) and then cooled to 25 °C (blue).
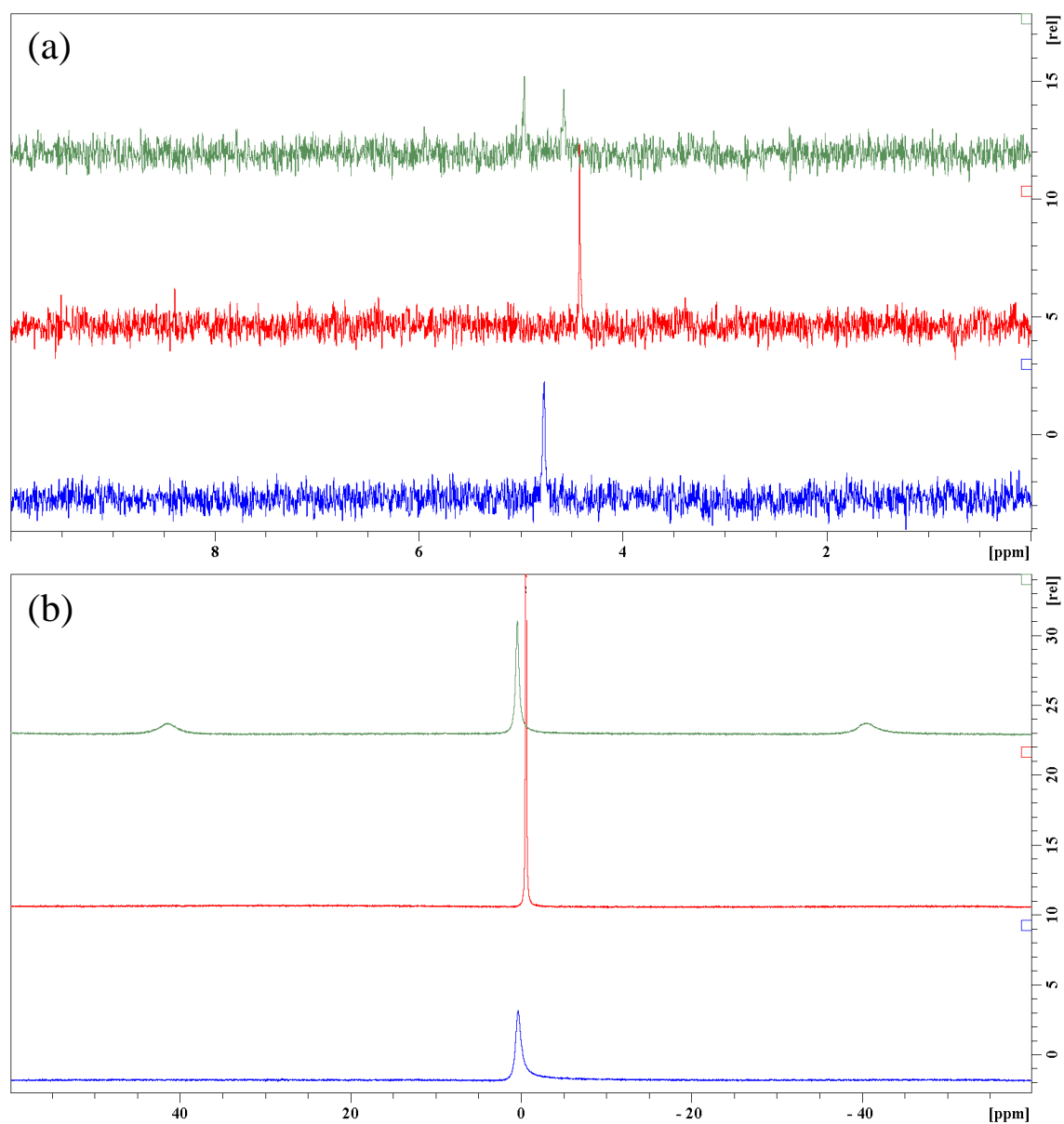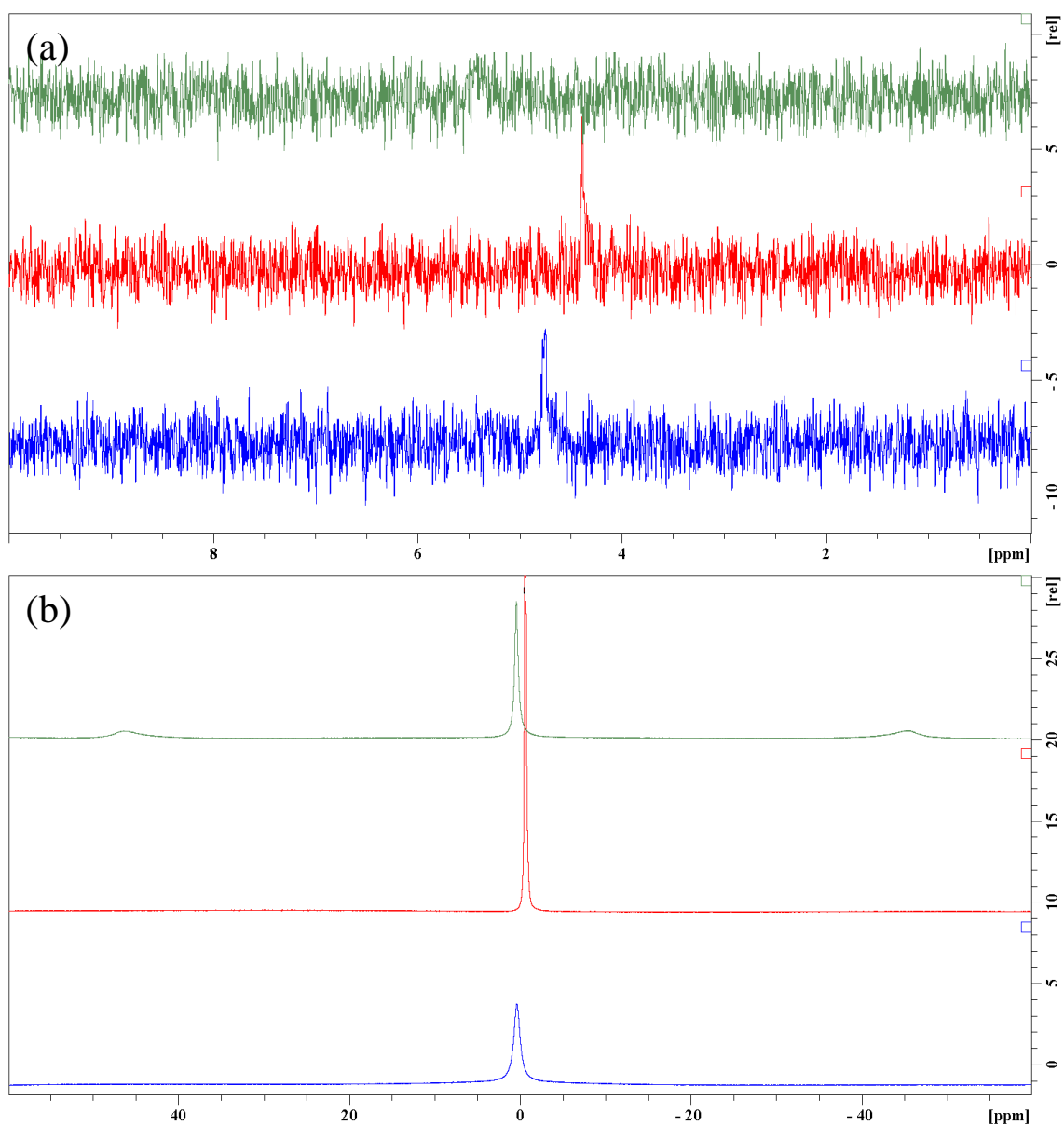
Figure 6.19. (a) ^{2}H and (b) ^{23}Na heat-cool NMR spectroscopy data for 30 mg/mL 2NapFF-Na. Data were collected at 25 °C (green), at 60 °C (red) and then cooled to 25 °C (blue).
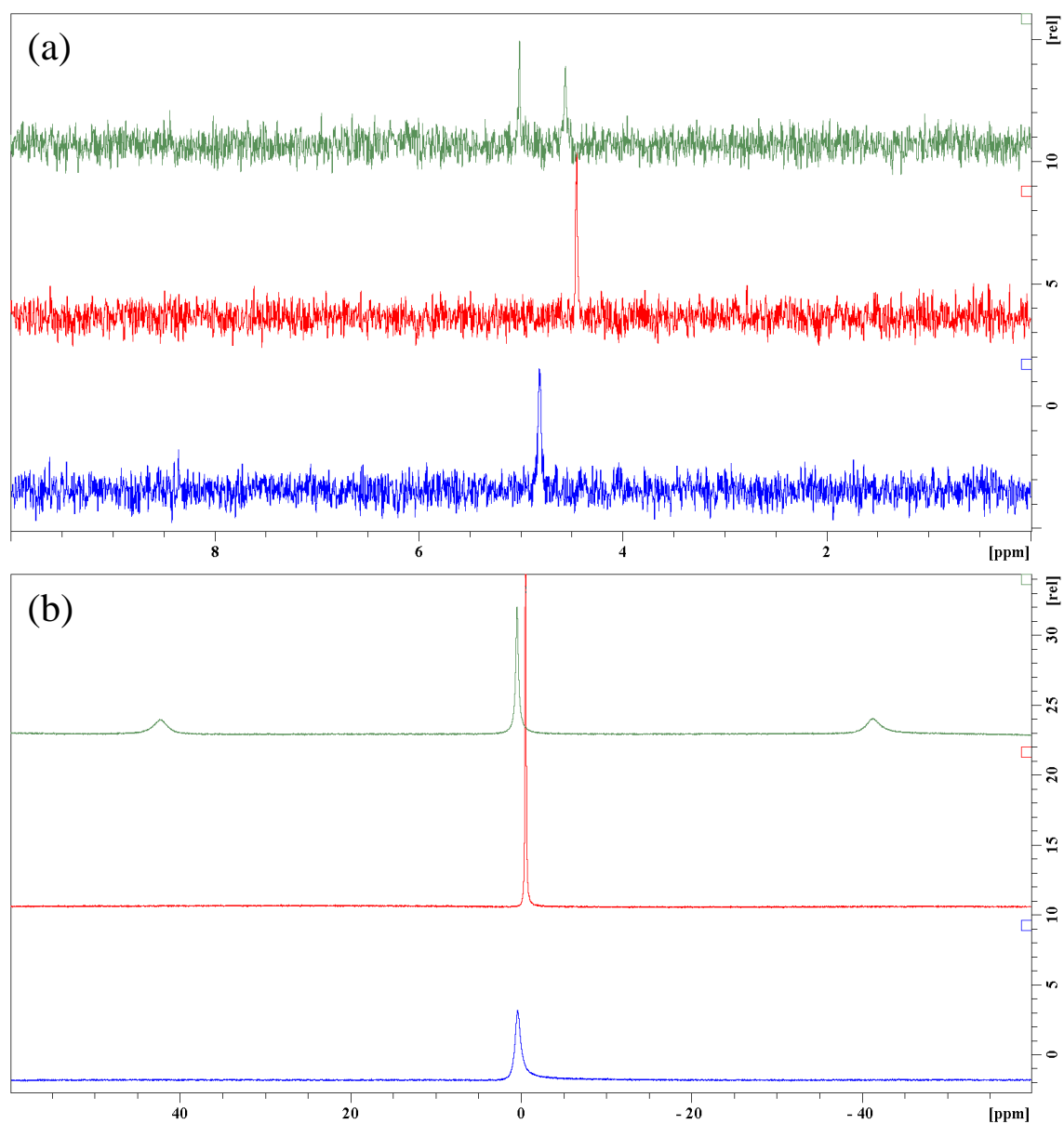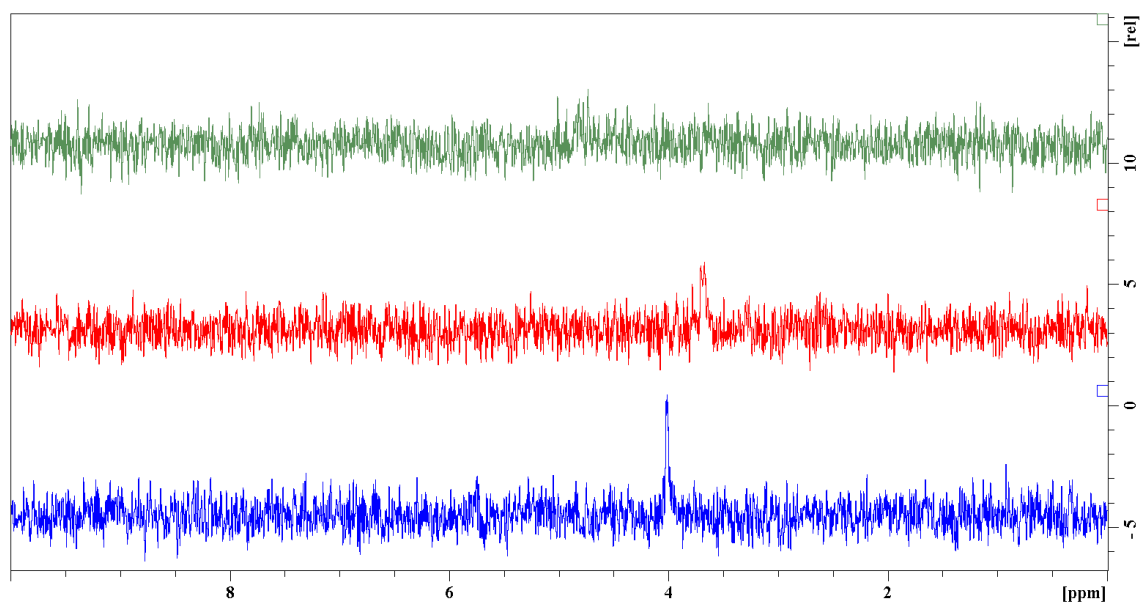
Figure 6.20. (a) ^{2}H and (b) ^{23}Na heat-cool NMR spectroscopy data for 35 mg/mL 2NapFF-Na. Data were collected at 25 °C (green), at 60 °C (red) and then cooled to 25 °C (blue).
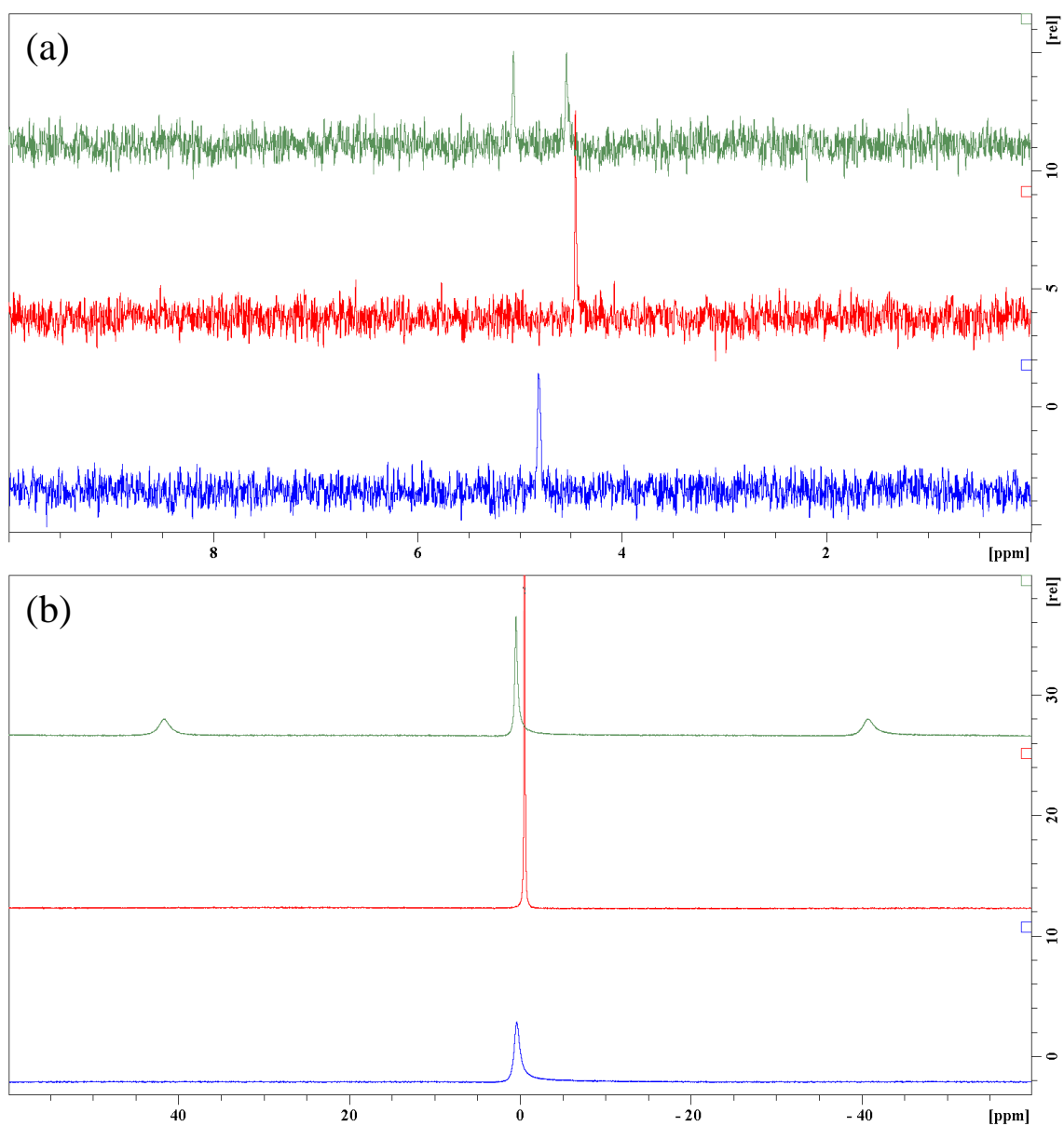
Figure 6.21. (a) ^{2}H and (b) ^{23}Na heat-cool NMR spectroscopy data for 40 mg/mL 2NapFF-Na. Data were collected at 25 °C (green), at 60 °C (red) and then cooled to 25 °C (blue).

Figure 6.22. (a) ^{2}H and (b) ^{23}Na heat-cool NMR spectroscopy data for 45 mg/mL 2NapFF-Na. Data were collected at 25 °C (green), at 60 °C (red) and then cooled to 25 °C (blue).

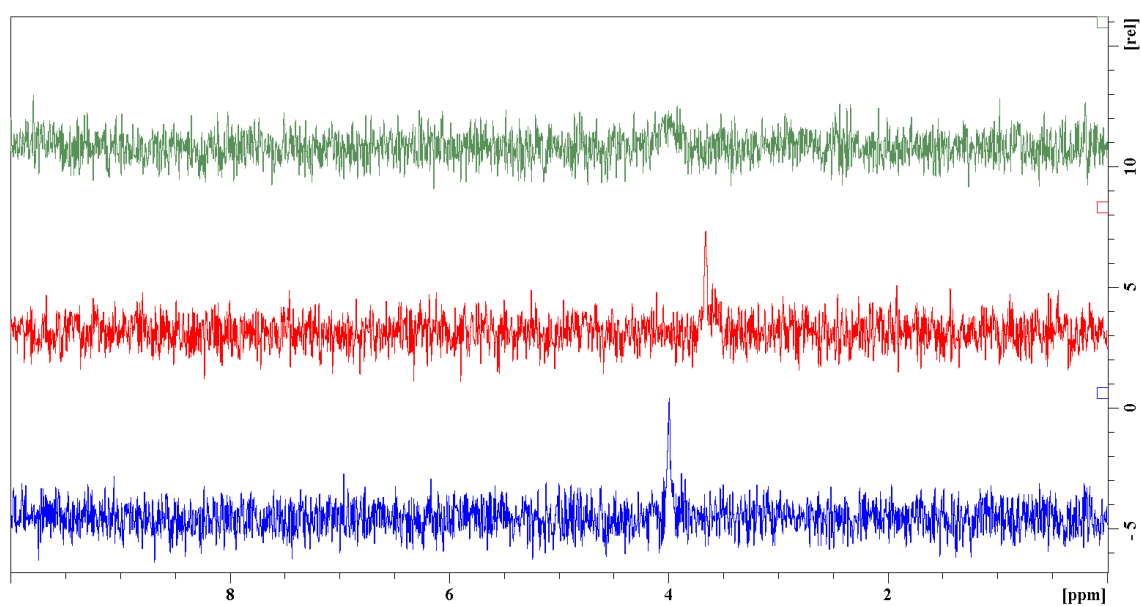**Figure 6.23.** (a) ^{2}H and (b) ^{23}Na heat-cool NMR spectroscopy data for 50 mg/mL 2NapFF-Na. Data were collected at 25 °C (green), at 60 °C (red) and then cooled to 25 °C (blue).
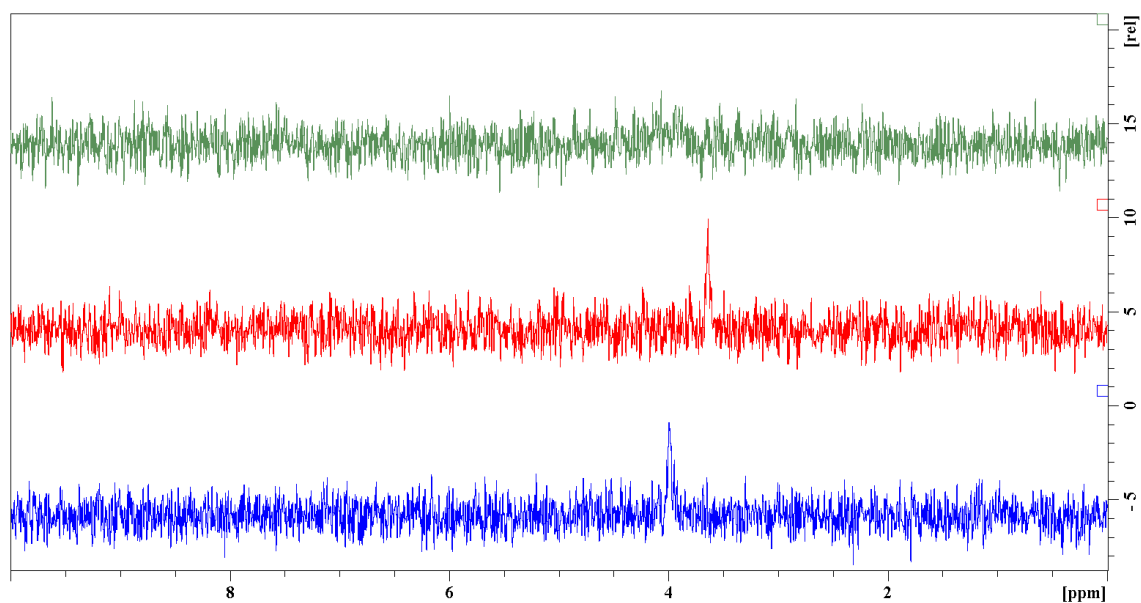
Figure 6.24. (a) ^{2}H and (b) ^{23}Na heat-cool NMR spectroscopy data for 60 mg/mL 2NapFF-Na. Data were collected at 25 °C (green), at 60 °C (red) and then cooled to 25 °C (blue).

Figure 6.25. (a) ^{2}H and (b) ^{23}Na heat-cool NMR spectroscopy data for 75 mg/mL 2NapFF-Na. Data were collected at 25 °C (green), at 60 °C (red) and then cooled to 25 °C (blue).
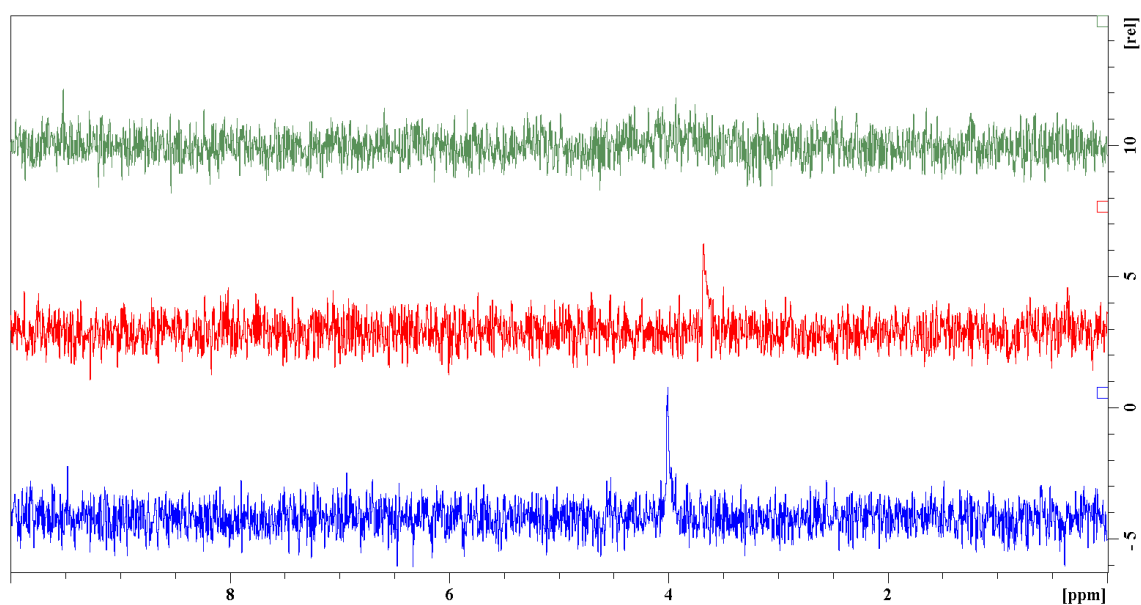
Figure 6.26. (a) ^{2}H and (b) ^{23}Na heat-cool NMR spectroscopy data for 100 mg/mL 2NapFF-Na. Data were collected at 25 °C (green), at 60 °C (red) and then cooled to 25 °C (blue).

Figure 6.27. ^{2}H heat-cool NMR spectroscopy data for 5 mg/mL 2NapFF-TBA. Data were collected at 25 °C (green), at 60 °C (red) and then cooled to 25 °C (blue).

Figure 6.28. ^{2}H heat-cool NMR spectroscopy data for 10 mg/mL 2NapFF-TBA. Data were collected at 25 °C (green), at 60 °C (red) and then cooled to 25 °C (blue).
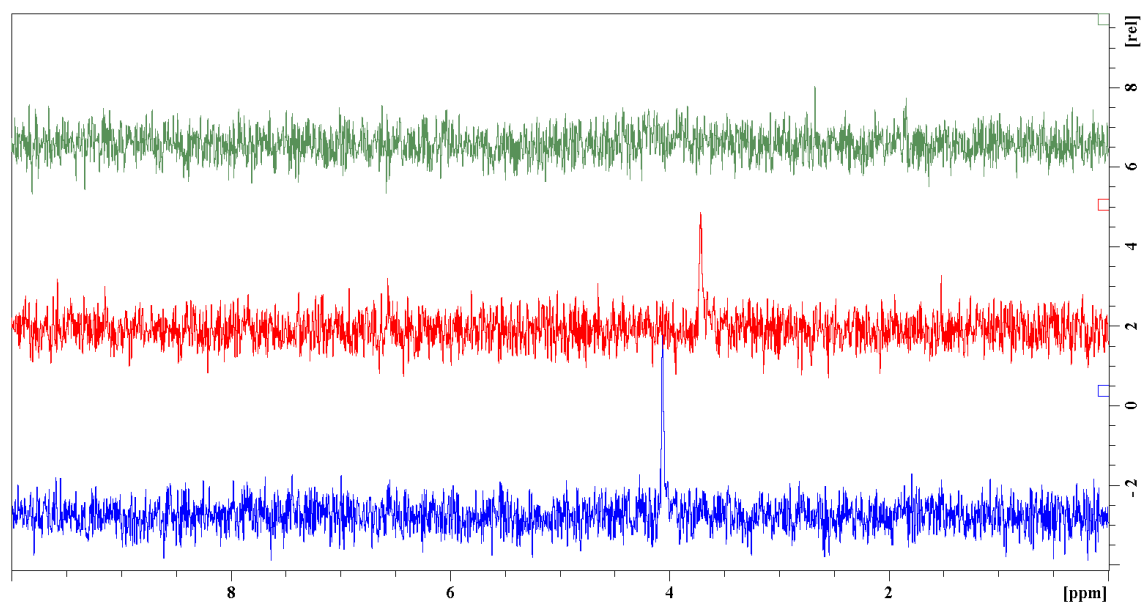
Figure 6.29. ^{2}H heat-cool NMR spectroscopy data for 15 mg/mL 2NapFF-TBA. Data were collected at 25 °C (green), at 60 °C (red) and then cooled to 25 °C (blue).
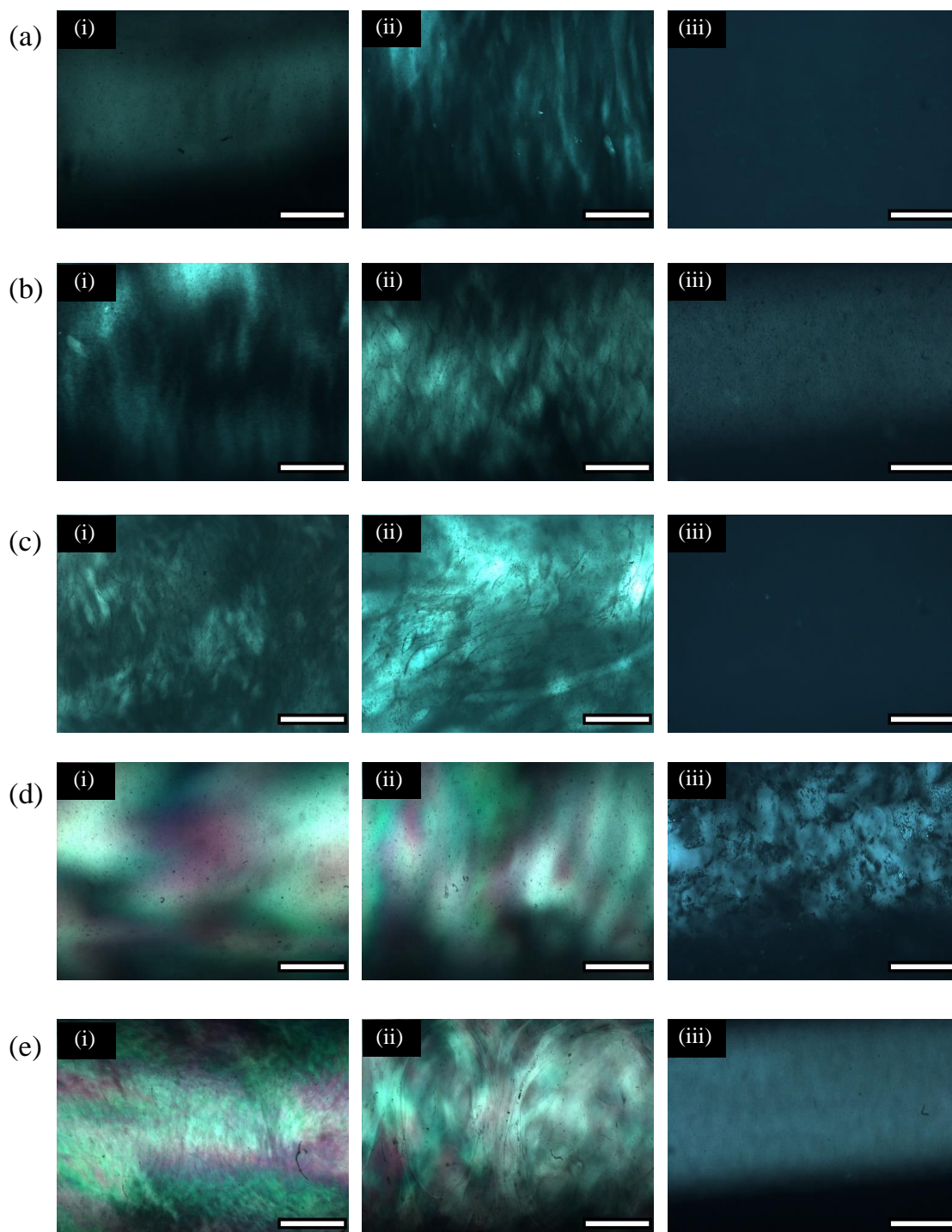

Figure 6.30. ^{2}H heat-cool NMR spectroscopy data for 20 mg/mL 2NapFF-TBA. Data were collected at 25 °C (green), at 60 °C (red) and then cooled to 25 °C (blue).

Figure 6.31. ^{2}H heat-cool NMR spectroscopy data for 25 mg/mL 2NapFF-TBA. Data were collected at 25 °C (green), at 60 °C (red) and then cooled to 25 °C (blue).

Figure 6.32. POM images of 2NapFF-Na at concentrations of (a) 5 mg/mL; (b) 10 mg/mL; (c) 15 mg/mL; (d) 20 mg/mL; (e) 25 mg/mL taken (i) before inserting the sample into the NMR spectrometer; (ii) after inserting the sample into the NMR spectrometer; (iii) after heating the sample to 60 °C and cooling back to 25 °C inside the NMR spectrometer. Scale bars represent 500 µm.
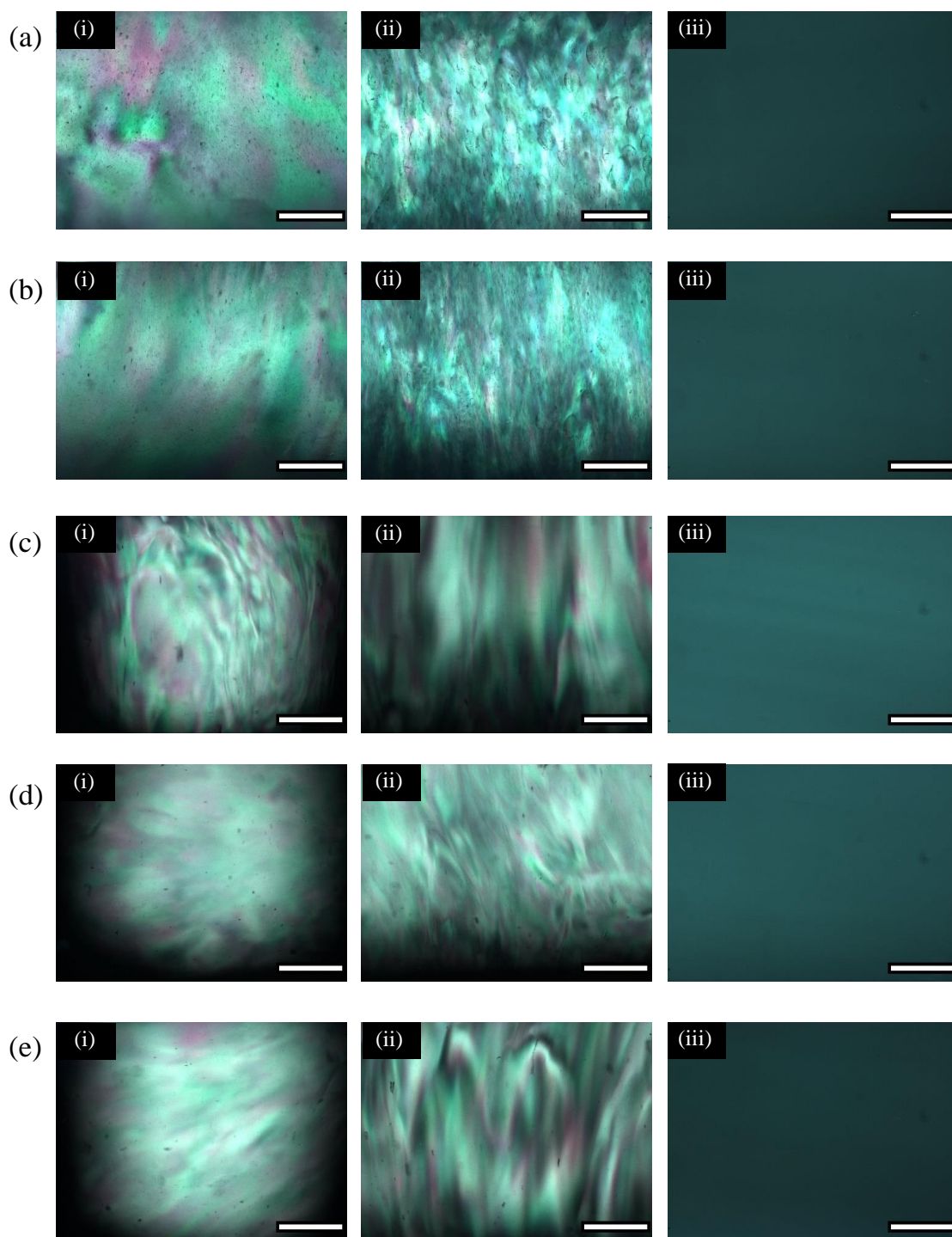
Figure 6.33. POM images of 2NapFF-Na at concentrations of (a) 30 mg/mL; (b) 35 mg/mL; (c) 40 mg/mL; (d) 45 mg/mL; (e) 50 mg/mL taken (i) before inserting the sample into the NMR spectrometer; (ii) after inserting the sample into the NMR spectrometer; (iii) after heating the sample to 60 °C and cooling back to 25 °C inside the NMR spectrometer. Scale bars represent 500 μm.
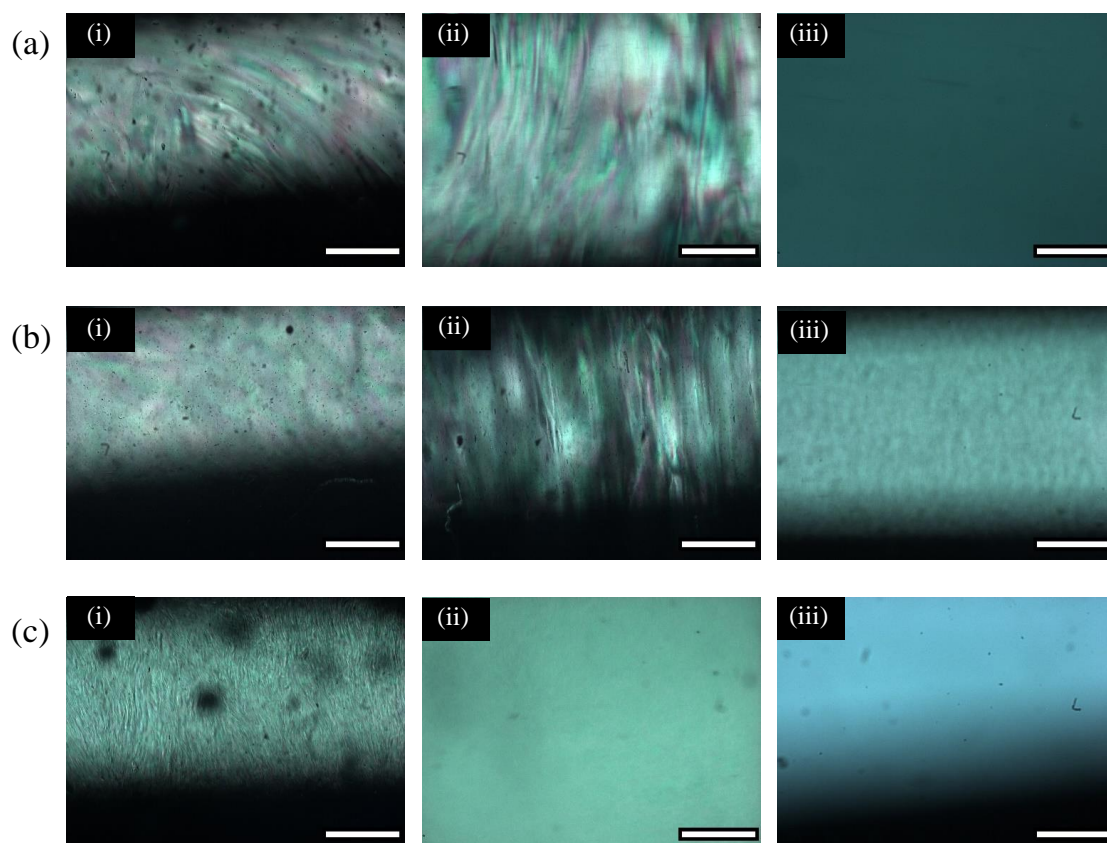
Figure 6.34. POM images of 2NapFF-Na at concentrations of (a) 60 mg/mL; (b) 75 mg/mL; (c) 100 mg/mL taken (i) before inserting the sample into the NMR spectrometer; (ii) after inserting the sample into the NMR spectrometer; (iii) after heating the sample to 60 °C and cooling back to 25 °C inside the NMR spectrometer. Scale bars represent 500 µm.
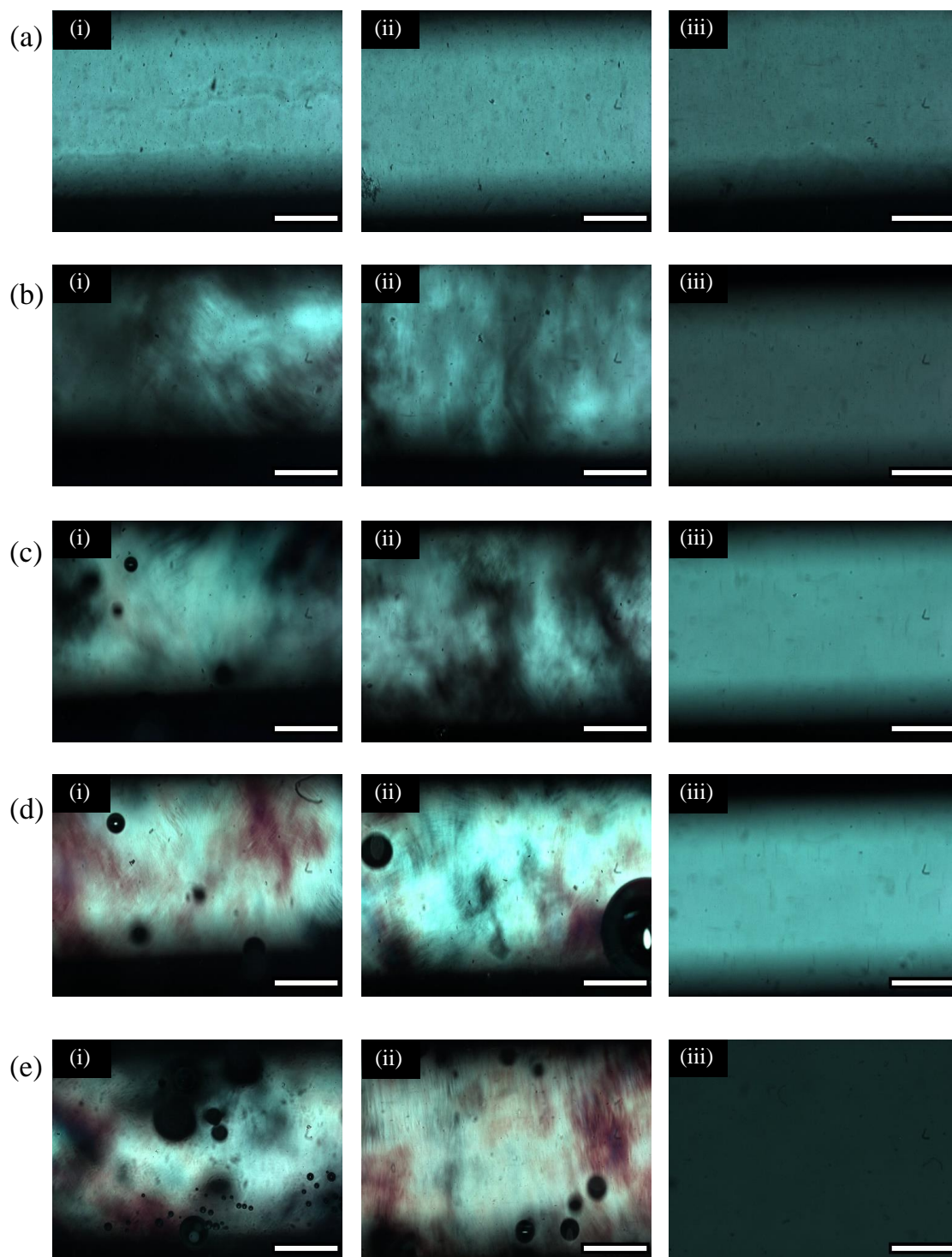
Figure 6.35. POM images of 2NapFF-TBA at concentrations of (a) 5 mg/mL; (b) 10 mg/mL; (c) 15 mg/mL; (d) 20 mg/mL; (e) 25 mg/mL taken (i) before inserting the sample into the NMR spectrometer; (ii) after inserting the sample into the NMR spectrometer; (iii) after heating the sample to 60 °C and cooling back to 25 °C inside the NMR spectrometer. Scale bars represent 500 μm.

6.3. References

1. D. J. Adams and I. Young, *J. Polym. Sci., Part A: Polym. Chem.*, 2008, **46**, 6082-6090.

2. L. Chen, K. Morris, A. Laybourn, D. Elias, M. R. Hicks, A. Rodger, L. Serpell and D. J. Adams, *Langmuir*, 2010, **26**, 5232-5242.

3. B. Dietrich, Coupling of Boc-phenylalanine with phenylalanine ethyl ester hydrochloride; Ethyl (2S)-2-[(2S)-2-{[(tert-butoxy)carbonyl]amino}-3-phenylpropanamido]-3-phenylpropanoate, http://cssp.chemspider.com/Article.aspx?id=924, (accessed 9th May 2022).

4. B. Dietrich, Boc deprotection of BocPhePheOEt; Ethyl (2S)-2-[(2S)-2-amino-3-phenylpropanamido]-3-phenylpropanoate trifluoroacetate salt, http://cssp.chemspider.com/Article.aspx?id=924, (accessed 9th May 2022).

5. B. Dietrich, Coupling of ethyl (2S)-2-[(2S)-2-amino-3-phenylpropanamido]-3-phenylpropanoate trifluoroacetate salt with 2-naphthoxyacetic acid; Ethyl (2S)-2-[(2S)-2-[2-(naphthalen-2-yloxy)acetamido]-3-phenylpropanamido]-3-phenylpropanoate, http://cssp.chemspider.com/Article.aspx?id=924, (accessed 9th May 2022).

6. B. Dietrich, Deprotection of ethyl (2S)-2-[(2S)-2-[2-(naphthalen-2-yloxy)acetamido]-3-phenylpropanamido]-3-phenylpropanoate; (2S)-2-[(2S)-2-[2-(Naphthalen-2-yloxy)acetamido]-3-phenylpropanamido]-3-phenylpropanoic acid, 2-NapFF, 2NapFF, http://cssp.chemspider.com/Article.aspx?id=924, (accessed 9th May 2022).